

NORTHWESTERN UNIVERSITY

Stability and Performance of Oxygen Electrodes for Reversible Solid Oxide Cells

A DISSERTATION

SUBMITTED TO THE GRADUATE SCHOOL
IN PARTIAL FULFILLMENT OF THE REQUIREMENTS

for the degree

DOCTOR OF PHILOSOPHY

Field of Materials Science and Engineering

By

Justin Gary Railsback

EVANSTON, ILLINOIS

December 2016

Abstract

Stability and Performance of Oxygen Electrodes for Reversible Solid Oxide Cells

Justin Gary Railsback

Worldwide, governments are beginning to take action to reduce anthropogenic CO₂ emissions in order to mitigate the extent of global climate change. The largest fraction of global CO₂ emission comes from electrical power generation, which is rapidly being replaced by wind and solar installations. The intermittent nature of renewable resources requires that large scale energy storage be implemented to ensure grid stability. Pumped hydro storage is currently the only technology available for large scale energy storage; however, pumped hydro remains geographically confined and susceptible to seasonal fluctuations and offers limited discharge hours. Recent system level models predict that reversible solid oxide cells may be a competitive solution, but two key advancements are required to realize the technology: low cell resistance ($<0.2 \Omega \cdot \text{cm}^2$ at $<650 \text{ }^\circ\text{C}$), particularly low polarization resistance at the oxygen electrode, and low degradation rate ($<0.5\%/ \text{hr}$ for 50,000 hours). The oxygen electrode is typically the largest contributor to the total cell resistance, and when a cell is operated in electrolysis the oxygen electrode is known to degrade quickly. This work focuses on both aspects of the oxygen electrode.

A Pr₂NiO₄ based electrode is developed that has improved phase stability and good polarization resistance ($\sim 0.1 \Omega \cdot \text{cm}^2$ at $650 \text{ }^\circ\text{C}$). The electrode is prepared by wet chemical impregnation (infiltration) of Pr₂NiO₄ precursors into a La_{0.9}Sr_{0.1}Ga_{0.8}Mg_{0.2}O₃ scaffold. Electrochemical data for

a number cells is presented and the number of infiltrations is optimized. Preliminary life tests and x-ray data are presented.

Pressurization of the oxygen electrode is predicted to decrease its polarization resistance and pressurization of the reversible solid oxide cell system is desirable to achieve high round-trip efficiency. The electrochemical performance of mixed electronic-ionic conducting electrodes has not been reported above 1 atm. Four candidate electrodes are examined under pressurization up to 10 atm: Pr_2NiO_4 infiltrated $\text{La}_{0.9}\text{Sr}_{0.1}\text{Ga}_{0.8}\text{Mg}_{0.2}\text{O}_3$, $\text{Sm}_{0.5}\text{Sr}_{0.5}\text{CoO}_3$ infiltrated $\text{Ce}_{0.9}\text{Gd}_{0.1}\text{O}_2$, single phase $\text{La}_{0.6}\text{Sr}_{0.4}\text{Co}_{0.2}\text{Fe}_{0.8}\text{O}_3$, and single phase Nd_2NiO_4 . The role of the ion conduction mechanism (vacancy or interstitial) is explored in relation to the decrease in polarization resistance with increased pressure.

Current switched life-tests designed to emulate reversible solid oxide cell operating conditions were performed for a range of current densities and overpotentials on three candidate systems: composite $\text{La}_{0.7}\text{Sr}_{0.3}\text{MnO}_3\text{-Zr}_{0.84}\text{Y}_{0.16}\text{O}_2$, single phase $\text{La}_{0.6}\text{Sr}_{0.4}\text{Co}_{0.2}\text{Fe}_{0.8}\text{O}_3$, and La_2NiO_4 infiltrated $\text{La}_{0.9}\text{Sr}_{0.1}\text{Ga}_{0.8}\text{Mg}_{0.2}\text{O}_3$. The degradation mode of each system is determined by impedance spectroscopy and post-test microstructural analysis. Operating regions of improved stability are identified for each system based on the measured degradation rates. Overpotential is determined to be the major controlling factor in $\text{La}_{0.7}\text{Sr}_{0.3}\text{MnO}_3\text{-Zr}_{0.84}\text{Y}_{0.16}\text{O}_2$.

Analysis and modeling for predicting the long term degradation of an infiltrated electrode is presented. Coarsening of the nanoscale features is thought to be the main contributor to degradation under annealing for infiltrated electrodes and so a combined electrochemical – coarsening model is presented to understand the limitations of such an electrode. The model is fit to prior results to better understand the trade-off between coarsening rate and initial good

performance. A figure of merit is presented for selecting materials for infiltration that takes into account the coarsening behavior.

Acknowledgements

I'm deeply grateful to the mentors, colleagues, friends and family that supported me during production of this work. I could not have asked for a more patient, dedicated, and generally humane advisor than Prof. Scott Barnett. He's been a gold standard example of a good scientist and mentor, and I'm proud to have been his student.

I'd like to thank my colleagues in the lab who have always been a source of fun and inspiration. The students and mentors before me: Zhan Gao, Kyle Yakal-Kremski, Ann Call, Gareth Hughes, Beth Miller, Dan Fowler, Patrick Duffy, and David Kennouche were knowledgeable and a pleasure to work with. The work Gareth and Ann performed served as a foundation for many of the developed works presented in this thesis. Kyle has been a particularly good friend to me. I have also immensely enjoyed working with students that have joined since I've been here: Hongqian Wang, Qinyuan Liu, Xiankai Yu, Sam Miller, Max Dylla, and Matthew Lu. Matthew will be continuing the current switching work presented here.

Many thanks to my longtime friend and roommate Peter Girouard for being a light-hearted sounding board to my scientific frustrations. To Amelia Plunk for shaping much of my early experience here in Evanston and Chicago. Thanks to Dina Kats for her continued support and camaraderie. To my parents Brian and Sandra for being supportive of my desire to move to Illinois to become a scientist and everything else. To my siblings Travis and Cadence for their boundless

merriment and perspective. To my late grandparents Charles and Patricia who I'm sure would be proud. To all my other friends and colleagues who have made the past four years some of the best I've had. Thanks, folks! It wouldn't have happened without you.

Finally, I'd like to acknowledge the funding sources that made this work possible: The Institute for Sustainability and Energy at Northwestern (ISEN), Stanford Global Climate and Energy Project (GCEP), and the United States Department of Energy (DOE).

Contents

List of Tables.....	10
List of Figures	11
Chapter 1	19
1.1 Introduction and Overview.....	19
Chapter 2: Background.....	22
2.1 Climate Change, Renewable Energy Adoption, and Energy Storage	22
2.2 Solid Oxide Fuel Cells	26
2.2.1 Electrochemistry.....	27
2.2.1.1 Reactions	27
2.2.1.2 Nernst Potential	28
2.2.2 Kinetics.....	29
2.2.2.1 Activation Polarization.....	30
2.2.2.2 Ohmic Polarization.....	32
2.2.2.3 Concentration Polarization.....	32
2.3 Reversible Solid Oxide Cells	34
2.3.1 Introduction	34
2.3.2 Electrolysis and energy storage	35
2.3.2.1 Efficiency of storage	35
2.3.2.2 Storage Chemistry and Thermodynamic Considerations.....	37
2.3.3 Comparison to other storage methods.....	40
2.4 Current State of the Art Solid Oxide Cell Materials	41
2.4.1 Electrolytes.....	42
2.4.2 Fuel Electrode materials.....	44
2.4.3 Oxygen electrode materials.....	48
2.5 Degradation in SOC Oxygen Electrodes.....	63
2.5.1 Degradation in Electrolysis	63
2.5.2 Other Degradation Phenomena.....	68
2.5.2.1 Cation Segregation	68
2.5.2.2 Coarsening.....	70
2.5.2.3 Silver Migration	72

Chapter 3: Methods	73
3.1 Electrochemical Impedance Spectroscopy	73
3.1.1 General Method.....	73
3.1.2 Circuit Modeling	75
3.1.3 Current Switched Setup.....	79
3.1.4 Pressurized Setup	80
3.2 SEM/EDS	82
3.2.1 Sample Preparation	82
3.2.2 Imaging Conditions	83
Chapter 4: Oxygen electrode characteristics of Pr ₂ NiO _{4+δ} -infiltrated porous (La _{0.9} Sr _{0.1})(Ga _{0.8} Mg _{0.2})O _{3-δ}	85
4.1 Introduction	85
4.2 Experimental	87
4.3 Results and Discussion.....	89
4.3.1 Processing and Phase Formation.....	89
4.3.2 Phase Stability	92
4.3.3 Electrochemical Characteristics	94
4.3.4 Electrochemical Stability	97
4.3.5 Comparison with Other MEIC Electrodes	98
4.4 Conclusions	99
Chapter 5: High-Pressure Performance of Mixed-Conducting Oxygen Electrodes: Effect of Interstitial Versus Vacancy Conductivity	101
5.1 Introduction	101
5.2 Experimental	102
5.2.1 Single Phase LSCF Symmetric Cell Fabrication	103
5.2.2 Single Phase NNO Symmetric Cell Fabrication	103
5.2.3 SSC Infiltrated GDC Symmetric Cell Fabrication.....	104
5.2.4 Pr ₂ NiO ₄ Infiltrated LSGM Symmetric Cell Fabrication	104
5.2.5 Pressurized Electrochemical Impedance Spectroscopy (EIS) and Analysis.....	105
5.3 Results	106
5.4 Discussion	112
5.5 Conclusions	121

5.6 Acknowledgements	121
Chapter 6: Current-Switched Life Tests.....	122
6.1 Introduction	122
6.2 Degradation of $(\text{La}_{0.8}\text{Sr}_{0.2})_{0.98}\text{MnO}_{3-\delta}$ - $\text{Zr}_{0.84}\text{Y}_{0.16}\text{O}_{2-\gamma}$ Composite Electrodes During Reversing Current Operation	122
6.2.1 Introduction	122
6.2.2 Experimental	124
6.2.3 Results	125
6.2.3.1 Incrementally Stepped Cycled Current Density.....	125
6.2.3.2 Constant Cycled Current Density.....	128
6.2.3.3 SEM-EDS Analysis.....	132
6.2.4 Discussion	134
6.2.5 Conclusions	138
6.2.6 Acknowledgements	139
6.3 Separating the Roles of Current Density and Overpotential in $(\text{La}_{0.8}\text{Sr}_{0.2})_{0.98}\text{MnO}_{3-\delta}$ - $\text{Zr}_{0.84}\text{Y}_{0.16}\text{O}_{2-\gamma}$ Composite Electrodes During Reversing Current Operation.....	139
6.4 Degradation of $\text{La}_{0.6}\text{Sr}_{0.4}\text{Fe}_{0.8}\text{Co}_{0.2}\text{O}_{3-\delta}$ Oxygen Electrodes on $\text{Ce}_{0.9}\text{Gd}_{0.1}\text{O}_{2-\delta}$ During Reversing Current Operation	145
6.4.1 Introduction	145
6.4.2 Methods.....	146
6.4.2.1 Cell Fabrication.....	146
6.4.2.2 EIS Measurements.....	146
6.4.2.3 SEM-EDS.....	147
6.4.2.4 FIB-SEM.....	147
6.4.3 Results	147
6.4.4 Discussion	152
6.4.5 Summary and Conclusions.....	156
6.4.6 Acknowledgements	156
6.5 Preliminary current switched life tests of La_2NiO_4 wet-infiltrated into $(\text{La}_{0.9}\text{Sr}_{0.1})(\text{Ga}_{0.8}\text{Mg}_{0.2})\text{O}_3$	156
6.5.1 Introduction	156
6.5.2 Experimental	157

6.5.3 Results	159
6.5.4 Discussion	162
6.6 Summary	163
Chapter 7: Development and analysis of a combined electrochemical-coarsening model to describe degradation in nano-infiltrated electrodes	165
7.1 Acknowledgement and Note on the Context of this Work	165
7.2 Introduction	165
7.3 Experimental	167
7.3.1 Symmetric Cell Fabrication	167
7.3.2 Electrochemical Testing	168
7.3.3 FIB-SEM	169
7.4 Results and Discussion.....	169
7.5 Conclusions	191
Chapter 8: Summary and Outlook.....	193
References	196

List of Tables

Table 3.1 Overview of Circuit Elements

Table 5.1. Oxygen diffusion and surface exchange coefficients for LSCF and NNO

Table 6.1. Summary of microstructural parameters in post-test LSCF electrodes

Table 7.1. Average SSC particle sizes estimated from SEM images of as-prepared electrodes and electrodes coarsened at 800 °C

Table 7.2. Cathode microstructural parameters obtained from 3D tomographic reconstructions, as shown in the representative images in Figure 7.3.

Table 7.3. Model Parameters determined by fitting degradation data for SSC and LSCF oxygen electrodes

List of Figures

Figure 2.1. NREL projection of renewable energy curtailment as a function of the energy mix.

Figure 2.2. Capital cost of power system versus round-trip cost of stored energy

Figure 2.3. Power rating versus discharge time for various storage technologies

Figure 2.4. Diagram of a solid oxide fuel cell

Figure 2.5. IV curve and associated voltage losses in a typical SOFC

Figure 2.6. Illustration of exchange current density

Figure 2.7. Diagram of a reversible Solid Oxide Cell

Figure 2.8. Typical I-V behavior of a ReSOC indicating the thermoneutral voltage

Figure 2.9. (a) corner of the O-H-C phase diagram (b) methane content as a function of temperature and pressure

Figure 2.10. Thermoneutral voltages as a function of temperature at 1 and 10 atm

Figure 2.11. Comparison between existing storage technologies and ReSOC

Figure 2.12. Conductivity of electrolyte materials

Figure 2.13. Theoretical polarization resistance for a Ni-YSZ anode

Figure 2.14. Ni infiltrated LSGM

Figure 2.15. Microstructure of a typical LSM-YSZ oxygen electrode

Figure 2.16. Qualitative sketch of utilization length

Figure 2.17. Structures of a) perovskite b) double perovskite and c) Ruddlesden-Popper MIECs

Figure 2.18. Literature isotope exchange data for perovskite cobalt-ferrite materials

Figure 2.20. Literature isotope exchange data for cobalt-rich layered perovskite materials

Figure 2.21. Literature isotope exchange data for Ruddlesden-Popper nickelate materials

Figure 2.22. Schematic cross-sectional microstructures for low temperature oxygen electrodes a) single phase b) composite c) infiltrated

Figure 2.23. Expected polarization resistance of a generic single phase MIEC oxygen electrode

Figure 2.24. Surface resistance values of perovskite MIECs measured using thin film microelectrodes

Figure 2.25. SEM of delamination of the oxygen electrode after a long term electrolysis test in a full SOC stack

Figure 2.26. Diagram of the chemical potential of O_2 and electric potential across an SOC

Figure 2.27. Current-cycled life tests for LSM-YSZ showing the effects of current density and cycling period

Figure 2.28. EIS and OES-ICP data linking Sr segregation to increases in polarization in an LSCF electrode

Figure 2.29. Degradation in the polarization resistance of annealed infiltrated LSCF electrodes

Figure 2.30. FIB polished cross-section of a symmetric LSM-YSZ cell operated under DC current showing the migration of silver

Figure 3.1. Schematic of electrochemical impedance spectroscopy

Figure 3.2. Example Nyquist and Bode plots

Figure 3.3. Example of how an equivalent circuit is used to fit experimental data

Figure 3.4. Schematic drawing of a symmetric device and a full fuel cell

Figure 3.5. Diagram of current switched life-test setup for oxygen electrodes

Figure 3.6. Schematic of the pressurized atmosphere controlled furnace

Figure 3.7. Example SEM imaging conditions

Figure 4.1. X-ray diffractograms Pr_2NiO_4 powders

Figure 4.2. EDS, SEM, and X-ray data of a Pr_2NiO_4 infiltrated electrode

Figure 4.3. X-ray diffractograms of various Pr_2NiO_4 infiltrated electrodes and powders

Figure 4.4. Nyquist and Bode plots showing the optimization of infiltrate volume

Figure 4.5. Nyquist and Bode plots showing the temperature dependence of an optimized electrode

Figure 4.6. Pr_2NiO_4 infiltrated electrode performance data, polarization resistance versus temperature

Figure 4.7. Bode and Nyquist plots of a preliminary Pr_2NiO_4 life test

Figure 4.8. Polarization resistance versus time for three preliminary Pr_2NiO_4 life tests

Figure 4.9. Comparison between the optimized Pr_2NiO_4 electrode and other nickelate or infiltrated electrodes

Figure 5.1. Nyquist and Bode plots as a function of oxygen pressure at 550 °C for $(\text{Sm}_{0.5}\text{Sr}_{0.5})\text{CoO}_3$ infiltrated into GDC

Figure 5.2. Nyquist and Bode plots as a function of oxygen pressure at 550 °C for Pr_2NiO_4 infiltrated into LSGM

Figure 5.3. Polarization resistance and time constants as a function of oxygen pressure at 550 °C for PNO/LSGM and SSC/GDC

Figure 5.4. Bode and Nyquist plots of an NNO symmetric cell at 700 °C in the pressure range from 0.2 to 10 bar $p\text{O}_2$ with equivalent circuit fits

Figure 5.5. Bode and Nyquist plots of an LSCF symmetric cell at 700 °C in the pressure range from 0.2 to 10 bar $p\text{O}_2$ with equivalent circuit fits

Figure 5.6. Polarization resistance versus $p\text{O}_2$ for LSCF and NNO at 700 °C with t_G values

Figure 5.7. Oxygen non-stoichiometry δ versus oxygen pressure for $\text{Nd}_2\text{NiO}_{4+\delta}$ (a) and $\text{La}_{0.6}\text{Sr}_{0.4}\text{Co}_{0.2}\text{F}_{0.8}\text{O}_{3-\delta}$ (b) at 700 °C. With literature data comparison

Figure 5.8. a) Measured polarization resistance versus $p\text{O}_2$ for Nd_2NiO_4 compared to values calculated from derived x_δ^0 b) Measured and calculated time constants versus $p\text{O}_2$

Figure 5.9. a) Measured polarization resistance versus $p\text{O}_2$ for LSCF compared to values calculated from derived x_δ^0 b) Measured and calculated time constants versus $p\text{O}_2$

Figure 6.1 Nyquist and Bode plots of selected EIS measurements, taken at zero current during brief interruptions in a reversing-current life test in which J was incrementally stepped up to higher values for an LSM-YSZ electrode

Figure 6.2 Total, ohmic, and polarization resistance values versus time during a reversing-current life test in which the current density was incrementally stepped for an LSM-YSZ electrode

Figure 6.3 Nyquist and Bode plots of selected EIS measurements taken at zero current during brief interruptions in reversing-current life tests in which the current density was maintained at (a,b) 0.9 or (c,d) 0.8 A/cm² for an LSM-YSZ electrode

Figure 6.4 (a) Ohmic (b) polarization and (c) total resistance versus time during reversing-current life tests at current density values of 0.6, 0.8 and 0.9 A/cm² for LSM-YSZ

Figure 6.5. Degradation rates versus current density and overpotential for LSM-YSZ

Figure 6.6. Post-test SEM/EDS data for LSM-YSZ

Figure 6.7 EDS linescans for a) annealed b) 0.8 A/cm² and c) 0.9 A/cm² cells

Figure 6.8. Ohmic, Polarization, and Total resistance values comparing a stable current cycled LSM-YSZ symmetric cell operated at 800 °C to an identical cell operated at 750 °C

Figure 6.9. Nyquist and Bode plots for an LSM-YSZ symmetric cell operated at 0.5 A/cm² under a 12-hour current switched cycle at 800 °C

Figure 6.10. Nyquist and Bode plots for an LSM-YSZ symmetric cell operated at 0.5 A/cm² under a 12-hour current switched cycle at 750 °C

Figure 6.11. SEM images of the post-test LSM-YSZ cell operated at 750 °C and 0.5 A/cm² near electrode/electrolyte interface

Figure 6.12. Total resistance of a current switched LSM-YSZ symmetric cell operated at 0.5 A/cm² on a 12-hour cycling period with the temperature switched between 750 and 800 °C every 200 hours

Figure 6.13. Nyquist and Bode plots at selected time points of the current switched life test performed at a current density of 0.7A/cm² for LSCF

Figure 6.14. Nyquist and Bode plots at selected time points of the current switched life test performed at a current density of 1.5A/cm² for LSCF

Figure 6.15. a) Ohmic resistance, b) Polarization resistance, and c) Total resistance of the current switched life tests performed at 0.7, 0.9, 1.0, and 1.5 A/cm² on LSCF

Figure 6.16. Polished cross-sections of LSCF symmetric cells operated at zero, 0.7, 1.0, and 1.5 A/cm²

Figure 6.17. Total degradation rate versus J and η for LSCF

Figure 6.18. Nyquist and Bode plots of a current switched LNO/LSGM cell at selected time points in the 1.0 A/cm² current switched life test at 650 °C

Figure 6.19. Nyquist and Bode plots of a current switched LNO/LSGM cell at selected time points in the 2.0 A/cm² current switched life test at 650 °C

Figure 6.20. Summary of the ohmic, polarization, and total resistance values of the LNO life tests

Figure 6.21. Post-test SEM/EDS cross sections of LNO infiltrated cells

Figure 7.1. Illustration of the testing program used to collect EIS data during coarsening of SSC infiltrated GDC electrodes

Figure 7.2. SEM images of $\text{Sm}_{0.5}\text{Sr}_{0.5}\text{CoO}_3$ (SSC) particles on Gd-doped Ceria (GDC) surfaces

Figure 7.3. Cross-sectional SEM images and FIB-SEM 3D reconstructions of GDC scaffold (A) and GDC scaffold infiltrated with SSC (B)

Figure 7.4. Bode and Nyquist plots of EIS data taken at different times during a life test of an SSC-GDC electrode aged at 800 °C

Figure 7.5 Oxygen electrode polarization resistance of SSC-infiltrated symmetric cells, taken from EIS data measured in air at 600 °C

Figure 7.6. Cathode polarization resistance of SSC-infiltrated symmetric cells with different SSC volume fractions

Figure 7.7. Model fit to polarization resistance data of LSCF-infiltrated symmetric cells aged at temperatures ranging from 650-850 °C

Figure 7.8. Predicted polarization resistance versus time for oxygen electrodes with initial SSC particle sizes of 10, 25, 50, and 100 nm

Figure 7.9. Predicted polarization resistance versus time for infiltrated SSC-GDC electrodes

Figure 7.10 A plot of critical SSC particle diameters that provide target performance and stability values, versus cell operating temperature

Figure 7.11. A plot of critical LSCF particle diameters that provide target performance and stability values, versus cell operating temperature

Figure 7.12. Predicted resistance versus time for infiltrated SSC-GDC electrodes operated at a temperature of 600 °C with different electrode thicknesses

Chapter 1

1.1 Introduction and Overview

The expansion of renewable power sources in recent years is motivated by the desire to mitigate anthropogenic CO₂ emissions and avert global catastrophe. An effect of the conversion of the established power grid to renewable sources is an increasing need for large scale energy storage technology due to the fluctuating nature of wind, solar, and water resources. Recent developments in reversible solid oxide cells (SOCs) suggest that the technology is competitive with other storage schemes in terms of round-trip efficiency and cost per kWh stored, and has a unique key advantage of very high maximum discharge hours. However, there are two issues that need to be addressed for this technology to become a reality: the cell resistance at low temperature ($\sim 0.2 \Omega \cdot \text{cm}^2$ at $< 650^\circ\text{C}$) and the durability under current switching conditions ($< 0.5 \%$ /khr degradation). These two technological challenges motivate the developments that compose the body of work here.

Low cell resistance at low temperature is required to achieve high round-trip efficiency, as described in chapter 2. The cell component that typically contributes the highest resistance at low temperatures is the oxygen electrode, as the oxygen reduction reaction typically has a higher activation energy than oxygen transport through the electrolyte or fuel oxidation at the fuel electrode. The polarization resistance at the oxygen electrode can be lowered by changing the structure, chemistry, or oxygen pressure at the electrode (Chapters 4 and 5).

Previous work on the durability of the oxygen electrode under current switched conditions (mimicking electrolysis and fuel cell cycles of a storage system) have shown that the degradation in LSM-YSZ electrodes is similar to degradation in solid oxide electrolysis cells. However, the root cause of degradation remains an open question. Therefore it's of interest to extend current life

tests to other systems and look for similarities in the context of previously developed theories (Chapter 6). Moreover, current switched life tests at a range of current densities and overpotentials are required to determine whether stable operating conditions exist and what those conditions are (Chapter 6).

Nanostructured electrodes are widely known to offer a path to low polarization resistance at the oxygen electrode, owing to the high volume specific surface area of the active material. However there is a trade-off between the high surface area and long term durability of the nanostructured electrodes: high surface areas provide a driving force for coarsening at operating temperatures where surface diffusion is sufficiently active. It is therefore desirable to determine what the right combination of particle size and operating temperature is to have sufficiently low degradation at an acceptable polarization resistance and to determine how to select materials that can meet those criteria (Chapter 7).

The focus of each chapter is described briefly:

Chapter 2 outlines the fundamentals of SOCs including the thermodynamics and kinetics of operation as they relate to energy conversion and storage. The materials properties and microstructures of modern SOCs are reviewed with a focus on the oxygen electrode and low temperature (450-650 °C) operation. The known degradation mechanisms that affect the oxygen electrode in SOCs are reviewed and discussed.

Chapter 3 discusses specific methods used in this work in more detail than would be appropriate for the experimental section of any particular chapter. These include sample preparation for SEM, imaging conditions for SEM/EDS, and Impedance spectroscopy and circuit modeling.

Chapter 4 discusses the development of a new low resistance Pr_2NiO_4 based oxygen electrode that may be a good candidate for reversible SOCs. The electrode has improved phase stability compared to other Pr_2NiO_4 electrodes and sufficiently low polarization resistance compared to other oxygen electrodes generally.

Chapter 5 reports the operating characteristics of four different candidate electrodes for SOCs under oxygen pressures up to 10 atm. Two of the electrodes are analyzed in detail to investigate the role of different itinerant oxygen ion defects on observed changes in pressurized performance. The results suggest that rare-earth nickelates may have an advantage in pressurized conditions compared to perovskite materials and confirm trends from lower pressure studies.

Chapter 6 explores the durability of oxygen electrodes under current switching operation. Three different materials systems are used and subjected to thousands of hours of current switched operation under varying current densities. Electrochemical data of the life-tests are presented along with microstructural data to establish trends in how these electrodes degrade under different operating conditions. More stable operating conditions are determined, and some failure mechanisms are determined.

Chapter 7 explores the role of nanoparticle coarsening in the degradation of nanostructured oxygen electrodes. A refined electrochemical coarsening model is presented and fit to a previous student's data. Predictions on the long term performance of the electrodes and a figure of merit for the selection of nanostructured electrodes is presented.

Chapter 8 summarizes the work performed here and gives a perspective on future directions for research relating to the stability of oxygen electrodes for reversible solid oxide cells.

Chapter 2: Background

2.1 Climate Change, Renewable Energy Adoption, and Energy Storage

Following the grim evaluation of the climate future written in the International Panel on Climate Change (IPCC) 2014 report ¹, international cooperation has intensified to combat anthropogenic climate change ². The United States has recently committed to the first universal agreement on emissions reduction from the Paris talks ³ that mandates our CO₂ production be limited to a total of 6.6 million additional gigatons of CO₂ by 2100. The overarching goal is to limit the temperature anomaly to 2° C by the end of the century by reducing greenhouse gas emissions. Half of this goal would be met if just 36% of energy production were renewable by 2030². In the United States, about half of CO₂ emissions are from power generation and related industrial activity ⁴, so compliance with the agreement means increasing the fraction of electricity generated by renewable sources, especially by developing wind and solar resources. Detailed plans at a state by state level exist for utilizing our renewable resources to meet or exceed the entire current energy demand⁵. The rapid decline in the cost of solar energy and advancements in offshore wind technology are bringing the cost of renewable energy on a levelized cost/kWh basis very close to our already developed coal and natural gas sources (including tax credit)⁶. The combination of international cooperation and increasingly cost competitive renewable technology makes it ever more likely that the worst consequences of anthropogenic climate change may be averted. However, one of the last technological hurdles damping the adoption of more widespread renewables is the issue of large scale energy storage.

Wind and solar resources are fluctuating and intermittent over hours, days, and seasons. Moreover, electricity demand also fluctuates daily and seasonally, making it difficult to rectify these supply and demand curves. Currently, matching electricity supply to demand is accomplished using peaker plants and by changing production rates at baseload facilities. Wind and solar have less control over production rate than a natural gas or nuclear power plant and so a similar rectification strategy is not possible. Increasing the fraction of renewable power sources in the US electrical grid(s) will therefore lead to instability or significant power curtailment without a large scale storage option. Figure 2.1 shows the National Renewable Energy Laboratory's projections for curtailment as a function of renewable production fraction. Curtailment in this case is a term meaning the purposeful conversion of over-production of electricity to heat through a variety of methods including turbine breaking, shunting to resistors, and impedance shifting⁷.

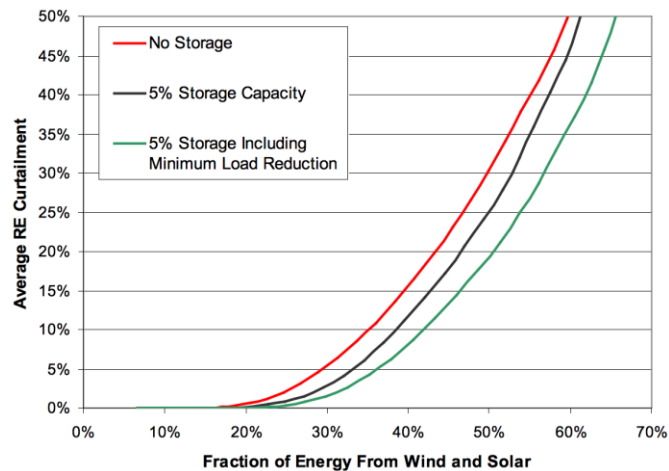


Figure 2.1. NREL projection of renewable energy curtailment as a function of the energy mix.

Reproduced from⁸

Recent studies of power usage in the United States indicate that, in order to have a 100% renewable energy grid, between 15-20% of annual power output must be stored at any one time⁹. As of 2014

the annual US electricity production was 4.1×10^{18} Wh, suggesting about 8.1×10^{17} Wh of energy storage space is required to meet US demand¹⁰. Energy storage development is consequently a very active area including advancements in flow batteries¹¹, pumped hydroelectricity^{12,13}, compressed air energy storage¹⁴, and hydrogen storage^{15,16}. The energy storage association (ESA) compiles data on energy storage advancements for power conditioning and longer term storage Figures 2.2 and 2.3.

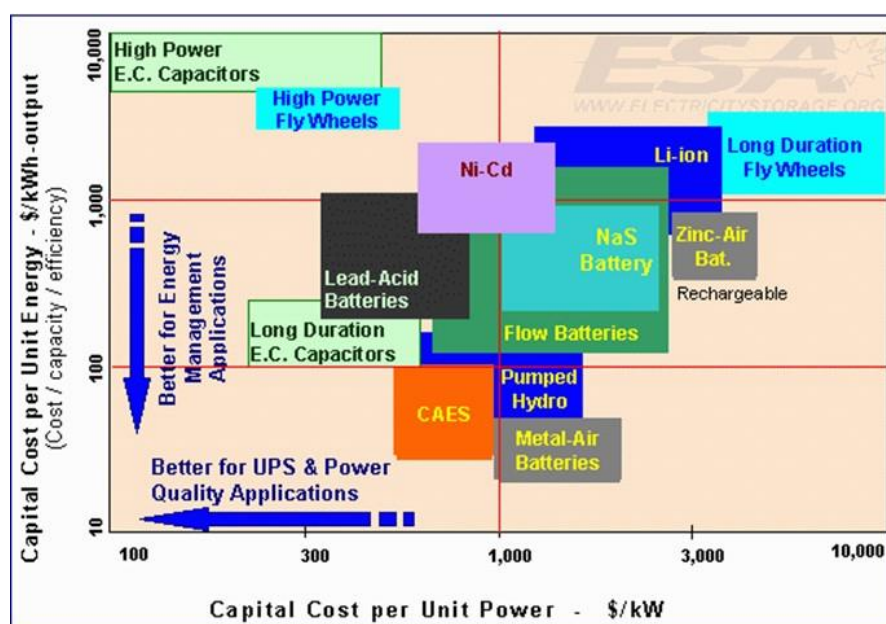


Figure 2.2. Capital cost of power system versus round-trip cost of stored energy¹⁷

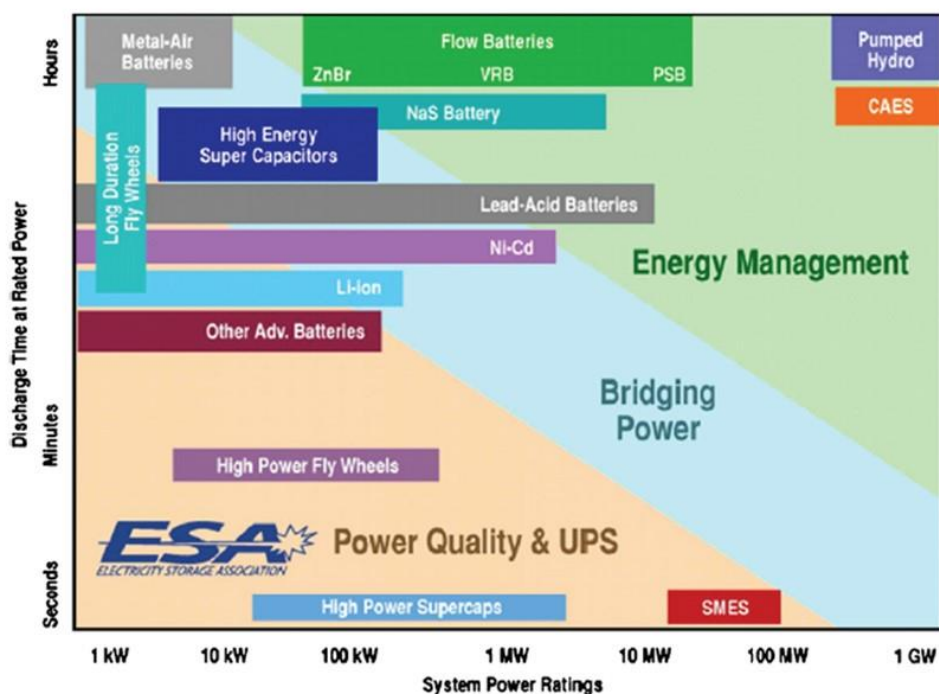


Figure 2.3. Power rating versus discharge time for various storage technologies¹⁷

Currently, the only large scale energy storage technology in use is pumped hydroelectricity, but this technology is affected by seasonal variations and is limited to wet, mountainous regions. Stable storage time on the order of months is a difficult challenge (note y-axis of figure 2.3) and a more promising solution is electrolysis of a feedstock to stable products^{18,19}. Many technologies must also be cost competitive with activating a peaker plant on a levelized basis unless storage becomes federally subsidized or mandated. A good storage technology will therefore have storage times of thousands of hours, round trip efficiencies commensurate with electricity cost ($> \sim 70\%$), and levelized cost/kWh stored on the order of a few cents/kWh (2016 USD)^{18,19}.

While developments in flow battery technology and compressed air energy storage are gaining notice, solid oxide cells (SOCs) have also recently become a promising technology^{19,20}. Solid oxide

cells offer stable, energy dense storage products through the co-electrolysis of water and CO₂ while also delivering high round-trip efficiencies. Solid oxide cells have historically been a high cost option for energy conversion, but high round-trip efficiencies and new low-temperature materials are beginning to enable competitive embodiments for energy storage¹⁹. This work focuses on the performance and degradation of one of the components of a solid oxide cell, the oxygen electrode, with the aim of understanding and improving the component's durability and performance for grid scale energy storage applications.

2.2 Solid Oxide Fuel Cells

A solid oxide cell is an electrochemical energy conversion device that converts chemical energy to useful electrical work by separating a combustion reaction into two half reactions mediated by an external electrical circuit and a ceramic membrane that transports oxygen ions. When operated in forward mode to consume fuel it is known as a solid oxide fuel cell, and when operated in reverse is it known as a solid oxide electrolysis cell, or for simplicity just a solid oxide cell for either direction (SOC). The electrodes (fuel electrode and oxygen electrode) play critical roles in catalyzing the half reactions and transporting ions to and from the electrolyte and electrons to and from the circuit. Figure 2.4 shows a schematic embodiment of a solid oxide fuel cell.

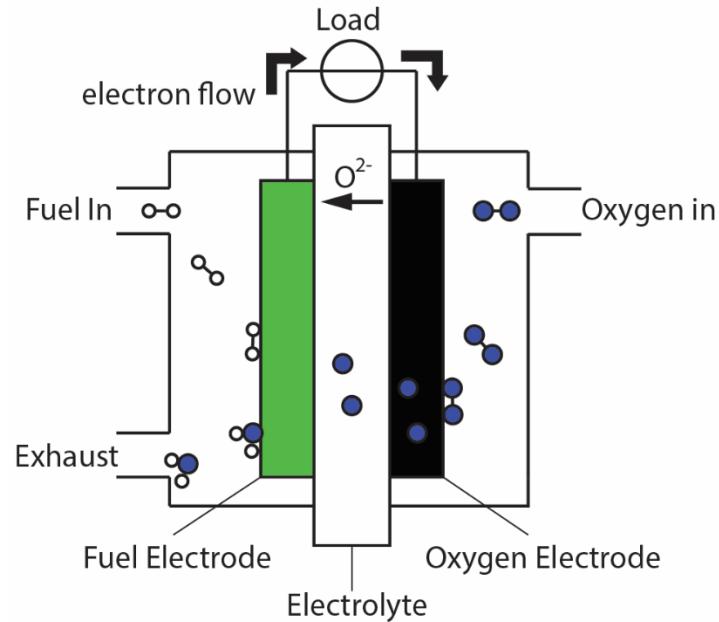


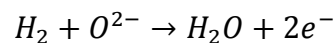
Figure 2.4. Diagram of a solid oxide fuel cell

2.2.1 Electrochemistry

2.2.1.1 Reactions

Fuel is supplied to the anode of a solid oxide fuel cell as hydrogen or a hydrocarbon where it is oxidized by oxygen ions from the electrolyte material. The anode reaction for the hydrogen case is:

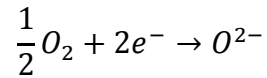
(Equation 2.1)



An oxygen chemical potential gradient is formed across the electrolyte between the fuel side and the air side and both oxygen vacancies and oxygen ions move in response. Oxygen from the air side of the device adsorbs into the cathode and is split into atomic oxygen, charged, and enters

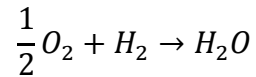
available vacancy sites to be transported across the electrolyte. The cathode reaction can be written as:

(Equation 2.2)



Reactions on both sides of the device are completed by exchanging electrons with an external circuit where the electron flow is opposite the oxygen ion flow. The complete reaction is then:

(Equation 2.3)



2.2.1.2 Nernst Potential

The work, in the form of electricity and heat, extracted for use by an SOFC is directly related to the Gibbs' free energy of the electrochemical reaction at standard conditions:

(Equation 2.4)

$$W_{rev} = \Delta G = -nFE$$

Where n is the number of moles of electrons involved in the reaction, F is faraday's constant (96,480 C/mol), and E is the ideal cell (Nernst) potential. The potential which arises from a chemical potential of oxygen across the electrolyte can be written:

(Equation 2.5)

$$E = E^\circ - \frac{RT}{nF} \ln \left(\frac{\Pi \text{ product fugacity}}{\Pi \text{ reactant fugacity}} \right)$$

The fugacity of the product and reactant gases are generally approximated to be equal to the partial pressures of the gases. The Nernst potential is:

(Equation 2.6)

$$E = E^\circ - \frac{RT}{nF} \ln \left(\frac{p(H_2O)}{p(H_2)p(O_2)^{\frac{1}{2}}} \right)$$

This is the ideal voltage of an SOFC at these operating conditions in open circuit. However, this voltage is never actualized and the observed voltage, particularly under a current load, due to kinetic losses in the device.

2.2.2 Kinetics

Voltage losses in an SOFC are the result of slow reaction rates at the electrodes, ohmic losses in the electrolyte, and gas diffusion limitations. These losses are displayed graphically in figure 2.5 showing the theoretical cell potential and a typical current-voltage plot for an SOFC.

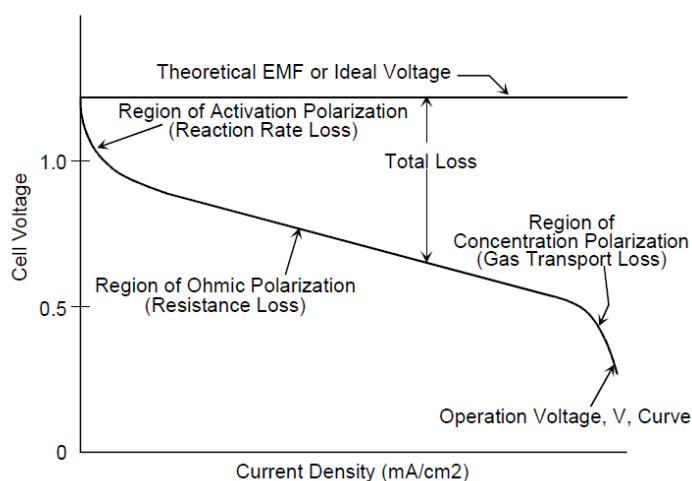


Figure 2.5. IV curve and associated voltage losses in a typical SOFC²¹

2.2.2.1 Activation Polarization

The activation polarization is caused by languid reaction kinetics at the electrodes. The atomistic details and exact reaction pathways of the half reactions at the electrodes (eqs. 2.1 and 2.2) are complex and involve many steps dependent on the exact surface structure and chemistry of the electrodes. Each step of each half reactions has its own rate and activation energy that can vary between materials and operating conditions. Practically, these series of steps are characterized by a single lumped activation overpotential and associated polarization resistance. The activation overpotential is typically described by the semi-empirical Tafel equation for a typical overpotential (50-200 mV):

(Equation 2.7)

$$\eta_{act} = \frac{RT}{\alpha nF} \ln \left(\frac{j}{j_0} \right)$$

Where R, T and F have their typical meaning, n is the number of moles of electrons involved in the reaction, α is electron transfer coefficient of the electrode (typically ~0.5), j is the applied current, and j_0 is the exchange current density. The exchange current density is described by the linearization of the IV plot using the Tafel equation (Figure 2.6). Physically it is a description of the rate of forward and reverse reactions at open circuit voltage.

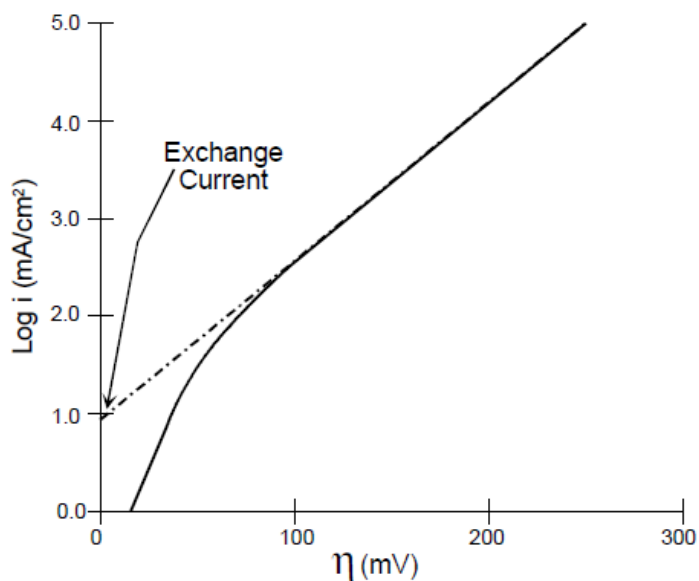


Figure 2.6. Illustration of exchange current density.²¹

At lower currents the activation polarization is better approximated as:

(Equation 2.8)

$$\eta_{act} = \frac{2RT}{nF} \operatorname{asinh} \left(\frac{j}{2j_0} \right)$$

Using this form, the derivative is closely approximated by another easily experimentally accessible value defined as the polarization resistance, owing to its similarity to Ohm's law:

(Equation 2.9)

$$R_p = - \left[\frac{dV}{dj} \right]_{j=0} \approx - \frac{RT}{nFj_0}$$

The large voltage drop at low currents in figure 2.5, highlights the importance of using an electrode that promotes fast reaction kinetics. j_0 depends on the chemistry, microstructure and gas environment of the electrode.

2.2.2.2 Ohmic Polarization

The ohmic polarization arises due to conduction losses in the electronic, ionic, and contact components of the cell and is defined:

(Equation 2.10)

$$\eta_{ohm} = j(R_{electronic} + R_{ionic} + R_{contact})$$

For electrolyte supported cells and button cells generally, the ionic component is far greater than either the electronic or contact resistances and is typically approximated:

(Equation 2.11)

$$R_{ohmic} = R_{ionic}$$

Contact resistance becomes significant in large planar anode supported cells. The large losses in the resistance loss portion of figure 2.5 highlight the importance of using an electrolyte with high ionic conductivity.

2.2.2.3 Concentration Polarization

Concentration polarization, also known as gas transport loss, results from depleting the reactant at the electrode faster than it can be supplied and so is limited by gas phase diffusion of reactants. This loss typically appears at higher current densities or low reactant concentrations for typical

electrodes and is affected by electrode microstructure and diffusion properties of the gas.

Mathematically, the concentration polarization can be described:

(Equation 2.12)

$$\eta_{conc} = \frac{RT}{nF} \ln \left(1 - \left(\frac{j}{j_L} \right) \right)$$

Where j_L is the limiting current defined as the current density resulting in zero cell voltage.

2.1.1 Efficiency

The efficiency of an SOFC is a combination of the reactant thermodynamics, kinetic losses, and fuel utilization. The reversible thermodynamic efficiency of the reactants is defined as the ratio of the extractable work to the change in enthalpy of the products and reactants. The higher heating value of enthalpy is used as the products are exhausted and returned to ambient temperature:

(Equation 2.13)

$$\epsilon_{thermo} = \frac{\Delta G}{\Delta H}$$

The voltage efficiency is the ratio of the Nernst potential of the cell and the actual operating voltage:

(Equation 2.14)

$$\epsilon_{voltage} = \frac{V_{actual}}{E_{Nernst}} = \frac{E_{Nernst} - \eta_{act} - \eta_{ohmic} - \eta_{conc}}{E_{Nernst}}$$

The fuel utilization efficiency arises from the fact that not all the fuel fed to the anode will be oxidized and is described as the conversion rate divided by the molar flow rate:

(Equation 2.15)

$$\epsilon_{fuel} = \frac{i}{nF v_{fuel}}$$

Where v_{fuel} is the fuel flow rate (mol/sec). The overall SOFC efficiency is then:

(Equation 2.16)

$$\epsilon_{total} = \epsilon_{thermo} \cdot \epsilon_{voltage} \cdot \epsilon_{fuel}$$

An implication of this efficiency formulation is that operating at higher current densities leads to lower efficiencies, and yet higher power densities per cell are desirable for reasonable capital costs. Ultimately, from figure 2.5 and equation 2.14, the best way to maintain high efficiency at reasonable power density is to minimize the activation and ohmic losses.

2.3 Reversible Solid Oxide Cells

2.3.1 Introduction

The reversible solid oxide cell (ReSOC) refers to an SOFC that is designed to operate under electrolysis conditions for a significant period of its lifetime. The target application for the ReSOC is closed loop energy storage for a more stable grid coupled with renewable sources (Figure 2.7). Under electrolysis conditions, the fuel side of the device is enriched in reaction products and current is driven backward through the device to reverse the half reactions at the electrodes (green

arrows). The device can be operated in fuel cell mode (red arrows) to provide efficient energy conversion.

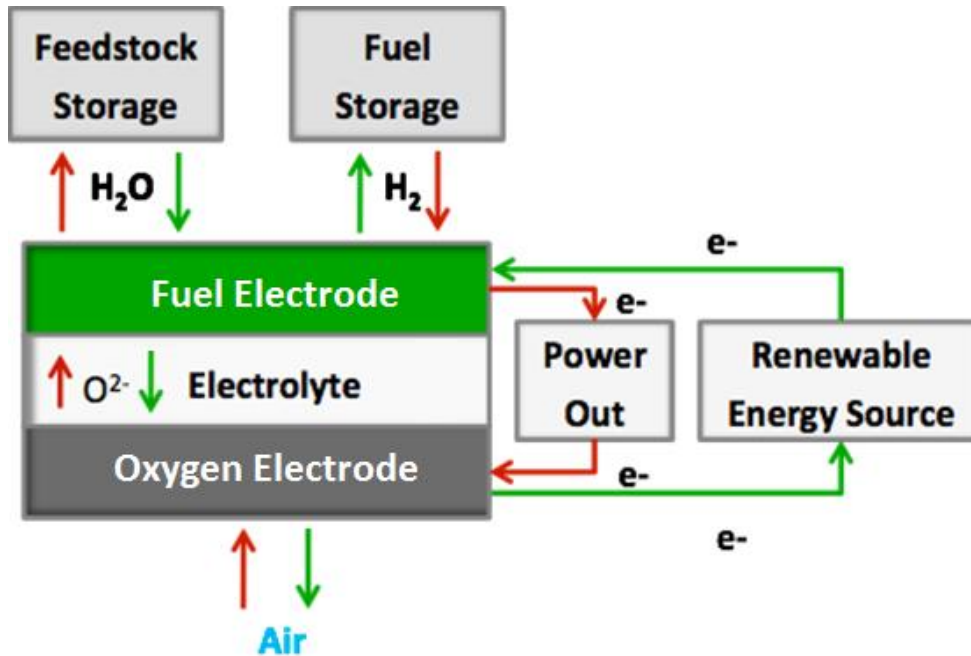


Figure 2.7. Diagram of a reversible Solid Oxide Cell adapted from²²

2.3.2 Electrolysis and energy storage

2.3.2.1 Efficiency of storage

The ideal round-trip efficiency of a ReSOC at the cell level is defined as:

(Equation 2.17)

$$\epsilon = \frac{V_{SOFC}}{V_{SOEC}}$$

Where V_{SOFC} is the operating voltage actual in forward mode and V_{SOEC} is the operating voltage actual in reverse mode. These voltages are subject to the same losses compared to the Nernst potential as discussed in section 2.3. Note there is no fuel utilization term as a reversible fuel cell

is a closed system and waste streams are not exhausted. However, an additional requirement for ReSOCs is that they be thermally self-sustaining in electrolysis mode. This is not an issue for SOCs operated in forward mode as the overall reaction (eq. 2.3) is exothermic. Rather than employ heaters, a typical method for overcoming the heat requirement of the endothermic electrolysis reactions is to operate at a voltage such that the joule heating of ions moving through the electrolyte balances the energy requirements. This voltage is known as the thermoneutral voltage V_{TN} :

(Equation 2.18)

$$V_{SOEC} \geq V_{TN} = \frac{\Delta H}{nF}$$

Figure 2.8 illustrates a typical I-V curve for a ReSOC operated on 50% H₂/50% H₂O mixture, indicating the thermoneutral voltage. The thermoneutral voltage requirement puts hard limits on the round-trip efficiency that present a challenge for the commercialization of the technology. For example, at 800 °C and 1 atm, for H₂O electrolysis, $\Delta H = 248.3 \text{ kJ mole}^{-1}$, $V_{SOEC} \geq 1.3 \text{ V}$, and for CO₂ electrolysis, $\Delta H = 282.4 \text{ kJ mole}^{-1}$, $V_{SOEC} \geq 1.48 \text{ V}$. A reasonable operating voltage in forward mode (at about 0.5 A/cm²) is 0.87 V, which would yield efficiencies of 67% for H₂O and 59% for CO₂.

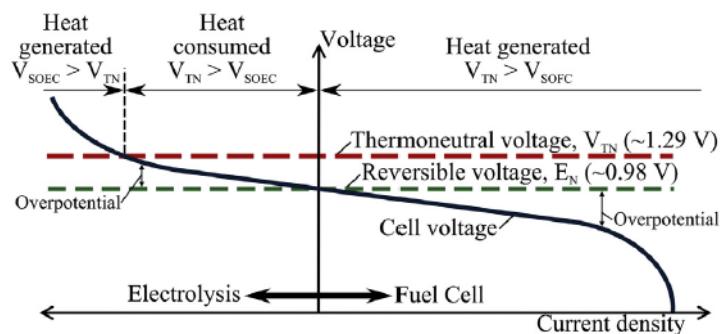


Figure 2.8. Typical I-V behavior of a ReSOC indicating the thermoneutral voltage reproduced from²³.

2.3.2.2 Storage Chemistry and Thermodynamic Considerations

The outlook on round-trip efficiency is not as bleak as the thermoneutral voltage requirements might make it seem, as the ΔH term in equation 2.18 can be changed by temperature, pressure, and chemistry. The storage chemistry in particular is important as the co-electrolysis of water and CO_2 that occurs at lower temperatures to produce methane is less endothermic than either the H_2O or CO_2 electrolysis reactions alone. Figure 2.9 shows the pressure and temperature effects on the methane content of outlet gas stream using a water and CO_2 feedstock.

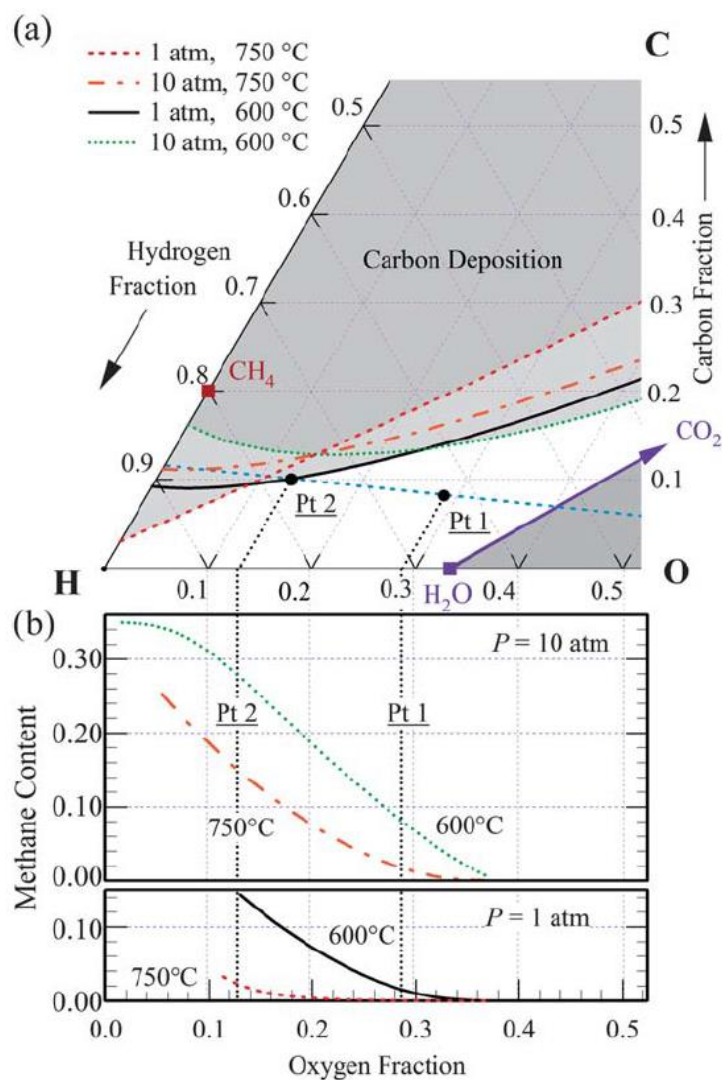


Figure 2.9. (a) corner of the O-H-C phase diagram showing the gas constitution of the feedstock tank (Pt. 1) and Fuel tank (Pt.2) as well as graphite forming boundaries at 600 °C and 700 °C and 1 and 10 atm. (b) methane content at Pt. 2 as a function of temperature and pressure simulated using thermocalc software reproduced from²².

The less endothermic electrolysis reactions that form high methane fractions at higher pressures and lower temperatures result in a lower thermoneutral voltage. The temperature and pressure effects on the thermoneutral voltage are displayed in figure 2.10.

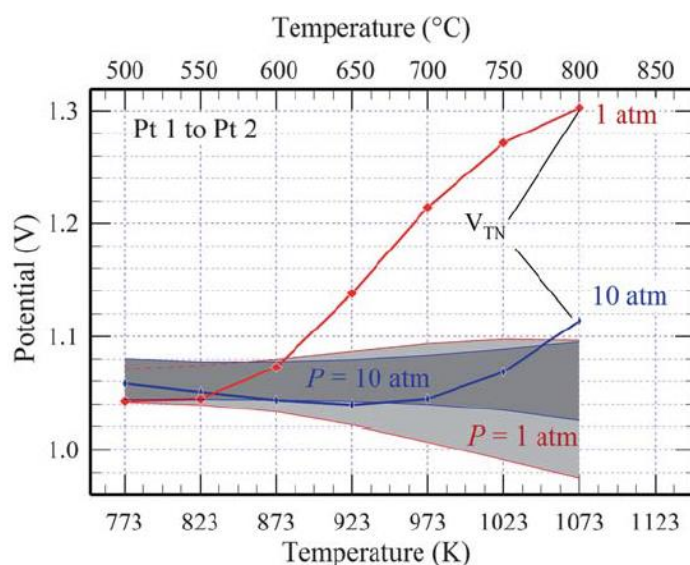


Figure 2.10. Thermoneutral voltages as a function of temperature at 1 and 10 atm. The shaded regions represent the Nernst potential as a function of temperature and at the storage and fuel gas constitutions. Reproduced from²²

The closer the thermoneutral voltage is to the Nernst potential, the more efficiently the cell can be operated and maintain temperature. The ability to drive the thermoneutral voltage toward the Nernst potential was the fundamental development that allowed ReSOCs to become competitive as a storage technology, as they are no longer limited to low round-trip efficiencies. Therefore, the pressurization of the SOC stack is a key feature that transforms an unworkable technology into a competitive one. This development has motivated recent system-level simulations to understand how a realized ReSOC system would compare to existing storage technologies. It is important to note however, that relatively little is known about the behavior of an SOC, especially the electrode components, under pressurization. Later chapters investigate oxygen electrode pressurization experimentally.

2.3.3 Comparison to other storage methods

Large scale energy storage is necessary to convert the energy grid to a distributed, renewable system. A good storage system is judged on the basis of three main criteria: cost per kilowatt-hour stored, maximum discharge hours, and round-trip efficiency. The round-trip efficiency was addressed in the previous section, and for a ReSOC operating at 600 °C with an R_p of $0.2 \Omega \cdot \text{cm}^2$ at about 0.5 A/cm^2 , a round trip efficiency of 80% at the cell level is possible. This is comparable to the round trip efficiency of a Li-ion battery, for example. The stable storage time for a ReSOC fuel supply is essentially on a geologic time scale since the fuels are stable. The fuels are also energy dense compared to compressed air or water and so have a longer discharge time for a given volume. Discharge on times on the order of months are possible. However, the cost for a ReSOC system is high, and difficult to estimate because of the sophisticated balance of plant. Recent studies were performed exploring the techno-economic performance of a ReSOC system^{19,24}. The study by Jensen et. al. proposes an embodiment that utilizes geologic storage for the ReSOC fuels and CO₂ feedstock, largely because the storage tanks are the largest single cost component of the system. Figure 2.11 shows the result of this simulation as compared to other storage technologies. Without geologic storage, using steel pressure vessels, the ReSOC is about twice as expensive as displayed on the chart.

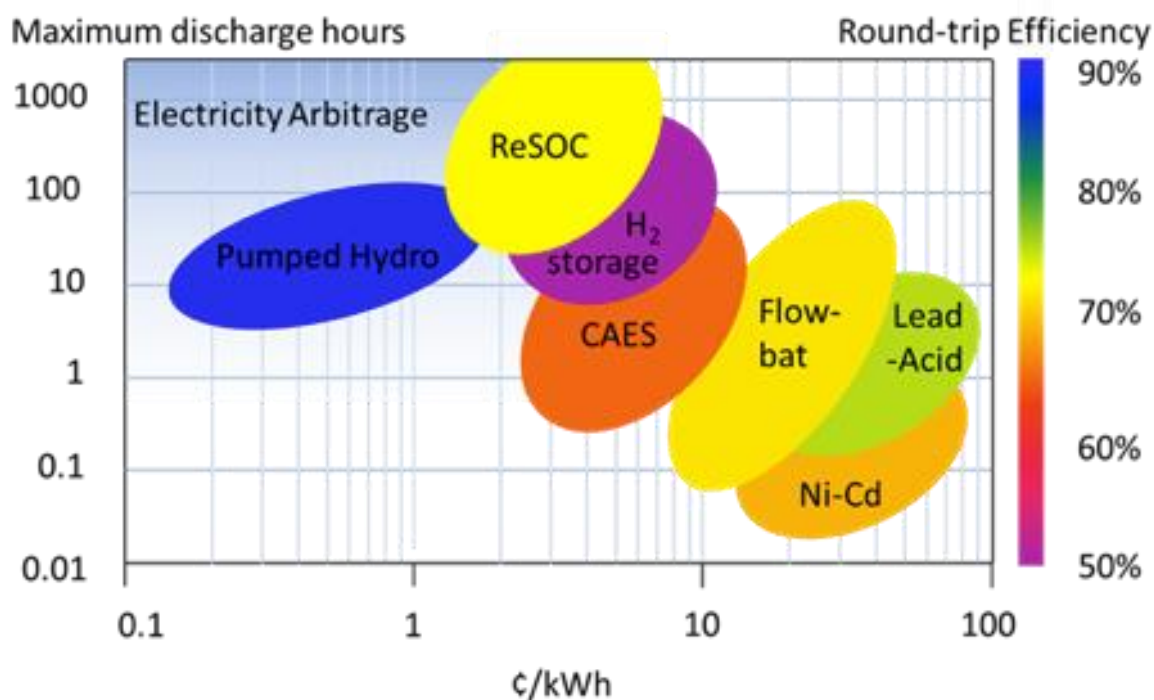


Figure 2.11. Comparison between existing storage technologies and ReSOC reproduced from¹⁹

Currently the only technology competitive with ReSOCs is pumped hydroelectricity, but it's only available in certain geographical regions and is subject to seasonal variations. H₂ storage suffers from low round-trip efficiencies due to limitations in the thermoneutral voltage for SOCs operated on water, and high overpotentials for PEM fuel cells. Other technologies are useful for power conditioning and daily storage, but are incapable of long-term storage.

2.4 Current State of the Art Solid Oxide Cell Materials

The projected economic performance of a reversible solid oxide cell energy storage system depends on being able to achieve low cell resistances ($<0.2 \Omega \cdot \text{cm}^2$) at low temperatures (450-650 °C). Reducing the operating temperature of a solid oxide cell while maintaining low cell resistance is difficult because the reactions at the electrodes and oxygen transport through the electrolyte are

Arrhenius processes. This challenge can be met by optimizing both the microstructure of the cell and the materials of which it is composed. The following is a brief review of current materials and microstructures as they relate to low-temperature SOCs.

2.4.1 Electrolytes

The primary function of an SOC electrolyte is to transport oxygen ions and block electronic conduction. The metrics used to describe these characteristics are the oxygen ion conductivity σ and ionic transference number:

(Equation 2.19)

$$\sigma_i T = A \exp\left(-\frac{E_a}{kT}\right)$$

and,

(Equation 2.20)

$$T_{ion} = \frac{\sigma_i}{\sigma_i + \sigma_e}$$

Where σ_i is the ionic conductivity, σ_e is the electronic conductivity, T_{ion} the transference number, A an exponential prefactor, E_a the activation energy for oxygen diffusion, and k and T have their usual meaning.

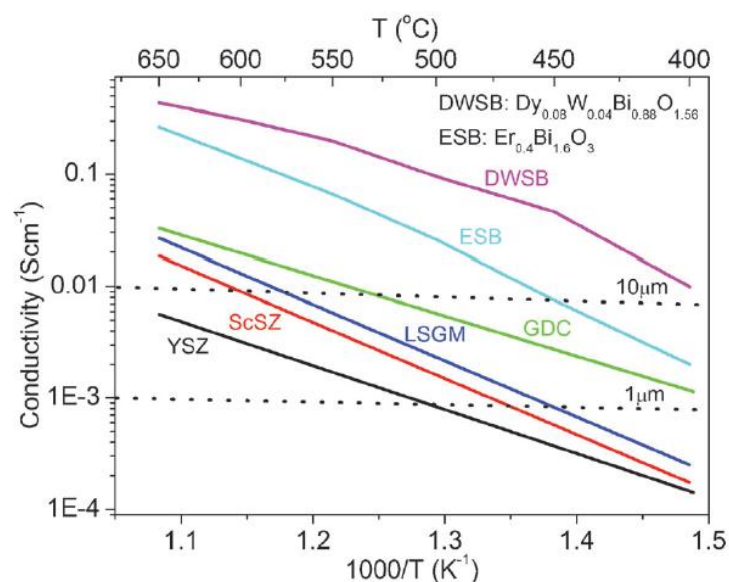


Figure 2.12. Conductivity of electrolyte materials that have been successfully employed in low temperature SOCs. The dotted lines represent the thickness of the electrolyte to achieve an ohmic resistance of $0.1 \Omega \cdot \text{cm}^2$ at 10 and 1 μm . Reproduced from²⁵

Figure 2.12 shows the ionic conductivity of electrolyte materials under investigation for low temperature SOCs. Yttria stabilized zirconia $\text{Zr}_{0.84}\text{Y}_{0.16}\text{O}_{2-\delta}$ (YSZ) is the prototypical electrolyte material owing to its good ionic conductivity, near unity transference number, good mechanical strength, favorable thermal expansion coefficient, low cost, phase stability between 25 and 1000 °C, and stability in both reducing and oxidizing conditions. However, this electrolyte must be processed to less than ~ 3 microns to achieve the target resistance ($0.1 \Omega \cdot \text{cm}^2$) value at ~ 600 °C, which can be challenging (Figure 2.12). Scandia stabilized zirconia (ScSZ) has a notably higher conductivity than YSZ²⁶ and meets the requirements for operation at 600 °C, though it comes with challenging stability issues²⁷. $\text{La}_{0.8}\text{Sr}_{0.2}\text{Ga}_{0.9}\text{Mg}_{0.1}\text{O}_{3-\delta}$ (LSGM) is a promising material, having many of the same qualities as YSZ, and with higher ionic conductivity²⁸. Several examples of high performing LSGM based cells exist^{29, 30, 31}, and it has the added benefit of being chemically

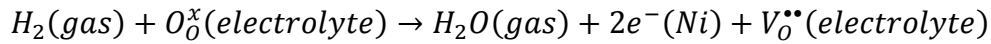
compatible with many high performance cathode materials. However, there are concerns about LSGM's reactivity with nickel, a typical anode material^{32,33}. Anodes for LSGM electrolyte cells must therefore be either processed at low temperatures when using a Ni-based anode^{34,35}. $\text{Ce}_{0.9}\text{Gd}_{0.1}\text{O}_{2-\delta}$ (GDC) has high conductivity, low-cost, and simple processability, sharing many characteristics with YSZ^{36,37}. Many examples of GDC based cells exist including a metal supported variety produced commercially by Ceres Power. However, GDC is known to be mixed conducting in the low $p\text{O}_2$ environment at the anode³⁸. For thin electrolytes, mixed conductivity at the anode leads to a reduction in the open cell voltage and the power density achievable at practical operating conditions (around 0.7 V). Newer bismuth based electrolytes (DWSB and ESB) show promise but are not as well developed as YSZ, ScSZ, LSGM, or GDC. Concerns about the long term stability of bismuth based systems persist, though DWSB has seen fledgling commercial development at Redox Power³⁹. Chief concerns about bismuth based systems are the metastable phases observed upon cooling⁴⁰, and low melting point, limiting processing with other typical fuel cell materials. Moreover, they are not stable in contact with the low $p\text{O}_2$ fuel atmosphere and must be used with a barrier layer such as ceria⁴¹. The materials space for SOC electrolytes is not fully explored, and remains an area of active research.

2.4.2 Fuel Electrode materials

Fuel electrode materials will be discussed briefly here for completeness, but are somewhat outside the scope of this work. Important concepts and some design considerations are introduced here. The archetypal SOC fuel electrode consists of a porous cermet, typically a mixture of electrolyte particles and metallic nickel. The electrochemical half reaction to oxidize the supplied fuel occurs

in the vicinity of the three phase boundary (TPB) between the gas phase, nickel metal, and electrolyte material:

(Equation 2.21)



Under electrolysis this reaction proceeds in the reverse direction. The nickel provides an electronic conduction path, the electrolyte material provides an ionic conduction path, and the gas phase allows for fast mass transport of reactants and products. The reaction is confined to within a few nanometers of the TPB and so is thought of as a 1 dimensional curve in 3-space⁴². Anodes of this type are therefore typically described in terms of their volumetric TPB density. The transmission line model (modified in chapter 7) provides the link between the microstructure and polarization resistance for an electrode⁴³:

(Equation 2.22)

$$R_p = \sqrt{\frac{R_{LS}}{\sigma_i l_{TPB}}} \coth \left(L \sqrt{\frac{l_{TPB}}{\sigma_i R_{LS}}} \right)$$

Where R_p is the polarization resistance of the fuel electrode, R_{LS} is the polarization resistance per unit length of TPB, σ_i is the ionic conductivity of the ion conducting phase (electrolyte), l_{TPB} is the length of TPB per unit volume, and L the thickness of the electrode. For a typical anode composed of a YSZ-Ni cermet, there has been extensive work done in determining the value of R_{LS} at various temperatures and typical anode atmospheres using model electrodes⁴⁴. For a cermet with similar volume fractions of YSZ and Ni, the theoretical polarization resistance in the thick anode limit can be calculated for a range of temperatures and particle sizes (Figure 2.13).

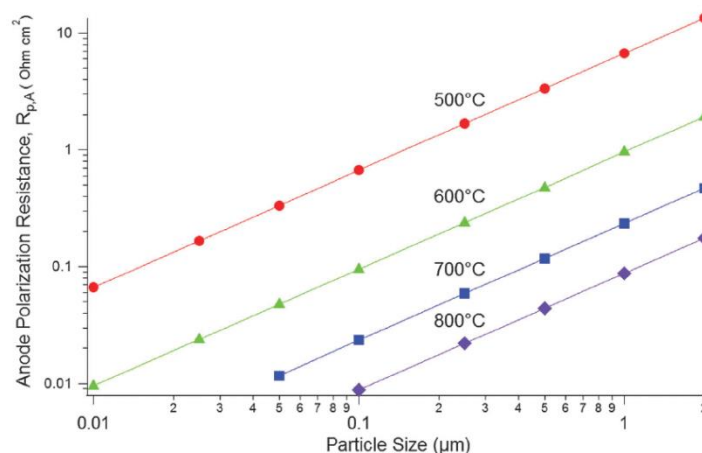


Figure 2.13. Theoretical polarization resistance for a Ni-YSZ anode in the thick electrode limit for a range of particle sizes and temperatures, reproduced from²⁵.

This shows that to meet the target resistance ($<0.1 \Omega \cdot \text{cm}^2$) between 550 and 650 °C for a Ni-YSZ anode, the microstructure must be very fine, ~ 100 nm particles. This type of microstructure may leave the electrode susceptible to coarsening over the operational lifetime due to high surface area to volume ratios in the nickel phase. Moreover, it may be difficult to achieve such a fine microstructure through typical powder processing due to the high sintering temperature of YSZ (~ 1400 °C), and more novel low temperature methods such as infiltration may have to be employed.

In the previous section it is noted that electrolyte materials will likely be different than YSZ, and have higher ionic conductivity. Equation 2.22 shows that increasing the ionic conductivity in the thick electrode limit reduces the expected polarization resistance. R_{LS} values are not as well known for Ni-GDC or Ni-LSGM, though there are reports showing low total polarization for full cells utilizing these anodes^{29,45}. Nanostructured anodes produced by infiltration in LSGM have been

shown to possess high triple phase boundary densities and low polarization resistance (Figure 2.14).

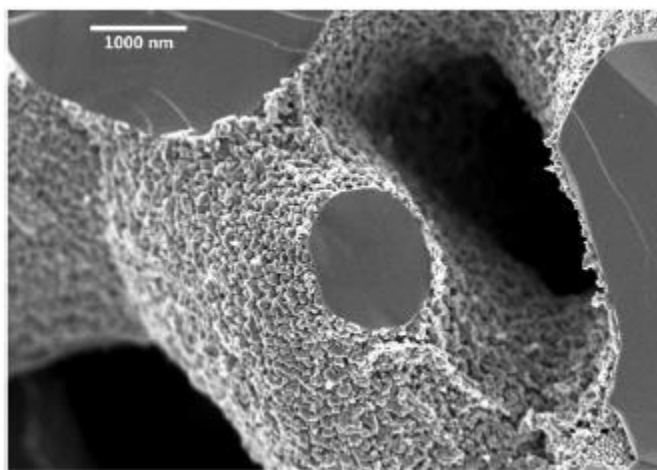


Figure 2.14. Ni infiltrated LSGM showing fine Ni particles supported on an LSGM scaffold with high TPB density²⁵.

The coarsening of these nanostructured electrodes under reduced operating conditions remains an open question as to whether they will maintain low enough polarization resistance at required device lifetimes (50,000 hours).

An exciting new direction in anode materials is utilizing mixed conducting oxides to serve as both the electronic and ionic conducting components, effectively allowing the electrochemical reaction to take place anywhere on the surface of the oxide. These materials also have the benefit of low coking during operation as carbon allotropes to not typically build up on oxide surfaces compared to transition metal surfaces. Lanthanum chromates, strontium titanates⁴⁶, and strontium molybdenates⁴⁷ substituted with various transition metals have proved to be promising candidate materials delivering polarization resistances of $0.1 \Omega \cdot \text{cm}^2$ as low as $750 \text{ }^\circ\text{C}$ ⁴⁸. Moreover small

amounts of precious metals have been substituted into these oxides to yield evolved nanoparticles during operation⁴⁹. These materials show promise in moving toward a mixed conducting oxide anode. However, to date these materials have much higher polarization resistances than Ni cermets at temperatures where reversible SOC operation is most economical (550-650 °C). The materials space for all oxide anode materials has not been fully explored and there may be materials yet to be discovered that work for low temperature applications.

2.4.3 Oxygen electrode materials

To prepare the reader for the rest of the experimental work which focuses on the oxygen electrode, this section will cover details of oxygen electrode chemistry, structure, materials parameters, and microstructure.

The most well studied high temperature solid oxide cell oxygen electrode is a composite of ionically conducting YSZ and electronically conducting $(La_{1-x}Sr_x)MnO_3$ (LSM) (Figure 2.15). The A-site in this perovskite material is typically engineered deficient to prevent Sr reactivity with YSZ. The optimized Sr value for x is 0.5⁵⁰, though most groups use 0.2 or 0.1 to prevent zirconate phase formation if higher temperature firing steps are used^{51,52}. Similar to the Ni/YSZ anode, the electrochemical reaction takes place at TPB sites where the LSM meets the YSZ. These electrodes can be described by the Tanner-Fung-Virkar model similar to (equation 2.22) using a line specific resistance⁵³. The resistivity of the TPB joining the gas phase, YSZ and LSM at a typical operating temperature of 800 °C is $1.26 - 1.9 \times 10^5 \Omega \cdot cm$ as determined by patterned electrodes and full electrode 3-D reconstruction^{51,54}. The processing and microstructure for this material has been optimized. The LSM-YSZ electrode is only useful at high temperatures (800-1000 °C) due to its high area specific resistance at lower temperatures and so is not viewed as suitable for a realized

ReSOC system. However, the abundance of literature available for this electrode makes it an ideal model for life-tests as treated in section 6.2.

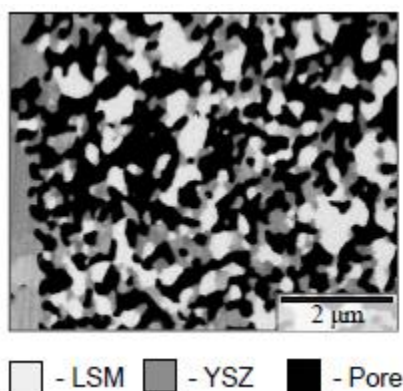


Figure 2.15. Microstructure of a typical LSM-YSZ oxygen electrode⁵¹

The polarization resistance associated with the oxygen electrode R_p is a key issue for meeting resistance targets for ReSOCs at low temperatures. The large activation energy associated with the oxygen reduction reaction causes R_p to be the dominant cell loss as temperatures are reduced.⁵⁵⁻⁵⁷

A good cathode material for low temperatures must have sufficient electronic conductivity (typically > 100 S/cm at 600 °C), good thermal expansion coefficient matching with electrolyte materials $\approx 10 - 12.5 \times 10^{-6} K^{-1}$ and phase stability over the processing and operating temperature range⁵⁵. Long term stability is also a critical issue that will be examined later in this document (Chapters 6 and 7). If these above criteria can be met, then the R_p can be understood and even predicted by a combination of other materials parameters and microstructural parameters. The oxygen reduction reaction is a complex process that includes surface exchange processes (including O-adsorption, dissociation and charge transfer), O-ion diffusion (along the oxide surface or bulk), and O-ion transfer across the electrode/electrolyte interface. However it is typically understood that the rate limiting steps are grouped as oxygen surface exchange and

oxygen bulk/surface diffusion.^{56,57} Following this understanding, the best low temperature cathode materials are mixed electronic and ionic conductors (MIECs) as the ORR can take place on the surface of the material rather than just the TPBs⁵⁸. These materials are characterized by high oxygen surface exchange coefficients k and oxygen bulk diffusion coefficients D_δ . The microstructure of the electrode also plays a role as the electrode must have high internal surface area to maximize the number of sites available for the oxygen reduction or evolution reaction. The electrode must also have sufficient porosity and tortuosity for gas phase transport of oxygen. These microstructural and materials parameters are related to the R_p through the Adler-Lane-Steele model⁵⁸ which predicts a chemical resistance R_{chem} , typically the main contributing factor to R_p :

(Equation 2.23)

$$R_{chem} = \frac{RT}{4F^2} \frac{1}{\sqrt{4a \frac{1-\epsilon}{\tau} R_0 c_0 x_\delta^0 D_\delta}}$$

Where R, T , and F have their usual meanings, a is the specific surface area of the solid phase, ϵ is the porosity of the electrode, τ is the tortuosity of the solid phase, R_0 is the molar surface exchange rate which is related to k through the incorporation mechanism⁵⁹, c_0 is the concentration of mobile oxygen in the solid, and x_δ^0 is the itinerant O-ion defect concentration (vacancies or interstitials). This description of the polarization resistance of the oxygen electrode is valid for a single phase material where the total electrode thickness is greater than the utilization length l_δ and the characteristic particle size of the electrode is smaller than l_δ :

(Equation 2.24)

$$l_{\delta} = \sqrt{\frac{(1 - \epsilon)D_{\delta}c_0x_{\delta}^0}{4a\tau R_0}}$$

Physically this describes the situation where oxygen vacancies or interstitials can move quickly enough from the electrolyte to the surface of the MIEC such that the surface of the MIEC is used more evenly active and out of the TPB-like regime used to describe anodes (Figure 2.16).

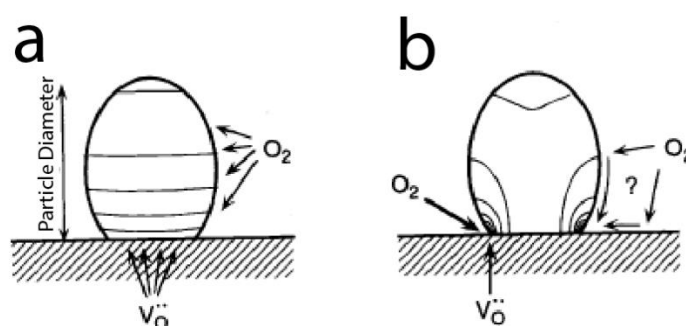


Figure 2.16. Qualitative sketch of an MIEC particle where the particle size is a) smaller than l_{δ} and b) larger than l_{δ} . The lines in the particles are vacancy concentration contours. Adapted from⁵⁸.

For poor ion conductors such as the prototypical high temperature cathode material ($\text{La}_{1-x}\text{Sr}_x$) MnO_3 (LSM), this utilization length is on the order of a few tens of nanometers, leading to a TPB description for these high temperature oxygen electrodes, while MIECs such as $\text{La}_{0.6}\text{Sr}_{0.4}\text{Co}_{0.2}\text{Fe}_{0.8}\text{O}_3$ (LSCF) can have utilization lengths larger than 10 microns^{53,58}. From equation 2.23, the R_p can be minimized by maximizing the internal surface area of the electrode, the surface exchange rate, and the oxygen diffusion. However, nanostructuring the electrode for high surface area may lead to fast degradation rates even at reduced temperatures because of the high driving force for coarsening leads to reduced surface area within the device lifetime (Chapter

7). The surface exchange rate and the oxygen diffusion are dependent on the chemistry of the materials.

Among candidate MIECs for oxygen electrodes there are three main families of perovskite related materials: cubic perovskites (ABO_3), layered perovskites ($AA'B_2O_6$), and Ruddlesden-Popper (RP) phases ($A_{n+1}B_nO_{3n+1}$). Layered perovskites are not used experimentally later in this work, but are described here for completeness. Figure 2.17 shows the structures of these oxides. All of these materials have a 6-fold coordinated transition metal (BO_6) scaffold joined at the vertices along which electronic conduction takes place. At the A-site exists either lanthanide or alkaline earth metals, the distribution of which determines the crystal structure and the type and amount of O-ion point defects⁶⁰. For cubic perovskites, the alkaline earth (Ca, Sr, Ba) and lanthanide (Ln= La, Nd, Pr, Sm etc.) metals are randomly distributed on the A-sites and oxygen vacancies are randomly distributed on the oxygen sublattice (Figure 2.17a). In the double perovskite compounds a large difference in radius between two A-site cations drives ordering into layers. Typically Ba is the large alkaline earth metal used with an A' Ln. In these layered perovskites, the Ln ion decreases its coordination number, localizing oxygen vacancies to the LnO layers. This leads to two dimensional oxygen ion transport in these materials, leading to different k and D_δ values for different crystallographic directions, but decreased electrical conductivity perpendicular to oxygen transport^{61,62}. In the RP series materials, the $n=1$ phase (A_2NiO_4) is typically of greater interest than higher order phases. In these materials, the bond length difference between the B-O and the A-O bonds leads to layering of AO and ABO_3 layers that can be thought of as alternating rock salt and perovskite structures (Figure 2.17c). The free space in the rock-salt layers allows the introduction of O-interstitial defects to reduce the free energy of the structure⁶³. Within $n=1$ RP

materials these interstitial oxygen defects are the primary mobile species for oxygen transport, though vacancies may still exist in the perovskite layers. The layered transport of oxygen causes anisotropy of the material's activity toward the oxygen reduction reaction⁶⁴.

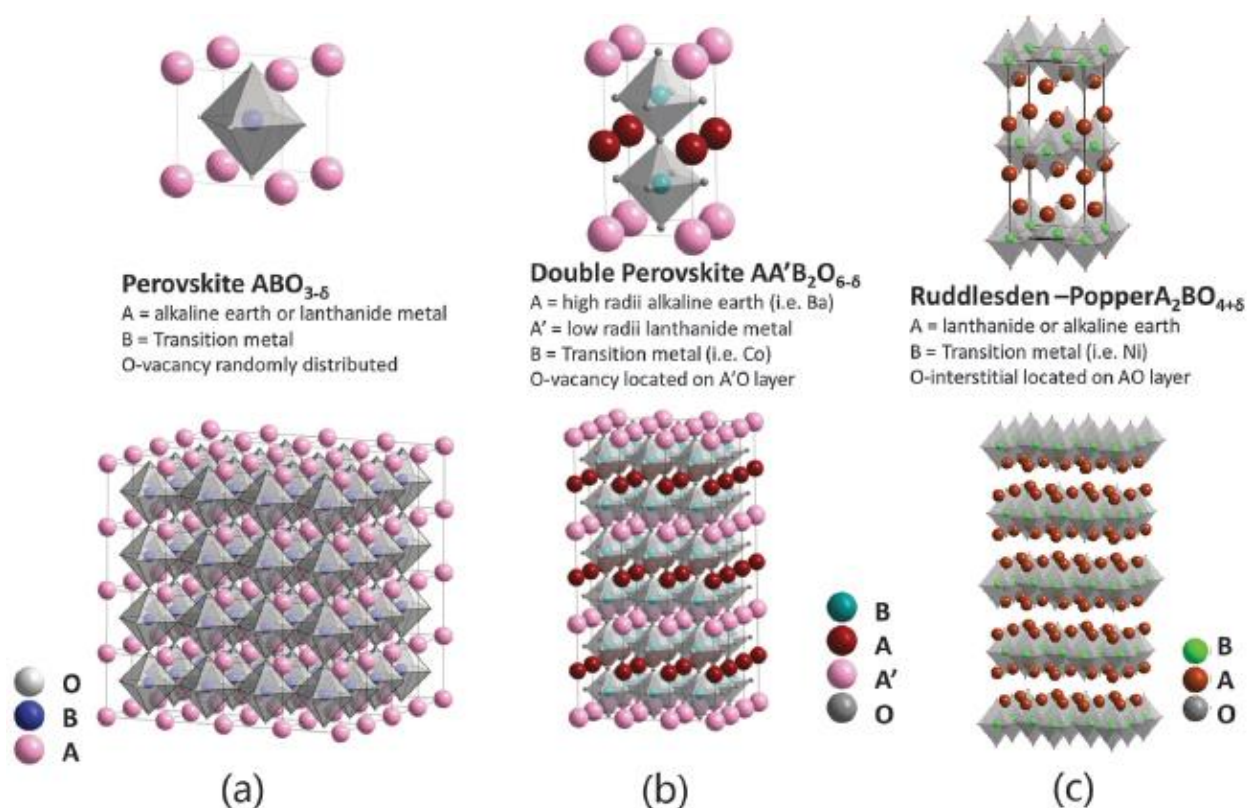


Figure 2.17. Structures of a) perovskite b) double perovskite and c) Ruddlesden-Popper MIECs.

Reproduced from²⁵

Perovskite MIECs have been studied extensively for use as oxygen electrodes, and a wide range of kinetic data is available for these materials (k and D). Figure 2.18 shows kinetic data for the most active and well-studied perovskite compounds including the $La_{1-x}Sr_xCo_{1-y}Fe_yO_{3-\delta}$ (LSCF) system, the $Ba_{0.5}Sr_{0.5}Co_{1-y}Fe_yO_{3-\delta}$ (BSCF) system, and the $Sm_{1-x}Sr_xCoO_{3-\delta}$ (SSC) system. LSCF is an especially attractive material because it is stable across the whole Fe-Co composition space and

has good electronic (100-1000 S/cm) and ionic conductivities (0.001-0.1 S/cm) at 600 °C⁶⁵. The iron rich LSCF $\text{La}_{0.6}\text{Sr}_{0.4}\text{Co}_{0.2}\text{Fe}_{0.8}\text{O}_3$ is widely used because its thermal expansion coefficient matches more closely with commonly used electrolyte materials, despite the Co rich compounds typically having smaller polarization resistances⁶⁶. Note in figure 2.18 that there is a wide dispersion of k^* and D^* values for similar composition and even identical compositions of LSCF. The surface of the material is especially important for k^* as different surface reconstructions, contaminants and SrO surface segregation are thermal history dependent and change the measured k^* . Exacerbating this situation further is that a number of techniques exist to perform isotope exchange depth profiling and conductivity relaxation that must be matched to the correct sample geometry (pellet, porous sample, film etc.) without knowing the utilization length *a priori*^{67,68}. This leads to further errors as some techniques are more surface sensitive than others and the sample geometry may or may not be appropriate for the method applied.

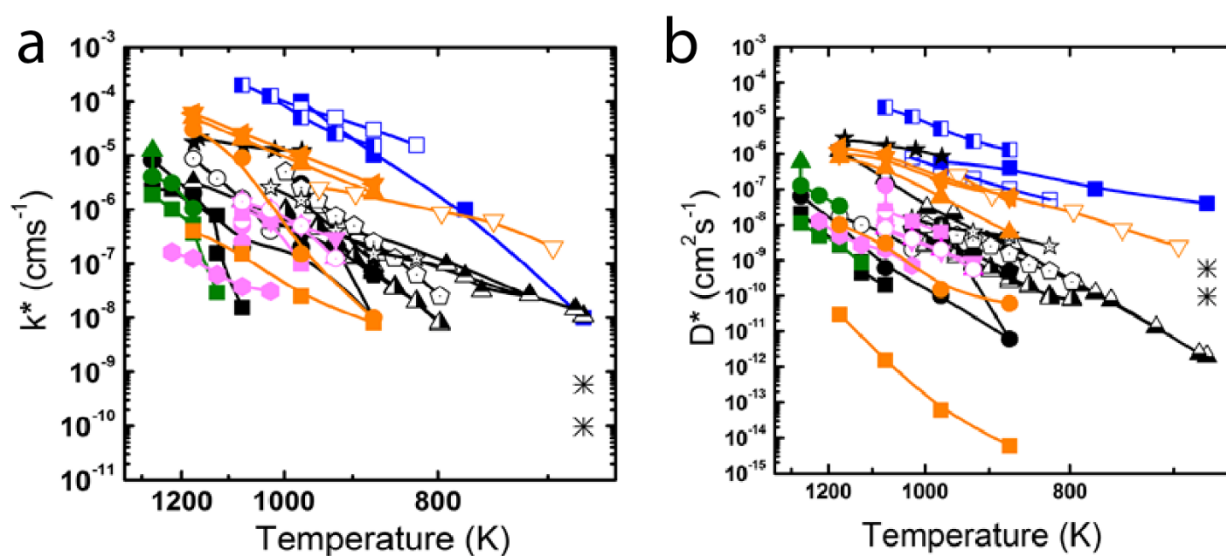


Figure 2.18. Literature isotope exchange data for perovskite cobalt-ferrite materials, including (a) k^* versus temperature and (b) D^* versus temperature. In those cases where chemical coefficients

were reported, the isotopic oxygen diffusion and exchange coefficients were estimated by using thermodynamic factor and oxygen concentration data of the same or similar compositions (*).

Symbols represent literature data for: $\text{Ba}_{0.5}\text{Sr}_{0.5}\text{Co}_{0.8}\text{Fe}_{0.2}\text{O}_{3-\delta}$: \blacksquare ⁶⁹, \square ⁷⁰ (*), \blacksquare ⁷¹ (*). $\text{La}_{0.6}\text{Sr}_{0.4}\text{Co}_{1-y}\text{Fe}_y\text{O}_{3-\delta}$: $y = 0.2$: \blacksquare ⁷² (*), \blacktriangle ⁷³ (*); $y = 0.4$: \bullet ⁷⁴ (*); $y = 0.5$: \blacktriangledown ⁷³ (*); $y = 0.8$: \bullet ^{75,76} (*), \circ ⁷³ (*). $\text{La}_{1-x}\text{Sr}_x\text{CoO}_{3-\delta}$: $x = 0.1$: \blacksquare ⁷⁷; $x = 0.2$: \bullet ⁷⁸, \bullet ⁷⁹, \circ ⁸⁰ (*), *⁸¹; $x = 0.4$: \blacktriangle ⁸², \blacktriangle ⁸², \triangle ⁸³ (*), \blacktriangle ⁸⁴ (*); $x = 0.5$: \bullet ⁸⁰ (*), \square ⁸³ (*), $x = 0.7$: \star ⁸⁵, \star ⁸⁰ (*). $\text{Sm}_{1-x}\text{Sr}_x\text{CoO}_{3-\delta}$: $x = 0.0$: \blacksquare ⁸⁶; $x = 0.2$: \bullet ⁸⁶; $x = 0.4$: \blacktriangle ⁸⁶; $x = 0.5$: \blacktriangledown ⁸⁶, \blacktriangledown ⁸⁷ (*); $x = 0.6$: \blacktriangleleft ⁸⁶. $\text{La}_{1-x}\text{Sr}_x\text{FeO}_{3-\delta}$: $x = 0.1$: \blacksquare ⁶⁹; $x = 0.25$: \bullet ⁶⁹; $x = 0.4$: \blacktriangle ⁶⁹. Adapted from [Ref²⁵]

Still, some general trends within the kinetic data from the perovskites can be identified. In cases where the A-site is co-doped with a lanthanide and strontium, the Sr-rich compounds exhibit faster kinetics. Sr additions decrease the energy for oxygen vacancy formation and promote hole creation in the O-2p band associated with B-site transition metal reduction to maintain charge balance⁸⁸. Increased oxygen vacancy content promotes surface exchange and oxygen diffusion. Compounds with Sm at the A-site generally show faster kinetics than La containing compounds which has sparked great interest in SSC, despite its restriction to low processing temperatures (~800 °C) due to cobalt volatility. BSCF compounds generally have the fastest transport kinetics, but the large size mismatch between Ba and Co places the compound at the edge of stability for the cubic phase⁸⁹. A hexagonal phase has been observed to form in BSCF electrodes over time with lower electronic conductivity and oxygen transport kinetics^{90,91}. LSCF and SSC are utilized in chapters (5, 6, and 7) because they have fewer stability concerns than BSCF while still having good oxygen transport properties, making them the most promising perovskite based electrode materials.

Layered perovskites, notably the $\text{LnBaCo}_2\text{O}_{5+\delta}$ system, are attractive due to their high electronic conductivity ($\sim 1000 \text{ S/cm}$) and good oxygen transport kinetics. Figure 2.20 shows the kinetic data available for layered perovskites as a function of temperature. Note that the data for PCBO may be exaggerated due to measurement artifacts⁹², but otherwise the layered perovskites show kinetic coefficients comparable to LSCF and SSC. These compounds, unlike BSCF, are phase stable, and are a promising area of development for oxygen electrodes. The anisotropic movement of oxygen vacancies make these materials intriguing for use in electrodes with selective orientations of the active material, as reducing the amount of exposed c-plane oriented material may increase the apparent surface exchange rate. The layered perovskites are not further explored in later chapters, but are worth mentioning as a possible development path for high performance oxygen electrodes.

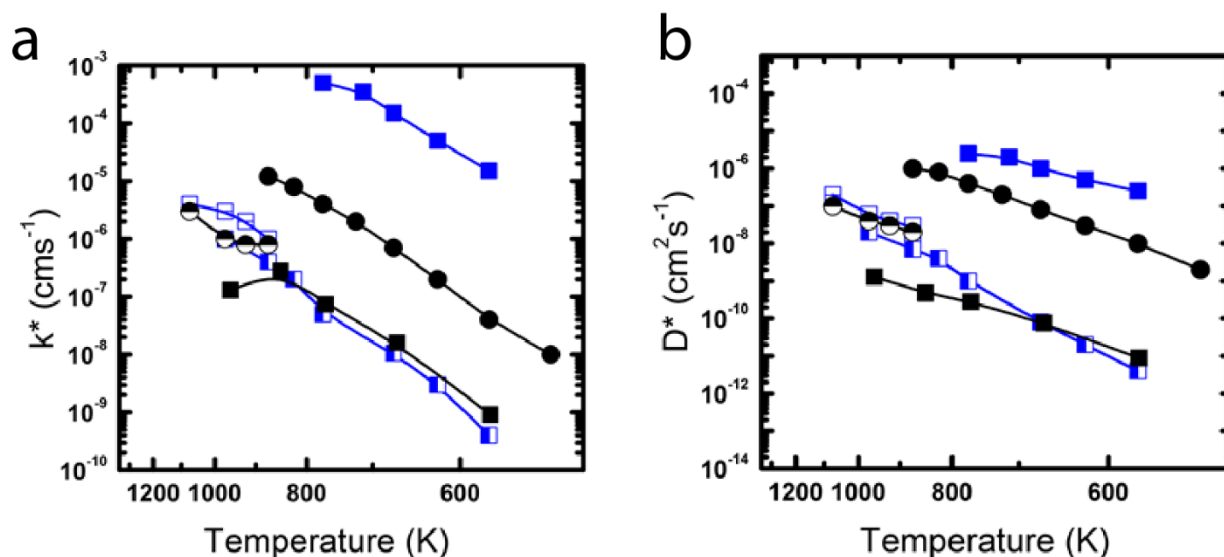


Figure 2.20. Literature isotope exchange data for cobalt-rich layered perovskite materials, including (a) k^* versus temperature and (b) D^* versus temperature. In those cases where chemical coefficients were reported, the isotopic oxygen diffusion and exchange coefficients were estimated by using thermodynamic factor and oxygen concentration data of the same or similar

compositions(*). Symbols represent literature data for: PrBaCo₂O_{6-δ}: ■ 92 (*) □ 93 ▣ 94. GdBaCo₂O_{6-δ}: ■ 95 ● 96. PrBaCo_{1.5}Fe_{0.5}O_{6-δ}: ⊖ 93. [adapted from ref²⁵]

Ruddlesden-Popper (RP) phases (AO)(ABO₃)_n (A= La, Nd, Pr) (B= Cu, Ni, Co), where n=1, are perovskite-related MIECs that transport oxygen ions interstitially along rocksalt layers.^{97,98} Their electronic conductivities at low temperatures are not as high (~ 50 – 100 S/cm vs 100-1000 S/cm) as the other perovskite-related compounds, but their thermal expansion coefficients closely match those of commonly used electrolyte materials. Most of the work has focused on compounds with Ni as the B-site constituent. RP cuprates have also been explored, but only Pr₂CuO₄ has a sufficient electronic conductivity, k^* , and D^* to make it potentially suitable for applications.⁹⁹ Figure 2.21 shows selected literature k^* and D^* data. Some of the compounds, *e.g.*, Pr₂NiO₄ and La₂NiO₄, are of interest as LT-SOFC cathodes because their k^* and D^* values are similar to those of the best perovskite materials. Interestingly, in these nickelates such as La_{2-x}Sr_xNiO_{4+δ}, A-site doping with Sr decreases D^* and, to a lesser extent, k^* , opposite the trend noted for perovskites^{100,101}.

Stability issues are a concern for some RP materials. In particular, Pr₂NiO₄ (n=1) decomposes to Pr₄Ni₃O₁₀ (n=3) and Pr₆O₁₁ over time below 1000°C¹⁰²⁻¹⁰⁴. Substitution with La, Cu, or Ga may stabilize this material in the n=1 phase¹⁰⁵⁻¹⁰⁷. The stability of Pr₂NiO₄ is discussed in chapter 4. Higher order RP phases containing La or Pr appear to have useful MIEC properties as well¹⁰⁸. Lanthanum nickelate is particularly interesting in this regard as the n = 1, 2, 3 phases are stable at typical SOC operating temperatures.¹⁰⁸⁻¹¹¹ The higher order phases have different characteristics than the n=1 compound, most notably higher electronic conductivity and vacancy-dominated oxygen diffusion.¹¹² This is somewhat intuitive since a larger fraction of the material is composed of perovskite blocks. A pseudo-ternary phase diagram in the relevant operating temperature range

has been reported for the $\text{La}_{m+1}\text{Ni}_m\text{O}_{(3m+1)+\delta}$ system¹¹³, and similar information on other RP higher-order phases will be useful towards their further exploration as electrode materials. The $n=1$ phase is used as an electrode in chapter 6. Pr_2NiO_4 , Nd_2NiO_4 , and La_2NiO_4 appear in this work owing to their good fundamental properties and relatively fewer reports with these materials compared to perovskite compounds. Moreover, chapter 5 shows that the interstitial oxygen conduction plays an interesting role in a practical electrode at high pressure.

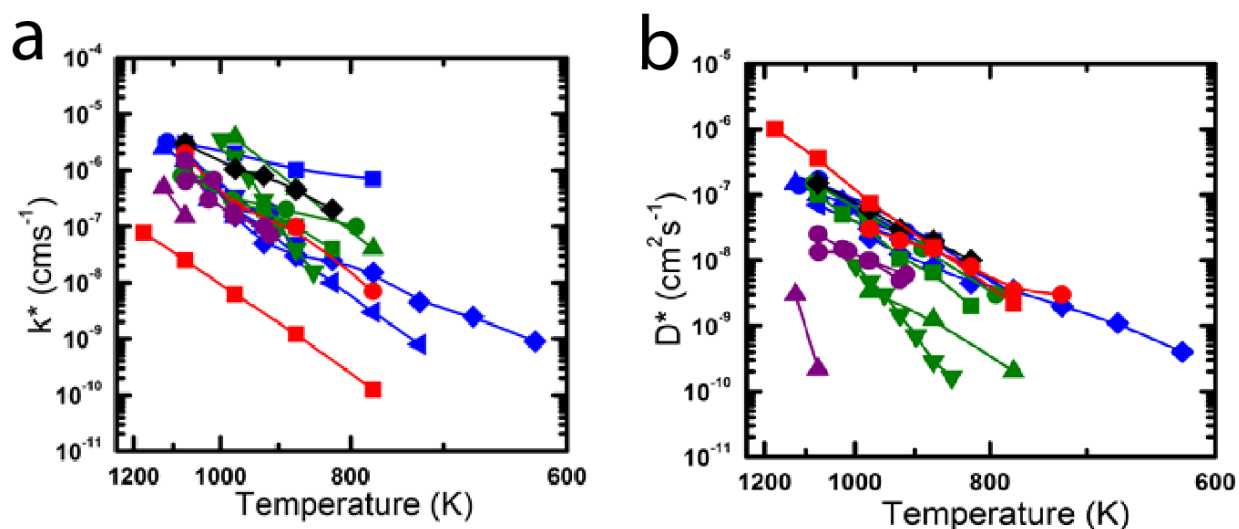


Figure 2.21. Literature isotope exchange data for Ruddlesden-Popper nickelate materials, including (a) k^* versus temperature and (b) D^* versus temperature. In those cases where chemical coefficients were reported, the isotopic oxygen diffusion and exchange coefficients were estimated by using thermodynamic factor and oxygen concentration data of the same or similar compositions (*). Symbols represent literature data for: $\text{La}_2\text{NiO}_{4+\delta}$: \blacksquare ¹¹⁴, \bullet ¹⁰⁰, \blacktriangle ¹⁰¹, \blacktriangledown ⁹⁷, \blacklozenge ¹¹⁵, \bullet ¹¹⁶; $\text{La}_{2-x}\text{Sr}_x\text{NiO}_{4+\delta}$: $x = 0.2$ \bullet ¹⁰¹, $x = 0.1$: \blacktriangle ¹⁰⁰; $\text{Nd}_2\text{NiO}_{4+\delta}$: \blacksquare ⁹⁷, \bullet ¹¹⁷; \blacktriangle ¹¹⁸ (*), \blacktriangledown ⁸⁴ (*); $\text{Pr}_2\text{NiO}_{4+\delta}$: \blacklozenge ⁹⁷; $\text{La}_2\text{Ni}_{0.5}\text{Cu}_{0.5}\text{O}_{4+\delta}$: \blacksquare ¹¹⁴, \bullet ¹¹⁴. [adapted from ref²⁵]

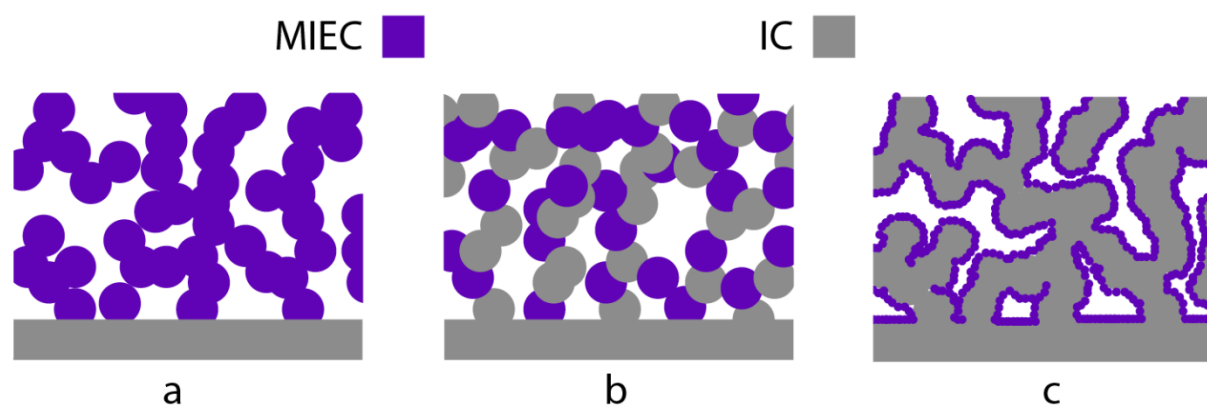


Figure 2.22. Schematic cross-sectional microstructures for low temperature oxygen electrodes a) single phase b) composite c) infiltrated

Three basic microstructures describe oxygen electrodes: single-phase, composite, and infiltrated (figure 2.22). The porous single phase electrode is the most basic oxygen electrode structure and is described by the ALS model (equation 2.23). Using the kinetic data described in the previous section it is possible to predict the polarization resistance for a chosen material of any imagined single phase microstructure, provided it lies within the utilization length requirements. Figure 2.23 shows the predicted polarization resistance for a single phase electrode as a function of $k \cdot D^*$ and specific surface area in air at 600 °C. The plot demonstrates that a reduction in feature size from 1 micron to 1 nanometer results in a factor of 30 reduction in the polarization resistance. However, at small feature sizes there is a trade-off between performance and durability due to coarsening at useful operating temperatures (discussed in chapter 7). Most single phase electrodes have particles sizes greater than 100 nm, but there are examples of LSC electrodes with features sizes on the

order of a few tens of nanometers¹¹⁹.

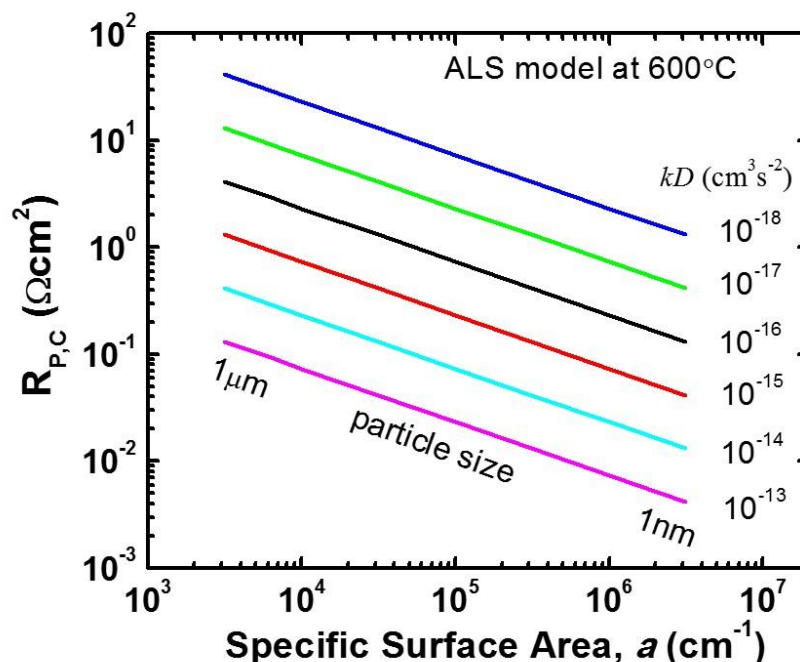


Figure 2.23. Expected polarization resistance in air ($p_{O_2} = 0.21$ atm) at 600 °C versus the specific surface area, for a generic electrode with k^*D^* values ranging from 10^{-13} - 10^{-18} cm^3s^{-2} . [reproduced from ref²⁵]

Composite oxygen electrodes consist of a MIEC mixed with an ionic conductor (IC), typically the same as the electrolyte material. If the ionic conductor has a much greater oxygen diffusivity than the MIEC, then it will provide a short circuit diffusion path and effectively increase the utilization length allowing for thicker cathodes with more active surface area. An analytical model by Mortensen et. al.¹²⁰ shows explicitly how a composite electrode increases the effective vacancy diffusivity for a perovskite-type MIEC composite:

(Equation 2.25)

$$\overline{D_V} = \frac{\phi_{IC}}{\tau_{IC}} \frac{c_{v,IC}}{c_{v,MIEC}} D_{v,IC} + \frac{\phi_{MIEC}}{\tau_{MIEC}} D_{v,MIEC}$$

Where $\overline{D_V}$ is the effective oxygen vacancy diffusivity, ϕ_i is the volume fraction of the *i*th phase, τ_i is the tortuosity of the *i*th solid phase, $c_{v,i}$ is the vacancy concentration of the *i*th phase, and $D_{v,i}$ is the vacancy diffusivity of the *i*th phase. If the IC has a much greater diffusivity, then the effective diffusivity increases, and it is possible to increase the active surface area in a thicker electrode, leading to a lower polarization resistance. Composite electrodes are found commonly in SOC literature for this reason, and many examples exist^{120,121}. Note that MISC/IC composites are different than LSM/YSZ composites used in chapter 6, as the goal is to improve oxygen transport to and from the reaction site rather than to increase the volumetric density of TPBs.

Infiltration, also known as wet chemical impregnation, is a general method by which high surface area electrodes can be produced without subjecting the active materials to high processing temperatures¹²². A solvent solution, typically water, containing metal salts and surfactants is introduced to a pre-fired porous scaffold or backbone composed of and prepared on an electrolyte material. The solution is then dried and calcined to drive off water and precursor small molecules and pyrolyze any organics. The remaining oxidized metal ions form either a film or islands on the scaffold depending on the wetting properties¹²². The infiltration step is repeated until the desired loading fraction is reached, after which a final firing step produces the desired phase in the active material. Electronic percolation is essential for the electrode to work properly which is why higher loadings (>15 vol%) are typically preferred¹²³. There are also less common examples of infiltration being applied to single phase MIEC electrodes to enhance the activity of the existing material^{122,124,125}. Infiltrated electrodes have generally the lowest polarization resistances of the

three microstructures discussed here owing to the small particle sizes of the fired material and the high specific surface area that results. Additionally, the oxygen diffusivity is somewhat less important for infiltrated MIECs and the surface exchange plays a more important role because of the small diffusion distance between an infiltrated particles surface and the ionic conductor backbone. This suggests that materials like Nd_2NiO_4 that have high k^* and low D^* would benefit from an infiltrated microstructure. Following this, infiltrated materials are sometimes characterized by a surface resistance in order to predict their properties in a real electrode (Figure 2.24). The surface resistance is measured as the area specific polarization resistance of a thin film microelectrode. This sample geometry is thought to closely mimic the performance of an infiltrated MIEC particle. The SIMPLE model^{126,127} is an example of one model used to describe the polarization resistance of an infiltrated electrode in terms of a surface resistance.

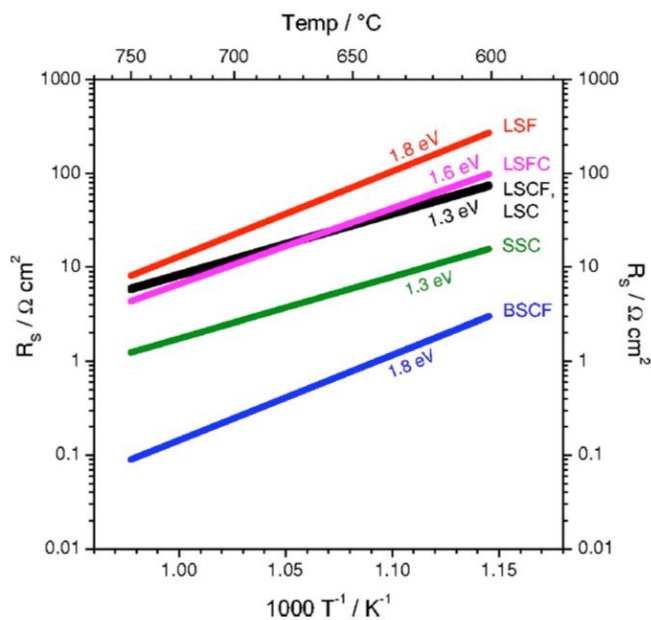


Figure 2.24. Surface resistance values of perovskite MIECs measured using thin film microelectrodes. Reproduced from¹²⁸

2.5 Degradation in SOC Oxygen Electrodes

Long term durability is a key scientific and economic issue for the adoption of SOCs. The United States Department of Energy has issued target degradation rates for SOCs as part of an ongoing effort to expand the use of SOCs in distributed generation and electrolysis applications¹²⁹. The overall measure of degradation in an SOC is the increase in polarization resistance or voltage over time, typically reported in %/khr. Degradation at the oxygen electrode can occur as (1) structural changes that modify the TPB density or specific surface area, (2) chemical segregation at the electrodes that slow the reaction kinetics, (3) impurity migration to active sites from sealing or contact components, (4) catastrophic electrode delamination under electrolysis. The degradation at the oxygen electrode under electrolysis severely limits the device lifetime and has been the subject of intense investigation in recent years. An overview of known degradation mechanisms in fuel cell mode and electrolysis mode for SOCs is given.

2.5.1 Degradation in Electrolysis

Degradation of the oxygen electrode in solid oxide electrolyzers and degradation in fuel cell mode has been observed in multiple studies using LSM, LSCF, and LSM-YSZ electrodes¹³⁰⁻¹⁴⁰. In long term stack tests in fuel cell mode, the primary degradation is slow and associated mainly with interconnects and Mn diffusion into the electrolyte¹⁴¹. For high current densities in fuel cell mode, the LSM has been observed to coarsen and accumulate near the cathode/electrolyte interface¹³¹. In electrolysis, often the degradation, often by delamination, begins within the first 1000 hours of operation, limiting the practical use of these devices for high temperature steam electrolysis^{132,137,142,143}. The delamination mode of failure is of interest in ReSOCs because about

half the operational life of the oxygen electrode will be operating in conditions similar to these high temperature steam electrolysis studies: applied negative current, air or enriched oxygen atmosphere, and 550-800 °C. The failure of the electrode/electrolyte interface does not appear to be a sudden process, but happens gradually and continuously over several hundred hours allowing the process to be observed over time in EIS measurements¹⁴³. In post-test analysis of SOEC stacks, the delamination is observed by SEM to occur at the electrode electrolyte interface with less severe degradation within the electrode or electrolyte¹³⁷ (Figure 2.25).

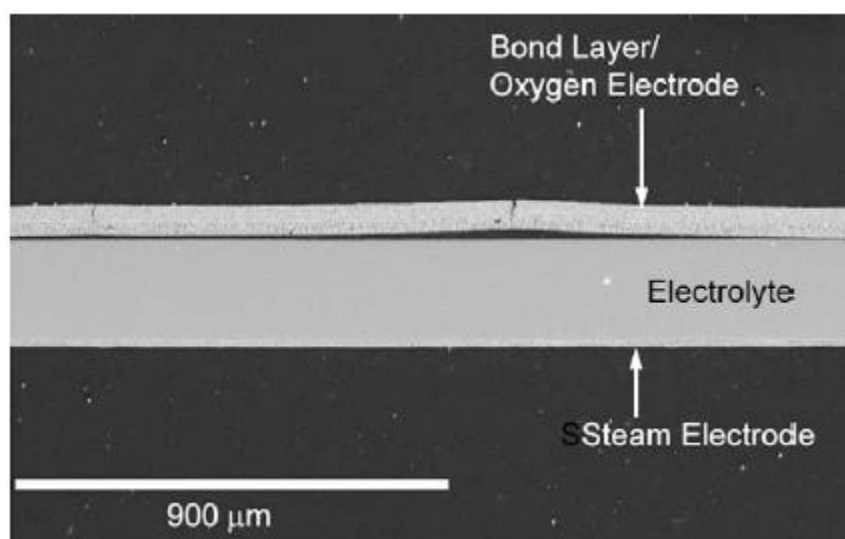


Figure 2.25. SEM of delamination of the oxygen electrode after a long term electrolysis test in a full SOC stack. Adapted from ¹³⁷

The delamination at the electrode/electrolyte interface has only been observed for the LSM-YSZ system, but only because this system is the most standard and intensely investigated. A few theories persist that attempt to explain the origin of this failure including LSM lattice contraction/zirconate formation¹⁴³ and oxygen bubble nucleation¹⁴⁰. In the LSM lattice contraction case, stable electrolysis is not possible, as the high effective pO_2 at the LSM TPB will always result

in excess oxygen content in LSM and zirconate formation and thus lattice contraction and stresses that cause crack formation and delamination; there is no prediction of stable condition. In the case of the oxygen bubble nucleation explanation, the effective oxygen pressure in the electrolyte at the electrode/electrolyte interface must exceed the stresses required for crack growth, giving hope for a region of stable operation. Figure 2.26 shows the electric and chemical potential across a device at the open cell voltage, fuel cell mode, and electrolysis mode.

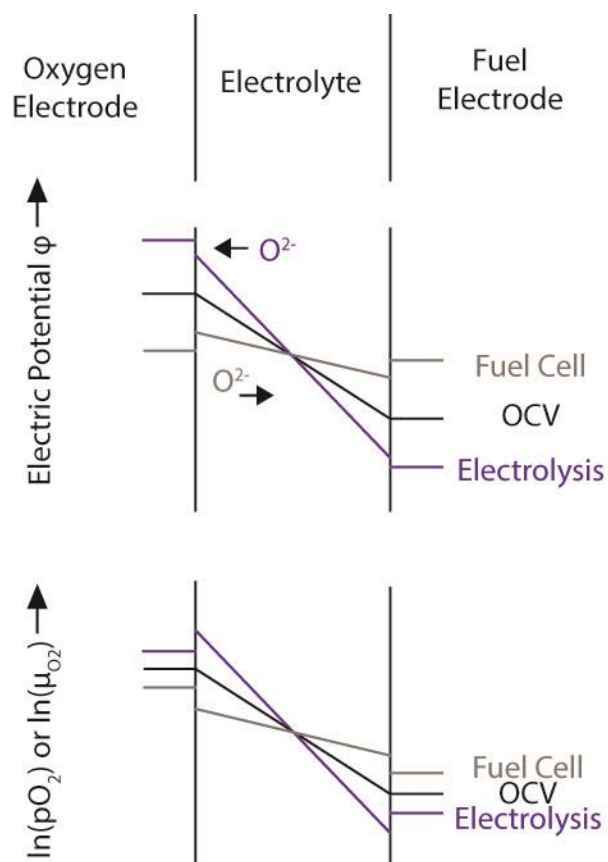


Figure 2.26. Diagram of the chemical potential of O_2 and electric potential across an SOC at open cell voltage, fuel cell mode, and electrolysis mode.

The large chemical potential of oxygen in the electrolyte leads to a high effective pressure of oxygen in pores and cracks in the electrolyte near the electrode electrolyte interface. Since the oxygen chemical potential is linked to the cell voltage, the effective pressure at the electrode electrolyte interface is controlled by the applied overpotential. This value is positive in electrolysis and is related to crack growth through equation 2.26:

(Equation 2.26)

$$E_A \geq E_{cr} = \frac{RT}{4F} \ln \left\{ \sqrt{\frac{\pi}{(1-\nu)^2 c} \frac{K_{Ic}}{2p_o}} \right\}$$

Where E_A is the applied overpotential, E_{cr} is the critical overpotential required for stable crack growth, K_{Ic} is the electrolyte material fracture toughness, p_o is the oxygen partial pressure of the atmosphere, ν is the poisson ratio, c is the initial crack length, and $R, T, F,$ and π have their usual meanings. At 800 °C in air, assuming an initial crack length of 10 microns and a YSZ electrolyte the critical overpotential is 0.245V. Estimating the overpotential as the product of the cathode polarization resistance and current density, values of overpotential smaller than 0.24 are achievable at moderate current densities. One consequence of this reasoning is that oxygen electrodes with smaller polarization resistances should be more stable under electrolysis conditions. Moreover, from section 2.4.2 this implies that co-electrolysis of water and CO₂ at a lower voltage may not only have a higher round-trip efficiency, but also may make the device more durable in

electrolysis. Experimental evidence for oxygen bubble nucleation and crack growth exists in TEM analysis of a post-test electrode¹⁴⁴.

Recent works by Hughes et. al. and Jensen et. al. show that for the LSM-YSZ system, current cycling between SOFC and SOEC modes results in delamination failure similar to SOEC mode. However, an important distinction is that the rate of degradation decreases with an increase in cycling frequency compared to DC electrolysis. Jensen et. al. found that periods of SOFC mode between mostly SOEC mode slow the degradation rate dramatically. Hughes et. al. current cycled several LSM-YSZ symmetric cells for 1000 hour tests. The results showed that for a constant current density, the degradation rate was slowest for a 1 hour cycle (30 minutes DC operation in each direction) , followed by a more realistic 12-hour cycle, and fastest degradation for DC electrolysis (Figure 2.27)¹⁴⁵.

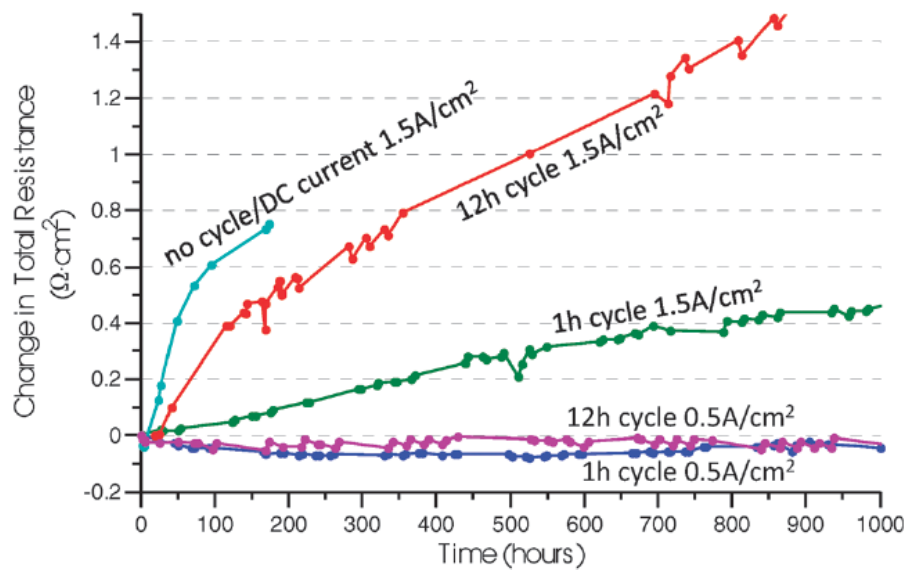


Figure 2.27. Current-cycled life tests for LSM-YSZ showing the effects of current density and cycling period. Reproduced from¹⁴⁵

Additionally it showed that smaller current densities are linked to slower degradation rates. In the context of the oxygen bubble theory, the suggestion is also that since current density and overpotential are linked, that there may be an operational region where stable current switching operation is possible. This is explored further in chapter 6.

2.5.2 Other Degradation Phenomena

2.5.2.1 Cation Segregation

Oxygen electrode polarization resistance degradation over time is often attributed to phase segregation, typically the surface enrichment of strontium, as observed in many Sr-containing perovskites including LSCF,¹⁴⁶ LSM¹⁴⁷, LSC^{148,149}, and STF¹⁵⁰. In experiments on dense LSCF pellets, Sr surface segregation at zero bias was observed as SrO islands, along with subsurface depletion of strontium and transition metals.¹⁵¹ LSC thin film results show a clear link between Sr surface enrichment, as measured by time of flight secondary ion mass spectrometry (ToF-SIMS) and inductively coupled plasma optical emission spectrometry (ICP-OES) over time at cell operating temperature (no applied bias and zero current density), and increased R_P ¹⁴⁹. Similar Sr segregation has been observed in LSCF electrodes prepared on GDC where the performance degradation is linked directly to the quantity of SrO present¹⁵². Figure 2.28 shows the R_P evolution during aging and after a chemical etching cleaning the surface. Recent work utilizing low energy ion scattering has demonstrated that A-site surface enrichment occurs generally in

perovskite compounds, double perovskites, and RP materials¹⁵³. Sr segregation and degradation was also observed for porous LSCF electrodes in anode-supported cells.¹⁴⁶

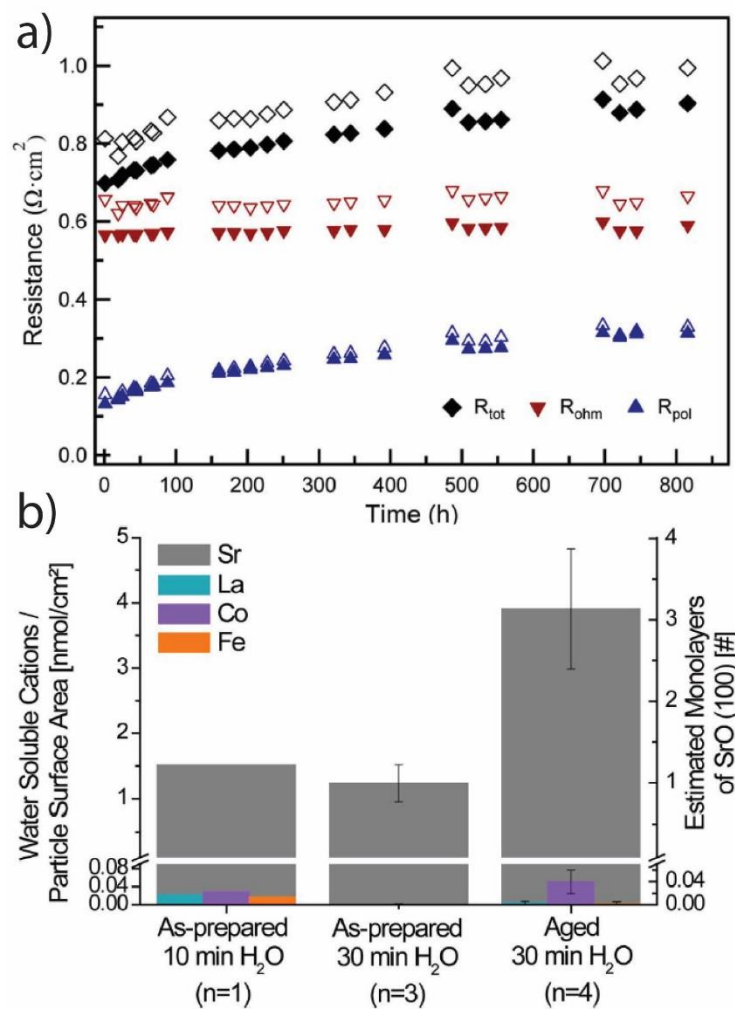


Figure 2.28. a) EIS data showing performance degradation for two LSCF/GDC cells annealed at 800 °C for 800 hours b) ICP-OES data comparing water etched control and aged samples controlled for internal surface area. Adapted from¹⁵²

The effect of potential or current density on the kinetics of Sr segregation is an open question, but there is some evidence pointing to operation dependent enrichment^{154 155}. Periodic applications of

large anodic DC biases has been shown to reduce surface resistance and drive excess Sr away from the surface of Co-rich $\text{La}_{0.6}\text{Sr}_{0.4}\text{Co}_{1-x}\text{Fe}_x\text{O}_{3-\delta}$ microelectrodes¹⁵⁶. The authors attribute this effect to a change in vacancy concentration at different overpotentials that affects how Sr moves to the surface.

2.5.2.2 Coarsening

The ALS model informs our understanding of the relationship between the structure and performance of the oxygen electrode. Maximizing the surface area of an MIEC, or maximizing the TPB density of an LSM-YSZ composite will minimize the polarization resistance. Nanostructuring the electrode to maximize surface area is then a logical step to achieve better SOC performance. Nanostructuring an oxygen electrode through infiltration is a common practice in a research setting. However, even low temperature solid oxide cells still operate above 550 °C where cation surface diffusion is still prevalent. The particle coarsening is described generally by equation 2.27:

(Equation 2.27)

$$l^n - l_0^n = K_D t$$

Where l is the effective particle diameter l_0 is the original particle diameter, K_D is the effective cation diffusion rate, t is time, and n is an exponent based on the mechanism at work (typically 4 for surface diffusion)^{157,158}.

Consequently, the coarsening of the finely structured electrode is a concern as the specific surface area is directly linked to the polarization resistance. This implies a trade-off between performance and stability for a chosen material. The rate of degradation by coarsening and whether there is a point at which the resistance is acceptably low and the degradation rate is also acceptably low is an open question. This trade-off is a major criticism of electrodes produced by infiltration. The process of coarsening has been described for LSCF infiltrated into GDC¹⁵⁹. Figure 2.29 shows the degradation of infiltrated LSCF at a range of temperatures described by a coarsening model.

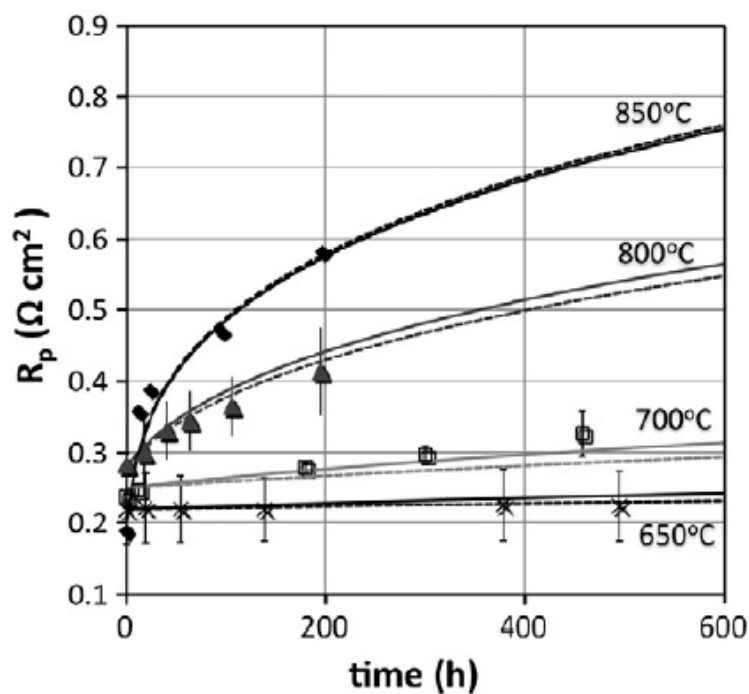


Figure 2.29. Degradation in the polarization resistance of an infiltrated LSCF electrode reproduced from¹⁶⁰.

2.5.2.3 Silver Migration

In SOCs, the metal contacts to the SOC must be designed to avoid migration of metals to the active sites in the SOC. In laboratory settings, gold or platinum is used to contact the cell as they are non-reactive and have high melting points. However, both are expensive and platinum may produce spurious results due to its high catalytic activity. Silver is often used to contact symmetric cells, but has been known to migrate to the active sites in full cells or symmetric cells where current is flowing for extended periods of time. Figure 2.29 shows a case where silver has migrated to TBP regions near the electrolyte in an LSM-YSZ electrode¹⁶¹.

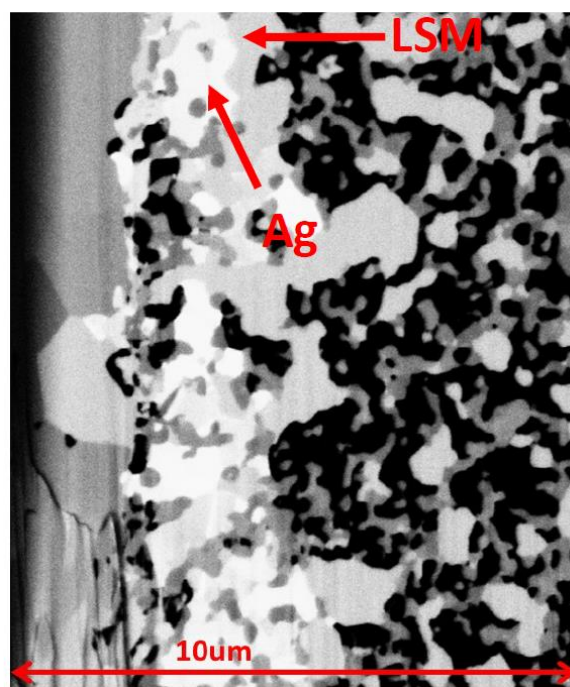


Figure 2.30. FIB polished cross-section of a symmetric LSM-YSZ cell operated under DC current showing the migration of silver from the contact to the active region near the electrolyte¹⁶¹

Chapter 3: Methods

This chapter briefly explains characterization methods and experimental apparatuses used in chapters 4, 5, 6, and 7.

3.1 Electrochemical Impedance Spectroscopy

Electrochemical impedance spectroscopy (EIS) is one of the few characterization methods available that allows the kinetics of the electrochemical reactions occurring at SOC electrodes to be probed under operating conditions. EIS is used heavily throughout this work to characterize the performance of cell components including oxygen electrodes and electrolytes. An overview of the theory, data analysis and specific experimental setups for EIS are described.

3.1.1 General Method

In its most basic embodiment, EIS is used to deconvolute the total cell resistance into ohmic resistance (ion transport through the electrolyte) and polarization resistance (reaction kinetics at the electrode). This is possible because the characteristic frequency for the chemical reactions at the electrodes occurs at a much lower frequency than electronic or atomic transport processes in the electrolyte bulk. In EIS, a small perturbing AC signal (5-20 mV) is introduced to the cell and the current response is measured (Figure 3.1).

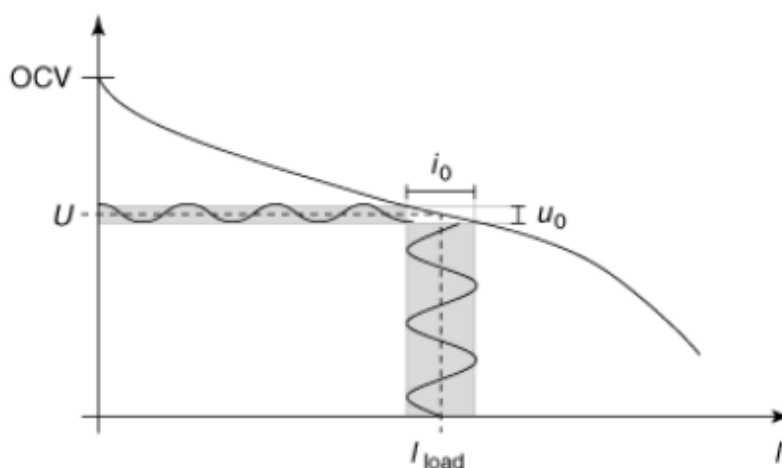


Figure 3.1. Schematic of electrochemical impedance spectroscopy where at an applied DC bias (typically zero, OCV) a small perturbing voltage signal is introduced and the current response is measured. The relationship between the signals gives the impedance. Reproduced from¹⁶²

The relation between the phase lag and the amplitude change gives the complex impedance. The voltage signal is then stepped through a range of frequencies from about 10^6 - 10^{-1} Hz. The upper frequency is typically limited by inductance in the test setup (high-frequency cut-off) and the lower frequency is the DC limit where the imaginary portion of the impedance drops to zero and the real impedance matches the resistance in DC operation. Practically, the frequency may not go all the way to the DC limit because at very low frequencies, the collection time becomes unreasonably large. The data is displayed as a Nyquist plot that plots the real versus the imaginary impedance, and a Bode plot that plots the imaginary impedance versus the frequency of the AC voltage signal (Figure 3.2). The ohmic resistance is taken to be close to the lower x-intercept (this is shifted by the inductance), the total resistance is the upper x-intercept (matches the DC resistance), and the polarization resistance is roughly the difference between the intercepts. Note in figure 3.2, the

inductance in the test setup returns positive imaginary losses above $\sim 2 \times 10^4$ Hz even though the scan runs from 10^6 - 10^{-1} Hz, the high frequency ‘cut-off’.

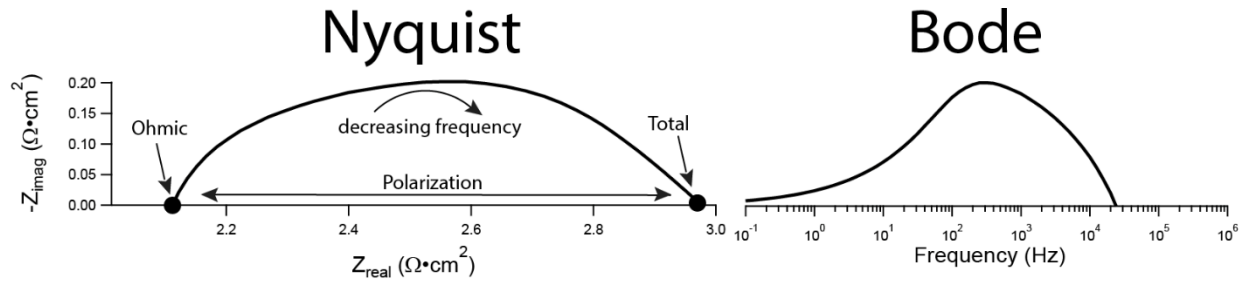






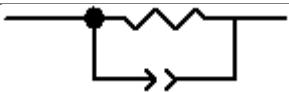
Figure 3.2. Nyquist and Bode plots showing the ohmic, polarization, and total resistance for a generic SOC device.

3.1.2 Circuit Modeling

In order to obtain accurate values of the ohmic, polarization, and total resistance, equivalent circuit modelling is often employed. The simplest function of an equivalent circuit is to correct for the inductance in the test setup to obtain an accurate value of the ohmic resistance, and extrapolate the low frequency portion to the x-intercept to obtain an accurate value of the polarization and total resistance. More than apportioning the resistance values, an equivalent circuit model informed by physical intuition can also provide insight to other physical processes occurring in the device.

Table 3.1 gives an overview of the circuit element types used in this work.

Table 3.1. Overview of circuit element types used in this work

Element (Label)	Symbol	Mathematical form	Comments
Inductor (L)		$Z = i\omega L$	Imaginary contribution dependent on test setup
Resistor (R)		$Z = R$	Describes ohmic resistance of the electrolyte
Constant Phase Element (QPE)		$Z = \frac{1}{(Qi\omega)^n}$	Describes chemical capacitance and accounts for distribution of relaxation times
Gerischer Element (G)		$Z = \frac{R}{(1 + i\omega\tau)^{1/2}}$	Describes ORR when the ALS model applies
RQ Element (RQ)		$Z = \frac{R}{1 + R(Qi\omega)^n}$	Generic kinetic process at an electrode

*Z = impedance, R = resistance (Ω), Q = chemical capacitance(F), i = imaginary number,
 $\omega = \text{angular frequency (Hz)}, L = \text{inductance (H)}, \tau = \text{time constant (s)}, \text{ and } 0 < n < 1$*

EIS interpretation through equivalent circuit models is prone to error as once enough degrees of freedom are introduced, anything can be fit. The object then is to use the fewest number of equivalent circuit elements that captures the physics of the response while also achieving an adequate fit. This typically means a single inductor and resistor in series to describe the wire inductance and electrolyte followed by one or more RQ or Gerischer elements to describe the process at the electrodes. Gerischer elements are assigned for mixed electronic ionic conductors where the ALS model applies, due to the similarity of the mathematical form between the gerischer element and the physical parameters predicted by the ALS model⁵⁸. A more detailed discussion of

the Gerischer element appears in chapter 5. Otherwise, in this work, generic RQ elements are assigned to each individual response observed in the impedance response. These RQ elements can also be used to describe the characteristic frequency (f_{\max}) of these processes. It can become very useful to measure the EIS response at a range of temperatures and gas compositions to determine what is limiting the performance of the electrode and to better assign the right number of circuit elements to a system for interpretation. Figure 3.3 shows an example of a real data set. It is clear that there are two distinct processes, so two elements were assigned to describe the response. Often the circuit model is written in shorthand ‘Boukamp’ notation, the one in figure 3.3 can be written as L-R-RQ-G, denoting series connection with a dash and parallel elements with parentheses or simply putting them adjacent. Note the shift in the real ohmic resistance in the Nyquist plot (0.8 rather than 0.815). The sum of the inductor, resistor, RQ and G elements give the red curve. The sum of the RQ and G arcs gives the polarization resistance. The first x-intercept of the RQ arc gives the real ohmic resistance. Note that the total resistance can be read directly from the plot without adjustment. Knowing more about the physical system can lead to more accurate models and a better understanding. For example, charge transfer and gas diffusion could have different rates and both be contributing to the polarization resistance, but if the EIS response was collected at varying oxygen pressures, it would be clear which response changes and with what magnitude. Measuring the device response under different conditions can clarify which processes are occurring.

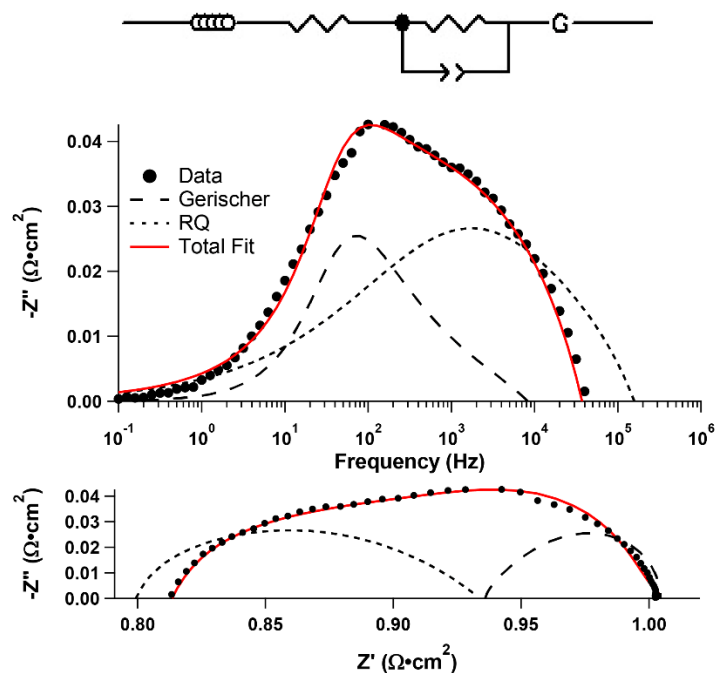


Figure 3.3. Example of how an equivalent circuit is used to fit experimental data, the inductor is not shown as it is below the x-axis. The inductor has a large magnitude at high frequencies.

3.1.2 Full versus symmetric cells

It is desirable to understand the EIS response of each electrode so that a focused effort can be made to improve the SOC and reduce the polarization resistance. However, a weakness of EIS is that the fuel electrode response often overlaps with the oxygen electrode response and can be difficult to deconvolute. In order to examine the oxygen electrode response in detail, symmetric devices are often utilized. In a symmetric device, oxygen electrodes are processed on both sides of an electrolyte (Figure 3.4).

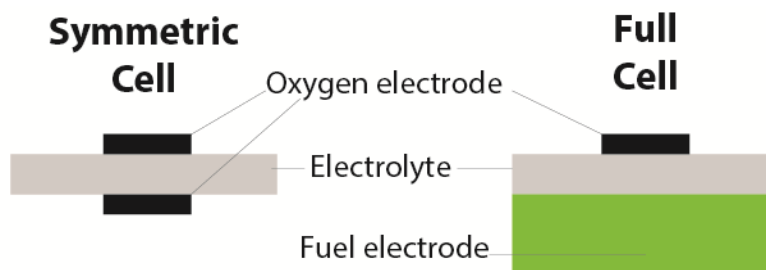


Figure 3.4. Schematic drawing of a symmetric device and a full fuel cell

A symmetric device is typically tested in a single chamber atmosphere, there is typically no gas seal between the electrodes. No voltage evolves as there is no net chemical reaction. However, if a current is driven through the device from an external source, the oxygen reduction reaction (ORR) will occur on one electrode, and the oxygen evolution reaction (OER) will occur on the other as oxygen is pumped from one side to the other through the electrolyte. In zero current, the polarization resistance of both electrodes can be probed, similar to a fuel cell at the open cell voltage. These diagnostic devices also have the benefit of simplifying the test setup as fuel does not have to be supplied to them, only ambient air, or a single chamber controlled atmosphere. If both electrodes are processed the same way, the area normalized resistances divided by two yields the resistances (ohmic, polarization, total) of an individual electrode.

3.1.3 Current Switched Setup

A real ReSOC will operate in DC electrolysis and in DC fuel cell mode for roughly equal portions of time, and the consequences of this kind of operation on electrode degradation need to be assessed (Chapter 6). To simulate this operation on an oxygen electrode, a current switched setup was used (Figure 3.5).

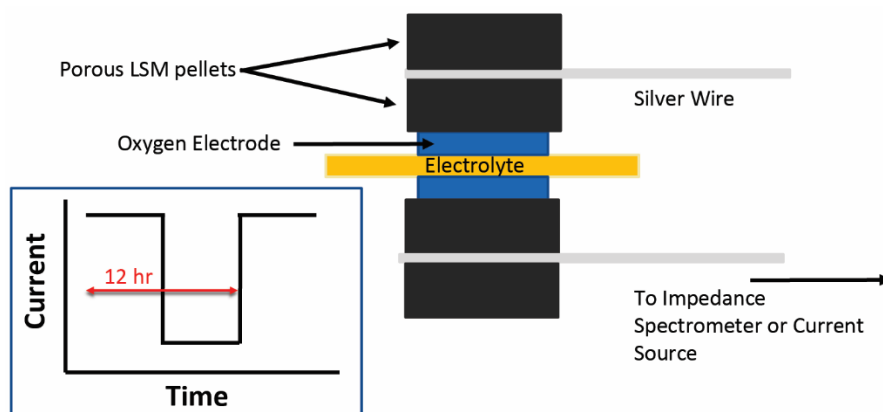


Figure 3.5. Diagram of current switched life-test setup for oxygen electrodes

A symmetric cell is contacted by two porous LSM pellets initially affixed to the device by an LSM paste composed of LSM particles and an organic vehicle that burns out upon ramping to operating temperature. The purpose of using ceramic contacts is to prevent electromigration from the silver wires to the electrode electrolyte interface¹⁶¹. A current is driven through the cell using an external sourcemeter that is programmed to switch polarity in a 12 hour cycle. The applied current effectively pumps oxygen through the cell each direction on a 12 hour cycle. The operation of the cell and interpretation of the EIS spectra is greatly simplified since each electrode experiences an equal amount of time operating in fuel cell mode and electrolysis mode, and the only responses are coming from the oxygen electrodes. This setup is used for all EIS results displayed in chapter 6.

3.1.4 Pressurized Setup

A custom designed pressurized furnace (Deltech) was utilized for the pressure and atmosphere dependent work in chapter 5. Figure 3.6 shows a schematic drawing of the pressure chamber. The separated hot-zone and lower area allows for polymer insulated wires and electronics. The separate

outer chamber and inner gas chamber allows an inert gas to be flowed over the heating elements and not subjected to the more oxidizing atmosphere within the quartz tube. Inside the quartz tube, a symmetric cell may be suspended at the end of the alumina gas manifold. The alumina insulated silver wires provide the mechanical support for the symmetric cell. The wires are attached to the cell using a silver based resin DAD-87 from the Shanghai Institute of Polymer Science. The chambers are pressurized passively from compressed gas cylinders that feed into them. Mass flow controllers for nitrogen and oxygen control the gas composition at the inlet. The pressure is controlled by relief valves (Brooks Instruments) at the outlets at the base of the chamber. The small volume of the quartz tube allows the gas composition around the cell to be replaced quickly such that a series of measurements can be taken within a day and negligible changes to the cell take place over time between measurements.

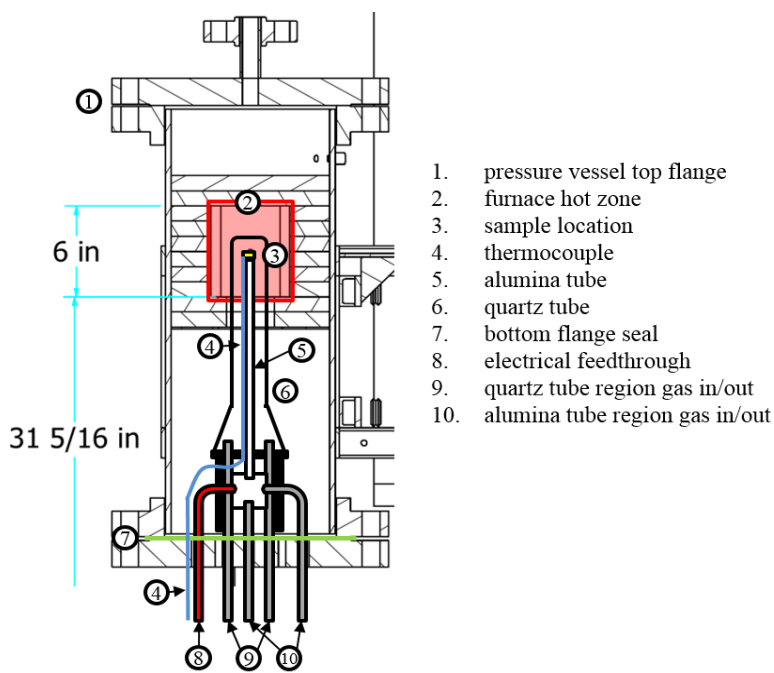


Figure 3.6. Schematic of the pressurized atmosphere controlled furnace used in this work¹⁶³

3.2 SEM/EDS

Scanning electron microscopy (SEM) and energy dispersive spectroscopy (EDS) are both very common techniques in materials science and so only special considerations for sample preparations and imaging conditions for this work are discussed in this section.

3.2.1 Sample Preparation

In order to evaluate microstructural changes that occur over the length of a current switched life test (~1000 hours), large cross-sectional areas of the cell must be imaged by a scanning electron microscope. However, fracture cross-sections are inappropriate as damage from fracture would be indiscernible from microstructural changes that may have occurred over the lifetime of the test. Therefore, to more cleanly image a post-test electrode epoxy infiltration is utilized. Following similar sample preparation utilized in FIB-SEM tomography^{51,164}, symmetric cells are first fractured and vacuum infiltrated with EpoThin Epoxy. This step holds the microstructure in place for subsequent polishing steps and gives good contrast between the pores and the solid phases. The resulting epoxy puck that contains a piece of the device is then diced into a small cube appropriate for mounting on an SEM stub (~3-5 mm on an edge) using an accutom 5 saw with an alumina cut-off wheel. The cube containing the sample is then glued to an SEM stub and hand polished down to a 1 micron diamond slurry (Buehler). This step allows for the controlled removal of material near the original fracture surface, so that a pristine region of the device is presented at the top surface for imaging. To provide appropriate electronic conductivity to prevent sample charging, the cubes are coated in 15 nm of Osmium using a commercial Os plasma enhanced chemical vapor

deposition chamber (SPF). Carbon tape is placed near the sample and provides an additional path to ground.

In some cases, due to imaging limitations in the epoxy infiltrated samples, fracture cross-sections are imaged. These samples are simply fractured, osmium coated, and carbon taped to a stub. It is appropriate to do this when the feature sizes of interest are significantly smaller than 1 micron. This kind of sample preparation is performed for infiltrated electrodes where the individual particles are of interest.

3.2.2 Imaging Conditions

To get a better understanding of what occurs microstructurally after a life-test, or even to characterize a freshly fabricated cell, it is desirable to image large areas of the electrode and electrode/electrolyte interface. This becomes challenging when the epoxy and solid phases are non-conductive and a uniform conductive coating is placed on the surface of the polished sample. In typical imaging conditions, such as those used in FIB-SEM (Table 3.2), only the top surface is visible, showing a uniform coating of osmium (Figure 3.7).

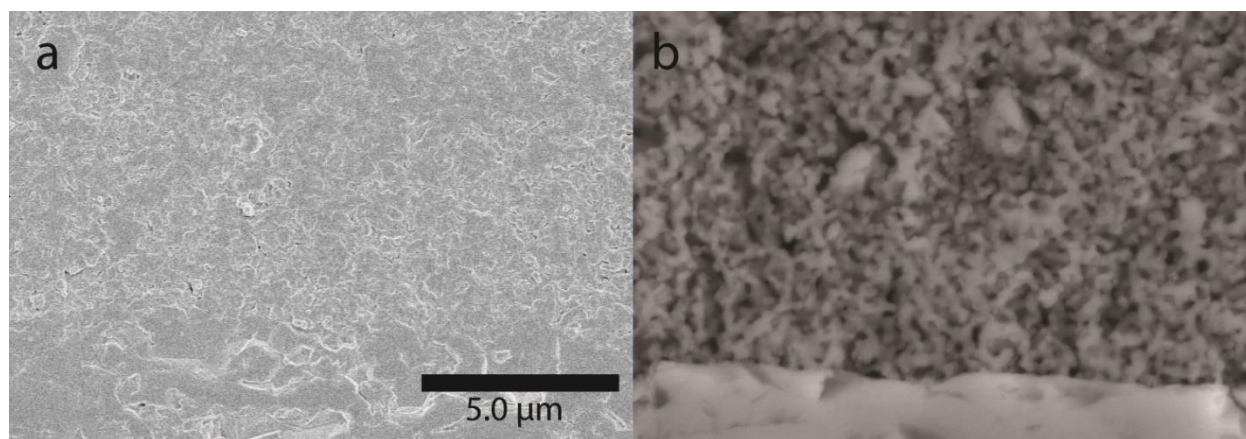


Figure 3.7. A polished and Os coated SOC sample at a) 2kV, 5 mm WD, upper detector b) 25kV, 15 mm, lower detector

In order to image the features of interest contained in the subsurface layer the interaction volume of the sample and the electron beam has to be increased by increasing the accelerating voltage. Moreover, information from the top layer is not valuable, and so every effort should be made to filter out the high energy secondary and backscattered electrons originating from this layer. To accomplish the electron filtering, the lower detector of the Hitachi SU8030 is used so a larger fraction of back scattered (and lower energy) electrons are collected. The net effect is that a much larger fraction of electrons from the subsurface layer are imaged compared and so there appears to be better contrast between the pores and the solid phase. These imaging conditions are also used for EDS, as the 20 kV operating voltage is high enough to collect $K\alpha$ x-rays from all elements of interest. Figure 3.7 shows the difference in imaging conditions and detectors for a typical epoxy infiltrated SOC.

Table 3.2

Condition	FIB-SEM	SEM	EDS
Accelerating Voltage (keV)	2	20-25	20-25
Working Distance (mm)	4	15	15
Detector	Upper	Lower	X-ray
Osmium thickness (nm)	0*	15	15
*The imaged area has no Os as it's milled away, but the rest of the sample has a 30 nm coating			

Chapter 4: Oxygen electrode characteristics of Pr₂NiO_{4+δ}-infiltrated porous

(La_{0.9}Sr_{0.1})(Ga_{0.8}Mg_{0.2})O_{3-δ}

4.1 Introduction

Reducing the polarization resistance of the oxygen electrode in SOCs for reversible operation is key to increasing the round-trip efficiency and may play a role in improving the device stability (discussed in chapter 6). Thus there is considerable interest in creating an electrode that operates below 650 °C with low polarization resistance and with good stability. Equally important to the materials properties for the oxygen electrode is processibility into the desired microstructure and the long term stability. Rare earth nickelates with the Ruddlesden-Popper (RP) structure (Ln₂NiO_{4+δ}, Ln=lanthanide) are a promising class of MIEC oxygen electrode materials owing to their good electronic conductivity, good TEC match to common electrolyte materials, and high *k* and *D* values. These materials avoid the Sr segregation problem at the outset because they are Sr free. La_{*n*+1}Ni_{*n*}O_{3*n*+1} has attracted much attention since it is both stable in contact with common electrolytes and exhibits relatively fast oxygen transport coefficients^{97,165}. La_{*n*+1}Ni_{*n*}O_{3*n*+1} has been prepared in the *n*=1, 2, and 3 phases^{18,166}, and even in combination as a functionally graded cathode that combines the high surface exchange of the *n*=1 phase with the superior electronic conductivity of the *n*=3 phase¹⁰⁸, representing the current best-in-class cathode for La_{*n*+1}Ni_{*n*}O_{3*n*+1} with a polarization resistance of 1.06 Ω•cm² at 650 °C. Nd_{*n*+1}Ni_{*n*}O_{3*n*+1} has proven to be reactive with some common electrolytes and has moderate oxygen transport coefficients compared with other rare earth nickelates¹⁶⁷⁻¹⁷¹.

Pr_{*n*+1}Ni_{*n*}O_{3*n*+1} electrodes have shown the lowest *R_P* amongst the RP materials^{172,173}, but there are significant stability issues. The *n*=1 compound powder has been observed to decompose to the

$n=3$ phase and Pr_6O_{11} below ~ 1000 °C¹⁷⁴. The material is also reactive with yttria stabilized zirconia (YSZ) and unstable on ceria electrolytes¹⁷⁰. Pr_2NiO_4 (PNO) in contact with (GDC) has been reported to decompose to PrNiO_3 and Pr_6O_{11} , and perhaps NiO ,¹⁶⁵ different than for PNO powder alone. The decomposition of PNO on $(\text{La}_{0.9}\text{Sr}_{0.1})(\text{Ga}_{0.8}\text{Mg}_{0.2})\text{O}_{3-\delta}$ (LSGM) does not follow the same sequence as on GDC or in powder form¹⁶⁵. PNO based cathodes on LSGM¹⁷² have yielded $R_P = 0.87 \Omega\cdot\text{cm}^2$ at 600 °C. PNO based cathodes on GDC¹⁷³ have been reported to yield R_P as low as $0.08 \Omega\cdot\text{cm}^2$ at 600 °C (although more recent reports by the same group give a value of $0.28 \Omega\cdot\text{cm}^2$)¹⁶⁵; these relatively low resistances are somewhat surprising given that the nickelate is unstable and may react with the electrolyte as suggested by the appearance of NiO peaks in X-ray¹⁶⁵. Substitution of Sr ¹⁷⁵, La , Cu or Ga ^{176,177} in Pr_2NiO_4 has been shown to improve stability, polarization resistance, and oxygen diffusivity.

There is relatively little information on the long-term resistance stability of RP electrodes, an especially important question given the above-mentioned phase stability issues. One report of a PNO electrode prepared on LSGM showed good stability,¹⁷² but there are no reports of polarization resistance versus time for praseodymium nickelate on GDC.

Finally, even though infiltration has been widely used to produce high-performance perovskite electrodes^{126,127,178}, there are only two prior reports of infiltrated RP electrodes – La_2NiO_4 and $\text{La}_4\text{Ni}_3\text{O}_{10}$ on YSZ¹⁸ and $\text{Nd}_2\text{NiO}_{4+\delta}$ on scandia stabilized zirconia¹⁷⁹. These yielded relatively low R_P values at 750°C of $0.120 \Omega\cdot\text{cm}^2$, $0.068 \Omega\cdot\text{cm}^2$ and $0.059 \Omega\cdot\text{cm}^2$, respectively, despite reactivity with YSZ¹⁷⁰.

This chapter describes the fabrication, performance, and stability of infiltrated Pr_2NiO_4 cathodes on LSGM. Besides providing R_p values comparable to the best prior reports of RP electrodes, the infiltrated Pr_2NiO_4 shows improved stability compared to prior reports on this material.

4.2 Experimental

The oxygen electrodes were prepared on LSGM electrolyte supported symmetrical cells. LSGM powder was synthesized from stoichiometric amounts of SrCO_3 (Sigma), La_2O_3 (Sigma), Ga_2O_3 (Sigma), and MgO (Alfa Aesar), which were ball milled for 24 hours in ethanol, dried, and then reacted at $1250\text{ }^\circ\text{C}$ for 12 hours. This LSGM powder was then ball milled in ethanol and 2 wt. % polyvinyl butyral (Aldrich) binder, dried, and pressed into 500 mg 19 mm diameter pellets. The green bodies were then sintered at $1450\text{ }^\circ\text{C}$ for 4 hours. LSGM scaffolds were screen printed onto the electrolyte pellets using an ink composed of commercially available LSGM (Praxair), Heraeus 737 vehicle, and 30 wt% of KS4 graphite flakes (Timrex) as pore former. Four screen printed layers were applied to each side, then heated to $600\text{ }^\circ\text{C}$ for one hour to burn away the pore former, and then fired at $1200\text{ }^\circ\text{C}$ for 4 hours to form a porous scaffold layer with interconnected LSGM particles 1-3 microns in size. A current collector was then applied on each scaffold by screen printing one layer of an $(\text{La}_{0.6}\text{Sr}_{0.4})(\text{Co}_{0.8}\text{Fe}_{0.2})\text{O}_{3-\delta}$ ink consisting of the same vehicle, pore former, and LSCF powder (Praxair). Note that the current collector was omitted for samples to be studied with X-ray diffraction, in order to avoid additional reflections from LSCF. The entire assembly was then fired at $1100\text{ }^\circ\text{C}$ for one hour to produce a suitably porous current collector that was also well bonded to the scaffold. The resulting scaffold thickness was $\sim 40\text{ }\mu\text{m}$ and the LSCF layer was $\sim 10\text{ }\mu\text{m}$ thick.

The electrode infiltrate was a 2 M nitrate solution prepared by dissolving stoichiometric amounts of $\text{Pr}(\text{NO}_2)_3 \cdot 6\text{H}_2\text{O}$ (Aldrich) and $\text{Ni}(\text{NO}_2)_3 \cdot 3\text{H}_2\text{O}$ (Fischer) in water and subsequently adding 0.06 mol of Triton X-100 (VWR). This solution was stirred for 24 hours to ensure good mixing. Each scaffold was infiltrated with this solution using excess fluid ($\sim 6 \mu\text{L}$) and removing the excess after allowing solution to infiltrate the porous scaffold for 5 minutes. The infiltrate was decomposed by heating to $450 \text{ }^\circ\text{C}$ for 0.5 hours, leaving oxides of the respective metal ions. After the desired number of infiltrations, ranging from 4 to 16, was complete, the symmetric cells were typically fired at $1000 \text{ }^\circ\text{C}$ for 4 hours. All specimens were cooled no faster than $5 \text{ }^\circ\text{C}/\text{min}$. Infiltrate volume fractions were determined from the mass difference between the final cell and the structure prior to infiltration. The infiltrate volume fraction was obtained from this mass difference and the theoretical density of Pr_2NiO_4 , and then dividing by the total electrode volume. Finally, powders were produced by drop casting the infiltrate solution onto an alumina plate and subjecting it to a similar firing program as above with the maximum temperature ranging from 900 to $1100 \text{ }^\circ\text{C}$. The resulting material was gently scraped from the plate and ground by mortar and pestle for powder X-ray.

A silver current-collector grid was screen printed onto each electrode using Heraeus unfritted silver paste, and a silver wire attached for electrochemical impedance testing. Impedance testing was performed using a Zahner IM6 between 10^5 and 10^{-1} Hz . All EIS data sets were modeled using an equivalent circuit consisting of three RQ elements and a resistor in series. The fits were used to obtain polarization resistances and the ohmic resistance. X-ray diffraction data was collected using a Scintag XDS2000 using $\text{Cu K}\alpha$ 1.54 \AA and a solid state detector.

4.3 Results and Discussion

4.3.1 Processing and Phase Formation

Figure 4.1 shows that nitrate solutions fired at 900 and 950 °C for 4 hours result in a mixture of NiO and Pr₆O₁₁. Nitrate solutions fired at 1000 °C and 1100 °C for four hours result in the n=1 R-P phase (Pr₂NiO₄) with small amounts of Pr₆O₁₁. These x-ray results suggest that the nickelate-forming reaction between the NiO and Pr₆O₁₁ phases is not spontaneous below 950-1000 °C, but that Pr₂NiO₄ is formed at higher temperature. This is consistent with previous studies,^{174,180} which indicated that Pr₂NiO₄ is stable at temperature >850-950 °C.

Similar to the powder results in Figure 4.1, Pr₂NiO₄ is also obtained after infiltrating and firing at 1000 °C in the scaffold, as shown by XRD (Figure 4.2b). Based on these results, all further PNO infiltrated electrodes in this study were treated at 1000 °C for 4 hours.

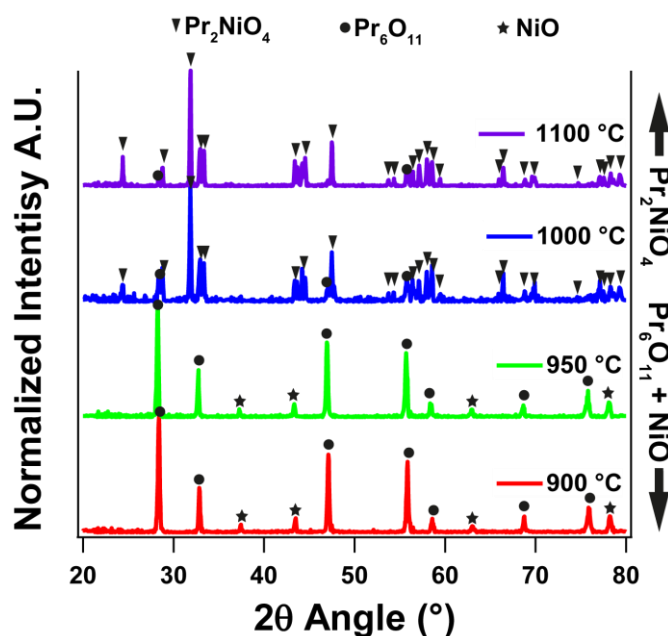


Figure 4.1. X-ray diffractograms of the PNO powders after 4 hour heat treatments in air at 900, 950, 1000, and 1100 °C. Reacting the oxides at 1000 °C for 4 hours produces Pr₂NiO₄.

Figure 4.2a shows a fracture cross-section SEM image of the infiltrated scaffold, current collector, and a portion of the electrolyte of a typical as-prepared cell after infiltrate firing at 1000 °C. The current collector and infiltrated LSGM scaffold show similar porous contrast, whereas the LSGM appears reasonably dense. The EDS line scan superimposed on the image shows that both porous electrode layers contain Pr and Ni, including the region near the electrode/electrolyte interface. The apparent Pr signal in the LSGM was due to an overlap of the Pr peak with the La peak. Figures 4.2c and d show higher magnification fracture cross-sectional SEM images of an un-infiltrated LSGM scaffold, for comparison with similar images taken from an infiltrated but otherwise identical scaffold (Figures 4.2e and f). Although there was low contrast between the LSGM and the infiltrated phase, the presence of the infiltrate is suggested by the slight roughness seen at high magnification.

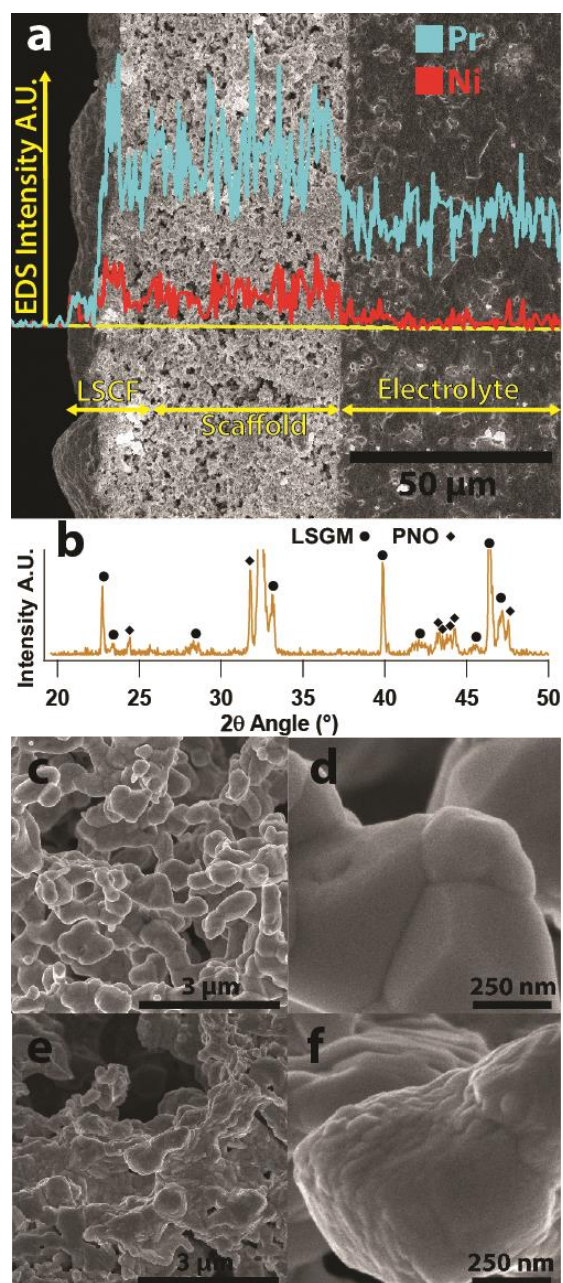


Figure 4.2. a) EDS line scan of an infiltrated cell showing the entire thickness of the cathode contains Pr and Ni. b) X-ray scan of an infiltrated cathode fired at 1000 °C and without current collector. The microstructure of an uninfiltrated scaffold is shown in c) and d), and compared with that of an 8-times infiltrated scaffold shown in e) and f).

4.3.2 Phase Stability

Figure 4.3 compares the X-ray diffractograms from the as-prepared bulk Pr_2NiO_4 powder (prepared at 1000 °C as described above and also shown in Figure 4.1 (a) and the same powder subsequently annealed in air for 100 hours at 650 °C (b). The X-ray results shows that the lower-temperature treatment fully decomposed the Pr_2NiO_4 powder into $\text{Pr}_4\text{Ni}_3\text{O}_{10}$ (the $n=3$ R-P phase) and Pr_6O_{11} . That is, Pr_2NiO_4 is unstable at 650 °C. This is consistent with prior reports showing that Pr_2NiO_4 decomposes to $\text{Pr}_4\text{Ni}_3\text{O}_{10}$ and Pr_6O_{11} in air at temperatures below 900 °C.^{174,180} Thus, while Pr_2NiO_4 can be produced by firing at ≥ 1000 °C, it is expected to decompose if used in a solid oxide cell at lower temperature.

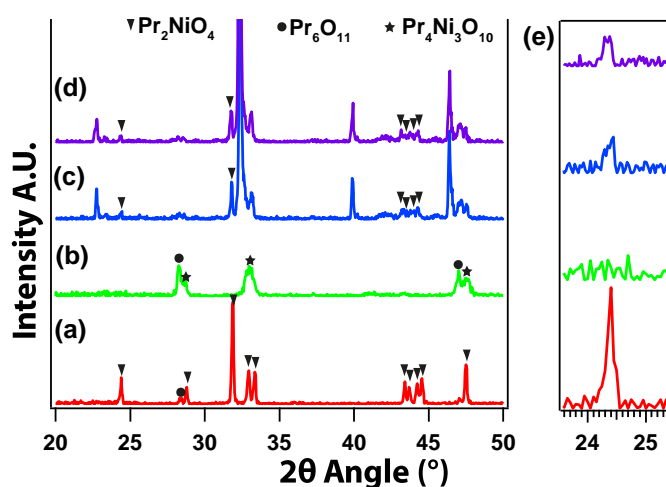


Figure 4.3. X-ray diffractograms from (a) as-prepared Pr_2NiO_4 powder; (b) the powder shown in (a) after aging for 100 hours at 650 °C; (c) the 12-times infiltrated Pr_2NiO_4 cathode and (d) the cathode shown in (c) after aging for 100 hours at 650 °C. The inset (e) highlights the reflection at 24.4°, the only Pr_2NiO_4 peak not overlapped with a peak from another phase. All unlabeled peaks

correspond to LSGM. The infiltrated cathodes were prepared the same as those used in EIS measurements, except that the LSCF current collector was omitted to eliminate its extra x-ray reflections.

Figure 4.3 also compares the x-ray scans from the as-prepared PNO infiltrated cathode, shown in Figure 2 to be predominantly Pr_2NiO_4 (c) compared with the same electrode annealed in air for 100 hours at 650 °C (d). Unlike the powder results, there is little apparent effect of annealing; both scans show peaks as expected for $\text{Pr}_2\text{NiO}_{4+\delta}$, along with peaks from the LSGM scaffold. This suggests that the n=1 phase is retained when annealed in the LSGM scaffold. This can be seen more clearly in Figure 4.3 (e), which shows a magnified view of the n=1 peak at 24.4°, the only RP-phase peak not overlapped with another peak, for all four samples. This peak is present in the as-prepared powder (a), but is not present in the aged powder (b) because of the transformation from n=1 to n=3. For the infiltrated LSGM scaffolds, this peak does not change after annealing at 650 °C, indicating that, at most, only a small fraction of the material transformed to n=3. That is, the n=1 phase in the LSGM scaffold was more stable than the powder. This may be explained by the physical constraint on any transformation with an associated volume change or distortion, caused by the intimate contact between the infiltrate and LSGM. In particular, the a and b lattice constants remain relatively unchanged for the transformation from n=1 to n=3, but the c direction in the n=3 phase (27.50 Å) is smaller than would be expected relative to the n=1 (12.45 Å) phase given the number of atoms in the unit cell^{174,180}. Alternatively, there may be significant interdiffusion during infiltrate firing at 1000 °C: diffusion of lanthanum, strontium or gallium from the LSGM into the PNO could help stabilize the n=1 phase. Both lanthanum and gallium have

been shown to increase the low temperature stability of the n=1 phase, material^{167,176,181}. Phillippeau *et al* reported a reaction between PNO and LSGM at 1150 °C forming a praseodymium gallate, which is not observed for our processing temperature, but does show the possibility of gallium diffusion¹⁶⁵.

4.3.3 Electrochemical Characteristics

Cells were infiltrated 4, 8, 12, or 16 times, resulting in measured volume fractions of ~ 10, 12, 14, and 16%, respectively. Five cells were fabricated for each level of loading, and considerable variation in polarization resistance, by as much as a factor of 2, were observed, but the shapes and peak frequencies of the impedance responses did not vary significantly. Figure 4 shows Nyquist and Bode plots of the EIS data measured in air at 650 °C from the best devices at each infiltrate loading. There was one main depressed arc in all cases, peaked at a frequency of ~ 30 Hz, that decreased with increasing loading. A smaller response is also observed at ~1000 Hz. The polarization resistance R_p , measured by fitting the responses using an equivalent circuit, decreased with increasing loading to a minimum of 0.11 $\Omega \cdot \text{cm}^2$ at 12 infiltrations, and appeared to increase slightly at 16 infiltrations. This is similar to the loading dependence observed previously for infiltrated LSCF and SSC perovskite cathodes^{127,178}. This dependence has been explained by an increase in the infiltrate surface area and an increase in the fraction of infiltrated particles that are electrically percolating and, therefore, active for the oxygen reduction reaction^{178,182}.

Figure 4.5 shows Nyquist and Bode plots of the EIS data taken from the 12-infiltration cathode at various temperatures. The main polarization response increases rapidly in magnitude with decreasing temperature, and also shifts to lower frequency, as expected given the resistance increase. The model used for fitting is shown in figure 4.5. Two R-Q elements are used to model

the main polarization response as they resulted in better fits for all EIS data, especially at longer times where two responses are apparent (Figure 4.7). Both responses are thought to correspond to a co-limited ORR process involving oxygen surface exchange and bulk diffusion, similar to previous work on infiltrated cathodes^{127,178}. A third response at high frequency, $> 10^5$ Hz, also appears at low temperature. This high frequency response is likely an interfacial process, either from grain boundaries or from the transport of oxygen across the PNO/LSGM interface.

Figure 4.6 shows the R_p values measured for all samples at each loading, plotted versus inverse temperature. The activation energies versus infiltration number, obtained by fitting the temperature dependences for each cell, are displayed as an inset in figure 4.6. The value obtained is $1.4 \text{ eV} \pm 0.2 \text{ eV}$. Loading beyond 12 infiltrations offers minimal further decrease in R_p , and may actually slightly increase R_p . The average polarization resistance for 8 devices at $650 \text{ }^\circ\text{C}$ and 12 infiltrations is $0.16 \text{ } \Omega \cdot \text{cm}^2$, with values ranging from 0.11 to $0.22 \text{ } \Omega \cdot \text{cm}^2$.

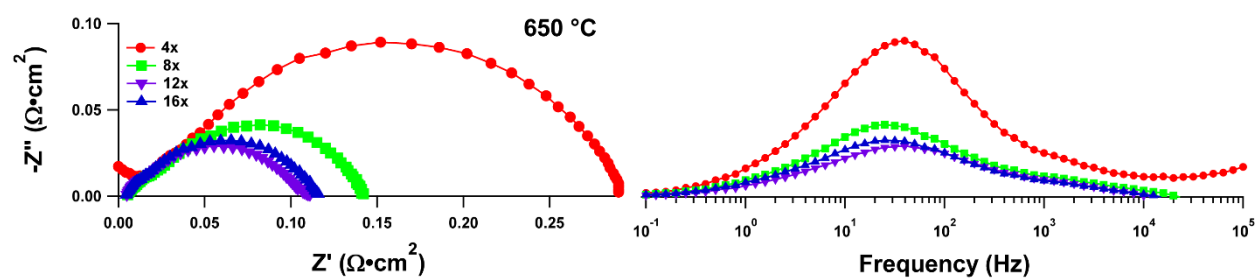


Figure 4.4. Nyquist and Bode plots of the electrochemical impedance response measured in air at $650 \text{ }^\circ\text{C}$ for cells infiltrated 4, 8, 12, and 16 times. The high-frequency intercept of the fitted equivalent circuit was set to zero in the Nyquist plots to allow easy comparison of the polarization arcs.

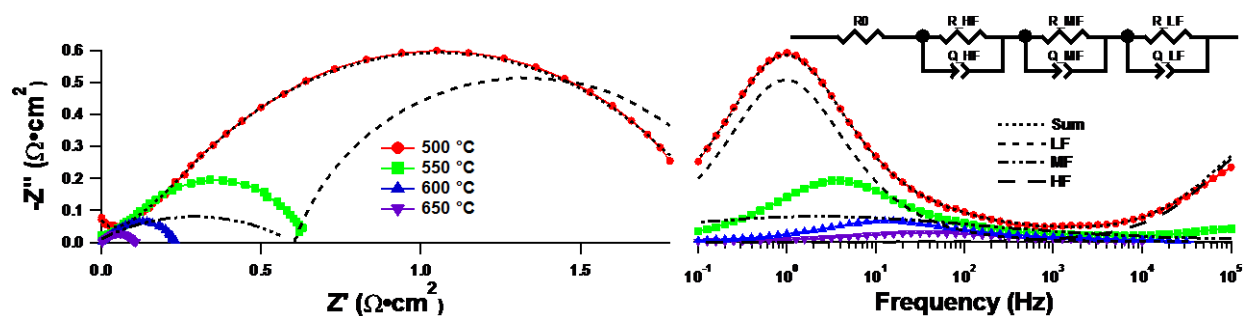


Figure 4.5. Nyquist and Bode plots of the electrochemical impedance response measured from a 12-times infiltrated cell in air at various temperatures. The high-frequency intercept of the fitted equivalent circuit was set to zero in the Nyquist plots to allow easy comparison of the polarization arcs. An example of an equivalent circuit is shown on the plot.

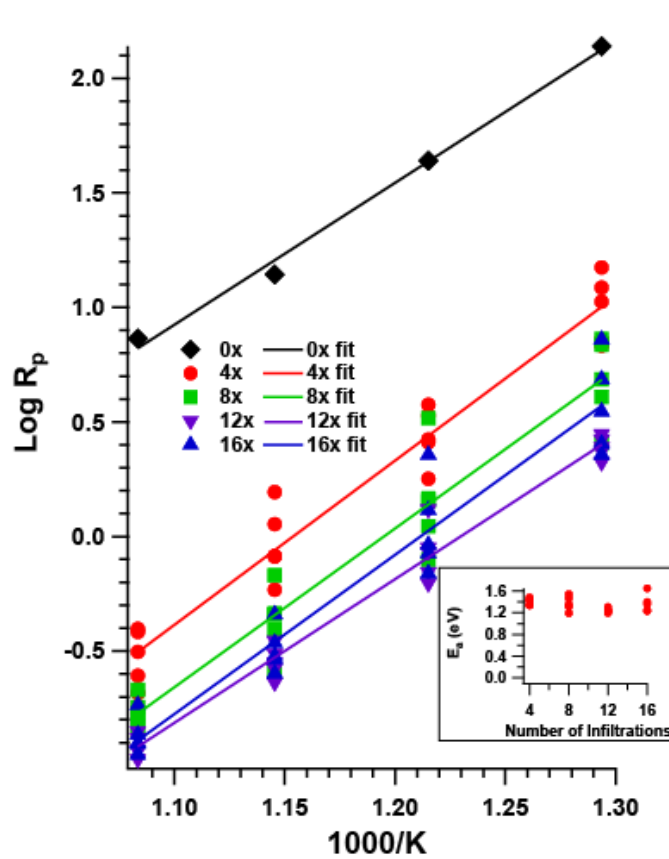


Figure 4.6. Polarization resistance plotted versus inverse temperature for all cells tested at each loading level. The lines show the best overall fits to an Arrhenius dependence for the data at each loading. The inset shows a plot of the activation energies obtained from Arrhenius fits to all cells, versus number of infiltrations.

4.3.4 Electrochemical Stability

In order to provide a preliminary measure of electrode stability, three identical symmetric cells, each infiltrated 12 times, were maintained at 650 °C in air for 500 hours. Figure 4.7 shows representative Nyquist and Bode plots of the EIS data taken periodically during the test. Figure 8 shows the R_P values versus time derived from fits to the EIS data. The response changes significantly in the first 100 hours – the main response at ~ 30 Hz decreases slightly and shifts to slightly higher frequency, while a new smaller response at ~ 1 Hz appears – resulting in a slight overall decrease in R_P . After ~ 100 h, the shape of the response does not change, but the size of the responses increases gradually, with R_P increasing by ~0.05 $\Omega\cdot\text{cm}^2/\text{kh}$ following the initial drop in the first 100 h. Longer term tests will be required to determine if R_P eventually stabilizes or continues to increase.

The initial changes in electrode response shown in Figures 4.7 and 4.8 are presumably caused by equilibration of the electrode to the testing conditions. The steady increase in R_P of both responses at longer times may be related to a decrease in the PNO surface area due to coarsening¹²⁶. It may also arise from a partial phase transformation of the n=1 nickelate phase, although the X-ray results shown in Figure 4.3 suggest that this was mostly suppressed in these electrodes. Recent reports utilizing low energy ion scattering suggest that A-site surface enrichment may occur in R-P materials, which may also account for the resistance increase.¹⁸³

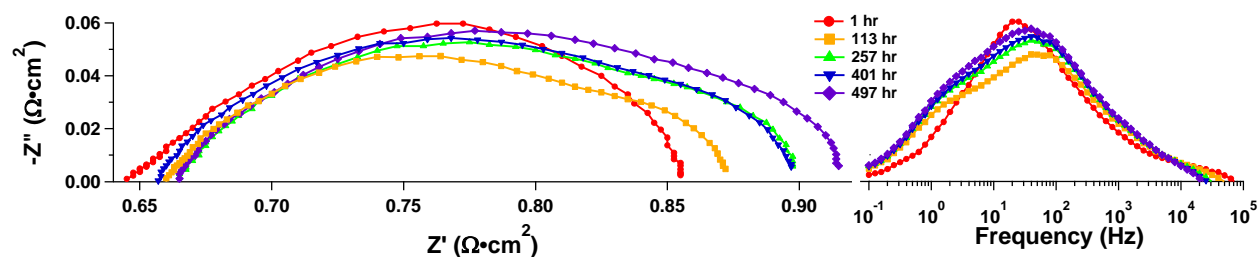


Figure 4.7. Bode and Nyquist plots of EIS data taken from a cell with 12-times infiltrated PNO/LSGM electrodes taken during a 500 h life test in air at 650 °C.

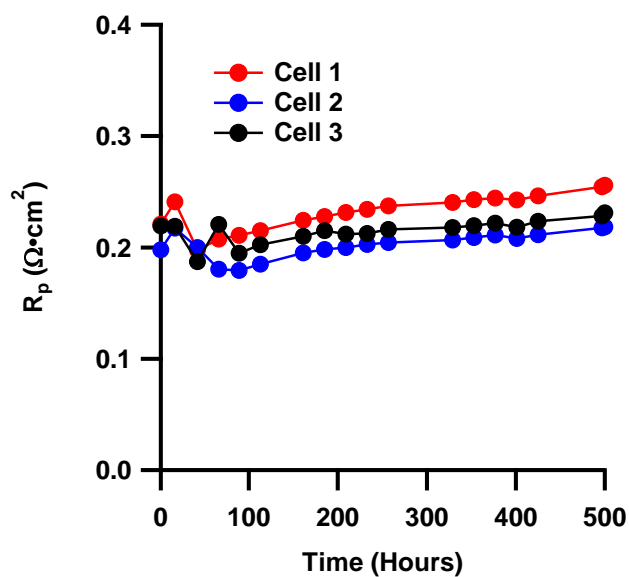


Figure 4.8. Polarization resistance versus time for 3 identically processed 12-times infiltrated cells at 650 °C.

4.3.5 Comparison with Other MEIC Electrodes

Figure 4.9 shows R_p as a function of temperature for the present best cathode compared to prior reported values for R-P electrodes. The present electrodes are as good or better than prior electrodes except for one report which gives a value of $0.08 \Omega \cdot \text{cm}^2$ at $600 \text{ }^\circ\text{C}$ ¹⁷³. Also shown for comparison are the values reported for the perovskite cathodes LSCF¹²⁷ and SSC.¹⁷⁸ These were

prepared using a similar infiltration method as the present nickelate cathodes, including infiltration with aqueous metal nitrates and optimized levels of active material loading. The infiltrated PNO electrodes provide similar R_p values as these state-of-the-art perovskite MIEC electrodes, although the comparison is not perfect as the LSCF and SSC cathodes were infiltrated into GDC scaffolds, not LSGM, and they were calcined at a lower temperature.

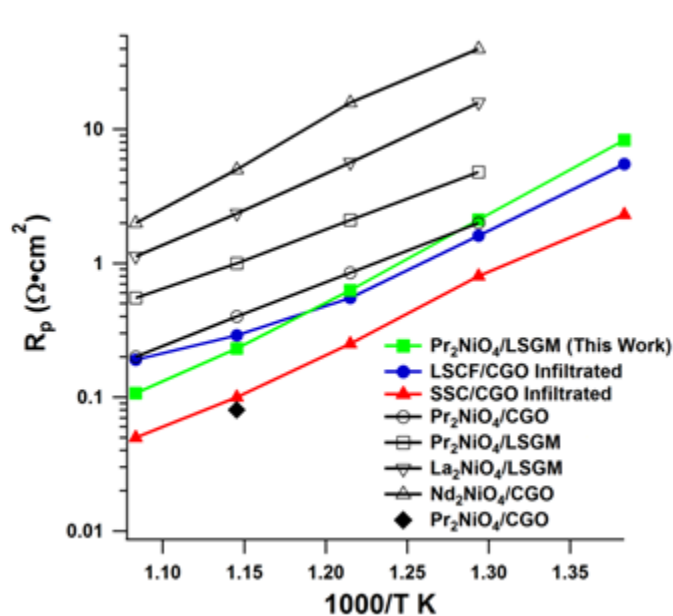


Figure 4.9. Comparison between single phase RP cathodes^{108,165,169}, and infiltrated LSCF¹²⁷, SSC¹⁷⁸, and PNO (this work) in the temperature range from 450-650 °C on the indicated electrolyte.

4.4 Conclusions

The Ruddlesden-Popper oxide Pr_2NiO_4 was synthesized by infiltration onto an LSGM scaffold and firing at a temperature > 950 - 1000 °C. The lowest polarization resistance was obtained for electrodes with 14 vol% PNO (12 infiltrations), ranging from 0.11 to $0.21 \text{ } \Omega \cdot \text{cm}^2$ measured at 650 °C in air. Preliminary life tests showed a polarization resistance increase of $\sim 10\%$ after 500 hours

operation at 650 °C. However, the infiltrated Pr_2NiO_4 electrodes showed no evidence of the decomposition to $\text{Pr}_4\text{Ni}_3\text{O}_{10}$ and Pr_6O_{11} normally observed for Pr_2NiO_4 powders and powder-based electrodes maintained below 900 °C. Given resistance values that are competitive with infiltrated perovskite cathodes, and the absence of the Sr segregation and cobalt disposal issues associated with the perovskites, infiltrated PNO on LSGM is a promising IT-SOFC oxygen electrode material. This electrode is further characterized in chapter 7 under pressurized conditions and future studies on the long term stability, especially under current loading, would be of interest in continuing to develop this electrode.

4.5 Acknowledgements

Much of the material and argumentation in this chapter is also published in *Solid State Ionics* (2015) ¹⁰³. Dr. Zhan Gao contributed useful discussions, ink formulations, and some of the cell test data. He also trained me on powder synthesis and EIS techniques used in this study.

Chapter 5: High-Pressure Performance of Mixed-Conducting Oxygen Electrodes: Effect of Interstitial Versus Vacancy Conductivity

5.1 Introduction

The pressurized operation of solid oxide cells (SOCs) has been proposed and investigated as a means to improve cell performance,^{20,184,185} to better interface with a downstream process or to alter reaction products.^{19,22} For example, solid oxide fuel cell – turbine hybrid systems are generally designed to operate at elevated pressure.¹⁸⁵⁻¹⁸⁸ Solid oxide electrolysis cells can be pressurized so that cell products can be easily introduced into pressurized catalytic reactors.^{20,189} Recently, reversible solid oxide cells have been proposed as the basis for a new electrical energy storage technology; however, achieving round-trip efficiencies >70% requires cell operation under pressurized conditions, and preferably at low temperature (< 600 °C)^{19,22,190,191}.

There have been a few reports describing the performance of SOFCs at high pressures^{20,185,192-194}, but few examples where the pressure dependent electrochemical characteristics of an individual SOC electrode has been characterized¹⁹⁵. One report in particular, examines the operational characteristics of short stacks of anode supported Ni-YSZ/YSZ/LSM-YSZ cells and notes a decrease in the total overpotential with increased pressure on both sides of the device¹⁹⁶. There are no reports, to our knowledge, showing the effect of pressurization on mixed ionically and electronically conducting (MIEC) electrodes, which are typically used as the oxygen electrodes in low-temperature SOCs.²⁵ Understanding MIEC electrochemical characteristics at high pressure is important for predicting how pressurized SOC stacks will perform. Furthermore, it is useful to identify specific materials that yield low oxygen electrode resistance under pressurization,

especially since oxygen electrodes are typically a primary factor limiting SOC performance, at low temperature.²⁵

Here new results are presented on the electrochemical characteristics of several promising low temperature MIEC electrode materials under pressurized conditions: two oxygen-ion vacancy conducting MIECs, $(\text{Sm}_{0.5}\text{Sr}_{0.5})\text{CoO}_{3-\delta}$ (SSC) and $(\text{La}_{0.6}\text{Sr}_{0.4})(\text{Co}_{0.2}\text{Fe}_{0.8})\text{O}_{3-\delta}$ (LSCF), and two oxygen-interstitial conducting MIECs, $\text{Nd}_2\text{NiO}_{4+\delta}$ (NNO), and $\text{Pr}_2\text{NiO}_{4+\delta}$ (PNO). The SSC and PNO electrodes were made by infiltration into ionic-conductor scaffolds, whereas the LSCF and NNO electrodes were made by conventional powder processing methods. In all cases, the interstitial-conducting MIECs show a larger decrease in polarization resistance with increasing oxygen pressure $p\text{O}_2$ than the vacancy conductors. It is proposed that increasing $p\text{O}_2$ improves defect transport kinetics in nickelate electrodes due to an increasing interstitial concentration, whereas defect transport kinetics in perovskite electrodes are degraded by decreasing vacancy concentration. This hypothesis is tested by manipulating the Adler-Lane-Steele (ALS) model in order to calculate pressure-dependent point defect concentrations in LSCF¹⁹⁷ and NNO¹⁹⁸ electrodes, utilizing measured electrochemical characteristics and 3D tomographic microstructural data.

5.2 Experimental

Four different types of symmetrical cells were prepared and electrochemically tested versus $p\text{O}_2$. Two of the cells had infiltrated electrodes, (1) PNO infiltrated into LSGM scaffolds with LSGM electrolyte, and (2) SSC infiltrated into GDC scaffolds with GDC electrolyte. Two of the cells had powder-processed single-phase porous electrodes, (3) NNO on LSGM electrolyte and (4) LSCF on GDC electrolyte.

5.2.1 Single Phase LSCF Symmetric Cell Fabrication

The cell fabrication method is similar to that described in Ref. ¹⁵². Briefly, gadolinium doped ceria (Rhodia) was ball milled in ethanol for 24 hours, dried, and pressed into 19 mm diameter 0.4 g pellets without binder. These pellets were fired at 1450 °C for 6 hours and served as the electrolyte support for symmetric LSCF electrodes. The LSCF (Praxair) was three-roll milled with Heraeus-V737 organic vehicle in a 1:1.17 mass ratio to form an LSCF ink. The LSCF ink was screen printed onto the sintered pellets and fired at 1100 °C for 1 hour resulting in a ~20 µm thick electrode. Silver metal grids were applied as current collectors for electrochemical testing.

5.2.2 Single Phase NNO Symmetric Cell Fabrication

The cell fabrication method is similar to that described in Ref. ⁵⁹. Briefly, commercial LSGM (Fuel Cell Materials) was pressed to 19 mm diameter pellets and sintered at 1500 °C for 4 hours to form the electrolyte support for the NNO symmetrical cells. NNO powders were synthesized by a sol-gel route.¹⁷⁰ Nd_2O_3 and $\text{Ni}(\text{CH}_3\text{COO})_3 \cdot \text{H}_2\text{O}$ were dissolved with acetic acid, hexamethylenetetramine (HMTA) and acetylacetone, using a ligand to metal molar ratio of 3:1. This solution was heated to gel and then fired at 400 °C and calcined at 950 °C for 12 hours. The resultant NNO powder was suspended with polyvinyl butyral (2wt%), polyethyleneglycol (1 wt%), ethanol (30 wt%) and α -terpineol (27 wt%), which were then deposited onto the LSGM pellets by spin coating. These electrodes were dried and fired at 1000 °C for 1 hour resulting in a final thickness of ~10 µm. Gold metal grids were applied as current collectors for electrochemical testing.

5.2.3 SSC Infiltrated GDC Symmetric Cell Fabrication

The cell fabrication method is similar to that described in Ref. ¹⁹⁹. Briefly, pellets of GDC were fabricated as above to serve as electrolyte supports. For the GDC scaffold inks, the GDC (Rhodia) powder was three-roll milled with Heraeus-V737 organic vehicle to form a 7.31 vol% GDC ink. The GDC ink was screen printed onto the sintered pellets and fired at 1100 °C for 4 hours with a final scaffold thickness of ~20 μm. A layer of LSM ink was then screen printed and fired at 800 °C for 1 hour as a current collector to a thickness of 10 μm. The SSC infiltrate solution was prepared by dissolving $\text{Sm}(\text{NO}_3)_3 \cdot 6 \text{H}_2\text{O}$, $\text{Sr}(\text{NO}_3)_2$, and $\text{Co}(\text{NO}_3)_2 \cdot 5 \text{H}_2\text{O}$ (Alfa Aesar) in deionized water, mixed with citric acid in a 1:1 metal nitrate to citric acid molar ratio, adjusted to pH 6.5 with ammonium nitrate, and diluted with deionized water to 1M. Excess SSC solution was infiltrated into the scaffolds, and fired at 450 °C for 0.5 hours to decompose the nitrates. The cells were infiltrated 8 times to about 20 vol% and finally fired at 800 °C for 1 hour. Silver metal grids were then applied as current collectors for electrochemical testing.

5.2.4 Pr_2NiO_4 Infiltrated LSGM Symmetric Cell Fabrication

The cell fabrication method is similar to that described in Ref. ¹⁰³. For the LSGM electrolyte, LSGM was first synthesized via solid state reaction. LSGM powder was synthesized from stoichiometric amounts of SrCO_3 (Sigma), La_2O_3 (Sigma), Ga_2O_3 (Sigma), and MgO (Alfa Aesar), which were ball milled for 24 hours in ethanol, dried, and then reacted at 1250 °C for 12 hours. This LSGM powder was then ball milled in ethanol and 2 wt. % polyvinyl butyral (Aldrich) binder, dried, and pressed into 0.5 g 19 mm diameter pellets. The green bodies were then sintered at 1450

°C for 4 hours. LSGM scaffolds were screen printed onto the electrolyte pellets using an ink composed of commercially available LSGM (Praxair), Heraeus 737 vehicle, and 30 wt% of KS4 graphite flakes (Timrex) as pore former. Four screen printed layers were applied to each side, then heated to 600 °C for one hour to burn away the pore former, and then fired at 1200 °C for 4 hours to form a porous scaffold layer with interconnected LSGM particles 1-3 microns in size. A current collector was then applied on each scaffold by screen printing one layer of an $(\text{La}_{0.6}\text{Sr}_{0.4})(\text{Co}_{0.8}\text{Fe}_{0.2})\text{O}_{3-\delta}$ ink consisting of the same vehicle, pore former, and LSCF powder (Praxair). The entire assembly was then fired at 1100 °C for one hour to produce a suitably porous current collector that was also well bonded to the scaffold. The resulting scaffold thickness was ~ 40 μm and the LSCF layer was ~ 10 μm thick. The cathode infiltrate was a 2 M nitrate solution prepared by dissolving stoichiometric amounts of $\text{Pr}(\text{NO}_2)_3 \cdot 6\text{H}_2\text{O}$ (Aldrich) and $\text{Ni}(\text{NO}_2)_3 \cdot 3\text{H}_2\text{O}$ (Fischer) in water and subsequently adding 0.06 mol of Triton X-100 (VWR). This solution was stirred for 24 hours to ensure good mixing. Each scaffold was infiltrated with this solution using excess fluid (~6 μL) and removing the excess after allowing solution to infiltrate the porous scaffold for 5 minutes. The infiltrate was decomposed by heating to 450 °C for 0.5 hours, leaving oxides of the respective metal ions. After 12 infiltrations, the symmetric cells were fired at 1000 °C for 4 hours to form Pr_2NiO_4 . Silver metal grids current collectors were applied for electrochemical testing.

5.2.5 Pressurized Electrochemical Impedance Spectroscopy (EIS) and Analysis

A custom designed pressure system (Deltech Furnaces Inc, Denver, CO) was used to collect EIS data. The system is capable of reaching pressures up to 11 atmospheres, and temperatures up to

850 °C. Details of the system geometry and controls are described elsewhere¹⁶³. The single-phases NNO/LSGM and LSCF/GDC symmetric cells were operated at 700 °C and the two-phases infiltrated PNO-LSGM and SSC-GDC symmetric cells were operated at 550 °C for the entire measured pressure range. EIS data was collected for a range of oxygen pressures for all cells from 0.2 bar to 10 bar. Below 1 bar oxygen, the total pressure in the system remains at 1 bar and is balanced with nitrogen with a total flow rate of 40 sccm. EIS data was collected in the frequency range 0.1-10⁶ Hz using a Zahner IM6 impedance spectrometer.

Equivalent circuit model fitting was performed using Matlab and Excel software²⁰⁰ in order to obtain the most accurate possible R_p values from the data. The circuit models used for the infiltrated electrodes were either (L-R-RQ) or (L-R-RQ-RQ), where L is an inductance, R is a resistance, and RQ represents a constant phase element. The circuit model used for powder electrodes cells was (L-R-G in Boukamp notation), where G represents a modified Gerischer element that accounts for the distribution of relaxation times²⁰¹. The inductor accounts for inductance in the wire leads through the system, the resistor represents the electrolyte resistance, and the Gerischer element represents the impedance associated with the co-limiting oxygen surface exchange and diffusion processes in the porous MIEC electrode, as described in the ALS model.⁵⁸ Other contributions to the polarization resistance (such as gas diffusion) were found to be negligible.

5.3 Results

Figure 5.1 shows the Nyquist and Bode plots of the EIS spectra taken at 550 °C from infiltrated SSC-GDC electrode cells at selected pO_2 values. Figure 5.2 shows the same for infiltrated PNO-LSGM electrode cells. Both electrodes have relatively low polarization resistance R_p , given the

relatively low operating temperature, that is further decreased with increasing pO_2 . The arcs are depressed and reasonably symmetric. The PNO-LSGM electrode arcs had peak frequencies that increased with increasing pO_2 , i.e., with decreasing R_P , - the normal dependence observed if the electrode capacitance remains approximately constant. The SSC-GDC electrode showed the reverse trend of peak frequency with pO_2 , suggesting a substantial increase in capacitance with increasing pO_2 .

Figure 5.3a shows the polarization resistance R_P of infiltrated SSC-GDC and PNO-LSGM electrode cells, derived best fits to EIS data such as that shown in Figures 5.1 and 5.2, as a function of oxygen pressure. R_P for the PNO infiltrated electrode has a stronger power-law dependence, $pO_2^{-0.24}$, than that for the SSC infiltrated electrode, $pO_2^{-0.15}$. Figure 5.3b shows the dependences of the time constant (taken as the inverse of the peak frequency) for the two electrodes. The time constants show opposite trends with pO_2 : increasing slightly in SSC/GDC as $pO_2^{0.11}$ and decreasing as $pO_2^{-0.37}$ in PNO/LSGM.

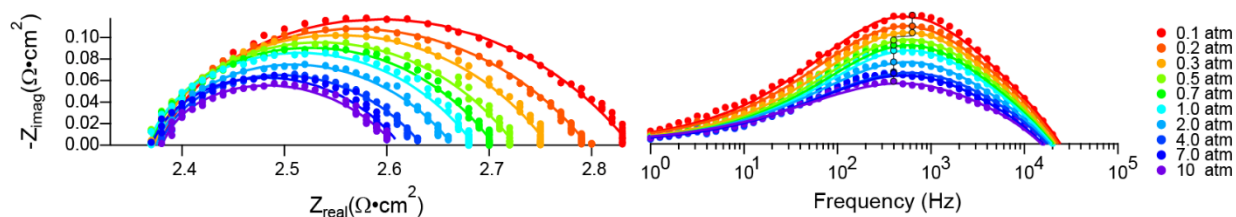


Figure 5.1. Nyquist and Bode plots as a function of oxygen pressure at 550 °C for $(\text{Sm}_{0.5}\text{Sr}_{0.5})\text{CoO}_3$ infiltrated into GDC. The resistance values are taken from fits using a general (L-R-RQ) circuit. Fits are displayed as solid lines on the plots and the maximum frequency is outlined on the Bode plot.

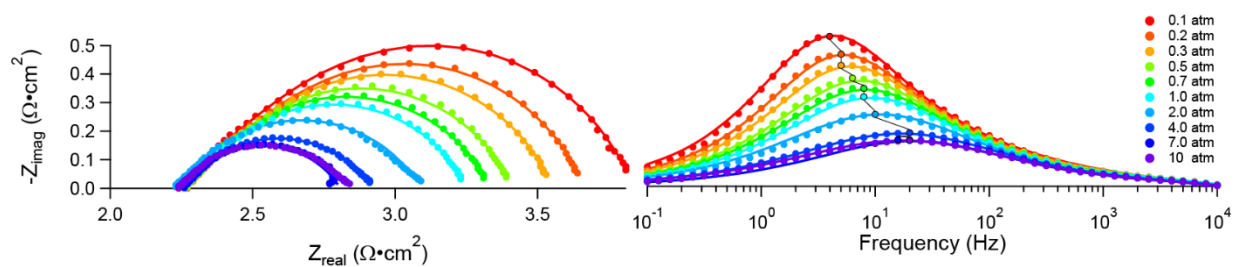


Figure 5.2. Nyquist and Bode plots as a function of oxygen pressure at 550 °C for Pr_2NiO_4 infiltrated into LSGM. The resistance values are taken from fits using a general (L-R-RQ-RQ) circuit. Fits are displayed as solid lines on the plots and the maximum frequency is outlined on the Bode plot.

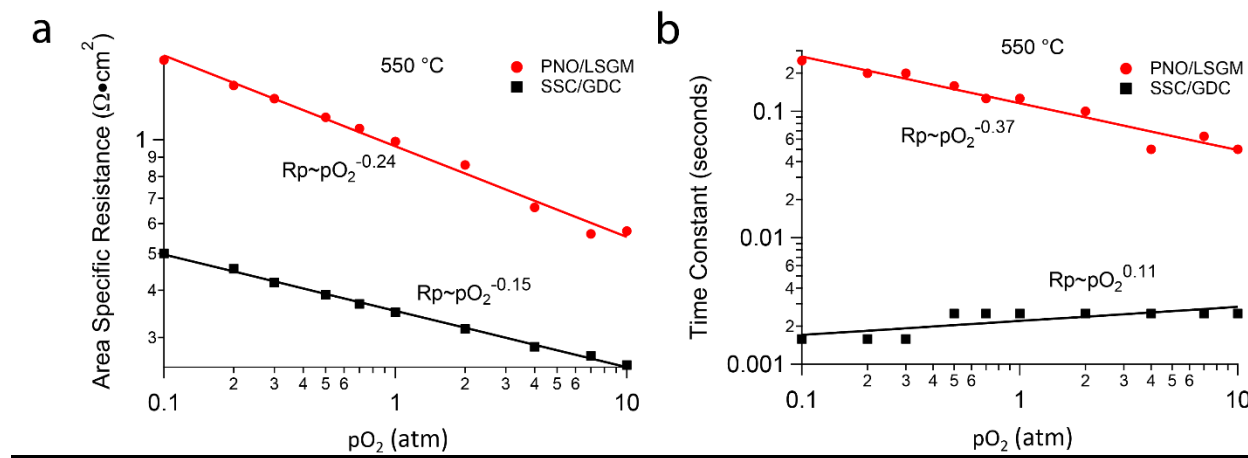


Figure 5.3. a) Polarization resistance as a function of oxygen pressure at 550 °C for PNO/LSGM and SSC/GDC. The resistance values are taken from fits in figures 1 and 2. b) Time constants as a function of oxygen pressure at 550 °C for PNO/LSGM and SSC/GDC. The time constants are the inverse of the peak frequency.

Figure 5.4 shows EIS data at selected $p\text{O}_2$ values for a Nd_2NiO_4 -electrode symmetric cell. Figure 5 shows EIS data at selected $p\text{O}_2$ values for an LSCF symmetric cell. For both cells, the characteristic frequency of the dominant process shifts to higher frequencies with increasing $p\text{O}_2$, as R_p decreases, but the shift is greater for LSCF. Fitting was done using a single Gerischer element, where the complex resistance (Z_G) is defined:

(Equation 5.1)

$$Z_G = R_G \sqrt{\frac{1}{1 + j\omega t_G}}$$

where R_G and t_G are measured from the EIS fit, ω is angular frequency, and j is the imaginary number. The fits are reasonably good for most pO_2 values, suggesting that the ALS model, where the electrode process is co-limited by surface exchange and diffusion processes, should provide a reasonable representation. This agrees with previous studies performed in the low pO_2 range below 1 atm.^{58,59} The deviations from a perfect Gerischer shape may indicate slight deviations from the ALS model, perhaps due to the electrode utilization length becoming either too large (comparable to the electrode thickness) or too small (comparable to the electrode feature size).^{58,59} Since there is only one element fitting the electrode polarization response (the response at $> 10^4$ Hz is attributed to the electrolyte), the fitted Gerischer resistance gives the total electrode polarization resistance, *i.e.*, $R_P = R_G$.

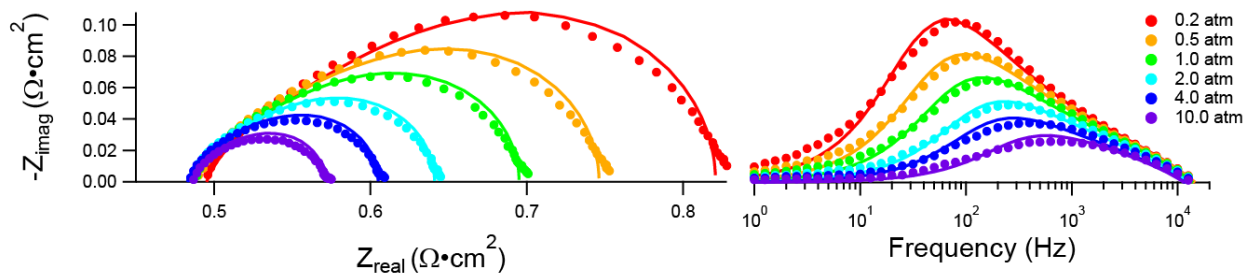


Figure 5.4. Bode and Nyquist plots of an NNO symmetric cell at 700 °C in the pressure range from 0.2 to 10 bar pO_2 . Solid lines are (L-R-G) equivalent circuit fits.

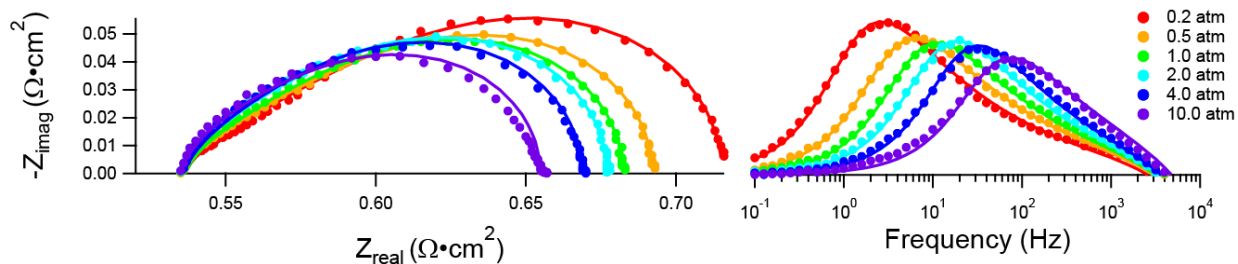


Figure 5.5. Bode and Nyquist plots of an LSCF symmetric cell at 700 °C in the pressure range from 0.2 to 10 bar pO_2 . Solid lines are (L-R-G) equivalent circuit fits.

Figure 5.6a plots the pO_2 -dependence of the Gerischer resistance R_G for the NNO and LSCF symmetric cells, obtained by fitting the EIS data at 700 °C as shown in Figs. 5.4 and 5.5. The data are fit reasonably well by a $pO_2^{-0.30}$ dependence for NNO and $pO_2^{-0.11}$ for LSCF, as shown. Figure 5.6b shows the t_G values obtained from the fits; the time constant values, the inverse of the peak frequencies discussed above, decrease with increasing pO_2 .

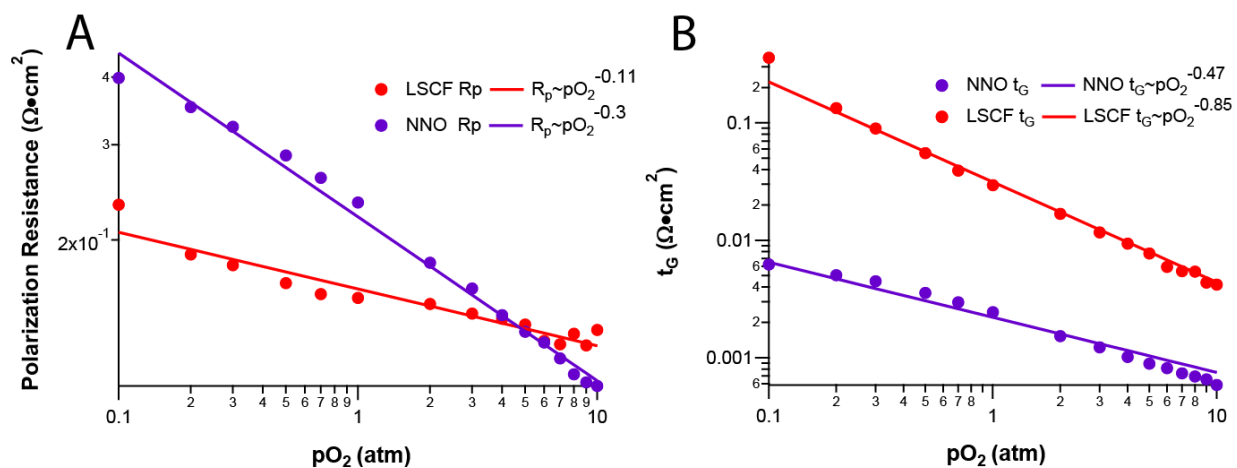


Figure 5.6. a) Polarization resistance versus pO_2 for LSCF and NNO at 700 °C. Data points are taken from L-R-G circuit models fits to the EIS data, and solid lines indicate power law fits. b) t_G values obtained from the fits versus pO_2 for LSCF and NNO at 700 °C

5.4 Discussion

The above results show a significant difference in the pO_2 dependences of electrode polarization resistance for nickelate versus perovskite electrodes. The difference is observed for two different nickelate and perovskite compositions, and for different electrode structures – single phase porous electrodes and electrodes formed by infiltration of the MIEC into a porous ion conducting scaffold. This suggests that the different pO_2 dependence arise from an inherent difference between perovskite and nickelate MIECs. We propose that this is related to the different dominant ionic-charge carrier types – oxygen vacancies in perovskites and oxygen interstitials in nickelates. In particular, oxygen pressurization is expected to reduce the oxygen vacancy concentration, which are the O-ion charge carriers in a perovskite, degrading its ability to transport oxygen ions, and mitigating the performance improvement expected because of the increased pO_2 . On the other hand, pressurization is expected to increase the oxygen interstitial concentration, responsible of the O-ion transport at the nickelates, improving oxygen ion transport and leading to a larger performance improvement. The differences between the pO_2 dependences are less for the infiltrated electrodes, perhaps because the ionically-conducting scaffold has a constant oxygen vacancy concentration that provides fast oxygen transport regardless of the pO_2 . In this case, the changes in MIEC defect concentration with pressure affect only the surface exchange process.

In the following, the ALS model^{58,59} is applied in an attempt to test the above hypothesis and quantify the defect concentration variations with pO_2 . As noted above, the utilization length should be much smaller than the electrode thickness and much larger than the electrode feature size;^{58,59,202} this criterion will be checked below. The ALS model predicts the Gerischer response shown in eq. 5.1 with t_G given by:

(Equation 5.2)

$$t_G = \frac{(1 - \epsilon)c_0x_\delta^0}{4aR_0A_0}$$

and R_G given by

(Equation 5.3)

$$R_G = \frac{RT}{4F^2} \sqrt{\frac{\tau}{4a(1 - \epsilon)R_0c_0x_\delta^0D}}$$

Where ϵ is the electrode porosity, a is the internal specific surface area of the solid phase, τ is the tortuosity of the solid phase, c_0 is the concentration of oxygen sites involved in diffusion, x_δ^0 is the molar fraction of interstitial or vacancy defects at equilibrium, A_0 is the thermodynamic factor, D is the oxygen diffusivity, and R_0 is the molar surface exchange rate defined as:

(Equation 5.4)

$$R_0 = \frac{k_{chem}}{A_0} (pO_2)^{0.5} c_0$$

Here, k_{chem} is the surface exchange coefficient and relates to k_δ and k^* as:

(Equation 5.5)

$$k_\delta = \frac{k^*}{x_\delta^0} = \frac{k_{chem}}{A_0}$$

Where k_δ and k^* refer to the normalized and isotope exchange derived surface exchange values.

Similarly,

(Equation 5.6)

$$D_\delta = \frac{D^*}{x_\delta^0} = \frac{D_{chem}}{A_0}$$

Where D_δ and D^* refer to the normalized and isotope exchange derived oxygen diffusion coefficients.

Substitution of eq. 5.4 into eq. 5.3 yields

(Equation 5.7)

$$R_G = \frac{RT}{4F^2} \sqrt{\frac{\tau A_0^2}{4a(1-\epsilon)k_{chem}c_0^2 x_\delta^0 D_{chem}}} (pO_2)^{-0.25}$$

Note that if all the terms in eq. 5.7 were independent of pO_2 , then $R_G \propto pO_2^{-0.25}$, as compared to the fits at $pO_2^{-0.11}$ for LSCF and $pO_2^{-0.30}$ for NNO shown in figure 6. The thermodynamic factor A_0 is a function of oxygen chemical potential,

(Equation 5.8)

$$A_0 = \pm \frac{1}{2RT} \left(\frac{\partial \mu_{O_2}}{\partial \ln(x_\delta^0)} \right) = \pm \frac{1}{2} \left(\frac{\partial \ln(pO_2)}{\partial \ln(x_\delta^0)} \right)$$

the (-) sign corresponds to O-vacancies and (+) to O-interstitials. A_0 can often be assumed constant with reasonable accuracy over the measured pO_2 range at low non-stoichiometric values.¹⁹⁷ Furthermore, k_{chem} and D_{chem} should be independent of pO_2 ^{59,203}. The only other term in eq. 7.7 that might be expected to vary with pO_2 is the oxygen non-stoichiometry x_δ^0 . Thus, the observed deviations of measured R_G from the $pO_2^{-0.25}$ dependence can be explained by variations in x_δ^0 .

An expression for x_δ^0 can be obtained by rearranging eq. 5.7:

(Equation 5.9)

$$x_\delta^0 = \frac{R^2 T^2 \tau A_0^2}{64 F^4 R_G^2 a (1 - \epsilon) c_0^2 k_{chem} D_{chem}} (pO_2)^{-0.5}$$

That is, the non-stoichiometry can be obtained from the R_G data, if the electrode material parameters A_0 , c_0 , k_{chem} , and D_{chem} are known along with the microstructural parameters a , ϵ , and τ . Alternatively, plugging eq. 5.4 into eq. 5.2 and re-arranging yields:

(Equation 5.10)

$$x_\delta^0 = \frac{4at_G k_{chem} (pO_2)^{0.5}}{1 - \epsilon}$$

Thus, the non-stoichiometry can also be determined from t_G data if select materials and microstructural parameters are known. Using eq. 5.9 with the measured R_G values yields x_δ^0 values for each pO_2 , but substitution in eq. 5.2 yields poor agreement with measured t_G values. Similarly,

using eq. 10 with the measured t_G values yields a set of x_δ^0 values, but substitution in eq. 5.7 yields poor agreement with measured R_G values. These disagreements could arise in part from the wide variations in literature k_{chem} . In order to obtain a set of x_δ^0 values that provide a good match to both the R_G and t_G values versus pO_2 , a combined expression, obtained by multiplying equations 5.9 and 5.10, was used:

(Equation 5.11)

$$x_\delta^0 = \frac{RTA_0}{4F^2R_G(1-\epsilon)c_0} \sqrt{\frac{t_G\tau}{D_{chem}}}$$

Note that both R_G and t_G appear in eq. 5.11, and the terms a , k_{chem} , and $(pO_2)^{0.5}$ are eliminated in the combined expression.

The molar fraction of vacancies or interstitials is obtained from eq. 5.11 for each pO_2 using the measured t_G and R_G values, τ and ϵ measured for each particular electrode microstructure^{59,152}, and literature values of $D_{chem} = 6.0 \times 10^{-6} \text{ cm}^2/\text{s}$ for LSCF²⁰⁴ and $2.9 \times 10^{-7} \text{ cm}^2/\text{s}$ for NNO⁵⁹. The NNO oxygen interstitial concentration in Figure 5.7a increases slowly with increasing pO_2 , and is fit reasonably well by the power law $pO_2^{0.03}$. This slope appears to be in good agreement with changes in x_δ^0 with pO_2 measured at $\leq 1 \text{ atm}$, also shown in the figure. The LSCF oxygen vacancy concentration x_δ^0 in Figure 5.7b decreases with increasing pO_2 , fitting to the power law $pO_2^{-0.35}$. This slope is in fair agreement with the variation in vacancy concentrations, for $\leq 1 \text{ atm}$, from Ref. 58. As shown in Table 5.1, there are different reported D_{chem} values, but their spread is relatively small. We have simply chosen the value that provides a better match to literature x_δ^0 values. Note that the calculated x_δ^0 values will shift slightly with the D_{chem} value chosen, but the slope with pO_2

will not. That is, the trends shown in Figures 5.7a and 5.7b are valid, even if the absolute values may have some error. Note that the A_0 values used in eq. 5.11 are obtained directly from the slopes in these figures, as per eq. 5.8, yielding 1.417 for LSCF and 14.47 for NNO.

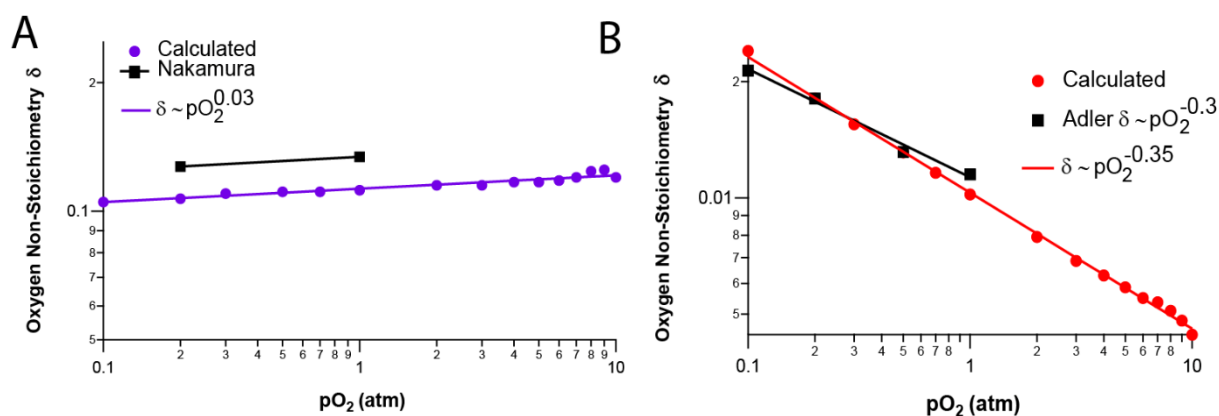


Figure 5.7. Oxygen non-stoichiometry δ versus oxygen pressure for $\text{Nd}_2\text{NiO}_{4+\delta}$ (a) and $\text{La}_{0.6}\text{Sr}_{0.4}\text{Co}_{0.2}\text{F}_{0.8}\text{O}_{3-\delta}$ (b) at 700 °C. Literature values for oxygen non-stoichiometry values are displayed in black.^{58,198}

The match between the measured and calculated R_G and t_G values, based on the above x_δ^0 dependences, is shown for NNO in Figure 8, and for LSCF in Figure 9. Note that calculation of these values using eqs. 5.7 and 5.2, respectively, requires values of k_{chem} . However, as mentioned earlier, there is a wide variation in reported k_{chem} values, making it difficult to choose a representative value. Thus, k_{chem} is used as a constant fitting parameter here to match the R_G and t_G data in figures 5.8 and 5.9. Table 5.1 shows that the k_{chem} values obtained – 3.83×10^{-6} (cm/s) for LSCF and 1.21×10^{-4} (cm/s) for NNO – are well within the range of values reported in the literature. There is generally good agreement with the experimental data shown in the figures (the only significant deviation is at 0.1 atm), verifying that eq. 5.11 yields x_δ^0 values that are consistent with

the measured data. That is, the change in the concentration of these defects can explain the different dependences of the measured R_G and t_G on pO_2 , for both NNO and LSCF. For NNO, R_G decreases slightly faster than the $pO_2^{-0.25}$ dependence shown in eq. 5.7, because the interstitial content increases modestly. For LSCF, R_G decreases much slower than $pO_2^{-0.25}$ because the vacancy content decreases substantially.

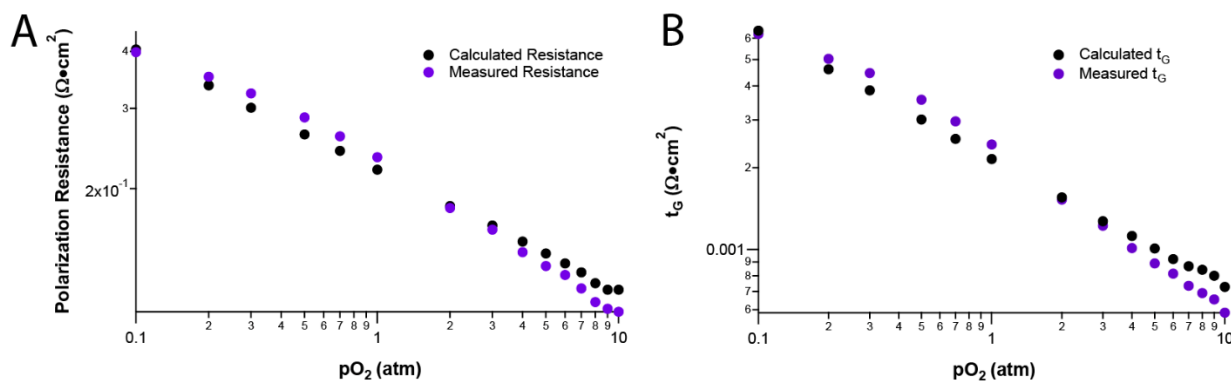


Figure 5.8. a) Measured polarization resistance versus pO_2 for Nd_2NiO_4 compared to values calculated from derived x_G^0 b) Measured and calculated time constants versus pO_2

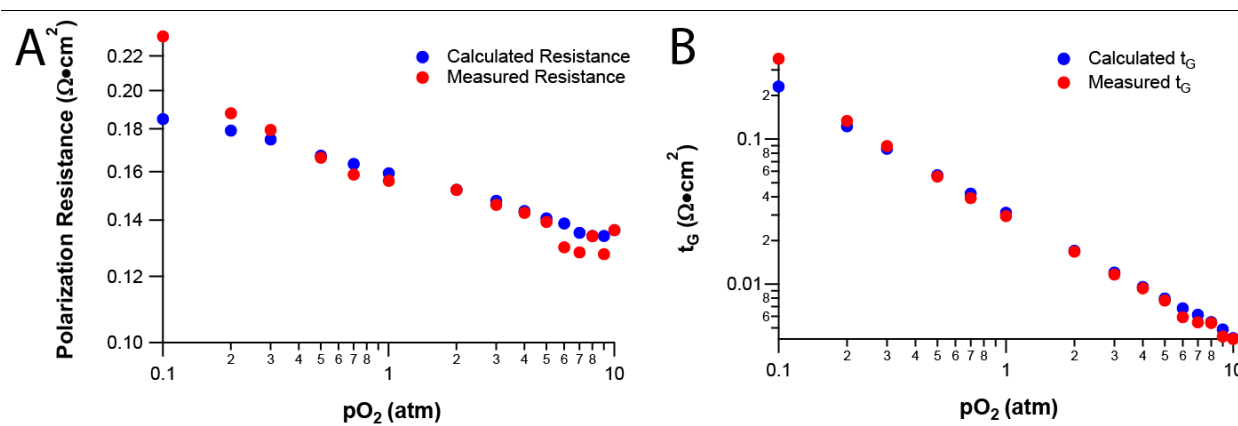


Figure 5.9. a) Measured polarization resistance versus pO_2 for LSCF compared to values calculated from derived x_δ^0 b) Measured and calculated time constants versus pO_2

Table 5.1. Oxygen diffusion and surface exchange coefficients for LSCF and NNO

LSCF D at 700 °C (cm^2/s)		NNO D at 700 °C (cm^2/s)	
D_{chem}^{205}	2.04×10^{-6}	D^{*97}	3.0×10^{-8}
D_{chem}^{204}	6.03×10^{-6}	D_δ^{59}	2.0×10^{-8}
D^{*152}	5.27×10^{-10}		
LSCF k at 700 °C (cm/s)		NNO k at 700 °C (cm/s)	
k_{chem}^{152}	9.56×10^{-5}	k_{chem}^{59}	1.82×10^{-4}
k_{chem}^{202}	1.05×10^{-5}	k_{chem}^{97}	8.00×10^{-5}
k_{chem}^{206}	1.04×10^{-6}	k_{chem} (this work)	1.21×10^{-4}
k_{chem} (this work)	3.83×10^{-6}		

As noted earlier, the ALS model is only valid for reasonable utilization lengths, which can be calculated using:

(eq. 5.12)

$$l_{\delta} = \sqrt{\frac{(1 - \epsilon)D_{\delta}c_0x_{\delta}^0}{4a\tau R_0}}$$

Using the above values, the utilization length for LSCF is found to range from 15.4 to 2.1 microns over the 0.1 to 10 atm pressure range. Utilization lengths in NNO were smaller, varying from 396 nm to 134 nm over the same range. The utilization lengths being smaller than the electrode thickness ~20 microns indicates that the electrodes satisfy the thick electrode assumption to be analyzed by the ALS model. However, the NNO electrode utilization length is comparable to the electrode particle size.

The above analysis using the ALS model is applicable to the porous single-phase electrodes. Although a defect concentration analysis was not done for the more complicated infiltrated composite SSC and PNO electrodes in this study, similar trends with pO_2 are observed. In analyzing the infiltrated composites, it should be considered that they contain ionic conductors (GDC or LSGM) with oxygen defect concentrations that, unlike the MIECs, do not vary with pO_2 . This probably explains why the difference in the pO_2 dependences for SSC and PNO is smaller than for the single-phase electrodes.

While there is little other data available for MIEC electrodes under pressurized conditions, data for $pO_2 \leq 1$ atm generally supports the present trends. That is, the perovskites show weaker pO_2 dependences, *e.g.*, $m \sim -0.13$ for LSCF at 750 °C²⁰⁷ and $m \sim -0.17-0.22$ for LSC at various

temperatures,²⁰³ whereas nickelates show stronger pO_2 dependence, *e.g.*, $m \sim 0.25-0.5$ for NNO at various temperatures^{59,208,209}. The unique feature of the present results is to demonstrate that these trends continue to pO_2 values up to 10 atm.

5.5 Conclusions

The polarization resistances of nickelate (NNO and PNO) electrodes were found to decrease more rapidly with increasing oxygen partial pressure up to 10 atm, than perovskite (LSCF and SSC) electrodes. The differences were explained based on the different oxygen defect types – the oxygen interstitial concentration in the nickelate electrodes increased with increasing pO_2 , whereas the oxygen vacancy concentration in the perovskites decreased. The different dependencies of R_P on pO_2 for single-phase porous NNO and LSCF electrodes were explained quantitatively by the ALS model for reasonable variations of interstitial and vacancy concentrations. The infiltrated composite nickelate (PNO) and perovskite (SSC) electrodes showed a similar effect, although there was less difference between their R_P dependences. Thus, if nickelate and perovskite electrodes shown similar R_P under ambient air, the nickelate electrode can be expected to provide lower R_P under pressurized conditions.

5.6 Acknowledgements

Much of the material and argumentation presented in this chapter will soon be published in the Journal of the Electrochemical Society (2016). Dr. Gareth Hughes collected the NNO data, Dr. Liliana Moggi fabricated the NNO cell and provided useful discussions on circuit modeling and theory, and Dr. Alejandra Montenegro-Hernandez contributed to the development and fabrication of the NNO cell.

Chapter 6: Current-Switched Life Tests

6.1 Introduction

The durability of the oxygen electrode in a reversible SOC system is a primary technological concern. System models predict that the SOC stack will be about 25% of the cost of a whole system, and so should degrade as slowly as possible. The DOE sets targets for SOFC systems and recommends that an SOFC stack for a stationary application should degrade slower than 25% over a 50,000 hour period, or about 0.5%/khr. Previous work by Hughes et. al. showed that degradation in LSM-YSZ follows a similar failure mode to DC electrolysis cells at high current densities, and lower current densities or faster cycling times slows degradation. In this chapter additional life testing on the LSM-YSZ system was done to clarify the degradation mechanisms at work and determine the stable operating conditions for LSM-YSZ. Similar life tests were performed on the lower temperature LSCF on GDC system to determine more stable operating conditions and how degradation proceeds. Preliminary life tests were performed on La_2NiO_4 infiltrated into LSGM, again to observe the degradation mode and find more stable conditions.

6.2 Degradation of $(\text{La}_{0.8}\text{Sr}_{0.2})_{0.98}\text{MnO}_{3-\delta}$ - $\text{Zr}_{0.84}\text{Y}_{0.16}\text{O}_{2-\gamma}$ Composite Electrodes During Reversing Current Operation

6.2.1 Introduction

Degradation in ReSOCs is similar to that observed during solid oxide electrolysis, which has been studied in some detail.^{130-140,210,211} Delamination of the oxygen electrode (electrolysis anode), typically $(\text{La}_{0.8}\text{Sr}_{0.2})_{0.98}\text{MnO}_{3-\delta}$ - $\text{Zr}_{0.84}\text{Y}_{0.16}\text{O}_{2-\gamma}$ (LSM-YSZ), is the dominant degradation mechanism.¹⁶¹ Furthermore, reversing current operation does not introduce new degradation mechanisms, and in fact reduces the delamination degradation when compared with DC

electrolysis operation.^{161,212} It was possible to essentially eliminate degradation at 1.0 A/cm² by using a cycle with very short periods of electrolysis separated by fuel cell operation,²¹² but such a cycle would not be practical for most storage applications. Current density J (or the electrode overpotential η) has a large impact on the degradation rate, with rapid degradation at 1.5 A/cm² ($\eta = 0.37$ V) but no detectable degradation at 0.5 A/cm² ($\eta = 0.18$ V).²¹³ Based on these ReSOC reports, and also prior reports on solid oxide electrolysis cells^{135,138}, it appears that there is a threshold current density of $\sim 0.5 - 1.0$ A/cm² above which oxygen electrode degradation is fast.

In order to design a ReSOC system and assess its performance and economic viability,²¹⁴⁻²¹⁶ it is important to know more accurately the maximum J and η values that are consistent with long-term stable operation. In order to be an economically viable storage method, cell lifetimes should exceed 40,000 h and 2,000 cycles (assuming a ~ 24 h storage cycle). Thus, degradation rates should be < 0.5 %/kh and < 0.0125 %/cycle, assuming that a cell resistance increase of $< 25\%$ over the stack life is acceptable. The prior reports discussed above do not provide such detailed information on degradation rates; in particular, there is no information in the critical range from 0.5 to 1.0 A/cm².

In this section, LSM-YSZ composite oxygen electrodes were investigated in order to more accurately determine the effect of J and electrode η on degradation rate in this critical range. (Note that the relative importance of J as opposed to η in causing degradation has not yet been elucidated, so both quantities are included in the present report.) In order to focus on the oxygen electrode, which appears to be the cell component most prone to degradation, symmetrical LSM-YSZ / YSZ / LSM-YSZ cells were tested. This has the advantage of minimizing extraneous degradation effects in full cells that may obfuscate the LSM-YSZ electrode degradation of interest here.

Furthermore, symmetric applied current cycles, with equal current densities and times in each direction, were utilized in order to maintain symmetrical electrodes throughout the test despite the tendency for more rapid degradation in electrolysis mode. This enables more straightforward electrochemical impedance analysis.

6.2.2 Experimental

LSM-YSZ / YSZ / LSM-YSZ symmetrical cells were fabricated by first die pressing YSZ electrolyte pellets from YSZ powder mixed with 1% PVB binder, and then sintering at 1400 °C for 4 hours. The resulting electrolyte pellets were ~ 0.6 mm thick and 19 mm in diameter. LSM-YSZ electrode functional layers were then screen printed on both sides of the pellets using an ink was produced as follows. A 1:1 mixture (by weight) of $Zr_{0.84}Y_{0.16}O_{2-\gamma}$ (Tosoh) with A-site deficient $(La_{0.8}Sr_{0.2})_{0.98}MnO_{3-\delta}$ (Praxair) was ball milled in ethanol for 24 hr. The solution was then dried, ground, and passed through a 125 μ m mesh sieve. This powder was then added to Heraeus organic vehicle 1:1.18 by weight and fully mixed with a three roll mill. After applying the ink by screen printing, the electrodes were fired at 1175 °C for 1 hour. A current collector layer of LSM ink, made similarly to the LSM-YSZ ink, was then screen printed on top of the LSM-YSZ layer and fired at 1025 °C. The final as-fired thicknesses of the LSM-YSZ functional layer and LSM current collector were both ~ 20 μ m thick and had a circular area of 0.5 cm². Note that this electrode fabrication procedure is essentially identical to that used in making full cells.

All cells were tested in an open-air furnace at 800 °C. Electrical contacts were made by pressure contacting circular porous LSM current collector pellets, with 0.5 cm² area, to the electrodes using a 14 g alumina weight. LSM was utilized to avoid artifacts that may arise from the transport of noble-metal current collector materials into the electrode active region.^{161,217} Current densities

between 0.5 A/cm^2 and 1.5 A/cm^2 were applied. Current was applied galvanostatically using a Keithley source meter controlled by a LabView program. The current cycle period was 12 h, with equal times and equal currents in each current direction. The program was paused roughly every 24 hours to run an EIS measurement at open circuit (zero) voltage. All cells were tested for ~ 1000 hours.

6.2.3 Results

An initial exploratory test was done wherein the current density J was increased incrementally in steps of ~ 150 h, starting at 0.5 A/cm^2 and finishing at 1.5 A/cm^2 ; this provided an approximate overview of the degradation rate versus J , and the results suggest that the degradation rate becomes significant just below $\sim 1 \text{ A/cm}^2$. Based on this result, 1000 h life tests were done at current densities of 0.6, 0.8 and 0.9 A/cm^2 . Prior data taken with identical cells and an identical test setup, but different current densities of 0.5 and 1.5 A/cm^2 , are also shown for comparison.²¹³ Section 6.2.3.1 describes the increasing current test, section 6.2.3.2 the constant current test, and section 6.2.3.3 the SEM-EDS analysis.

6.2.3.1 Incrementally Stepped Cycled Current Density

The incremental test was started at 0.5 A/cm^2 and the current was then increased to 0.7, 0.9, 1.0, 1.1, 1.2, 1.3, 1.4, and 1.5 A/cm^2 . The cell was maintained at each J for at least 150 hours. The results from selected EIS measurements are shown in Figure 6.1. The data were fit using the equivalent circuit shown in Figure 6.1, and an example fit is shown for 1.4 A/cm^2 . The fit using two R-Q elements is reasonably good; better fits can be achieved by adding more elements to the model, but the intent here was to quantify the main electrode responses with a

reasonably simple model. The two responses have peak frequencies at ~ 100 Hz and 30 kHz. As seen in the Nyquist plot, the ohmic resistance (approximately the high frequency intercept) first decreased during operation at up to ~ 1.2 A/cm², before increasing at higher J . As seen in the Bode plot, the main change with increasing time and J was an increase in the high-frequency response, while the lower frequency response remained approximately constant.

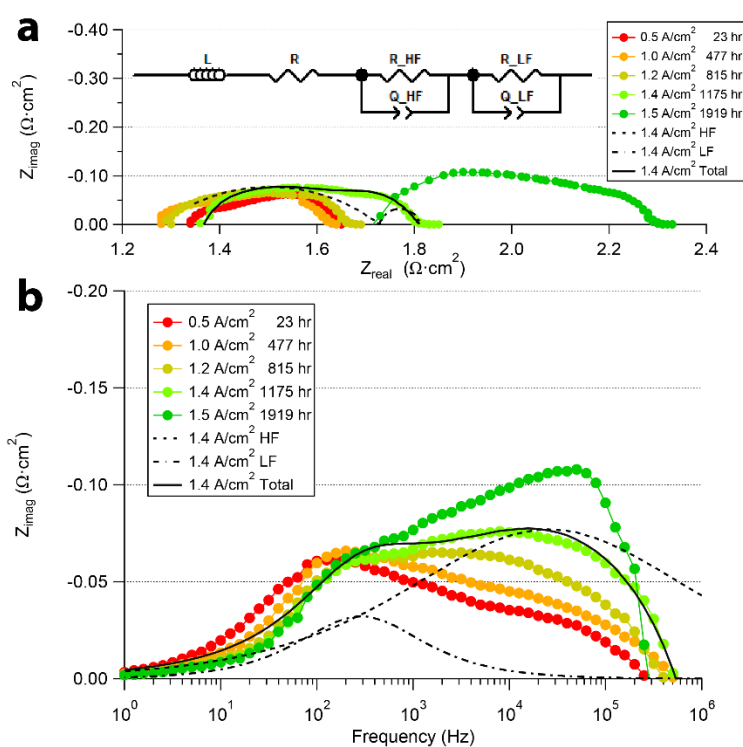


Figure 6.1 Nyquist and Bode plots of selected EIS measurements, taken at zero current during brief interruptions in a reversing-current life test in which J was incrementally stepped up to higher values.

Figure 6.2 shows a plot of measured total, ohmic, and polarization resistances versus time.

The values were obtained from the EIS fitting, rather than by observing the real-axis intercepts, in order to minimize errors in determining the intercepts. The same trends that were apparent in Figure 1 are also seen here: the total resistance changes relatively little at the lower J values, but then the resistance increase accelerates with increasing J . The polarization resistance increase begins early on, near 0.5 A/cm^2 . However, there was considerable variability of the ohmic and polarization resistance values in Figure 6.2, a result of errors introduced in the EIS fitting process. This made it difficult to assess their degradation rates given the relatively short constant-current intervals. Thus, the total resistance was used to estimate the onset of significant degradation: the resistance increase appears to begin at $> 0.7 \text{ A/cm}^2$, corresponding to $\eta > 0.22 \text{ V}$.

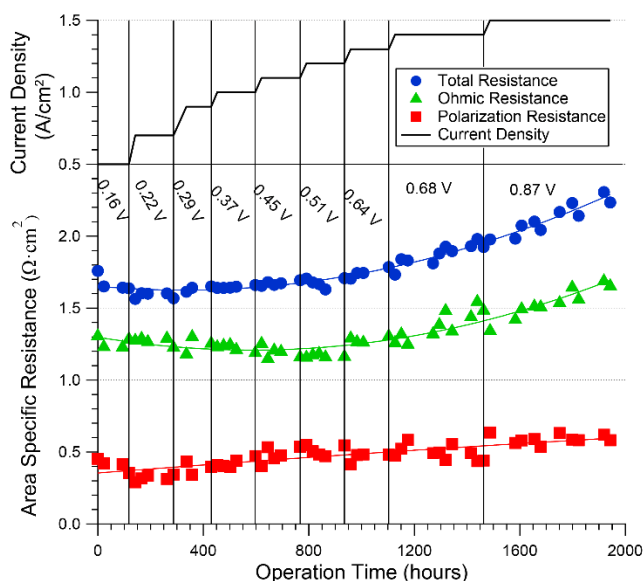


Figure 6.2 Total, ohmic, and polarization resistance values versus time during a reversing-current life test in which the current density was incrementally stepped up to higher values. The values are derived from EIS data as shown in Figure 1 from circuit models. The vertical

lines separate regions with different constant current densities, with values indicated. Voltage labels are electrode overpotentials at the start of each current step.

6.2.3.2 Constant Cycled Current Density

Based on the above results, current densities of 0.6 A/cm², 0.8 A/cm² and 0.9 A/cm² were chosen for three longer-term tests aimed at more accurately assessing the degradation rate. Figure 6.3 shows the EIS data from the 0.8 and 0.9 A/cm² life tests. There were differences between the initial cell responses in the ohmic resistance, due to electrolyte thickness variations. The ohmic resistance clearly increased with time for both cells. There were also minor differences in the shape of the polarization response, presumably due to cell-to-cell processing variations. On the other hand, after an initial decrease in the lower-frequency peak of the cell tested at 0.8 A/cm², the polarization resistance magnitude was almost identical for the two cells. After the initial break-in, the low-frequency response was essentially stable for both current densities. The high frequency response shows a slight increase with time, similar to the changes observed in the cell tested at multiple current densities (Figure 6.1), but the increases are much less, as expected given the lesser overall degradation observed.

The total, ohmic, and polarization resistance values, obtained from fits to the data in Figure 6.3, are plotted versus time in Figure 6.4. Prior data²¹³ also shown in Figure 6.4 are from life tests at 0.5 A/cm², showing no detectable change in resistance, and 1.5 A/cm², showing substantial increases in both ohmic and polarization resistance. In some cases, the cell resistance varied strongly initially, but then stabilized after ~ 70 h. The cell tested at 0.5 A/cm² showed a slight steady decrease in R_p that was almost exactly compensated by an increase in R_Ω , such that there

was no net change in total resistance. η across a single electrode, calculated from J and polarization resistance, was 0.17 V. For J increased from 0.6 to 0.9 A/cm² (initial η value from 0.33 to 0.38 V), the rate of decrease of R_P lessened, while the rate of increase of R_Ω increases, resulting in a faster total resistance increase. At $J = 1.5$ A/cm² (initial $\eta = 0.93$ V), both R_P and R_Ω increased rapidly with time.

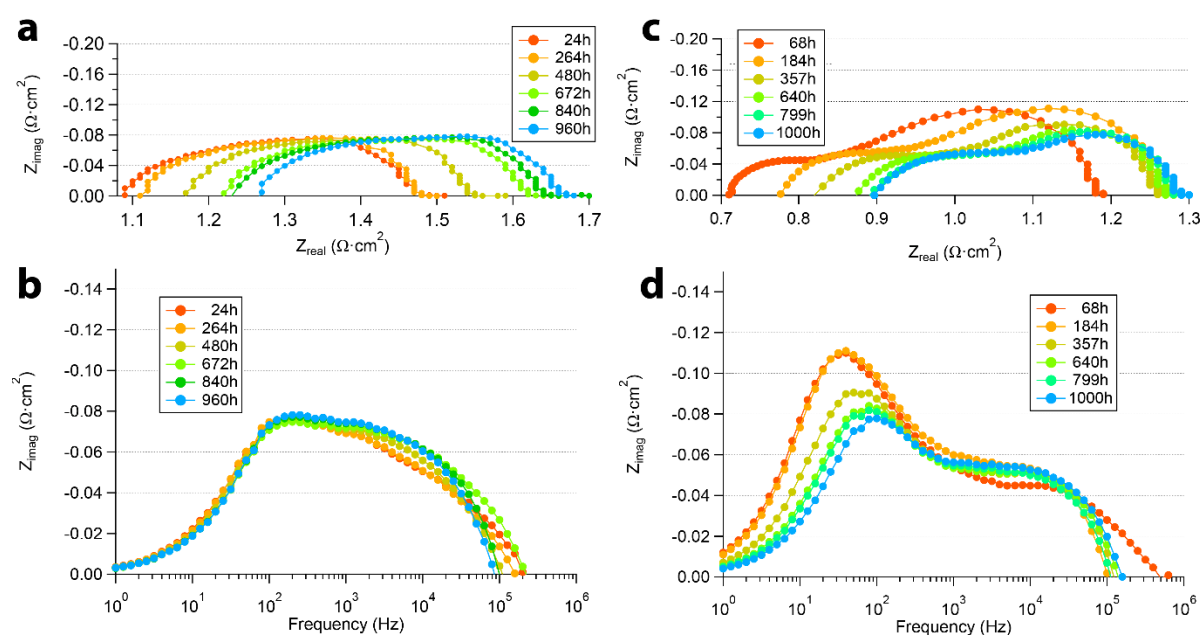


Figure 6.3 Nyquist and Bode plots of selected EIS measurements taken at zero current during brief interruptions in reversing-current life tests in which the current density was maintained at (a,b) 0.9 or (c,d) 0.8 A/cm².

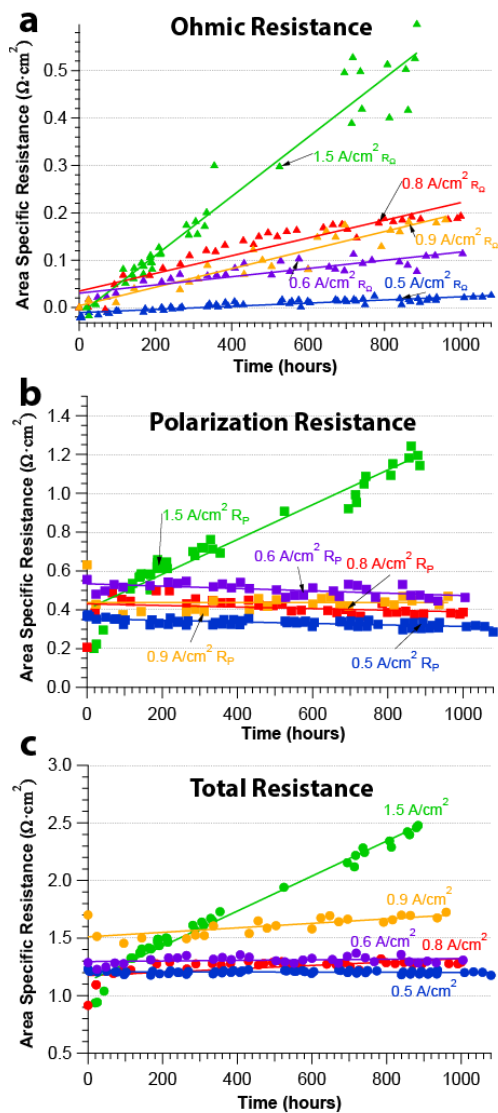


Figure 6.4 (a) Ohmic (b) polarization and (c) total resistance versus time during reversing-current life tests at current density values of 0.6, 0.8 and 0.9 A/cm^2 . The values are derived from fits to the EIS data shown in Figure 3. Also shown are data from a previous report in which identical cells

were tested in the same way in the same test setup at 0.5 A/cm^2 and 1.5 A/cm^2 .²¹³ The initial Ohmic resistance, which varied with electrolyte thickness, has been subtracted in part (a) to allow for easier comparison of the resistance changes.

Figure 6.5 plots the measured total resistance degradation rates, obtained from best fits to the cell resistance versus time data in figure 6.4 neglecting any initial break-in effects, versus η (a) and J (b). The constant-current life tests have relatively small error bars – they appear able to resolve $\sim 1 \text{ %/kh}$ degradation. However, the life test with incrementally increased current had only $\sim 150 \text{ h}$ hold times at each J , leading to much larger errors. Despite the relatively large errors in some of the data points, Figure 6.5 gives a reasonable idea of how the degradation rate increases with current. Furthermore, the constant-current 0.5 A/cm^2 and 0.6 A/cm^2 tests provide a fairly clear indication that measurable degradation starts at a current between these values.

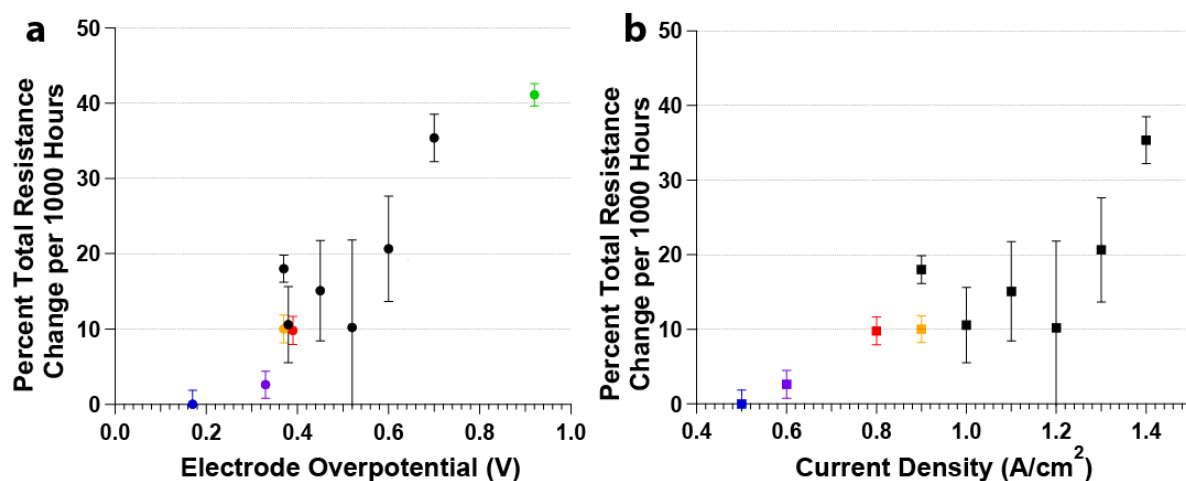


Figure 6.5. Degradation rates, derived from the slopes of the total resistance versus time data in Figures 2 and 4, as a function of a) current density and b) overpotential. Colored points correspond to the life tests in figure 4: 0.5 A/cm² blue, 0.6A/cm² purple, 0.8 A/cm² red, 0.9 A/cm² yellow, 1.5 A/cm² green.

6.2.3.3 SEM-EDS Analysis

SEM-EDS analysis was completed on a cell that was annealed with zero current along with the 0.8 and 0.9 A/cm² cells. Example images from these are shown in Figure 6.6. The cell annealed without current shows uniform electrode structure right up to the interface, whereas in the 0.8 A/cm² and 0.9 A/cm² cases there are microstructural changes near the electrode/electrolyte interface and throughout the active layer. The electrode structure near the electrode-electrolyte interface appears to be depleted of material, containing fewer electrode particles and larger pores. There is significant coarsening of the LSM particles in the active layer for the cells run at 0.8 A/cm² and 0.9 A/cm², compared to the no-current cell, but the YSZ particles remain un-coarsened.

Also, the electrolyte shows pits and pores near the electrode/electrolyte interface, especially in the 0.9 A/cm² cell.

The line scans in Figure 6.7 quantitatively show that La and Mn (i.e., LSM) are depleted near the electrode-electrolyte interface in the 0.8 and 0.9 A/cm² samples, in agreement with the images in Figure 6.6. The La and Mn signals increase with increasing distance from the electrolyte. On the other hand, the main effect of current on the Zr composition profile is a stronger local variation in intensity, presumably related to the presence of enlarged LSM particles.

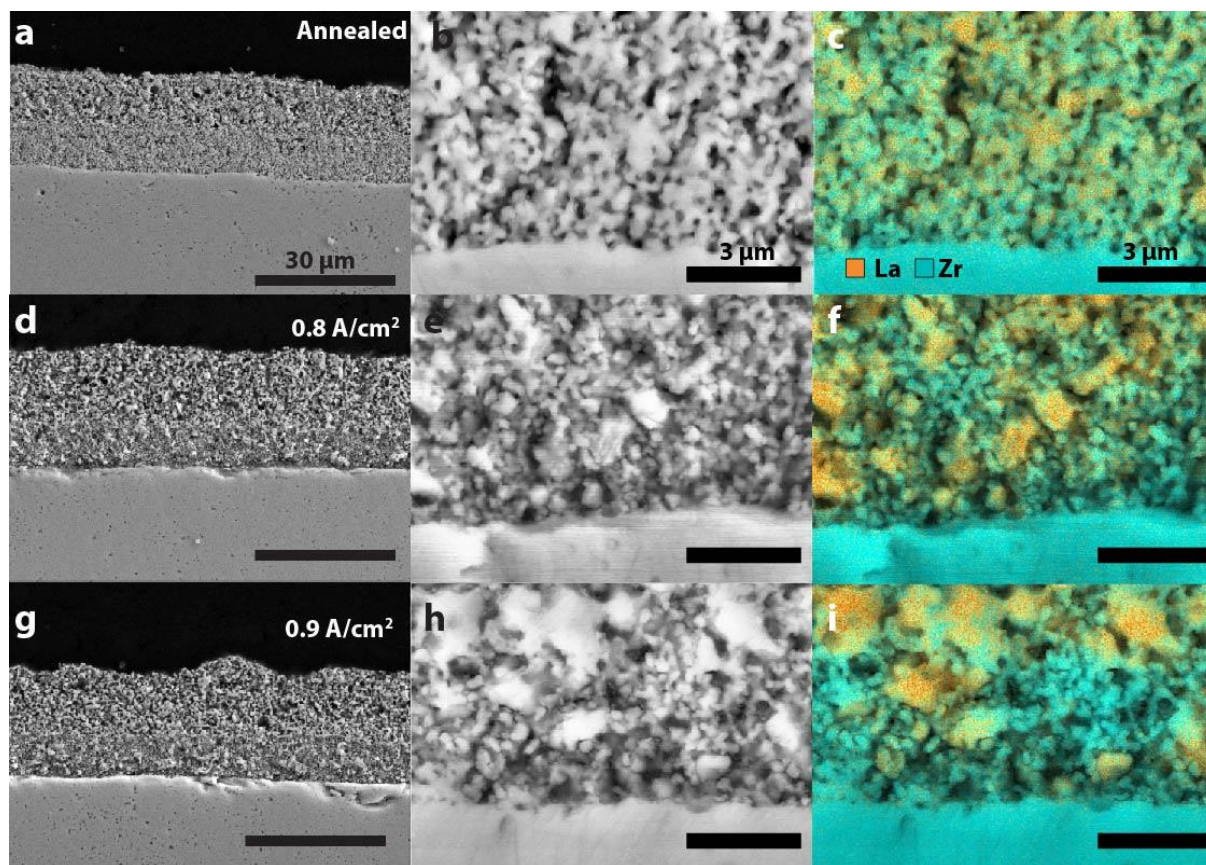


Figure 6.6 A summary of: low magnification SEM images (left column), higher magnification SEM images (middle column), and EDS compositional maps (right column) from the

electrode/electrolyte regions of cells with no current (top row), 0.8 A/cm² (middle row), and 0.9 A/cm² (bottom row). The color scheme of the composition maps is shown in the upper right frame.

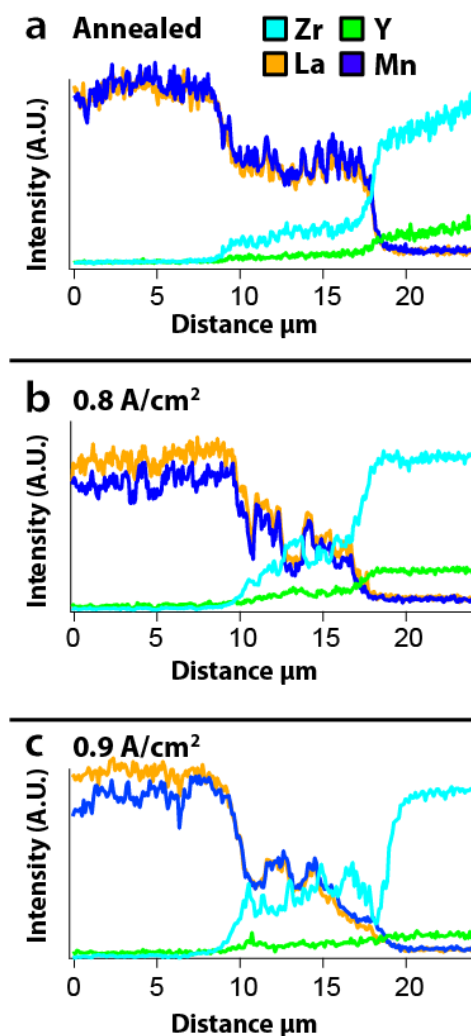


Figure 6.7 EDS linescans for a) annealed b) 0.8 A/cm² and c) 0.9 A/cm² cells.

6.2.4 Discussion

The present results show that the overall resistance degradation rate increases with increasing current density J (overpotential η), increasing above the present detection limit of 1%/kh for J somewhere between 0.5 and 0.6 A/cm² ($\eta = 0.17$ to 0.33 V). This result is consistent with SEM

observations: substantial changes in the near-interface structure were observed for $J = 0.8$ and 0.9 A/cm^2 ($\eta = 0.39$ and 0.37 V), whereas there was little observable change in structure reported previously (for the same cells and test conditions) at 0.5 A/cm^2 .²¹³ These results are consistent with a recent report²¹² where degradation was observed for $J = 1.0$ A/cm^2 ($\eta = \sim 0.25$ V), unless the fraction of the time in electrolysis mode during the reversing-current cycle was reduced. For J increased above 0.8 A/cm^2 (0.39 V), the rate of degradation increases rapidly to > 10 %/kh, fast enough to severely limit device lifetime and hence the total amount of energy that can be stored/converted. Since it is important to reach degradation rates well below 1%/kh, longer-term measurements at $J \sim 0.5 - 0.6$ A/cm^2 will be useful in the future to provide greater sensitivity to degradation.

For all J below 1.5 A/cm^2 , the degradation appeared to be mainly in the ohmic resistance (Figure 6.4a), while the polarization resistance showed little change (Figure 6.4b). In contrast, at 1.5 A/cm^2 , both resistance components contributed to the degradation. The ohmic resistance degradation can be understood via the observed formation of voids in the YSZ electrolyte near the electrode/electrolyte interface (see Figure 6.6 for 0.9 A/cm^2 , and Refs^{140,212}). At higher J (1.5 A/cm^2), where grain boundary pores join and produce extended regions of electrode/electrolyte separation,²¹³ ohmic resistance presumably also increases by current constriction.

In a previous report on similar LSM-YSZ symmetric cells, the response peaking at ~ 30 kHz was attributed to the grain boundary transport losses in the electrode YSZ phase.⁵¹ EIS measurements of the present LSM-YSZ cells with varied oxygen partial pressure (not shown) indicated no change in this high-frequency response, providing further evidence that this response arises from an interfacial (e.g., grain boundary transport) resistance. Given that pore formation on YSZ grain

boundaries within LSM-YSZ electrodes has been observed after reversing-current operation,²¹² it is reasonable to attribute the polarization resistance increase to increasingly resistive YSZ pathways because of degraded electrode grain boundaries. The SEM images in Figures 6.6 and 6.7 indicate depletion of YSZ from the electrode near the electrolyte, consistent with this interpretation. That is, formation of voids in the YSZ corresponds to a net local depletion of YSZ. The SEM-EDS results for 0.8 and 0.9 A/cm² suggest that the amount of LSM in the interface region also decreases after cell operation under current. There appears to be a gradual increase in the amount of LSM with increasing distance from the interface, perhaps indicating that material has been transported away from the interface during cell operation. Finally, the LSM particle size within the functional layers has increased after degradation. There does not appear to be a prior report of such changes in the LSM phase in LSM-YSZ functional layers. While there is no obvious explanation, cation transport has been observed in similar perovskite oxygen electrode materials under an oxygen gradient, as was present in the present experiments during cell operation.²¹⁸ Given the extensive structural/chemical changes within the electrode functional layer for 0.8 and 0.9 A/cm², it is perhaps surprising that the increases in polarization resistance are not larger. Indeed, SEM-EDS analysis of the electrode/electrolyte interface appears to be a very sensitive means for detecting low levels of degradation, perhaps more so than the EIS measurements.

The apparent removal of material from near the electrode/electrolyte interface presumably represents an early stage of the oxygen-electrode delamination that was reported for LSM-YSZ electrodes after ~ 1000 h at a higher J of 1.5 A/cm², both in current switching and electrolysis modes.²¹³ That is, continuing removal of material ultimately results in a complete interfacial

opening or delamination. Such delamination is likely even at the lower J of 0.8 A/cm^2 for sufficiently long-term cell operation.

As discussed previously²¹³, the degradation during reversing current operation appears to be similar to that seen in dc electrolysis operation, although the periods of fuel cell operation can partially mitigate degradation.^{161,212} The degradation presumably occurs during the electrolysis periods of reversible operation. Thus, the present results should be qualitatively similar to dc electrolysis. However, there is relatively little data that is directly comparable. Knibbe et al.¹⁴⁴ showed degradation of full Ni-YSZ/YSZ/LSM-YSZ cells at $J = 1 \text{ A/cm}^2$, but the initial η was only 0.19 V . While this is consistent with the J values causing degradation in the present results, no degradation would be expected at this η based on the present data. Note that most of the degradation was observed in the ohmic resistance,¹⁴⁴ similar to the present results. Reports on degradation of LSM electrodes are difficult to compare directly with the present LSM-YSZ results. In one case, delamination was observed after operation at 0.5 A/cm^2 ,¹³⁹ but the polarization resistance was quite high such that $\eta \sim 3 \text{ V}$, well above the value where degradation is expected. Tests on symmetric LSM electrode cells (on YSZ) showed rapid resistance increases and delamination after 100 h at $\sim 2.0 \text{ A/cm}^2$ and $\eta \sim 0.76 \text{ V}$.¹³⁶

Although there is no definitive experimental evidence showing whether J or η controls oxygen electrode degradation, models of the degradation mechanism suggest that η is the controlling parameter. Models are generally based on the large electrochemical oxygen potential developed near the electrode/electrolyte interface.^{136,139,140} This high effective oxygen pressure can drive the observed nucleation of oxygen bubbles in the region near the electrode-electrolyte interface.¹⁴⁰ In one case, a critical η required to nucleate oxygen bubbles in YSZ was predicted to be 0.28 V .²¹⁹

The present results, where the η value sufficient to cause degradation was between 0.18 V and 0.33 V, are consistent with this predicted value. Other models are based on $\text{La}_2\text{Zr}_2\text{O}_7$ formation¹³⁶ and LSM lattice contraction¹³⁹ due to the high oxygen potential, but these do not predict potential values where degradation is expected.

6.2.5 Conclusions

The present results represent an attempt to determine the J and η values below which LSM-YSZ electrode degradation becomes negligible during reversing current operation. The following conclusions can be made:

1. EIS tests over ~ 1000 h on symmetrical cells appear able to detect a degradation rate of 1%/kh.
2. SEM observations appear to be quite sensitive to the early stages of degradation, as seen by a decrease in the apparent amount of LSM and YSZ at the interface, and an increase in the size of LSM particles in the functional layer.
3. The present results show that degradation caused by reversing-current operation can be reduced below $\sim 1\%/kh$, the present detection limit, by operating at a current density between 0.5 A/cm^2 and 0.6 A/cm^2 with an oxygen electrode overpotential between 0.18 V and 0.33.
4. At higher current densities and overpotentials, the degradation rate increases rapidly, leading to device lifetimes that would be too short for practical application;
5. EIS measurements show a unique signature associated with the degradation – an increase in a high-frequency ($\sim 10^4$ Hz) response – which appears to be associated with YSZ grain

boundary transport losses. This could be a sign of oxygen bubble formation on grain boundaries.

6.2.6 Acknowledgements

This section (6.2) used material and argumentation from a paper published in the Faraday Discussions²²⁰. The work was done in collaboration with Dr. Gareth Hughes who contributed the current switching method, the stepped current density test, and current switched life-tests at 0.5, 0.9, and 1.5 A/cm². I contributed the circuit modeling to interpret the results, the 0.6 and 0.8 A/cm² tests, the SEM/EDS, argumentation, and the figures. Much of the work in Chapter 6 is founded on the ideas developed in this study.

6.3 Separating the Roles of Current Density and Overpotential in (La_{0.8}Sr_{0.2})_{0.98}MnO_{3-δ} - Zr_{0.84}Y_{0.16}O_{2-γ} Composite Electrodes During Reversing Current Operation

Section 6.2 shows that with both increasing current density J and increasing overpotential η , the degradation rate of a current switched LSM-YSZ electrode increases. It is important to attempt to distinguish between these causes of degradation because degradation at any J above a threshold value would place a guiding limit to the design of a ReSOC or an electrolysis cell; however, if η is the more controlling factor in the onset of degradation, the chemistry, structure, or operating temperature can be changed to offer stable operation at higher J . There is a theoretical basis for expecting η to be a controlling factor in degradation by oxygen bubble nucleation and subsequent cracking (Chapter 2.6). The structural changes in the LSM observed in the previous section are not explained by this theory, but may be a related phenomenon that leads to delamination. It is therefore still an open question whether J controls the degradation, or if η controls the degradation, or some combination. In this section a set of current switched life tests is performed designed to

separate these causes. For a constant J , the η will change exponentially with temperature because the polarization resistance changes exponentially with temperature. Following this logic, a current switched life test was performed at 0.5 A/cm^2 at $750 \text{ }^\circ\text{C}$ and compared to one at $800 \text{ }^\circ\text{C}$. The symmetric cell was fabricated in an identical process to the cells operated at $800 \text{ }^\circ\text{C}$ in the previous section, and the current switched operation was also identical. Figure 6.8 shows a comparison of the ohmic, polarization, and total resistances of an LSM-YSZ symmetric cell operated at 0.5 A/cm^2 at $750 \text{ }^\circ\text{C}$ and $800 \text{ }^\circ\text{C}$.

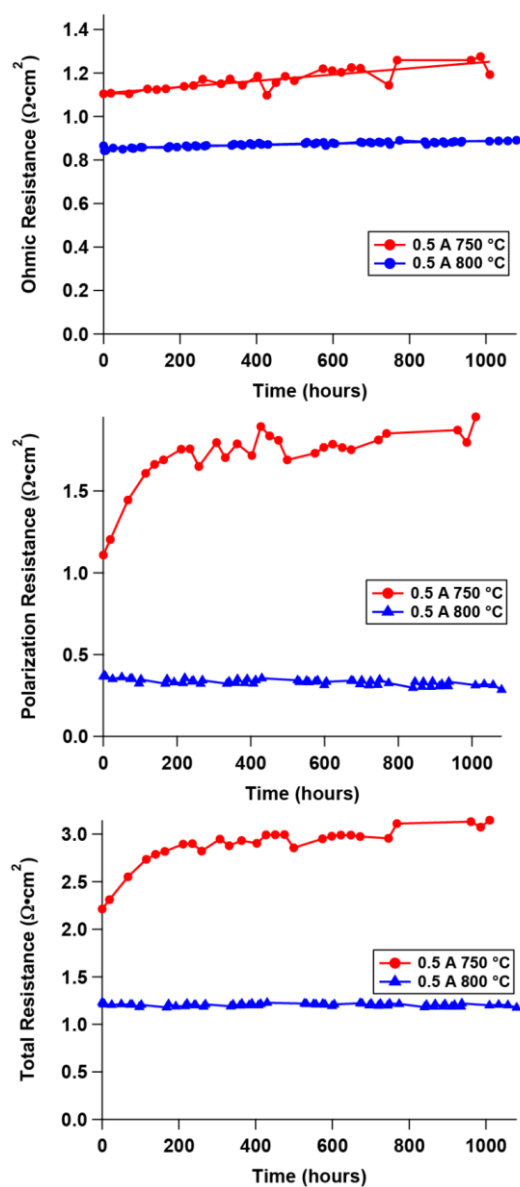


Figure 6.8. Ohmic, Polarization, and Total resistance values comparing a stable current cycled LSM-YSZ symmetric cell operated at 800 °C to an identical cell operated at 750 °C, values displayed are taken from L-R-RQ-RQ fits.

The resistance values come from a circuit model fit using the L-R-RQ-RQ model used in section 6.2. The initial η for the cell at 800 °C is 0.18 V while the η for the cell at 750 °C is 0.55 V. The

cell operated at an initial $\eta = 0.55\text{V}$ shows fast initial degradation until about 200 hours at which point degradation become slower at 10%/khr. Figures 6.9 and 6.10 show Nyquist and Bode plots for the two life tests.

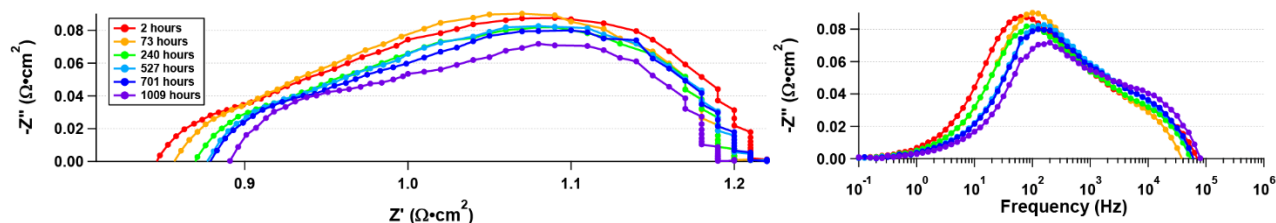


Figure 6.9. Nyquist and Bode plots for an LSM-YSZ symmetric cell operated at 0.5 A/cm^2 under a 12-hour current switched cycle at $800\text{ }^\circ\text{C}$

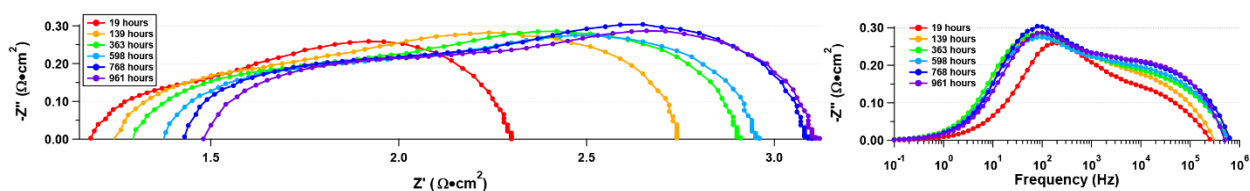


Figure 6.10. Nyquist and Bode plots for an LSM-YSZ symmetric cell operated at 0.5 A/cm^2 under a 12-hour current switched cycle at $750\text{ }^\circ\text{C}$.

The increase in the 50 kHz response in the $750\text{ }^\circ\text{C}$ cell is similar to the degradation seen in section 6.2 for symmetric LSM-YSZ. This implies that degradation by the same mechanism is accelerated at lower temperatures or higher overpotentials. Figure 6.11 shows the post-test SEM evaluation of the $750\text{ }^\circ\text{C}$ cell, showing cracking, pitting and material depletion near the electrode/electrolyte interface.

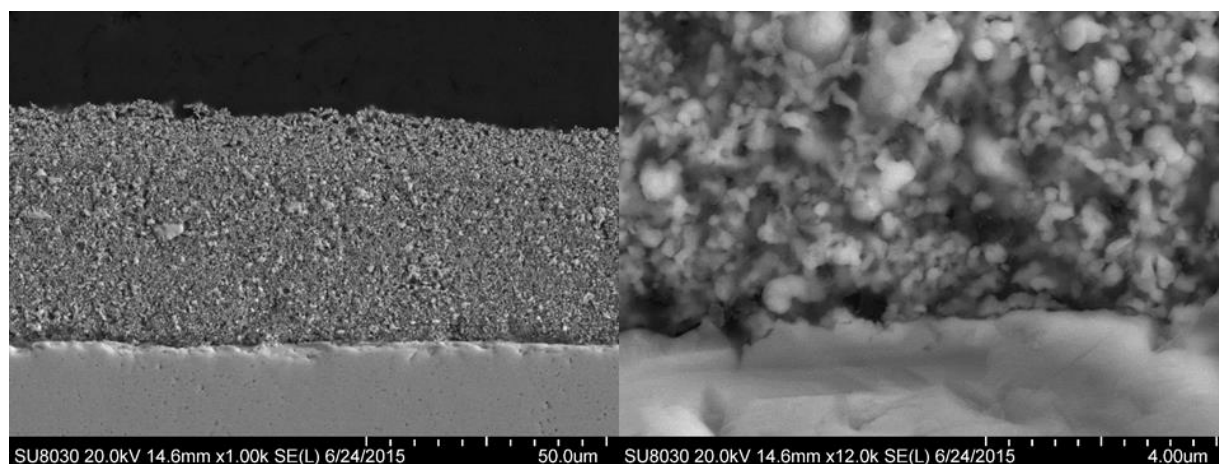


Figure 6.11. SEM images of the post-test LSM-YSZ cell operated at 750 °C and 0.5 A/cm² near electrode/electrolyte interface. The sample is epoxy infiltrated and polished to 1 μm diamond.

An additional current switched life test was performed to investigate whether degradation could be eliminated or reversed within the same cell by operating a 0.5 A/cm² current cycle and adjusting the temperature between 750 and 800 °C. Figure 6.12 shows the total resistance over time for a LSM-YSZ symmetric cell that was operated at 750 or 800 °C for 200 hour periods while running a 12-hour 0.5 A/cm² current cycling program.

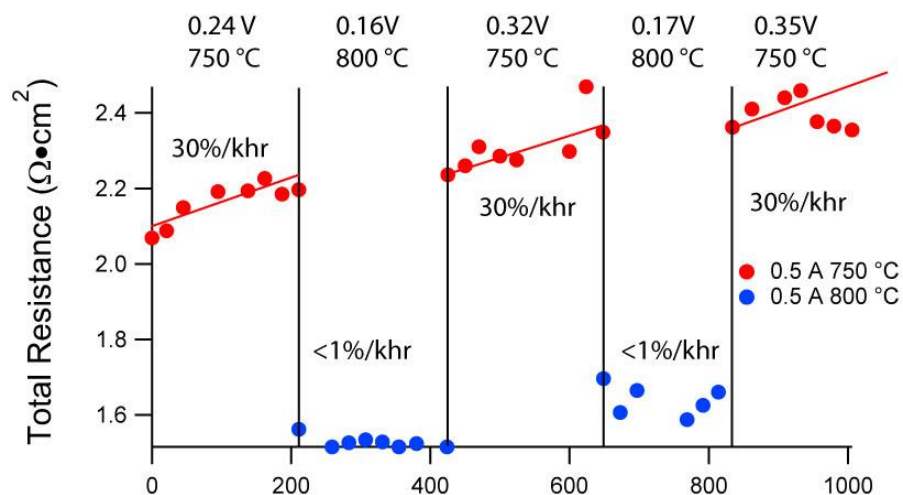


Figure 6.12. Total resistance of a current switched LSM-YSZ symmetric cell operated at 0.5 A/cm² on a 12-hour cycling period with the temperature switched between 750 and 800 °C every 200 hours. The overpotential at the start of each temperature period is labeled at the top of the figure.

The degradation rates shown for the 750 °C regions is 30%/khr, whereas the degradation in the 800 °C region is not measurable. The total resistance in the second 800 °C period at 625 hr shows that the degradation is not reversible, but the rate of degradation can be slowed by increasing the temperature (decreasing η).

The overall trend of increasing total resistance with η shows that degradation in the LSM-YSZ system is mostly controlled by η and operating conditions can be changed to slow the degradation. The slowed degradation at lower η also suggests that a cell with a smaller polarization resistance will be more stable against degradation. However, there are details in the EIS data that show η is not the entire descriptor of degradation. Despite a very stable total resistance in the 0.5 A/cm² current cycled test at 800 °C, the response at 10² Hz decreases at the same rate that the ohmic

resistance increases. This phenomenon has yet to be explained, but is a small change compared to the resistance increases associated with increased η . One possible interpretation is that LSM movement in the electrode occurs below the η threshold for oxygen bubble formation and cracking (section 2.6.1)¹⁴⁰. A reorganization of the LSM could reduce the TPB density which would increase the polarization resistance while LSM reorganization, especially in the current collector, could allow for larger local cross-sections, reduced grain boundary scattering leading to higher LSM conductivity.

6.4 Degradation of $\text{La}_{0.6}\text{Sr}_{0.4}\text{Fe}_{0.8}\text{Co}_{0.2}\text{O}_{3-\delta}$ Oxygen Electrodes on $\text{Ce}_{0.9}\text{Gd}_{0.1}\text{O}_{2-\delta}$ During Reversing Current Operation

6.4.1 Introduction

Previous work (section 6.2) on LSM-YSZ electrodes has shown degradation in current switching has features in common with DC electrolysis, particularly cracking and delamination at the electrode-electrolyte interface. Stable conditions (unmeasurable degradation in total resistance) for reversing current operation are available for the LSM-YSZ system (section 6.2), but there are an array of other materials systems of interest, especially moving toward lower temperatures where storage is more economical. The $\text{La}_{0.6}\text{Sr}_{0.4}\text{Fe}_{0.8}\text{Co}_{0.2}\text{O}_{3-\delta}$ (LSCF)/ $\text{Ce}_{0.9}\text{Gd}_{0.1}\text{O}_{2-\delta}$ (GDC) system has been under intense investigation for solid oxide cells (SOCs) operating around 700 °C and below²⁵, but little is known about this system under current switching operation. A few studies exist on the degradation of LSCF electrodes under electrolysis conditions²²¹⁻²²⁵, and one under brief (total 72 hr) current switching conditions²²⁶. Most degradation in LSCF electrodes under electrolysis has been studied using full cells that are typically composed of a dense YSZ electrode and a thin or porous GDC barrier layer to prevent detrimental side reactions²²¹⁻²²⁶. The few reports that examine

the degradation of LSCF in electrolysis conditions mainly attribute degradation to diffusion of Sr or Co through the GDC barrier layer to the underlying YSZ electrolyte²²⁵, causing side reactions^{223,225} or a phase change in the compositionally compromised LSCF²²¹. This is in contrast to LSM electrodes that degrade primarily by delamination, though one report of LSCF on YSZ does observe this mode of degradation²²¹. None of the studies mentioned here operate the electrode below 750 °C. Here we present life tests on symmetric LSCF/GDC cells operating under switching with a 12 hour period at a range of J (0.7-1.5 A/cm²) and η (0.03-0.12 V) at 700 °C to identify the range of stable operation and observe relevant degradation phenomena. In this study, an advantage of the LSCF/GDC/LSCF symmetric cells is that there is no driving force for the Co and Sr to react as there is no underlying YSZ electrolyte layer. Moreover, there are no reports that compare the effect of J or η on electrolysis or current switching degradation in the LSCF/GDC system.

6.4.2 Methods

6.4.2.1 Cell Fabrication

Ce_{0.9}Gd_{0.1}O₂ (Rhodia) was pressed into 0.5 g 19mm diameter pellets and sintered at 1450 °C for 6 hours. Commercial La_{0.4}Sr_{0.6}Co_{0.2}Fe_{0.8}O₃ powder (Praxair) was mixed with Heraeus V-737 in a 1:1.18 ratio on a three roll mill and screen printed on both sides of the sintered pellets. The symmetric cells were then fired at 1100 °C for 2 hours resulting in an electrode thickness of ~40 μm.

6.4.2.2 EIS Measurements

Cells were contacted with porous La_{0.8}Sr_{0.2}MnO₃ (LSM) pellets 0.4 cm in diameter to avoid artifacts associated with silver migration. A paste composed of LSM and V-373 was used to affix the LSM pellet to the electrode. A LabView controlled Keithley sourcemeter provided current

densities galvanostatically ranging from 0.7-1.5 A/cm² on a 12-hour cycle period. The sourcemeter was periodically disconnected to collect impedance spectra using a Zahner IM6 workstation in the range of 10⁵-10⁻¹ Hz approximately every 24 hours. Zview software was used to separate the ohmic, polarization, and total resistance contributions by fitting equivalent L-R-RQ-G circuits to the data.

6.4.2.3 SEM-EDS

Symmetric cells were fractured and vacuum infiltrated with EpoThin epoxy (Buehler) and polished to 1.0 μm with a diamond slurry (Buehler). Specimens were then coated with 7 nm of Os and contacted with carbon tape. The electrodes were imaged using a Hitachi SU 8030 scanning electron microscope at 25 kV and 20 nA using a lower secondary electron detector.

6.4.2.4 FIB-SEM

A control sample, a 0.7 A/cm² post-test fragment, and a 1.5 A/cm² post-test fragment were prepared for FIB-SEM serial sectioning by epoxy infiltration and mechanical polishing.^{51,164} The imaging was done on an FEI Helios with an accelerating voltage of 2 kV and the backscattered electron (BSE) detector because it provides optimal contrast between the epoxy-filled pores and the solid phase. Imaging segmentation and 3D reconstruction were done as described elsewhere.¹⁶⁴

6.4.3 Results

Figure 6.13 shows selected impedance spectra collected over the course of the 0.7 A/cm² current switched life test with equivalent circuit models overlaid. The 0.7 A/cm² case is mostly stable, showing minimal changes past the initial break-in period. Two distinct responses can be observed at about 1 Hz and 1 kHz. Figure 6.14 shows Nyquist and Bode plots for the 1.5 A/cm² current switched life test. The 1.5 A/cm² case shows increases in both ohmic and polarization resistances

throughout the life-test and an associated frequency shift in the response at 200 Hz that moves to about 20 Hz. At early times (<100 hours) all samples show some changes in both the ohmic and polarization resistances.

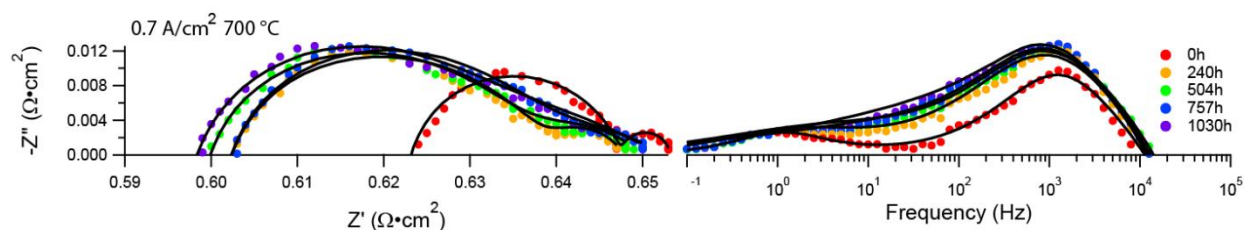


Figure 6.13. Nyquist and Bode plots at selected time points of the current switched life test performed at a current density of $0.7\text{A}/\text{cm}^2$.

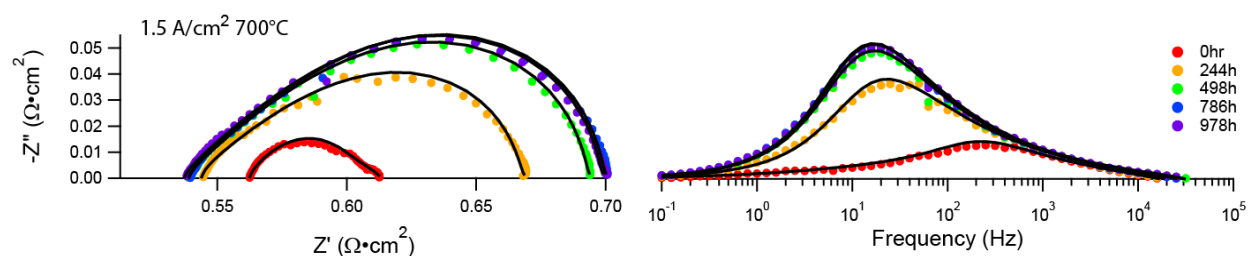


Figure 6.14. Nyquist and Bode plots at selected time points of the current switched life test performed at a current density of $1.5\text{A}/\text{cm}^2$.

An L-R-RQ-G circuit is used to model the electrode responses in figures 6.13 and 6.14. The inductor accounts for inductance in the test setup, while the series resistor models the ohmic resistance of the electrolyte. A Gerischer element is used to model the ORR, as the electrode is a single phase MIEC and should therefore be modeled well by a Gerischer element according to the Adler-Lane-Steele model⁵⁸. The RQ element accounts for an unknown response, clearly visible in the $0.7\text{A}/\text{cm}^2$ sample, and at early times in the $1.5\text{A}/\text{cm}^2$ sample. This RQ response at about 1 Hz is not observed in similarly processed single phase LSCF on GDC symmetric cells contacted with

silver wires (Chapter 5) and is therefore likely due to the gas diffusion through the thick LSM pellet and paste contacting the LSCF. The low frequency RQ response ($0.01 \Omega \cdot \text{cm}^2$) is relatively constant throughout all tests, and overlaps with the ORR response at late times in the 1.5 A/cm^2 case.

Figure 6.15 shows the ohmic, polarization, and total resistance over the course of four life-tests as well as the changes in resistance with respect to the starting values at the start of the test. The values plotted are from equivalent circuit fits to the EIS data. The total resistance for the 0.7 A/cm^2 case is $<1\%/ \text{hr}$, specifically $0.6\%/ \text{hr}$ with 95% confidence interval of $\pm 0.4\%/ \text{hr}$ and is the most stable sample examined. The 1.5 A/cm^2 case degraded more quickly at $14.5\%/ \text{hr} \pm 1.55\%$ overall. The error is calculated by fitting a line to the data, finding the standard deviation in the slope and multiplying by 2 to achieve a 95% confidence. Most of the degradation occurs as an increase in polarization resistance for all samples (3b and e). All samples show minimal or even negative changes in the ohmic resistance (0.7 and 1.5 A/cm^2 cases) (3a and d). The degradation rate in the polarization resistance for both the 1.0 and 1.5 A/cm^2 cases slows with time. This is especially apparent figure 6.14e that shows roughly identical degradation rates for the 0.9 and 0.7 A/cm^2 polarization resistance, and a pronounced, but stabilizing degradation for the 1.0 and 1.5 A/cm^2 cases. The slightly negative change in ohmic resistance almost completely cancels the increase in polarization resistance for the 0.7 A/cm^2 case.

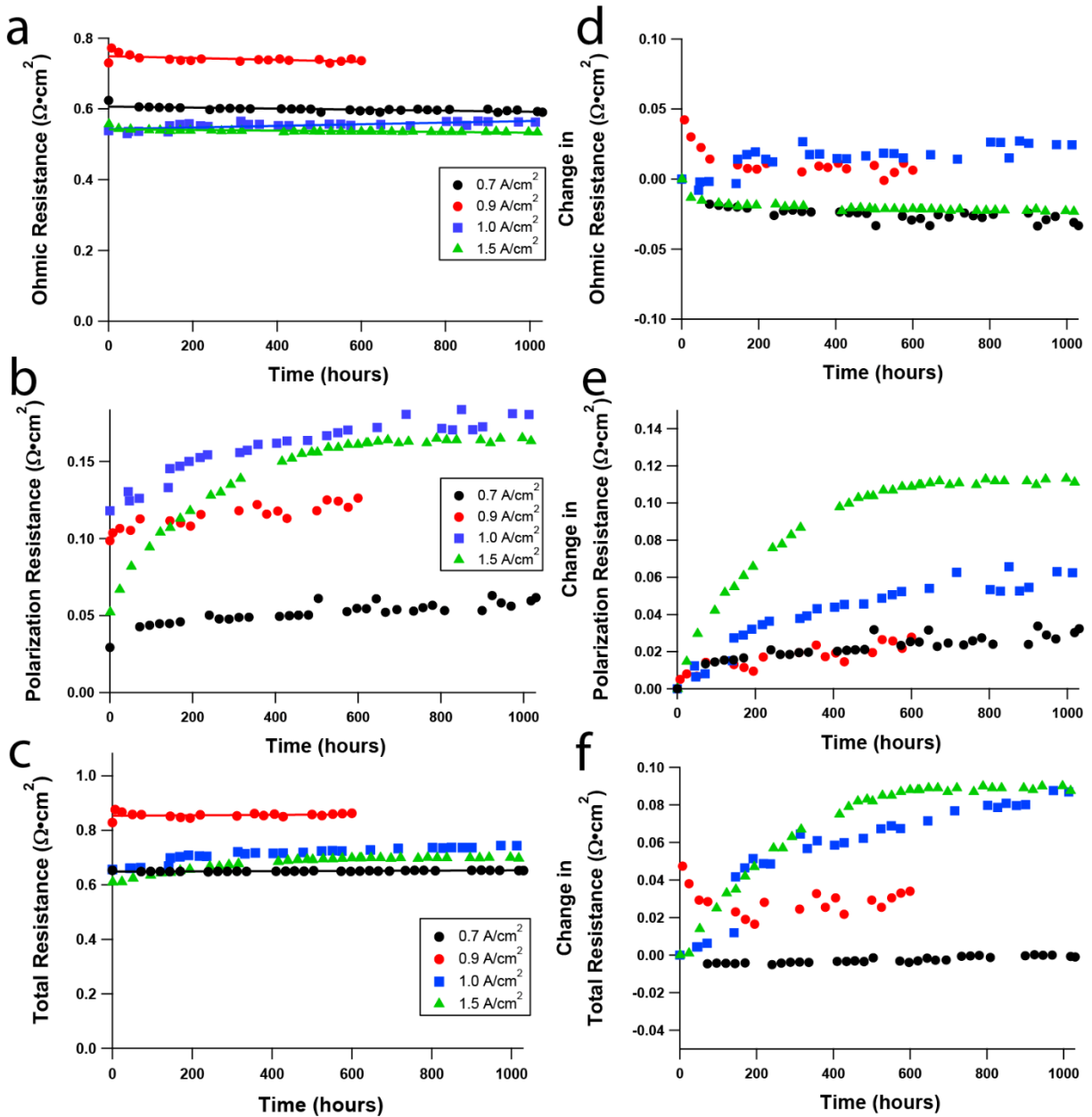


Figure 6.15. a) Ohmic resistance, b) Polarization resistance, and c) Total resistance of the current switched life tests performed at 0.7, 0.9, 1.0, and 1.5 A/cm². Data points show circuit model values. The changes in resistance with respect to the starting values are also shown (d-f).

Figure 6.16 shows polished SEM cross-sections of post life-tested cells showing the region near the electrode/electrolyte interface. Cracking and pitting is visible in the GDC near the interface for the 1.0 and 1.5 A/cm² samples, though the electrodes are still well connected to the electrolyte and there is no apparent material depletion. There are also apparent changes in the electrode microstructure with increasing J . Comparing the 0.7 and 1.5 A/cm² samples the LSCF particles in the 0.7 A/cm² appear on average smaller compared to the 1.5 A/cm² sample.

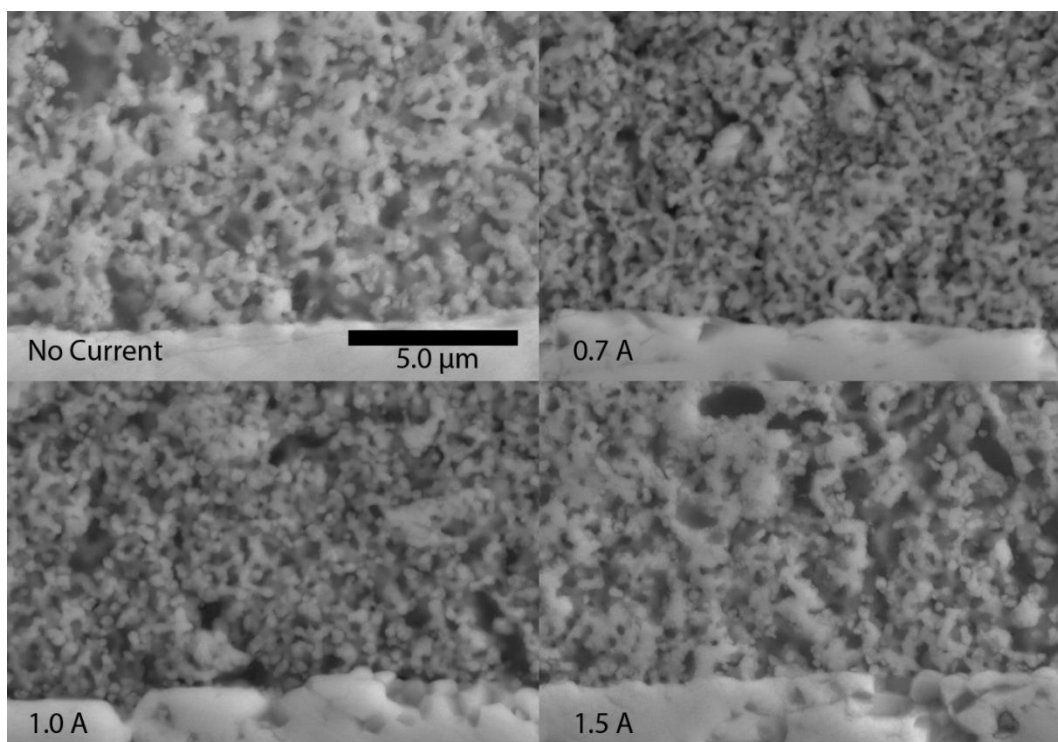


Figure 6.16. Polished cross-sections of LSCF symmetric cells operated at zero, 0.7, 1.0, and 1.5 A/cm².

Table 1 shows a summary of the reconstructions including the sample porosity, tortuosity of the solid phase, and surface area per electrode volume. There is a clear decrease in the porosity,

tortuosity, and specific surface area from the control sample to the 1.5A/cm² sample while relatively little change is seen between the control and 0.7 A/cm² samples.

Table 6.1. Summary of microstructural parameters in post-test LSCF electrodes

Sample	No Current	0.7 A/cm ²	1.5 A/cm ²
Porosity, ϵ , %	39.69	39.59	34.03
Tortuosity, τ	1.12	1.12	1.10
Specific Surface Area, a (μm^{-1})	5.62	5.96	4.47

6.4.4 Discussion

Figure 6.16 shows the degradation rates as a function of J and η . The error bars displayed are errors in the slopes of the linear regressions to the data in figure 6.15c within 95% confidence. Overpotentials are approximated by multiplying the J by the polarization resistance. The degradation in LSCF on GDC appears to be more strongly correlated with J than with initial η .

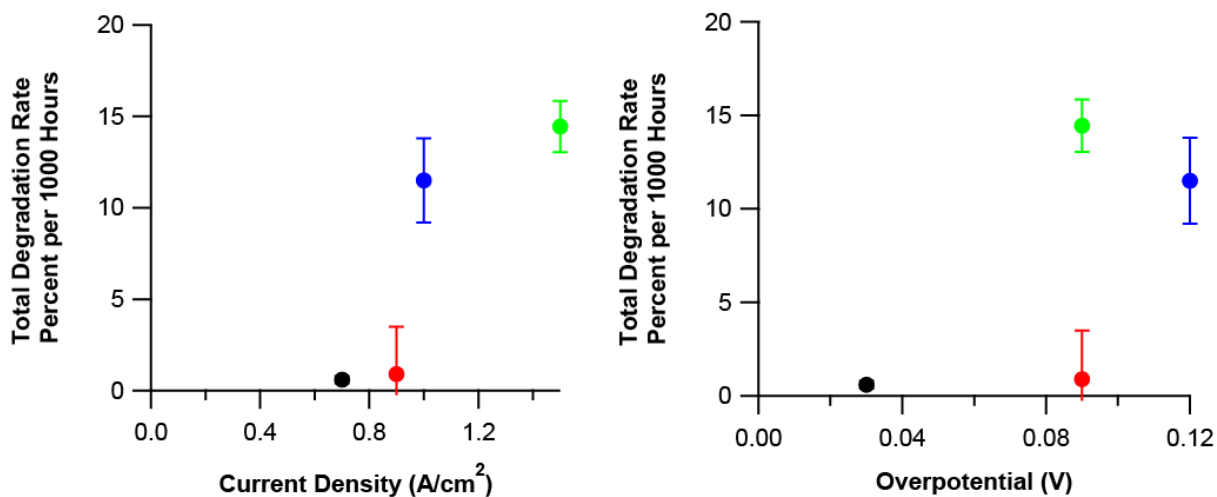


Figure 6.17. Total degradation rate versus J and η for 0.7 A/cm² (black), 0.9 A/cm² (red), 1.0 A/cm² (blue) and 1.5 A/cm² (green).

A theory by Virkar^{140,227} describes generally that degradation in solid oxide electrolyzers by cracking and delamination can be linked to the initial η and a critical η can be estimated by:

(Equation 6.1)

$$E_A \geq E_{cr} = \frac{RT}{4F} \ln \left\{ \sqrt{\frac{\pi}{(1-v)^2 c} \frac{K_{Ic}}{2p_o}} \right\}$$

Where $K_{Ic} = 1.53 \text{ MPa}\sqrt{\text{m}}$ ²²⁸, c is estimated to be between 1 and 10 μm , $v=0.33$, $p_o = 21.3 \text{ kPa}$, and R , T , and F have their typical meanings, a critical η for GDC can be estimated (0.24-0.22 V). In the present study, all degradation is occurring below the predicted η value for GDC (<0.12 V), though the η at the end of the 1.5 A/cm² test approaches 0.22V. Here most degradation occurs in the polarization resistance with very little change in the ohmic resistance, suggesting the majority of the changes are in the electrode. The rate of degradation in the polarization resistance is correlated with current density and may be explained by the microstructural changes quantified in Table 6.1 by FIB-SEM. Another possibility is that increased J or η accelerate the rate of strontium segregation (section 2.5.2.1). It is possible that a combination of microstructural changes and microchemical changes are responsible for what appears to be a leveling off of the polarization resistance at high current densities, as both scenarios would have a slowed effect as degradation progresses. For a current induced coarsening of the LSCF, eventually the rate of surface area change would slow, resulting in a leveling off of the polarization resistance as observed. For the case of strontium segregation accelerated by voltage, or current density, some equilibrium amount of strontium would segregate to the surface and again the polarization resistance would level off.

The Adler-Lane-Steele model may be an appropriate physical interpretation of the symmetric electrodes to quantify the observed microstructural and chemical changes with respect to the changes in polarization resistance. The low frequency response can be accounted for by the RQ element as described above, and so the ORR can be equated to the Gerischer element i.e., $R_G = R_P - R_{RQ}$. Equations 6.2 and 6.3 relate the Gerischer time constant and resistance to the chemical and physical descriptors of the LSCF electrode:

(Equation 6.2)

$$t_G = \frac{(1 - \epsilon)c_o x_\delta^0}{4aR_o A_o}$$

(Equation 6.3)

$$R_G = \frac{RT}{4F^2} \sqrt{\frac{\tau}{4a(1 - \epsilon)R_o c_o x_\delta^0 D}}$$

Where ϵ is the electrode porosity, a is the internal specific surface area of the solid phase, τ is the tortuosity of the solid phase, c_o is the concentration of oxygen sites involved in diffusion, x_δ^0 is the molar fraction of interstitial or vacancy defects at equilibrium, A_o is the thermodynamic factor, D is the oxygen diffusivity, and R_o is the molar surface exchange rate defined as:

(Equation 6.4)

$$R_o = \frac{k_{chem}}{A_o} (pO_2)^{0.5} c_o$$

For the 1.5 A/cm² sample, taking the ratio between the initial and final resistance and plugging the final surface area into equation 3, the internal surface area at the start of the test would have to be

$118.5 \mu\text{m}^{-1}$ to be commensurate with the observed resistance. However, this value seems unlikely when compared to the internal surface area of the control sample ($5.62 \mu\text{m}^{-1}$). Comparing the control sample microstructural parameters and 1.5 A/cm^2 microstructural parameters, the expected change in polarization resistance would be $0.01 \Omega\cdot\text{cm}^2$, which is only 10% of the actual change. The observed change in polarization resistance is then not wholly explained by a change in microstructure.

The other likely possibility is a change in the surface exchange parameter k_{chem} caused by strontium segregation. Using c_0 and x_{δ}^0 values from chapter 5 and the t_G determined from circuit modeling, the k_{chem} for the 1.5 A/cm^2 sample can be calculated using equations 6.2 and 6.4. The calculated value of k_{chem} for the 1.5 A/cm^2 sample microstructure at the end of the life test is $4.3 \times 10^{-5} \text{ cm/s}$, which is close to the center of mass compared to other reported values. In order to account for the resistance change, holding all other factors constant the k_{chem} at the start of the test would have to be $2.4 \times 10^{-4} \text{ cm/s}$, which is among the highest reported values for LSCF. Combining the two changes in the electrode, using the control microstructure at the start of the 1.5 A/cm^2 test and calculating the k_{chem} for the start of the test yields $1.84 \times 10^{-4} \text{ cm/s}$. Thus, excluding other possible mechanisms of degradation, ~10% of the degradation can be accounted for by microstructural changes, while ~90% could be explained by a change in the surface exchange rate. This suggests that increased J accelerates the rate of strontium segregation (discussed in chapter 2) to the surface of the electrode, though more work using independent characterization techniques would be needed to verify this possibility.

6.4.5 Summary and Conclusions

Current switched life tests of LSCF on GDC symmetric cells were performed for about 1000 hours at 0.7, 0.9, 1.0, and 1.5 A/cm². The rate of degradation increased with increasing J and the entire resistance increase attributed to the polarization resistance. The cell operated at 0.7 A/cm² had a slow degradation rate at 0.6 ± 0.4 %/khr while the 1.5 A/cm² sample degraded quickly at first, but leveled out after 700 hours. All degradation occurred at an η below that predicted to cause oxygen bubble formation and electrolyte cracking, and indeed there were no significant changes observed in SEM or in the ohmic resistance. FIB-SEM was performed on a control cell, the 0.7 A/cm² case, and the 1.5 A/cm² case to look for microstructural changes. Using the ALS model, only about 10% of the resistance change could be attributed to the changes in microstructure. Again using the ALS model, a change in surface exchange may account for most of the degradation (from 1.84×10^{-4} to 4.3×10^{-5} cm/s) suggesting that strontium segregation may be accelerated by higher J . The outlook for the long term stability of the LSCF electrode may be good if these changes are accounted for by Sr segregation, as the polarization resistance would saturate at a particular value.

6.4.6 Acknowledgements

The FIB-SEM reconstruction data presented in this section was collected by Hongqian (Sharon) Wang and Qinyuan Liu.

6.5 Preliminary current switched life tests of La₂NiO₄ wet-infiltrated into

(La_{0.9}Sr_{0.1})(Ga_{0.8}Mg_{0.2})O₃

6.5.1 Introduction

Rare-earth nickelates are a promising class of materials for use as oxygen electrodes, as demonstrated in chapters 4 and 5. In particular, they offer low polarization resistances at low

temperatures, implying they may be stable against degradation at temperatures low enough for a reversible SOC system if their degradation is controlled by overpotential, as in the LSM-YSZ system. Here we investigate the stability of La_2NiO_4 (LNO) infiltrated into $(\text{La}_{0.9}\text{Sr}_{0.1})(\text{Ga}_{0.8}\text{Mg}_{0.2})\text{O}_3$ (LSGM) during 12-hour current cycles. No rare earth nickelate material or LSGM has ever been used in an electrolysis or current switched degradation study. Infiltrated LNO was selected as the first rare-earth nickelate to undergo these tests because it is the most well explored nickelate, does not suffer from strontium segregation issues, is stable in contact with LSGM and is phase stable in the $n=1$ phase as prepared. The material can also be processed at lower temperatures than PNO, lowering the risk of any interdiffusion. This section shows current switching and EIS data for the infiltrated LNO/LSGM system, post-test SEM/EDS and a preliminary outlook on finding stable operating conditions for the LNO/LSGM system.

6.5.2 Experimental

Infiltrated LNO symmetric cells were prepared similarly to the Pr_2NiO_4 electrodes described in chapter 5¹⁰³. For the LSGM electrolyte, LSGM was first synthesized via solid state reaction. LSGM powder was synthesized from stoichiometric amounts of SrCO_3 (Sigma), La_2O_3 (Sigma), Ga_2O_3 (Sigma), and MgO (Alfa Aesar), which were ball milled for 24 hours in ethanol, dried, and then reacted at 1250 °C for 12 hours. This LSGM powder was then ball milled in ethanol and 2 wt. % polyvinyl butyral (Aldrich) binder, dried, and pressed into 0.5 g 19 mm diameter pellets. The green bodies were then sintered at 1450 °C for 4 hours. LSGM scaffolds were screen printed onto the electrolyte pellets using an ink composed of commercially available LSGM (Praxair), Heraeus 737 vehicle, and 30 wt% of KS4 graphite flakes (Timrex) as pore former. Four screen printed layers were applied to each side, then heated to 600 °C for one hour to burn away the pore

former, and then fired at 1200 °C for 4 hours to form a porous scaffold layer with interconnected LSGM particles 0.5-3 microns in size. A current collector was then applied on each scaffold by screen printing one layer of an $(\text{La}_{0.6}\text{Sr}_{0.4})(\text{Co}_{0.8}\text{Fe}_{0.2})\text{O}_{3-\delta}$ ink consisting of the same vehicle, pore former, and LSCF powder (Praxair). The entire assembly was then fired at 1100 °C for one hour to produce a suitably porous current collector that was also well bonded to the scaffold. The resulting scaffold thickness was ~ 40 μm and the LSCF layer was ~ 10 μm thick. The cathode infiltrate was a 2 M nitrate solution prepared by dissolving stoichiometric amounts of $\text{La}(\text{NO}_2)_3 \cdot 6\text{H}_2\text{O}$ (Aldrich) and $\text{Ni}(\text{NO}_2)_3 \cdot 3\text{H}_2\text{O}$ (Fischer) in water and subsequently adding 0.06 mol of Triton X-100 (VWR). This solution was stirred for 24 hours to ensure good mixing. Each scaffold was infiltrated with this solution using excess fluid (~6 μL) and removing the excess after allowing solution to infiltrate the porous scaffold for 5 minutes. The infiltrate was decomposed by heating to 450 °C for 0.5 hours, leaving oxides of the respective metal ions. After 12 infiltrations, the symmetric cells were fired at 850 °C for 4 hours to form La_2NiO_4 . Silver metal grids current collectors were applied for electrochemical testing. Two LNO infiltrated LSGM symmetric cells were current cycled for 1000 hours at 650 °C, one at 1.0 A/cm^2 and the other at 2.0 A/cm^2 . EIS spectra were taken once every 24 hours using a Zahner IM6 electrochemical work station working the 0.1-10⁶ Hz range. The EIS data were modeled using an L-R-RQ equivalent circuit model to extract the ohmic, polarization, and total resistances of the electrodes over time. Cross-sections of the LNO/LSGM cells are prepared by epoxy infiltration and polishing down to a 1 μm diamond slurry. SEM/EDS is performed as described in chapter 3.

6.5.3 Results

Figure 6.18 shows the Nyquist and Bode plots of the 1.0 A/cm^2 current switched LNO/LSGM symmetric cell. After a break-in period in the first 100 hours of operation very few changes are seen in the impedance response. The response can be described by a single depressed arc that encompasses the ORR kinetics. A small increase in the ohmic resistance is observed even after the break-in period.

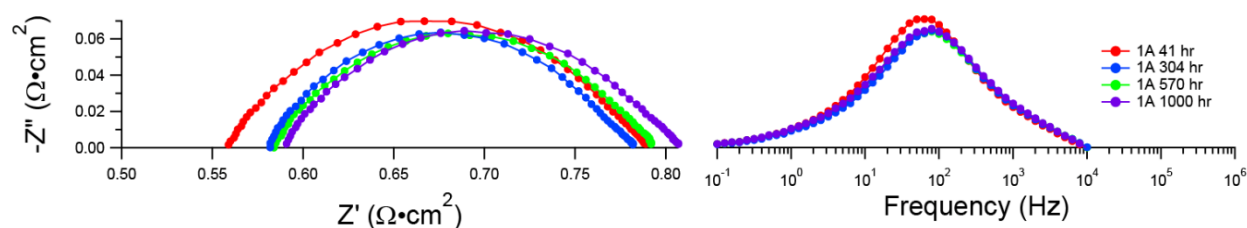


Figure 6.18. Nyquist and Bode plots of a current switched LNO/LSGM cell at selected time points in the 1.0 A/cm^2 current switched life test at $650 \text{ }^\circ\text{C}$

Figure 6.19 shows the Nyquist and Bode plots of the 2.0 A/cm^2 current switched LNO/LSGM symmetric cell. The EIS response is still modeled well using a single RQ element with a depressed arc. There are similar increases in both the ohmic and polarization resistances and a slight decrease in the peak frequency associated with the increased resistance. There are no significant changes in the arc shape or number of responses. The spurious sharp peak at about 50-60 Hz is the result of the particular test setup where the silver lead wires were coupling with the outlet AC voltage.

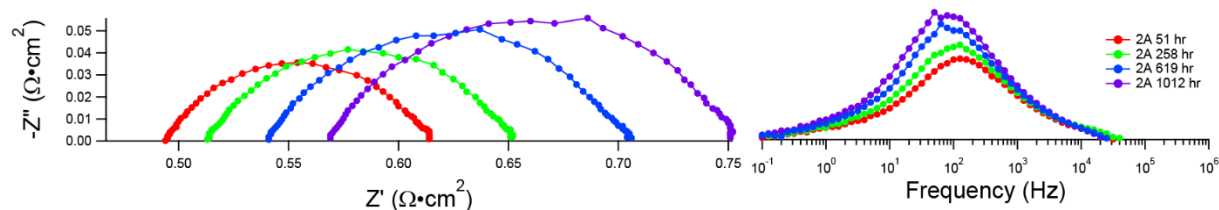


Figure 6.19. Nyquist and Bode plots of a current switched LNO/LSGM cell at selected time points in the 2.0 A/cm² current switched life test at 650 °C

Figure 6.20 summarizes the EIS response throughout each test by displaying the ohmic, polarization and total resistance from the circuit model fits.

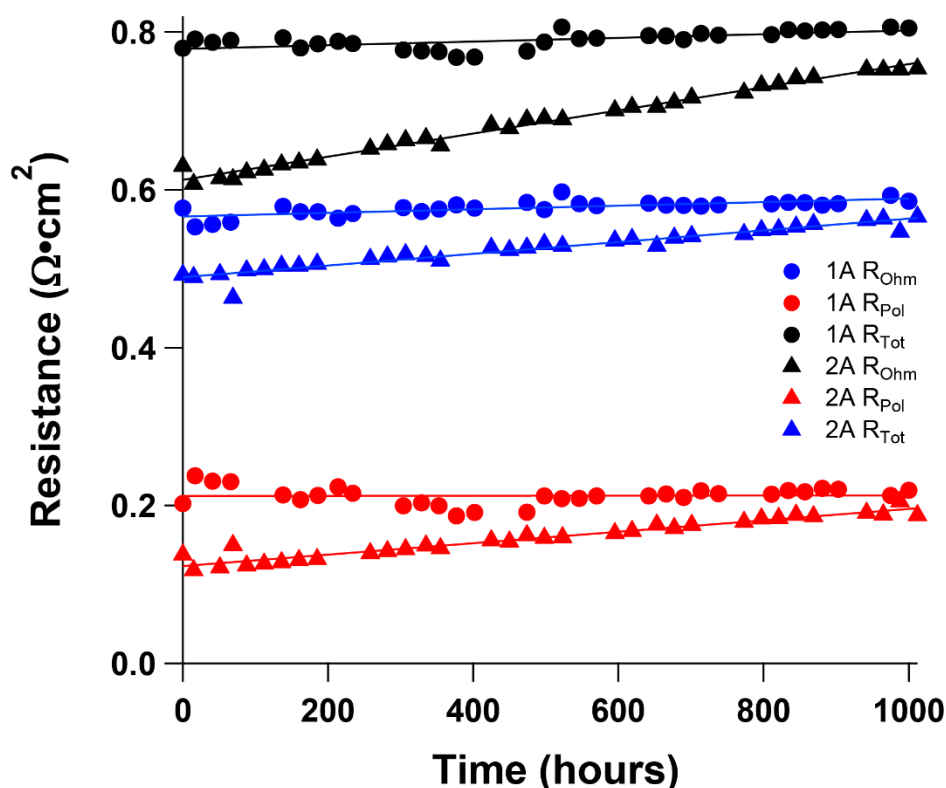


Figure 6.20. Summary of the ohmic, polarization, and total resistance values of the LNO life tests. Total resistances are displayed in black, polarization in red, and ohmic in blue. The 2.0 A/cm² results are displayed as triangles, and the 1.0 A/cm² results are displayed as circles.

The total rate of degradation for both samples is approximately linear. The degradation rate for the total resistance of the 2.0 A/cm² test is 23.3 ± 0.96 %/khr with increases coming relatively equally from changes in the ohmic and polarization resistances. The degradation rate for the total resistance

of the 1.0 A/cm^2 test is $2.9 \pm 1.3\%/ \text{hr}$ with all of the measurable degradation occurring in the ohmic portion. The initial overpotentials for the 1.0 A/cm^2 and 2.0 A/cm^2 tests were 0.2 V and 0.26 V respectively. The initial polarization resistance varies from cell to cell as similar to the infiltrated PNO cells in chapter 5. The initial polarization resistances for the 1.0 and 2.0 A/cm^2 cells were 0.2 and $0.13 \Omega \cdot \text{cm}^2$ at $650 \text{ }^\circ\text{C}$ respectively.

Figure 6.21 shows the post-test SEM cross-sections. The EDS here is used to delineate the infiltrated material from the LSGM scaffold. The LNO forms a high surface area structure and adheres well to the LSGM scaffold. The LSGM scaffold particles are between 0.5 and $3.0 \mu\text{m}$.

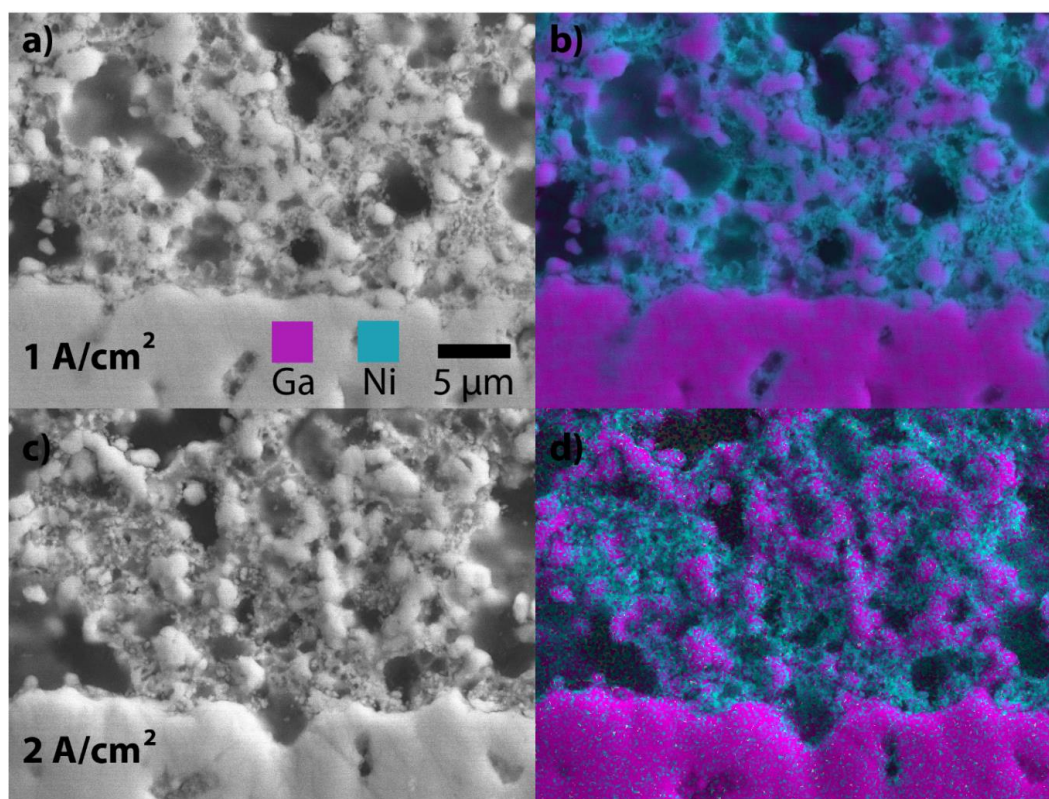


Figure 6.21. Post-test SEM/EDS cross sections a) 1.0 A/cm^2 SEM b) 1.0 A/cm^2 EDS c) 2.0 A/cm^2 SEM b) 2.0 A/cm^2 EDS

6.5.4 Discussion

Figures 6.18 and 6.19 show the impedance response for both tests and are fitted well by a single RQ element corresponding to the ORR. The polarization resistance of about $0.2 \Omega \cdot \text{cm}^2$ at $650 \text{ }^\circ\text{C}$ places the electrode in a similar performance range as infiltrated LSCF for this temperature^{126,160}. The low degradation rate at 1.0 A/cm^2 is not slow enough to meet the $<0.5\%/ \text{ khr}$ target considered stable, but it is likely not far from a stable operating condition. Some degradation may be due to particle coarsening^{160,199}, but large difference in degradation rate based upon the applied current suggests a J or η induced mechanism is dominant over a coarsening effect. No clear cracking or delamination is observed in SEM, though increases in the ohmic resistance for both the 1.0 and 2.0 A/cm^2 samples suggests changes in the LSGM either in the scaffold or the electrode/electrolyte interface consistent with observations in the LSM-YSZ system. Notably the overpotential at which degradation occurs in the ohmic resistance (between 0.2 and 0.26 V) is consistent with predictions from Virkar's model and observations in the LSM-YSZ system. Equation 6.1 gives an estimation of the critical overpotential to cause the onset of cracking and delamination based upon the K_{IC} of the material and the crack length. Inserting K_{IC} values for LSGM at $650 \text{ }^\circ\text{C}$ ($1.1 \text{ MPa}\sqrt{\text{m}}$, ref²²⁹) and estimating the crack length to be $1\text{-}10 \text{ }\mu\text{m}$ yields an estimated critical overpotential of $0.22\text{-}0.199\text{V}$, respectively. This just barely places the 1.0 A/cm^2 test in the lower range for degradation by oxygen bubble nucleation and cracking at $\eta = 0.2 \text{ V}$. More work will need to be done to confirm the dominant degradation mechanism at work in the LNO/LSGM system as well as find a baseline η or J for stable operation.

6.6 Summary

In this chapter three electrode types have been examined under current switching conditions: composite LSM/YSZ on a YSZ electrolyte, single phase LSCF on a GDC electrolyte, and LNO infiltrated into porous LSGM on an LSGM electrolyte. The LSM-YSZ electrode degrades quickly at high η where material depletion and cracking occurs near the electrode/electrolyte interface. The η at which the electrode degrades measurably seems to agree with the oxygen bubble nucleation theory proposed by Virkar. In the low η regime where degradation in the total resistance is not measurable, more subtle changes in the EIS occur and may be due to a slower degradation mechanism, possibly involving the rearrangement of LSM. In the LSCF on GDC electrode, degradation occurs at lower η than would be predicted by Virkar's theory. FIB-SEM reconstructions showed microstructural changes, but an ALS model analysis showed that the observed changes cannot account for the changes in polarization resistance. The degradation in LSCF at low η must come from a combination of the microstructural changes and a change in k_{chem} , probably from Sr segregation. Increased J increased the rate of change in the polarization resistance. Preliminary data for the infiltrated LNO on LSGM system shows that the onset of degradation is near a current density of $1.0\text{A}/\text{cm}^2$ and an η of 0.2 V . This η value is close to that predicted by Virkar's theory, and is suggestive of the η controlled degradation mechanism, similar to the LSM-YSZ system. From these studies a few observations can be made about the stability of a current switched electrode:

- (1) Low polarization resistances are required to keep the overpotential below the critical value of $\sim 0.2\text{ V}$ at acceptable current densities. Good performance leads to better stability.

- (2) Slow changes in the LSM-YSZ electrode take place even at nominally stable conditions and may or may not be problematic at very long operation times
- (3) In the case of LSCF, J promoted microchemical and microstructural changes occur even at low overpotentials, but may be sufficiently stable if J is kept at low enough levels because the critical η is not reached.
- (4) Rare earth nickelate materials are a promising direction as they provide good chemical stability compared to alkaline earth doped perovskites and offer low polarization resistances.
- (5) Increases in ohmic resistance above the predicted critical overpotential are indicative of oxygen bubble precipitation and cracking. This is a hard limit on the stable operating conditions of an SOC.

Chapter 7: Development and analysis of a combined electrochemical-coarsening model to describe degradation in nano-infiltrated electrodes

7.1 Acknowledgement and Note on the Context of this Chapter

Material and argumentation from this chapter also appears in the journal *Physical Chemistry Chemical Physics* (2016). All of the symmetric devices discussed here were painstakingly fabricated by Dr. Ann V. Call, and all the accelerated electrochemical testing data was likewise collected by Dr. Call. My contribution here is a development of Dr. Call's thesis work. Here I present analysis using a refined model for the electrochemical-coarsening based on the transmission line model. The objective was to fit and interpret Dr. Call's data. Further I make predictions about the lifetime and performance of nano-infiltrated electrodes. FIB-SEM was collected by Hongqian (Sharon) Wang.

7.2 Introduction

Low-temperature solid oxide cells (LT-SOCs) aim to operate from 400 – 600 °C, versus the 750 – 850 °C range used in current state of the art solid oxide cells.²³⁰ This temperature decrease is widely viewed as being critical for more widespread applications in fuel conversion to electricity (fuel cells),^{41,231,232} electricity conversion to fuel (electrolysis),²³³ electricity storage (reversible cells),^{19,22} and chemical processing (catalytic membrane reactors and oxygen generators).^{19,22,234-236} The oxygen reduction reaction at the oxygen electrode is usually the process limiting operating temperature reductions. Thus, there has been considerable activity on the discovery, study, development, and application of oxygen electrodes usually mixed ionically and electronically conducting (MIEC) oxide materials; the focus has been almost entirely on oxygen transport properties – oxygen diffusivity and vapor-solid oxygen exchange rate.^{56,237-239}

Achieving good LT-SOC performance generally also requires high surface area achieved using nano-scale oxygen electrode morphology.^{122,182} While LT-SOC oxygen electrodes that perform well down to 500 °C and below have been achieved in this way,^{122,127} life testing has been limited to relatively short times (< 500 h) compared to typical desired device lifetimes of > 40,000 h. It is well known that nano-scale structures coarsen at elevated temperatures²⁴⁰, and even relatively short-term MIEC oxygen electrode tests have often shown substantial degradation.²⁴¹ In one study, the electrochemical performance degradation of $\text{La}_{0.6}\text{Sr}_{0.4}\text{Co}_{0.2}\text{Fe}_{0.8}\text{O}_3$ (LSCF) oxygen electrodes fabricated by wet-chemical impregnation (infiltration), a commonly-used method for producing nano-scale oxygen electrodes, was measured at temperatures higher than nominal operating temperatures in order to accelerate any degradation.²⁴² Coarsening-related degradation was observed over relatively short life-test times (200 – 500 h) and the amount of data was limited, such that it was possible to make only approximate predictions of long-term degradation.

Here we show the time- and temperature-dependent performance of a state-of-the-art nano-scale MIEC oxygen electrode – $\text{Sm}_{0.5}\text{Sr}_{0.5}\text{CoO}_3$ (SSC) infiltrated into a $\text{Ce}_{0.9}\text{Gd}_{0.1}\text{O}_2$ (GDC) scaffold. The experiments were designed to improve upon prior accelerated life tests by making more extensive measurements out to longer times (1500 h). Some of the tests were done within 100 °C of a nominal cell operating temperature of ~ 600 °C, with the aim of allowing more accurate long-term predictions. A model is developed that accounts for SSC coarsening in order to quantitatively fit measured electrode polarization resistance degradation. The model enables one of the first predictions of electrode stability over the ~ 40,000 h times desired for SOC operation, and shows that there are clear limits on the starting MIEC particle sizes, operating temperatures, and polarization resistance values that can be achieved while maintaining acceptable stability.

7.3 Experimental

7.3.1 Symmetric Cell Fabrication

$\text{Ce}_{0.9}\text{Gd}_{0.1}\text{O}_{2-\delta}$ (GDC) (Rhodia) was ball milled in ethanol for 24 hours, dried, and sieved (#1600). The GDC powder was then pressed into 19.0 mm diameter pellets weighing 500 mg each. The green bodies were then fired at 1450 °C for 6 hours to form the electrolyte supports. GDC (Rhodia) was mixed in 1:1.28 mass ratio Heraeus V-737 by three roll milling to form an ink. The GDC ink was screen printed onto the electrolyte pellets and fired at 1100 °C for 4 hours. The final scaffolds were ~20 microns in thickness, as measured by profilometry, with an area of 0.5 cm². A solution for infiltration was synthesized by mixing Sr, Sm, and Co nitrates in stoichiometric ratio (0.5:0.5:1 mol) in 18.2 MΩ millipore water such that the solution contained 2.73 mol/L metal ions. Citric acid was added as a chelating agent to 2% of the solution by mass. Excess solution was added to the scaffolds, masked using tape to prevent solution spillover onto the electrolyte surface to ensure both maximum infiltration per cycle and even distribution of particles through the entire depth of the electrode. The excess solution was wicked away from the electrode surface using a lint free wipe and the mask removed. Electrodes were fired at 800 °C for 0.5 hours for each infiltration cycle. Electrodes were weighed between infiltrations and infiltration cycles were repeated until the electrode weight corresponded to the desired volume percent SSC (*e.g.*, ~8 infiltrations for 20 vol% SSC). A current collecting layer of $(\text{La}_{0.8}\text{Sr}_{0.2})_{0.95}\text{MnO}_{3-\delta}$ was then screen printed onto the electrodes and fired at 800 °C for 2 hours. Silver grids and wires were affixed to the cells for electrochemical testing.

7.3.2 Electrochemical Testing

The present life tests were done at temperatures higher than normal operating temperature in order to accelerate degradation. Such acceleration of degradation is successfully practiced in cases where device lifetimes are too long to allow extensive full-life tests, such as in integrated circuits.²⁴³

Electrochemical testing was performed in lab air at 600 °C, the target oxygen electrode operating condition, in all cases, regardless of the aging temperature (700-800 °C). Figure 7.1 shows the life-test schedule, which was repeated every 48 h. Most of the time (46 h) was spent at the aging temperatures, with 2 h (~4% of the life-test cycle) devoted to ramping down the temperature, stabilizing, measurement, and then returning to the aging temperature. Electrochemical testing was performed in the frequency range 10^6 - 10^{-1} Hz using a Zahner IM6 electrochemical testing station.

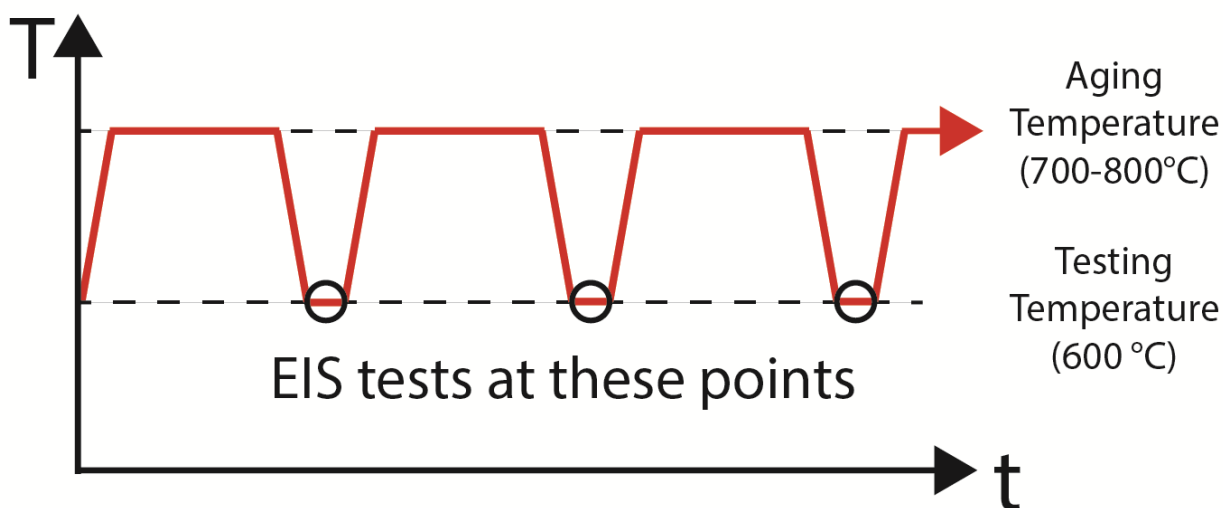


Figure 7.1. Illustration of the testing program used to collect EIS data during coarsening. The testing interruptions constituted ~4% of the total testing time, such that the cells were at the ageing temperature for ~ 96% of the testing time.

7.3.3 FIB-SEM

GDC scaffold samples without and with SSC were prepared for FIB-SEM serial sectioning by epoxy infiltration and mechanical polishing.^{51,164} The imaging was done on a FEI Helios and a dual-beam Zeiss 1540XB, with an accelerating voltage of 2 kV and the backscattered electron (BSE) detector because it provides optimal contrast between the epoxy-filled pores and the solid phase. Imaging segmentation and 3D reconstruction were done as described elsewhere.¹⁶⁴

7.4 Results and Discussion

The coarsening of nano-scale SSC particles is readily observed after ageing at elevated temperatures. Fig. 1 shows an example of SEM images taken from as-prepared SSC-infiltrated GDC scaffolds and after ageing at 800°C for 400 and 1471 h. The increase in size is clear. Analysis of the images indicates that the average size, 50 nm initially, increased to 65 nm after 400h and 173 nm after 1500 h ageing.

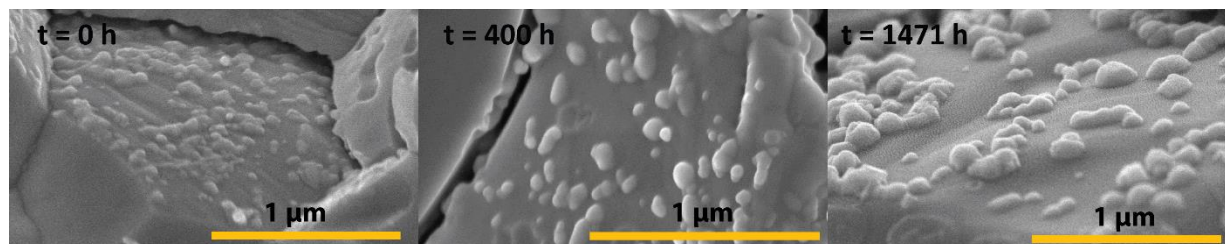


Figure 7.2. SEM images of $\text{Sm}_{0.5}\text{Sr}_{0.5}\text{CoO}_3$ (SSC) particles on Gd-doped Ceria (GDC) surfaces taken for ageing times $t = 0$ h (the as-prepared cathode), $t = 400$ h, and $t = 1500$ h at 800 °C. These images were taken at a flat portion of the GDC electrolyte at the electrode/electrolyte interface; this was done because it was not possible to resolve the SSC particles within the electrode via either contrast or size differences.

Imaging of the infiltrated oxygen electrodes was also carried out using FIB-SEM serial sectioning. Figure 7.3 shows typical 2D sections, for the GDC scaffold alone and also a GDC scaffold infiltrated with SSC.

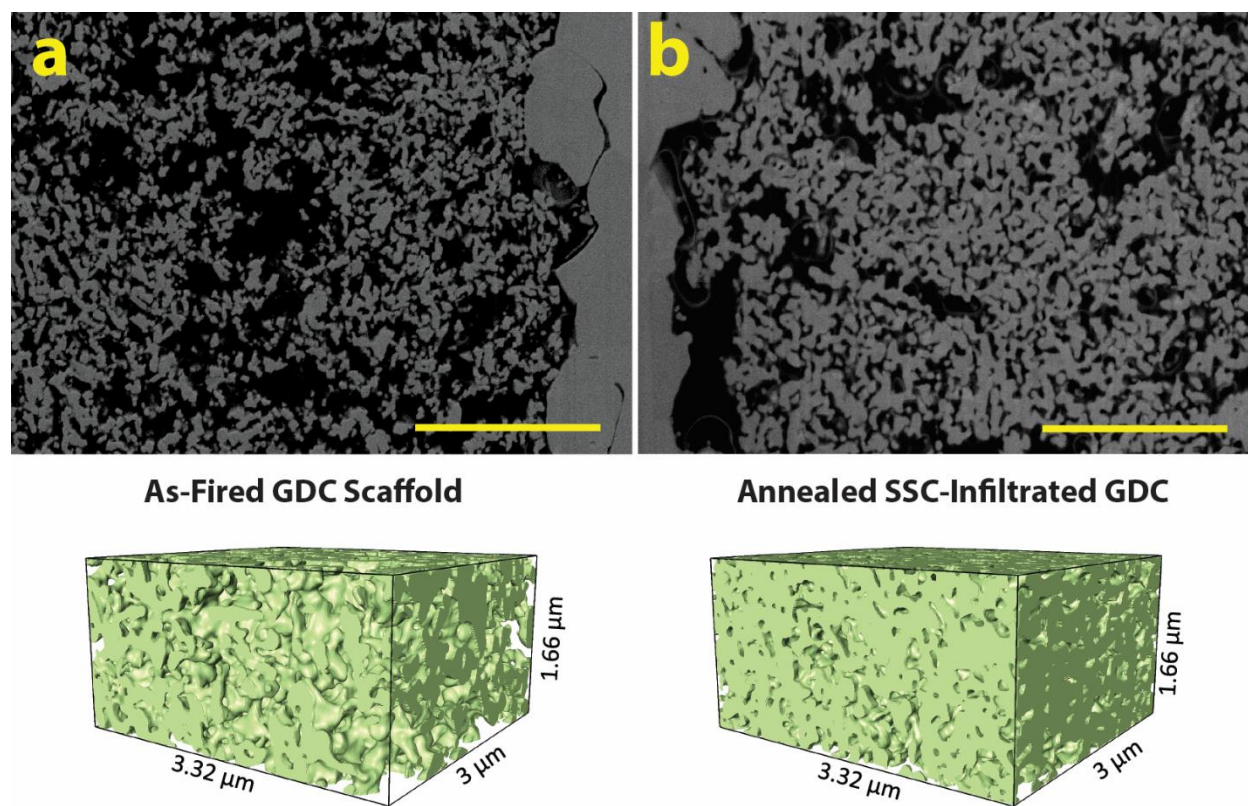


Figure 7.3. Cross-sectional SEM images and FIB-SEM 3D reconstructions of GDC scaffold (A) and GDC scaffold infiltrated with SSC (B). The GDC electrolyte is on the right side in A, and the left side in B. Samples were prepared for imaging by FIB polishing and epoxy infiltration. The solid fraction is displayed in green while the pore fraction is transparent. Note that the 3D views show smaller regions cropped from the full reconstruction volumes, for clarity. Scale bars are 3 μm .

The SSC is not distinguishable from the GDC scaffold by contrast, however, the cross section shows a smaller pore fraction and a less fine structure which is distinguishable due to the contrast difference between the ceramic materials and the epoxy infiltrated pores.^{51,164} The SSC particle size in these electrodes is too small, relative to the FIB-SEM resolution of ~ 20 nm, to allow accurate segmentation and 3D reconstruction of the oxygen electrode structure. However, it was possible to estimate averaged microstructural parameters, as shown in Table 7.1 and from the 3D FIB-SEM reconstruction (Table 7.2) the measured change in porosity between pristine and infiltrated scaffolds agrees with the $\sim 20\%$ volume change from adding SSC.

Table 7.1. Average SSC particle sizes estimated from SEM images of as-prepared electrodes and electrodes coarsened at 800 $^{\circ}\text{C}$

Temperature 800 $^{\circ}\text{C}$	
Time	Size
0	50 nm
400	65 nm
1500	173 nm

Table 7.2. Cathode microstructural parameters obtained from 3D tomographic reconstructions, as shown in the representative images in Figure 7.3.

Sample	GDC Scaffold As Fired	SSC-GDC Annealed
Porosity (%)	53.88	33.44
Particle Surface Area per Electrode Volume (μm^{-1})	7.56	8.85
Particle Specific Surface Area (μm^{-1})	16.39	13.30

Figure 7.5 summarizes the results of electrochemical impedance spectroscopy (EIS) measurements carried out during life tests of five different but identically-prepared symmetric cells. While the ageing was done at temperatures of 700, 750, or 800 °C, the EIS measurements were all done during short interruptions where the temperature was reduced to 600 °C, a typical IT-SOC operating temperature. The ageing/measurement cycle is shown schematically in figure 7.1. Figure 7.4 shows typical EIS spectra taken early and late in the life test done at 800 °C; the oxygen electrode polarization resistance R_P values shown in figure 7.5 were obtained from the difference between the real-axis intercepts in the Nyquist plots in figure 7.4. The samples all showed the same initial oxygen electrode polarization resistance R_P value, within ~ 10%, showing the good cell-to-cell reproducibility. Each of the life tests shown in figure 7.5 shows an increase in R_P with time. At 800 °C, the initially fast resistance increase slows gradually during the life test. At lower temperatures, the rate of increase is less, and remains essentially constant throughout the test. The two cells life tested at 800 °C showed excellent agreement. The two samples life tested at 700 °C degraded at approximately the same rate, but with a slight offset of their initial R_P values.

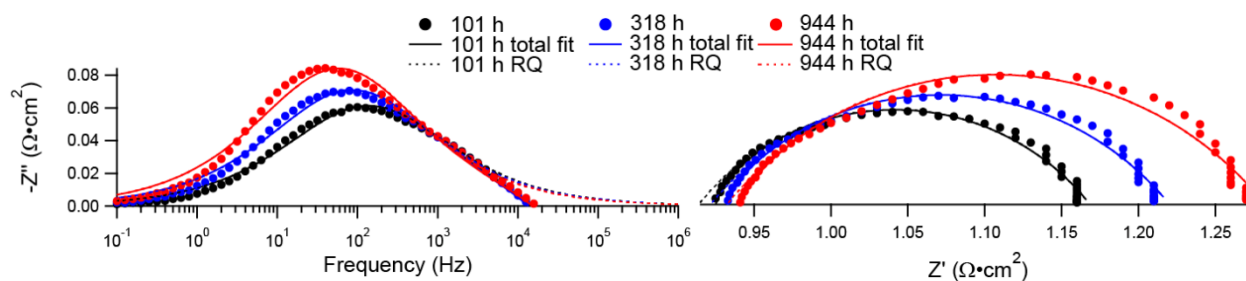


Figure 7.4. Bode and Nyquist plots of EIS data taken at different times during a life test of an SSC-GDC electrode aged at 800 °C and measured EIS tested at 600 °C in air. There appears to be one dominant response, initially centered at ~ 100 Hz. The results illustrate the steady increase in cathode polarization resistance with increasing time, along with a slight shift to lower frequency. The shape of the cathode response did not change appreciably during the life tests. The cathode polarization resistance values shown in Figures 2 and S7 were obtained as the difference between the real-axis intercepts in the Nyquist plots. Circuit model fits are also shown from an L-R-RQ equivalent circuit showing both the total fit and the RQ element. The difference between the high frequency intercept and the calculated RQ intercept is on the order of 1% difference.

The results in Figures 7.2 and 7.5 can both be explained by particle coarsening models that have been successfully applied to a range of materials, including catalyst nano-particles on oxide supports.²⁴⁴⁻²⁴⁶ In the present model, only the SSC coarsening is considered, because it is primarily the SSC surface area that determines R_p . The GDC backbone presumably evolves much less than the SSC because of its larger particle size and higher melting point; furthermore, any changes are not expected to greatly impact the role that GDC plays in the electrode – oxygen ion transport

between the electrolyte and the SSC. Coarsening data are usually fit using a power-law expression where the SSC feature size l_C grows with time t from an initial size $l_{C,0}$:²⁴²

(Equation 7.1)

$$l_C^n - l_{C,0}^n = K_D t$$

where t is time and n is the power.²⁴⁴ K_D is proportional to a cation diffusion coefficient:

(Equation 7.2)

$$K_D = K_{D,0} \exp(-E_D/kT)$$

where E_D is an activation energy, $K_{D,0}$ is a pre-factor, k is Boltzmann's constant, and T is the ageing temperature.

The feature size and other information on microstructure and materials properties can be related to R_P using a porous electrode theory expression obtained using the transmission-line model.²⁴⁷⁻²⁵¹

The expression has been successfully applied to infiltrated composite electrodes previously.²⁵⁰

The effective interfacial resistance is expressed in terms of the MIEC surface resistance R_S and surface area a , whereas the ion transport resistance is included as the effective ionic conductivity σ_{ion} of the oxide scaffold (GDC), yielding:

(Equation 7.3)

$$R_P = \sqrt{\frac{R_S}{\sigma_{ion} a}} \coth \left(L \sqrt{\frac{a}{\sigma_{ion} R_S}} \right)$$

Where L is the electrode thickness. In the limit where the argument of the \coth function is large, e.g., L and a are large, $\coth(x) \rightarrow 1$ and the oxygen electrode ASR varies as $(R_S/\sigma_{ion} a)^{-1/2}$. However, in the limit where the argument is small (thin electrode limit), $\coth(x) \rightarrow 1/x$, such that the oxygen electrode ASR varies as (R_S/aL) . This latter limit was used previously in fitting LSCF degradation data,²⁴² but here the more accurate full expression (eq. 7.3) is utilized (See Figure 7.12).

The SSC surface area a can be related directly to the feature size via the relation $a = fC/l_C$, where C is the surface to volume shape factor ratio that depends on the geometry of the SSC infiltrate particles²⁵², typically ~ 6 for a hemispherical cap, and f is the SSC volume fraction. Combining this expression with eq. 1 and substituting into eq. 3 yields the time dependence of the resistance:

(Equation 7.4)

$$R_P = \sqrt{\frac{R_S}{\sigma_{ion} Cf}} (l_{C,0}^n + K_D t)^{1/2n} \coth \left(L (l_{C,0}^n + K_D t)^{-1/2n} \sqrt{\frac{Cf}{\sigma_{ion} R_S}} \right)$$

Since the EIS measurements were always done at 600 °C, the values in eq. 4 that relate to electrode function were taken for this temperature, *i.e.*, $R_S(\text{SSC}) = 25 \cdot \Omega \text{ cm}^2$ ¹²⁷ and $\sigma_{ion}(\text{GDC}) = 0.0024 \text{ S/cm}$. The latter value is an effective conductivity, taken to be less than the conductivity of sintered sub-micron GDC at 600 °C (0.007 S/cm²⁵³), accounting for a oxygen electrode GDC solid fraction of 0.46 and a tortuosity factor of 1.29 as determined by FIB-SEM (Table 7.2). The values of C , ~ 6 , and f , ~ 0.2 , were allowed to vary somewhat for each cell corresponding to sample-to-sample variations in SSC particle shape and volume fraction, respectively.

Equation 7.4 yields good fits to the time- and temperature-dependent polarization resistance data. Best fits were obtained with $n = 4$, a value expected if cation transport takes place via surface diffusion.^{157,158} Figure 7.5 shows the overall best fit to the data that was obtained with the values $l_{C,0} = 50$ nm, $E_D = 2.81$ eV, and $K_{D,0} = 1.85 \times 10^{-13}$ cm/s. In order to probe the quality of the fitting results, a range of $K_{D,0}$ and E_D values were used, up to a point where the quality of fit χ^2 value increased by 10% above the optimal fit value. This yielded fit values that ranged from $E_D = 2.60$ eV and $K_{D,0} = 1.77 \times 10^{-14}$ cm/s at one extreme, to $E_D = 2.92$ eV and $K_{D,0} = 6.50 \times 10^{-13}$ cm/s at the other. Figure 7.5 shows the range of these fits as shaded regions. Note that life test data taken at different SSC loadings was also fit well using the same model, as shown in figure 7.6.

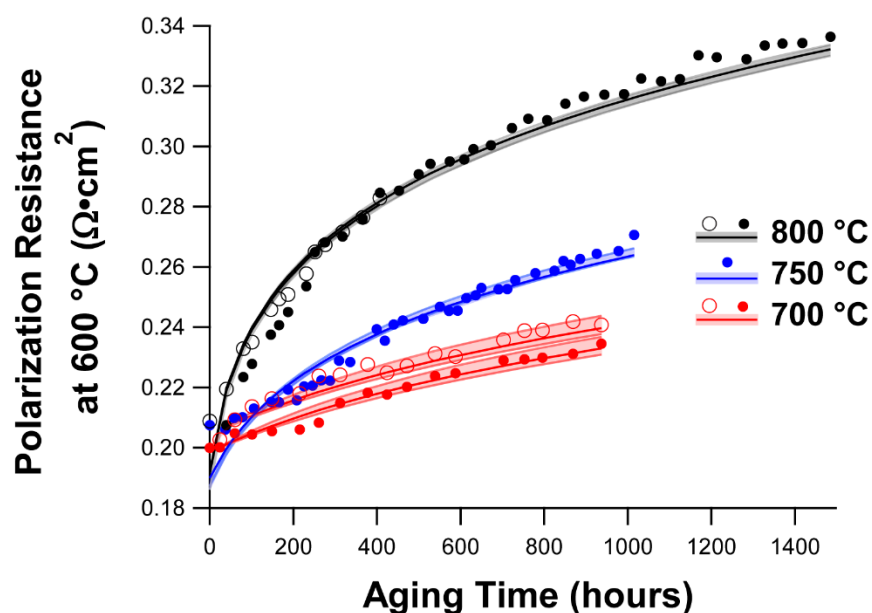


Figure 7.5 Oxygen electrode polarization resistance of SSC-infiltrated symmetric cells, taken from EIS data measured in air at 600 °C (see Figure 7.1), versus ageing time at various temperatures. Also shown are the overall best fits to the data using eq. 4 with the parameters given in Table S3. The slight cell-to-cell variations in the initial resistance were modeled by assuming slight

variations in the initial oxygen electrode, *i.e.*, the SSC volume fraction f and particle shape factor ratio C . Note that the fits to the two 800 °C aged cells were essentially identical, and so only one curve is visible. Solid curves indicate predictions using best fit values, while the broader shading indicates predictions for the range of $K_{D,0}$ and E_D values that provide good overall quality of fit.

The model fits above also indicate the particle coarsening that occurs during the life tests; the corresponding time-dependent particle size is readily obtained by inserting the fitted values into eqs. 7.1 and 7.2. For example, after 400 h at 800 °C, the predicted SSC particle size increase from 50nm is to 113 nm and after 1500 h to 156 nm. These values are in reasonable agreement with the particle sizes estimated from the images in Figs. 7.2 and 7.3, where the particle size increased from ~ 50 to 65 and 173 nm, respectively. Moreover, equation 7.3 can yield active surface area if the resistance is known at a particular time point, for example: after 1500 hours at 800 °C and 20% SSC loading, the model predicts $9.66 \mu\text{m}^{-1}$.

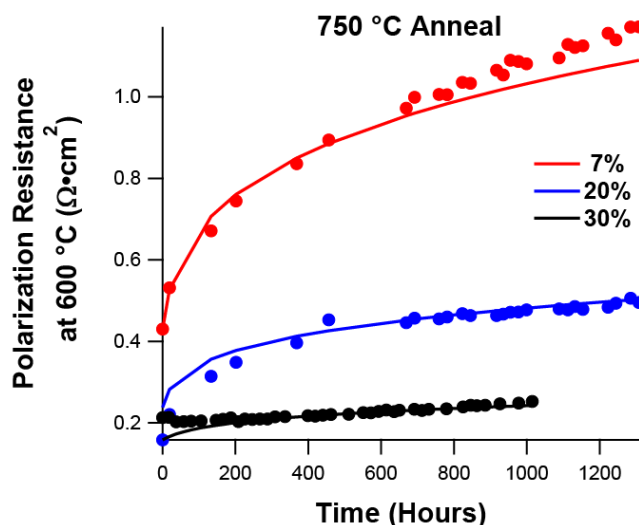


Figure 7.6. Oxygen electrode polarization resistance of SSC-infiltrated symmetric cells with different SSC volume fractions f , taken from EIS data measured in air at 600 °C (see Figure 7.4),

versus ageing time at 750 °C. Also shown are the overall best fits to the data using eq. 4 with the $K_{D,0}$ and E_D values given in Table 7.3; other parameters were slightly different from those used in Figure 7.5, presumably because these measurements were made on a different batch of cells. For the $f = 30\%$ electrode, a larger initial feature size $l_{c,0} = 70$ nm instead of 50 nm – was used accounting for a tendency for infiltrated particles to overlap at high SSC loading, leading to larger effective feature sizes.

The same model is applicable to other materials. To show this, eq. 7.4 was fitted to the $R_{P,C}$ vs time data previously reported for LSCF-infiltrated GDC oxygen electrodes. The fit to the data, shown in Figure 7.7, is reasonably good, and the resulting parameters are similar to those for SSC (Table 7.3). This is not surprising given the similarity in the properties of SSC and LSCF. Note that the fits here are different than those obtained using a similar coarsening model in Ref.²⁴². The main difference is that the full expression for R_P (eq. 7.3) is used here, whereas in the prior report the relatively poor thin electrode limit approximation, $R_{P,C} = (R_S/aL)$, was used.

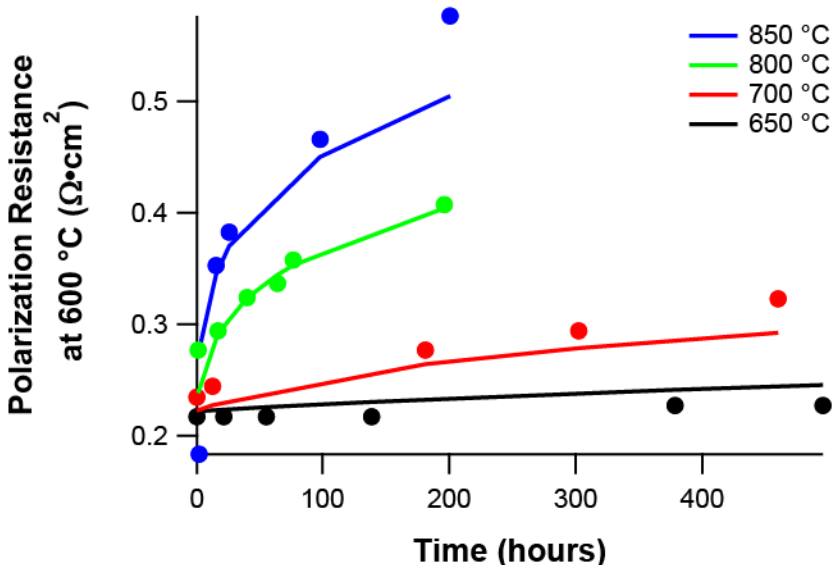


Figure 7.7. Oxygen electrode polarization resistance of LSCF-infiltrated symmetric cells aged at temperatures ranging from 650-850 °C taken from EIS data measured in air at 600 °C (see Figure 7.1), (from Ref¹⁶⁰). Also shown are the overall best fits to the data using eq. 7.4 with the $K_{D,0}$ and E_D values given in Table 7.3.

The model is used to make predictions of expected oxygen electrode performance for extended times under various conditions. Unlike Fig. 7.5 where the cell is maintained at higher temperatures to accelerate degradation but the resistance is measured at 600 °C, the predictions shown below are for a more conventional case – continuous cell operation at a fixed temperature. Figure 7.8 shows an example – the predicted R_P versus time for a cell operated at 600 °C with varying SSC particle sizes. The ranges shown as shaded regions indicate the variability in the predicted values based on the fitting variability shown in Figure 7.5. Reducing the size below 50 nm yields a substantial decrease in initial R_P , well below $0.2 \Omega\cdot\text{cm}^2$, but the coarsening is much faster, such that particle size and R_P increase rapidly in the first 10,000 h. In fact, after 10,000 h operation,

nearly the same particle size and R_P values are reached regardless of starting particle size below 50 nm.

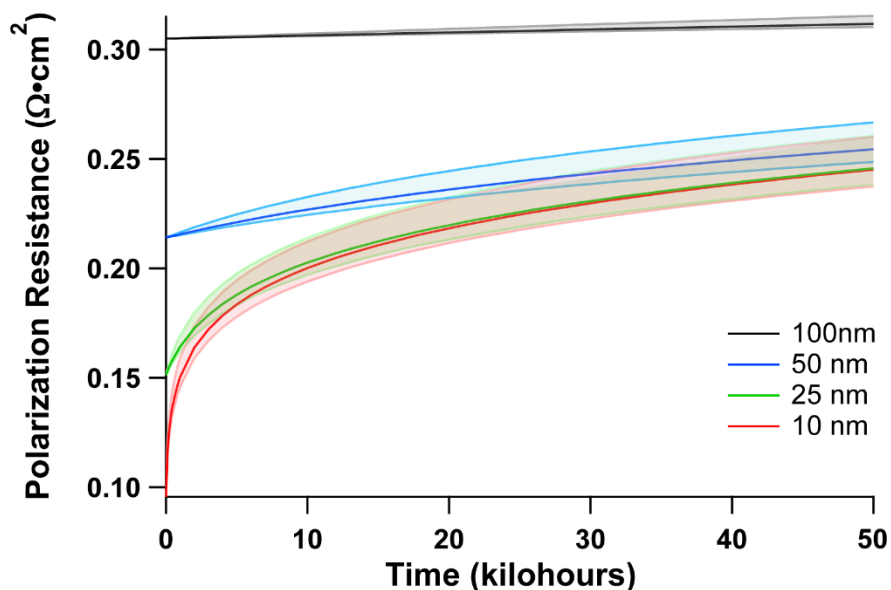


Figure 7.8. Predicted polarization resistance versus time for oxygen electrodes with initial SSC particle sizes of 10, 25, 50, and 100 nm, operated at a temperature of 600 °C. Solid curves indicate predictions using best fit values while the broader shading indicates predictions for the range of $K_{D,0}$ and E_D values that provide good overall quality of fit.

Figure 7.9 illustrates the pronounced effect of starting particle size on stability in a different way; there, the initial SSC particle size was varied in order to achieve initial R_P values of 0.2 or 0.1 $\Omega\cdot\text{cm}^2$, for cells operating at different temperatures. Oxygen electrodes designed to achieve low R_P at lower operating temperatures required smaller particle sizes, resulting in more rapid degradation.

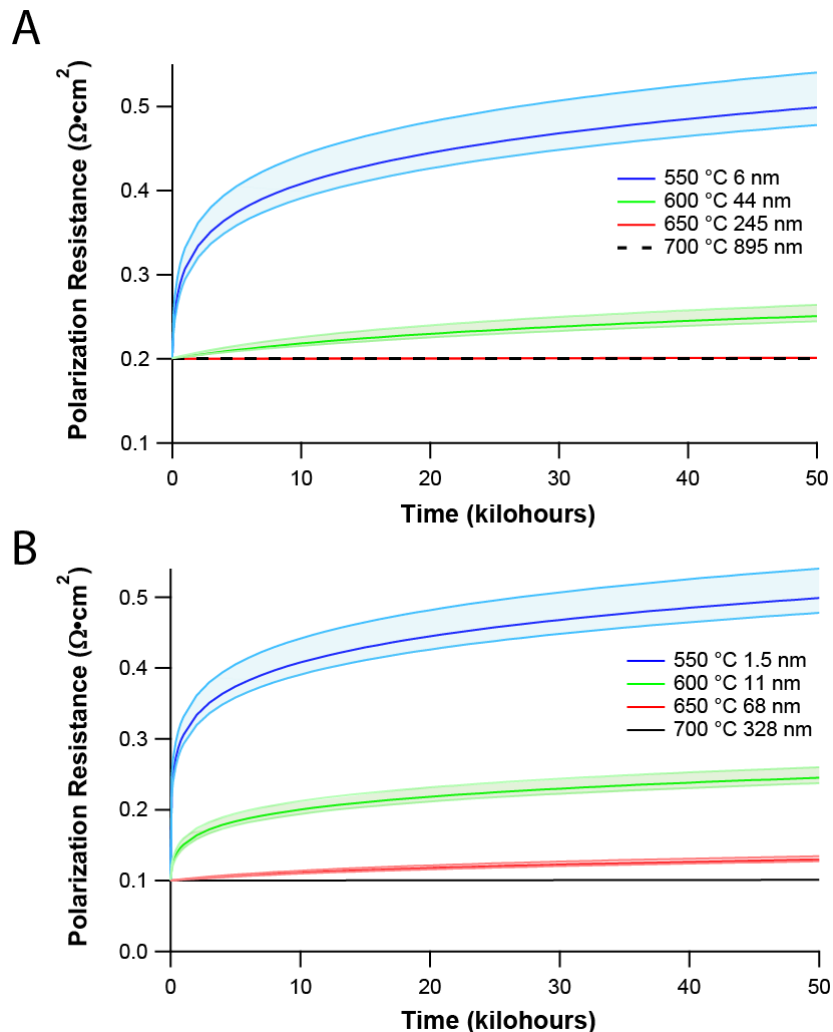


Figure 7.9. Predicted polarization resistance versus time for infiltrated SSC-GDC oxygen electrodes designed to yield a particular initial resistance; the initial cathode SSC feature size was chosen for each operating temperature in order to achieve an initial R_p of (a) $0.2 \Omega \cdot \text{cm}^2$ or (b) $0.1 \Omega \cdot \text{cm}^2$. This illustrates that the decrease in operating temperature that can be realized via reduction of cathode MIEC particle size is ultimately limited by excessive coarsening. Solid curves indicate predictions using best fit values, while the broader shading indicates predictions for the range of $K_{D,0}$ and E_D values that provide reasonable fits, as described in Figure 7.5.

These observations suggest dual criteria for infiltrated oxygen electrodes – the R_p value should be less than some acceptable value, e.g., 0.1 or 0.2 $\Omega\cdot\text{cm}^2$, and the degradation rate should be less than an acceptable value, e.g., 0.2 or 0.5 % resistance increase per kh of operation²⁵⁴. Figure 7.10 shows a combined plot of these criteria with the less stringent (0.5%/kh) degradation requirements related to the U.S. Department of Energy 2015 targets for stationary power and the more stringent requirements (0.2%/kh) being stricter than the 2020 targets (0.3%/kh)²⁵⁴. The blue curves show the initial particle size above which degradation rate is < 0.5%/kh (< 0.2%/kh) over 50,000 h, versus operating temperature. The red curve shows initial particle size below which the initial R_p value is < 0.2 $\Omega\cdot\text{cm}^2$ (<0.1 $\Omega\cdot\text{cm}^2$), versus operating temperature. A suitable oxygen electrode must satisfy both criteria, and hence must fall in the range of temperatures and particle sizes indicated by the shaded region in Figure 7.10. That is, these infiltrated SSC-GDC electrodes are useful only for operating temperatures > 590 °C, and for starting particle size > 40 nm. For the lower resistance and degradation rate targets, the minimum operating temperature is 670 °C and the minimum starting size is > 100 nm.

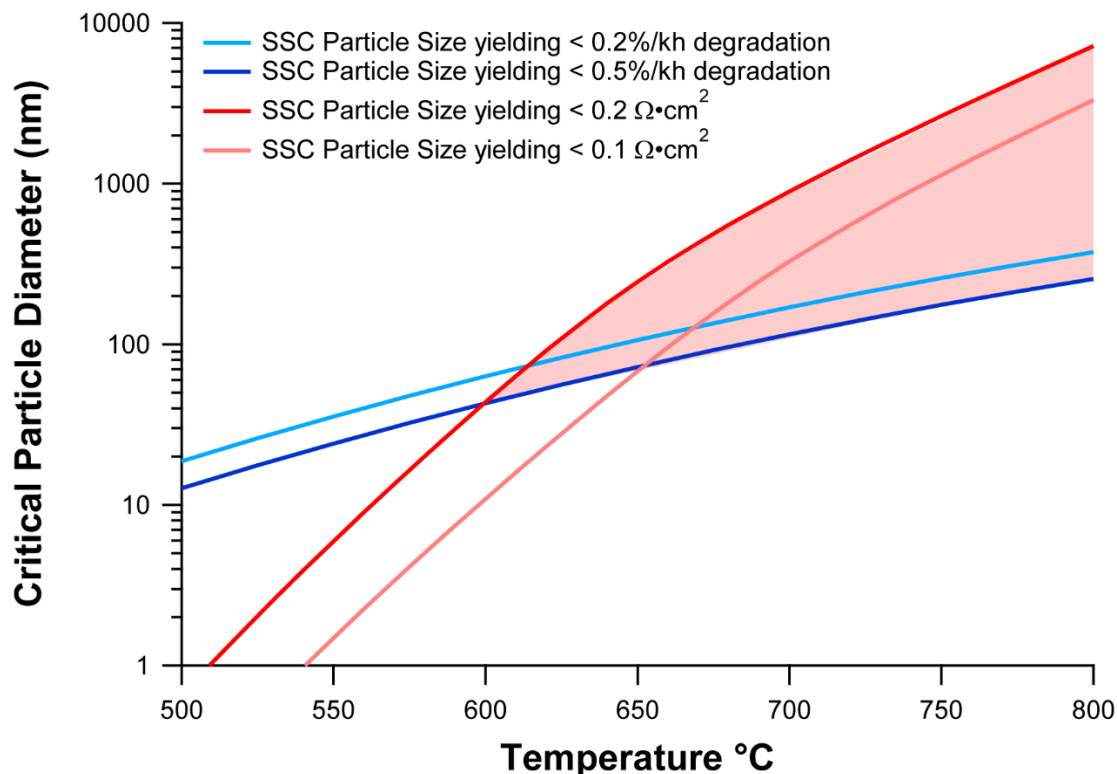


Figure 7.10 A plot of critical SSC particle diameters that provide target performance and stability values, versus cell operating temperature. The red curves show the diameter yielding target oxygen electrode resistance values of $R_p^T = 0.2$ or $0.1 \Omega\cdot\text{cm}^2$. The blue curves show the diameter yielding target degradation rate $\left(\frac{1}{R_p} \left(\frac{dR_p}{dt} \right) = 0.5 \text{ or } 0.2 \text{ %/kh} \right)$. The shaded area shows the SSC particle sizes and cell operating temperatures that yield the desired stability and performance; for clarity, the shading is shown only for the target values $R_p^T \leq 0.2 \Omega\cdot\text{cm}^2$ and $\frac{1}{R_p} \left(\frac{dR_p}{dt} \right) \leq 0.5 \text{ %/kh}$.

A similar plot based on fits the LSCF accelerated test data is shown in Figure 7.11. The curves again have similar meaning, but the higher surface resistance for LSCF ($28.5 \Omega\cdot\text{cm}^2$ at $600 \text{ }^\circ\text{C}$ versus $25 \Omega\cdot\text{cm}^2$ for SSC) and different K_D and E_D values (Table S3) narrows the range of

usefulness for this material compared to SSC. The model predicts the infiltrated LSCF electrode will be useful operating only above 595 °C with an initial particle size of >40 nm.

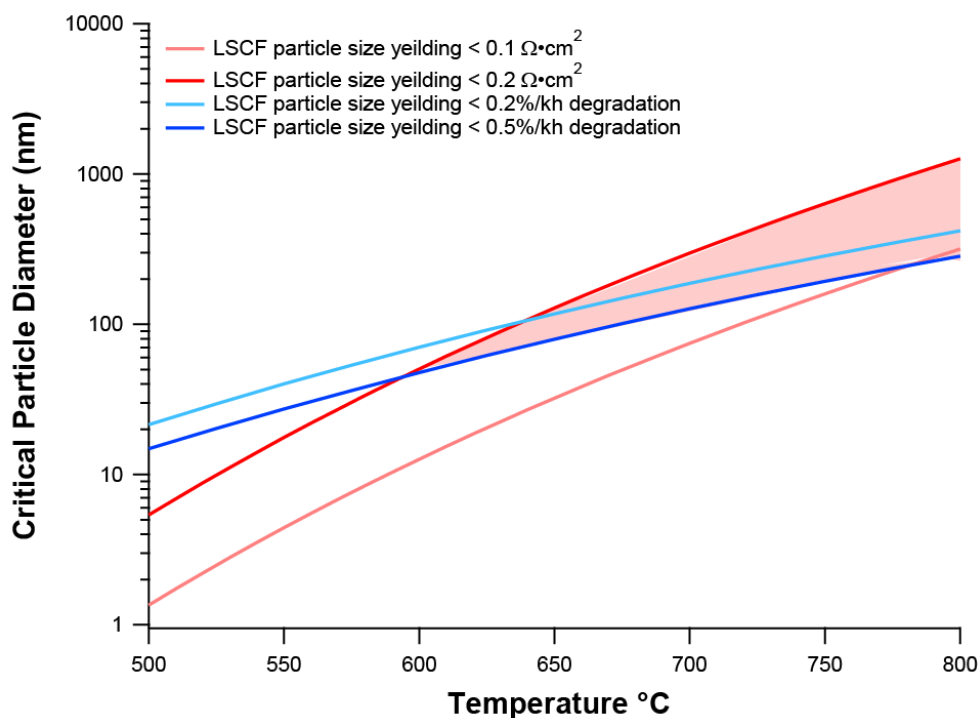


Figure 7.11. A plot of critical LSCF particle diameters that provide target performance and stability values, versus cell operating temperature. The red curves show the diameter yielding target cathode resistance values of $R_p^T = 0.2$ or $0.1 \Omega \cdot \text{cm}^2$. The blue curves show the diameter yielding target degradation rate $\left(\frac{1}{R_p} \left(\frac{dR_p}{dt}\right)\right) = 0.5$ or $0.2 \%/ \text{kh}$. The shaded area shows the LSCF particle sizes and cell operating temperatures that yield the desired stability and performance; for clarity, the shading is shown only for the target values $R_p^T \leq 0.2 \Omega \cdot \text{cm}^2$ and $\left(\frac{1}{R_p} \left(\frac{dR_p}{dt}\right)\right) \leq 0.5 \%/ \text{kh}$. Note that coarsening data for infiltrated LSCF is sparser than for SSC, so these predictions have greater uncertainty than those shown in Figure 4.

These results for SSC, combined with prior similar results for LSCF oxygen electrodes, suggest the generality of coarsening processes in this class of materials. The quantitative predictions described above are only valid for infiltrated SSC-GDC and LSCF-GDC oxygen electrodes. It seems likely, however, that other compositions consisting of an MIEC infiltrated into an ionically-conducting scaffold will exhibit qualitatively similar behavior. Structural differences between different oxygen electrodes can be expected to affect long-term degradation behavior. For example, co-infiltration of GDC with LSCF has been shown to reduce degradation rate,²⁵⁵ presumably because more-stable GDC particles, which are interspersed amongst the LSCF particles, will tend to constrain the LSCF coarsening. Similarly, atomic-layer deposition of thin ZrO_2 layers over infiltrated LSC has been shown to suppress degradation.²⁵⁶ As a first approximation, these structural changes can be assumed to slow coarsening kinetics by reducing the $K_{D,0}$ term in eq. 7.2. In this case, the main effect is a shift of the blue curve in Figure 7.10 downwards, allowing smaller particle sizes and lower useful operating temperatures. Nonetheless, the same basic coarsening process will ultimately limit the degree to which particle size and operating temperature can be decreased.

It should be noted that other mechanisms may also play a role in oxygen electrode degradation. For example, the present model calculates the resistance considering only the decrease in MIEC surface area, ignoring the possible loss of electronic percolation during coarsening. Furthermore, Sr segregation has been observed to degrade MIEC electrode performance over time.²⁵⁷⁻²⁵⁹ However, the observation that increases in R_P correlate quantitatively with increases in SSC particle size provides strong evidence that coarsening is the primary mechanism here.

Furthermore, the present results show that coarsening is fast, and hence is likely to be the dominant degradation mechanism. The results in Figure 7.8 suggest that this will be the case not only for the present ~ 50 nm particles but also for other MIEC electrodes with small enough particle sizes. For larger particle sizes, such as in conventional ~ 500 -nm-scale SOFC electrodes, coarsening should be very slow such that other degradation mechanisms may become dominant.

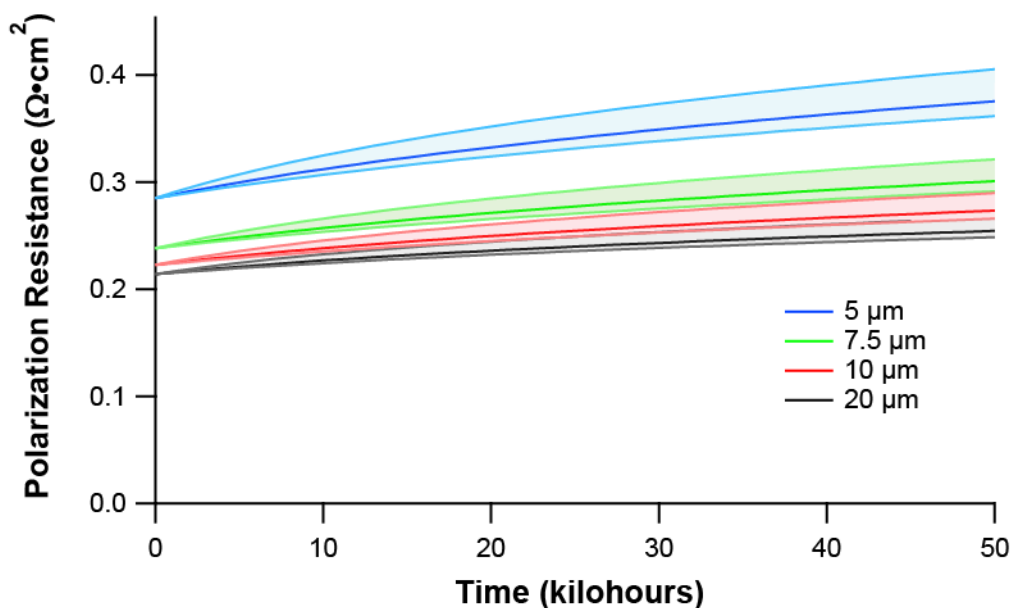


Figure 7.12. Predicted resistance versus time for infiltrated SSC-GDC electrodes operated at a temperature of 600 °C, for a SSC particle size of 50 nm and electrode thicknesses of 5 , 7.5 , 10 , and 20 μm . Note that the resistance does not decrease measurably further when the thickness is increased above 20 μm . This illustrates that thickness has relatively little effect on long-term stability, and that most of the electrochemical processes occur in a cathode region within 10 μm of the electrolyte.

These results represent the first example of SOFC oxygen electrode data and modeling leading to quantitative long-term stability predictions; however, further tests to validate the quantitative predictions are needed. On the other hand, the qualitative trends demonstrated here have a critical implication for the development of SOFC oxygen electrode materials: oxygen electrode long-term stability, particularly coarsening kinetics, must be considered together with oxygen transport properties to select optimal oxygen electrode materials. This can be seen by considering eq. 7.3, which shows that the electrode resistance depends not only on oxygen surface exchange rate, *i.e.*, surface resistance R_s , and oxygen conductivity σ_{ion} , but also on the electrode surface area a . For the present infiltrated oxygen electrodes, where σ_{ion} is associated with the fast-ion-conducting GDC scaffold, it is the ratio R_s/a of the infiltrated MIEC material in eq. 7.3 that determines R_p . (For porous single-phase MIEC electrodes, the MIEC oxygen ion conductivity also plays an important role.) As shown by the present results, the value of a has important implications on long-term stability. For example, a material with inferior oxygen exchange rate might be a superior oxygen electrode if it is characterized by slower coarsening kinetics, allowing a higher surface area a without coarsening. Experimental and theoretical studies of oxygen electrode materials have mostly ignored coarsening kinetics, focusing entirely on oxygen transport properties, *i.e.* oxygen surface exchange rate and oxygen diffusivity/conductivity.^{60,237} This approach could miss useful materials or promote non-viable materials, so a figure of merit should be developed to compare potential electrode materials.

Equation 7.4 can be used to obtain an expression for the resistance degradation rate, $\frac{1}{R_p} \left(\frac{dR_p}{dt} \right)$. The thick electrode limit in eq. 7.4 is used since it provides the best performance (lowest R_p) for any

given oxygen electrode material, and is readily reached for typical electrode thicknesses of ~ 20 μm (see Figure 7.12). Taking the time derivative of R_p yields

(Equation 7.5)

$$\frac{1}{R_p} \left(\frac{dR_p}{dt} \right) = \frac{1}{8(t + l_{c,0}^4/K_D)}$$

This illustrates that the degradation rate increases with the rate of cation diffusion K_D , and increases with decreasing initial infiltrate particle size $l_{c,0}$, as seen for example in Figure 7.8. A more practical expression can be developed by noting that one typically requires a target oxygen electrode resistance R_p^T to achieve desired cell power density. Using the value R_p^T , with $t = 0$ for simplicity, and again using eq. 7.4 in the thick-electrode limit, yields

(Equation 7.6)

$$R_p^T = \sqrt{\frac{R_S l_{c,0}}{\sigma_{ion} C f}}$$

Solving eq. 7.6 for $l_{c,0}$ and substituting into eq. 7.5 with $t = 0$ yields the initial degradation rate for an initial particle size that yields the desired R_p^T :

(Equation 7.7)

$$\frac{1}{R_p} \left(\frac{dR_p}{dt} \right)_{t=0} = \frac{K_D R_S^4}{8 (R_{p,C}^T)^8 \sigma_{ion}^4 C^4 f^4}$$

This shows that minimizing the MIEC surface resistance and maximizing the conductivity of the ionically-conducting phase are very important for minimizing degradation rate, but that cation

diffusion kinetics also play an important role. Note that the initial degradation rate is a good approximation of the long-term degradation in cases where degradation rate is relatively low (see, for example, Figure 7.8); these are, of course, the cases that are of actual practical interest.

Since the aim of oxygen electrode development is typically to minimize cell operating temperature, it is instructive to introduce the temperature dependences of the transport properties, *i.e.*, $K_D = K_{D,0} \exp(-E_D/kT)$, $R_S = R_{S,0} \exp(E_S/kT)$, and $\sigma_{ion} = \sigma_{i,0} \exp(-E_i/kT)$, where E_D is the activation energy for cation diffusion, E_S is the activation energy of the MIEC surface resistance, and E_i is the activation energy of the oxygen ion conductivity. Substituting these into eq. 7.7 and gathering the temperature-dependent terms yields:

(Equation 7.8)

$$\frac{1}{R_P} \left(\frac{dR_P}{dt} \right)_{t=0} = \frac{K_{D,0} R_{S,0}^4}{8 (R_{P,C}^T)^8 \sigma_0^4 C^4 f^4} e^{(4E_S + 4E_i - E_D)/kT}$$

Or,

(Equation 7.9)

$$\frac{1}{R_P} \left(\frac{dR_P}{dt} \right)_{t=0} \propto K_D \left(\frac{R_S}{\sigma_{ion}} \right)^4 \propto e^{(4E_S + 4E_i - E_D)/kT}$$

The term $K_D \left(\frac{R_S}{\sigma_{ion}} \right)^4$ is a figure of merit for an oxygen electrode to achieve both low polarization resistance and low degradation rate. For the present case of composite cathodes, K_D and R_S refer to the MIEC phase and σ_{ion} refers to the ionic conductor phase. For the case of a single-phase

MIEC oxygen electrode, the MIEC plays both roles such that σ_{ion} is a property of the MIEC. The argument in the exponential term in eq. 7.8 should be positive in all cases. In the case of SSC, for example, $E_S \sim 1.5$ eV, $E_i \sim 0.6$ eV for GDC, and $E_D = 2.81$ eV from the present results. Thus, the overall activation energy in the exponential term is ~ 5 eV, such that eq. 7.8 predicts a rapid increase in degradation rate with decreasing temperature. Although this result may seem counter-intuitive at first glance, it is reasonable considering that it arises from the constraint of maintaining a target oxygen electrode resistance - this requires much smaller oxygen electrode feature sizes as temperature decreases. Note that eq. 7.8 gives the initial slopes of the degradation rates shown in Figure 7.9. Comparison of Figures 7.9 (a) and (b) shows the strong increase in degradation rate with decreasing target oxygen electrode resistance R_p^T ; as indicated in eq. 7.6, a factor of 2 decrease in R_p^T necessitates a four-fold decrease in initial feature size, exacerbating coarsening. Finally, the key conclusion based on eq. 7.8 is that the activation energies for cation diffusion, in addition to those for oxygen transport, are important criteria in achieving low-temperature oxygen electrode that provides both low polarization resistance and low degradation rate.

Table 7.3. Model Parameters determined by fitting degradation data for SSC and LSCF oxygen electrodes

Sample	SSC	LSCF
E_d (eV)	2.81	2.90
$K_{D,0}$ (cm ² /s)	1.85×10^{-13}	8.98×10^{-13}
R^s at 600 °C ($\Omega \cdot \text{cm}^2$)	25	28.5
L (cm)	0.002	0.002
σ (S/cm)	0.0024	0.003
C	5-7	6
f	0.2-0.25	0.12
$l_{c,0}$ (cm)	5.0×10^{-5}	3.8×10^{-5}

7.5 Conclusions

In summary, the microstructural and electrochemical degradation of infiltrated SSC-GDC oxygen electrodes is observed at a range of accelerated aging temperatures for over 1000 hours. A coarsening model is presented that accurately fits the data, as well as previous accelerated life test data for infiltrated LSCF-GDC oxygen electrodes. The model is used to predict performance and long-term stability for a range of starting oxygen electrode feature sizes and operating temperatures. The results suggest that these nano-scale oxygen electrodes can provide both acceptable polarization resistance and long-term stability for operating temperature down to ~ 600 - 650 °C. Attempts to improve low-temperature performance by decreasing oxygen electrode feature size are expected to degrade performance stability. However, electrode nano-structures designed to suppress coarsening could be a useful avenue to improved low-temperature performance. A key conclusion is that an electrode materials' morphological stability, controlled

by cation transport kinetics, should be considered along with oxygen transport kinetics in LT-SOC oxygen electrode discovery and selection.

Chapter 8: Summary and Outlook

Large scale energy storage is a critical component of a completely renewable energy grid and is a need that is currently not well addressed. The reversible solid oxide fuel cell coupled with geological storage is a large scale energy storage application that is capable of seasonal discharge times, competitive round-trip efficiencies, and low cost per kWh stored. However, two key developments are required for the effective implementation of this technology: low cell resistance at ~ 600 °C and $<25\%$ degradation over about 5 years. The oxygen electrode is often thought to be the limiting component in both cases, as the resistance is high at low temperatures, and the electrode degrades quickly in electrolysis conditions. This work has advanced strategies to meet both low resistance and high durability needs:

- 1) A new infiltrated Pr_2NiO_4 electrode provided low resistance at low temperatures with improved stability using a Sr free material. The development of this electrode also informed the fabrication of the similarly promising La_2NiO_4 electrode in chapter 6.
- 2) High pressure operation is understood to be very helpful thermodynamically at the fuel electrode for round trip efficiency. At the oxygen electrode high oxygen pressure causes large reductions in the polarization resistance. An electrode with an otherwise large polarization resistance may be made useful under pressurization. The first pressurized measurements of MIEC electrodes were collected and analyzed. It was found that interstitial conductors such as the rare-earth nickelates have a fundamental advantage compared to vacancy conducting perovskites.
- 3) The degradation under current switching conditions for three electrodes was examined in order to obtain more stable operating conditions and understand how the electrodes

degrade. For LSM-YSZ on YSZ electrodes, the major controlling factor for degradation is overpotential. Overpotentials below 0.2 V result in minimal degradation, though other EIS features show not all changes stop. Slow enough degradation can be maintained operating below the critical value. For the LSCF electrode on GDC, significant degradation occurs below the overpotential predicted for degradation because of microstructural changes and a change in the surface exchange rate. The change in surface exchange rate is most likely due to the surface segregation of strontium. Low current densities were correlated with lower degradation rates in LSCF with 0.7 A/cm^2 being close to the acceptable degradation rate. The infiltrated LNO electrode shows slow degradation rates near the predicted critical overpotential and at high currents, however more work is required to understand this electrode more deeply. A hard design criterion for reversible cells is maintaining operating overpotentials below the critical limit for oxygen bubble nucleation.

- 4) Predictions on the limits of the degradation of infiltrated electrodes are described by a combined electrochemical-coarsening model. A figure of merit accounting for the kinetics of coarsening in the selection of infiltrated materials is presented. The predictions show that coarsening is a manageable degradation mechanism. Furthermore, strategies can be developed to improve the operable lifetime of an infiltrated electrode.

Future work focusing on the development of low temperature, low resistance, and durable reversible solid oxide cell electrodes would lead to a more competitive energy storage system. An infiltrated or composite rare-earth nickelate may be an exciting avenue of development based on the above summary and literature survey in chapter 2. The rare earth nickelates have promising k^* and D^* values and have been demonstrated to have low polarization resistances as the active

material in a real electrode. They are stable in contact with LSGM, and some are stable in contact with GDC. The rare-earth nickelates have a fundamental advantage at the high pressures essential for a reversible system owing to interstitial oxygen ion conduction. The preliminary current switched tests on La_2NiO_4 showed promising stability at higher currents, and should be explored further. Moreover, the known high temperature stability and melting point of La_2NiO_4 (compared to LSCF or SSC, which lose cobalt) suggests lower cation mobility and consequently better stability against coarsening. The rare earth nickelates also perform better without alkali earth doping and so avoid the Sr segregation issue altogether. It would be interesting to life test LNO/LSGM electrodes to determine stable conditions.

There is no data available for full reversible SOCs under pressurized conditions. Life tests under actual conditions and real devices would be worthwhile. It would be especially interesting to perform a pressurized life test of LSM/YSZ or LNO/LSGM to further explore the role overpotential in cell degradation. It is known that the polarization resistance is reduced under high oxygen pressure, so in principle higher current densities should be possible while maintaining low-degradation rates at typical operating temperatures.

Another interesting topic to explore in the context of the stability of infiltrated electrodes would be the effect of atomic layer deposition (ALD) coatings. There is some data already that shows thin ALD zirconia does not have a negative effect on the polarization resistance of $\text{La}_x\text{Sr}_{1-x}\text{CoO}_3$ electrodes. An ALD coating of a high melting point material over infiltrated MIEC particles may slow the rate of coarsening (adjusting K_D), making the materials space of acceptable infiltrated MIECs broader. Moreover it is not clear why the ALD coatings have little effect on the polarization resistance, as they would be expected to block active sites.

Also of interest would be to push the limits of the acceptable current density for a low polarization electrode at higher temperatures. This would reduce the overpotential to a very small value for high current densities. This experiment would be useful in the context of high temperature steam electrolysis combined with a nuclear source.

References

- 1 Change, I. P. o. C. *Fifth Assessment Report*, <<https://www.ipcc.ch/report/ar5/>> (2014).

- 2 Nations, U. *Paris Agreement*,
<http://unfccc.int/files/essential_background/convention/application/pdf/english_paris_agreement.pdf> (2015).
- 3 LANDLER, M. P., J. *Rare Harmony as China and U.S. Commit to Climate Deal*,
<<http://www.nytimes.com/2016/09/04/world/asia/obama-xi-jinping-china-climate-accord.html>>
(2016).
- 4 Agency, U. S. E. P. *Inventory of U.S. Greenhouse Gas Emissions and Sinks: 1990-2014*,
<<https://www.epa.gov/sites/production/files/2016-04/documents/us-ghg-inventory-2016-main-text.pdf>> (2016).
- 5 Jacobson, M. Z. *et al.* 100% clean and renewable wind, water, and sunlight (WWS) all-sector energy roadmaps for the 50 United States. *Energ Environ Sci* **8**, 2093-2117,
doi:10.1039/c5ee01283j (2015).
- 6 Administration, U. S. E. I. *Levelized Cost and Levelized Avoided Cost of New Generation Resources in the Annual Energy Outlook 2016*,
<https://www.eia.gov/forecasts/aeo/pdf/electricity_generation.pdf> (2016).
- 7 Bird, L. C., J. Wang, X. *Wind and Solar Energy Curtailment: Experience and Practices in the United States*, <<http://www.nrel.gov/docs/fy14osti/60983.pdf>> (2014).
- 8 Denholm, P. E., E. Kirby, B. The Role of Energy Storage with Renewable Electricity Generation (2010).
- 9 Becker, S. *et al.* Features of a fully renewable US electricity system: Optimized mixes of wind and solar PV and transmission grid extensions. *Energy* **72**, 443-458,
doi:10.1016/j.energy.2014.05.067 (2014).
- 10 Administration, U. S. E. I. *Electric Power Annual 2014*,
<<http://www.eia.gov/electricity/annual/pdf/epa.pdf>> (2016).

- 11 Soloveichik, G. L. Flow Batteries: Current Status and Trends. *Chem Rev* **115**, 11533-11558, doi:10.1021/cr500720t (2015).
- 12 Rehman, S., Al-Hadhrami, L. M. & Alam, M. M. Pumped hydro energy storage system: A technological review. *Renew Sust Energ Rev* **44**, 586-598, doi:10.1016/j.rser.2014.12.040 (2015).
- 13 Deane, J. P., Gallachoir, B. P. O. & McKeogh, E. J. Techno-economic review of existing and new pumped hydro energy storage plant. *Renew Sust Energ Rev* **14**, 1293-1302, doi:10.1016/j.rser.2009.11.015 (2010).
- 14 Budt, M., Wolf, D., Span, R. & Yan, J. Y. A review on compressed air energy storage: Basic principles, past milestones and recent developments. *Appl Energ* **170**, 250-268, doi:10.1016/j.apenergy.2016.02.108 (2016).
- 15 Chalk, S. G. & Miller, J. E. Key challenges and recent progress in batteries, fuel cells, and hydrogen storage for clean energy systems. *J. Power Sources* **159**, 73-80, doi:10.1016/j.jpowsour.2006.04.058 (2006).
- 16 Jena, P. Materials for Hydrogen Storage: Past, Present, and Future. *J Phys Chem Lett* **2**, 206-211, doi:10.1021/jz1015372 (2011).
- 17 Association, E. S. (2014).
- 18 Yang, Z. G. *et al.* Electrochemical Energy Storage for Green Grid. *Chem Rev* **111**, 3577-3613, doi:Doi 10.1021/Cr100290v (2011).
- 19 Jensen, S. H. *et al.* Large-scale electricity storage utilizing reversible solid oxide cells combined with underground storage of CO₂ and CH₄. *Energ Environ Sci* **8**, 2471-2479, doi:10.1039/c5ee01485a (2015).
- 20 Jensen, S. H., Sun, X. F., Ebbesen, S. D., Knibbe, R. & Mogensen, M. Hydrogen and synthetic fuel production using pressurized solid oxide electrolysis cells. *International Journal of Hydrogen Energy* **35**, 9544-9549, doi:10.1016/j.ijhydene.2010.06.065 (2010).
- 21 EG&G Technical Services, I. *Fuel Cell Handbook*. (U.S. Department of Energy, 2004).

- 22 Bierschenk, D. M., Wilson, J. R. & Barnett, S. A. High efficiency electrical energy storage using a methane-oxygen solid oxide cell. *Energ Environ Sci* **4**, 944-951, doi:10.1039/c0ee00457j (2011).
- 23 Wendel, C. H., Kazempoor, P. & Braun, R. J. A thermodynamic approach for selecting operating conditions in the design of reversible solid oxide cell energy systems. *J. Power Sources* **301**, 93-104, doi:10.1016/j.jpowsour.2015.09.093 (2016).
- 24 Wendel, C. H. & Braun, R. J. Design and techno-economic analysis of high efficiency reversible solid oxide cell systems for distributed energy storage. *Appl Energ* **172**, 118-131, doi:10.1016/j.apenergy.2016.03.054 (2016).
- 25 Gao, Z., Mogni, L. V., Miller, E. C., Railsback, J. G. & Barnett, S. A. A perspective on low-temperature solid oxide fuel cells. *Energ Environ Sci* **9**, 1602-1644, doi:10.1039/C5EE03858H (2016).
- 26 Fergus, J. W. Electrolytes for solid oxide fuel cells. *J. Power Sources* **162**, 30-40, doi:10.1016/j.jpowsour.2006.06.062 (2006).
- 27 Araki, W., Koshikawa, T., Yamaji, A. & Adachi, T. Degradation mechanism of scandia-stabilised zirconia electrolytes: Discussion based on annealing effects on mechanical strength, ionic conductivity, and Raman spectrum. *Solid State Ionics* **180**, 1484-1489, doi:10.1016/j.ssi.2009.09.001 (2009).
- 28 Huang, K. Q. & Goodenough, J. B. A solid oxide fuel cell based on Sr- and Mg-doped LaGaO₃ electrolyte: the role of a rare-earth oxide buffer. *J. Alloy. Compd.* **303**, 454-464 (2000).
- 29 Zhan, Z. L., Bierschenk, D. M., Cronin, J. S. & Barnett, S. A. A reduced temperature solid oxide fuel cell with nanostructured anodes. *Energy Environ. Sci.* **4**, 3951-3954, doi:10.1039/c1ee01982a (2011).

- 30 Pillai, M. R., Kim, I., Bierschenk, D. M. & Barnett, S. A. Fuel-flexible operation of a solid oxide fuel cell with Sr_{0.8}La_{0.2}TiO₃ support. *Journal of Power Sources* **185**, 1086-1093, doi:Doi 10.1016/J.jpowsour.2008.07.063 (2008).
- 31 Gao, Z., Barnett, S. & Braun, R. Develop high performance intermediate temperature solid oxide cells for energy storage. *submitted* (2016).
- 32 Lin, Y. B. & Barnett, S. A. Co-firing of anode-supported SOFCs with thin La_{0.9}Sr_{0.1}Ga_{0.8}Mg_{0.2}O_{3-δ} electrolytes. *Electrochem Solid St* **9**, A285-A288, doi:10.1149/1.2191132 (2006).
- 33 Zhang, X. G. *et al.* Ni-SDC cermet anode for medium-temperature solid oxide fuel cell with lanthanum gallate electrolyte. *J. Power Sources* **83**, 170-177, doi:Doi 10.1016/S0378-7753(99)00293-1 (1999).
- 34 Lu, C., An, S., Worrell, W. L., Vohs, J. M. & Gorte, R. J. Development of intermediate-temperature solid oxide fuel cells for direct utilization of hydrocarbon fuels. *Solid State Ionics* **175**, 47-50, doi:10.1016/j.ssi.2004.09.019 (2004).
- 35 Liu, Z. B. *et al.* Fabrication and modification of solid oxide fuel cell anodes via wet impregnation/infiltration technique. *J. Power Sources* **237**, 243-259, doi:10.1016/j.jpowsour.2013.03.025 (2013).
- 36 Mogensen, M., Sammes, N. M. & Tompsett, G. A. Physical, chemical and electrochemical properties of pure and doped ceria. *Solid State Ionics* **129**, 63-94 (2000).
- 37 Wright, J. & Virkar, A. V. Conductivity of porous Sm₂O₃-doped CeO₂ as a function of temperature and oxygen partial pressure. *J. Power Sources* **196**, 6118-6124, doi:10.1016/j.jpowsour.2011.03.043 (2011).
- 38 Zhan, Z. L. & Barnett, S. A. An octane-fueled solid oxide fuel cell. *Science* **308**, 844-847, doi:10.1126/science.1109213 (2005).

- 39 Jung, D. W., Nino, J. C., Duncan, K. L., Bishop, S. R. & Wachsman, E. D. Enhanced long-term stability of bismuth oxide-based electrolytes for operation at 500 A degrees C. *Ionics* **16**, 97-103, doi:10.1007/s11581-009-0402-9 (2010).
- 40 Sammes, N. M., Tompsett, G. A., Nafe, H. & Aldinger, F. Bismuth based oxide electrolytes - Structure and ionic conductivity. *J. Eur. Ceram. Soc.* **19**, 1801-1826, doi:10.1016/s0955-2219(99)00009-6 (1999).
- 41 Wachsman, E. D. & Lee, K. T. Lowering the Temperature of Solid Oxide Fuel Cells. *Science* **334**, 935-939, doi:10.1126/science.1204090 (2011).
- 42 Zhu, H. Y., Kee, R. J., Janardhanan, V. M., Deutschmann, O. & Goodwin, D. G. Modeling elementary heterogeneous chemistry and electrochemistry in solid-oxide fuel cells. *J. Electrochem. Soc.* **152**, A2427-A2440, doi:10.1149/1.2116607 (2005).
- 43 Utz, A., Leonide, A., Weber, A. & Ivers-Tiffée, E. Studying the CO-CO₂ characteristics of SOFC anodes by means of patterned Ni anodes. *J. Power Sources* **196**, 7217-7224, doi:10.1016/j.jpowsour.2010.10.056 (2011).
- 44 Bessler, W. G. *et al.* Model anodes and anode models for understanding the mechanism of hydrogen oxidation in solid oxide fuel cells. *Phys. Chem. Chem. Phys.* **12**, 13888-13903, doi:10.1039/c0cp00541j (2010).
- 45 Ahn, J. S., Yoon, H., Lee, K. T., Camaratta, M. A. & Wachsman, E. D. Performance of IT-SOFC with Ce_{0.9}Gd_{0.1}O_{1.95} Functional Layer at the Interface of Ce_{0.9}Gd_{0.1}O_{1.95} Electrolyte and Ni-Ce_{0.9}Gd_{0.1}O_{1.95} Anode. *Fuel Cells* **9**, 643-649, doi:10.1002/fuce.200900005 (2009).
- 46 Cho, S. *et al.* Fe-substituted SrTiO_{3-δ}-Ce_{0.9}Gd_{0.1}O₂ composite anodes for solid oxide fuel cells. *Energy & Environmental Science* **6**, 1850-1857, doi:10.1039/c3ee23791e (2013).
- 47 Huang, Y. H., Dass, R. I., Xing, Z. L. & Goodenough, J. B. Double perovskites as anode materials for solid-oxide fuel cells. *Science* **312**, 254-257, doi:10.1126/science.1125877 (2006).

- 48 Hou, S. E., Aguadero, A., Alonso, J. A. & Goodenough, J. B. Fe-based perovskites as electrodes for intermediate-temperature solid oxide fuel cells. *J. Power Sources* **196**, 5478-5484, doi:Doi 10.1016/J.jpowsour.2010.11.122 (2011).
- 49 Kobsiriphat, W., Madsen, B. D., Wang, Y., Marks, L. D. & Barnett, S. A. La_{0.8}Sr_{0.2}Cr_{1-x}Ru_xO_{3-δ}-Gd_{0.1}Ce_{0.9}O_{1.95} solid oxide fuel cell anodes: Ru precipitation and electrochemical performance. *Solid State Ionics* **180**, 257-264, doi:10.1016/j.ssi.2008.12.022 (2009).
- 50 Lee, H. M. Electrochemical characteristics of La_{1-x}Sr_xMnO₃ for solid oxide fuel cell. *Mater Chem Phys* **77**, 639-646, doi:Pii S0254-0584(02)00091-3 Doi 10.1016/S0254-0584(02)00091-3 (2003).
- 51 Cronin, J. S. *et al.* Effect of Firing Temperature on LSM-YSZ Composite Cathodes: A Combined Three-Dimensional Microstructure and Impedance Spectroscopy Study. *J Electrochem Soc* **159**, B385-B393, doi:10.1149/2.053204jes (2012).
- 52 Vanroosmalen, J. A. M. & Cordfunke, E. H. P. Chemical-Reactivity and Interdiffusion of (La, Sr) MnO₃ and (Zr, Y) O₂, Solid Oxide Fuel-Cell Cathode and Electrolyte Materials. *Solid State Ionics* **52**, 303-312, doi:Doi 10.1016/0167-2738(92)90177-Q (1992).
- 53 Tanner, C. W., Fung, K. Z. & Virkar, A. V. The effect of porous composite electrode structure on solid oxide fuel cell performance .1. Theoretical analysis. *J Electrochem Soc* **144**, 21-30, doi:Doi 10.1149/1.1837360 (1997).
- 54 Radhakrishnan, R., Virkar, A. V. & Singhal, S. C. Estimation of charge-transfer resistivity of La_{0.8}Sr_{0.2}MnO₃ cathode on Y_{0.16}Zr_{0.84}O₂ electrolyte using patterned electrodes. *J Electrochem Soc* **152**, A210-A218, doi:10.1149/1.1829415 (2005).
- 55 Jacobson, A. J. Materials for Solid Oxide Fuel Cells. *Chem Mater* **22**, 660-674, doi:10.1021/cm902640j (2010).

- 56 Adler, S. B. Factors governing oxygen reduction in solid oxide fuel cell cathodes. *Chem Rev* **104**, 4791-4843, doi:10.1021/cr020724o (2004).
- 57 Fleig, J. Solid oxide fuel cell cathodes: Polarization mechanisms and modeling of the electrochemical performance. *Annu Rev Mater Res* **33**, 361-382, doi:10.1146/annurev.matsci.33.022802.093258 (2003).
- 58 Adler, S. B., Lane, J. A. & Steele, B. C. H. Electrode kinetics of porous mixed-conducting oxygen electrodes. *J Electrochem Soc* **143**, 3554-3564, doi:Doi 10.1149/1.1837252 (1996).
- 59 Yakal-Kremiski, K., Mogni, L. V., Montenegro-Hernandez, A., Caneiro, A. & Barnett, S. A. Determination of Electrode Oxygen Transport Kinetics Using Electrochemical Impedance Spectroscopy Combined with Three-Dimensional Microstructure Measurement: Application to $\text{Nd}_2\text{NiO}_4+\delta$. *J Electrochem Soc* **161**, F1366-F1374, doi:10.1149/2.0521414jes (2014).
- 60 Chroneos, A., Yildiz, B., Tarancon, A., Parfitt, D. & Kilner, J. A. Oxygen diffusion in solid oxide fuel cell cathode and electrolyte materials: mechanistic insights from atomistic simulations. *Energ Environ Sci* **4**, 2774-2789, doi:10.1039/c0ee00717j (2011).
- 61 Mogni, L., Prado, F., Jimenez, C. & Caneiro, A. Oxygen order-disorder phase transition in layered $\text{GdBaCo}_2\text{O}_{5+\delta}$ perovskite: Thermodynamic and transport properties. *Solid State Ionics* **240**, 19-28, doi:10.1016/j.ssi.2013.03.021 (2013).
- 62 Kim, J. H. *et al.* High Temperature Crystal Chemistry and Oxygen Permeation Properties of the Mixed Ionic-Electronic Conductors $\text{LnBaCo}_2\text{O}_{5+\delta}$ (Ln = Lanthanide). *J Electrochem Soc* **156**, B1376-B1382, doi:10.1149/1.3231501 (2009).
- 63 Sayers, R., De Souza, R. A., Kilner, J. A. & Skinner, S. J. Low temperature diffusion and oxygen stoichiometry in lanthanum nickelate. *Solid State Ionics* **181**, 386-391, doi:10.1016/j.ssi.2010.01.016 (2010).

- 64 Bassat, J. M. *et al.* Anisotropic Oxygen Diffusion Properties in Pr₂NiO_{4+δ} and Nd₂NiO_{4+δ} Single Crystals. *J Phys Chem C* **117**, 26466-26472, doi:10.1021/jp409057k (2013).
- 65 Teraoka, Y., Nobunaga, T., Okamoto, K., Miura, N. & Yamazoe, N. INFLUENCE OF CONSTITUENT METAL-CATIONS IN SUBSTITUTED LACOO₃ ON MIXED CONDUCTIVITY AND OXYGEN PERMEABILITY. *Solid State Ionics* **48**, 207-212, doi:10.1016/0167-2738(91)90034-9 (1991).
- 66 Tai, L. W., Nasrallah, M. M., Anderson, H. U., Sparlin, D. M. & Sehlin, S. R. STRUCTURE AND ELECTRICAL-PROPERTIES OF LA_{1-x}SRXCO_{1-y}FEYO₃ .1. THE SYSTEM LA_{0.8}SR_{0.2}CO_{1-y}FEYO₃. *Solid State Ionics* **76**, 259-271, doi:10.1016/0167-2738(94)00244-m (1995).
- 67 Wan, T. H., Saccoccio, M., Chen, C. & Ciucci, F. Assessing the identifiability of k and D in electrical conductivity relaxation via analytical results and nonlinearity estimates. *Solid State Ionics* **270**, 18-32, doi:10.1016/j.ssi.2014.11.026 (2015).
- 68 Kilner, J. A., Skinner, S. J. & Brongersma, H. H. The isotope exchange depth profiling (IEDP) technique using SIMS and LEIS. *J Solid State Electr* **15**, 861-876, doi:10.1007/s10008-010-1289-0 (2011).
- 69 Wang, L., Merkle, R., Maier, J., Acartürk, T. & Starke, U. Oxygen tracer diffusion in dense Ba_{0.5}Sr_{0.5}Co_{0.8}Fe_{0.2}O_{3-δ} films. *Appl. Phys. Lett.* **94**, 071908, doi:10.1063/1.3085969 (2009).
- 70 Bucher, E., Egger, A., Ried, P., Sitte, W. & Holtappels, P. Oxygen nonstoichiometry and exchange kinetics of Ba_{0.5}Sr_{0.5}Co_{0.8}Fe_{0.2}O_{3-δ}. *Solid State Ionics* **179**, 1032-1035, doi:10.1016/j.ssi.2008.01.089 (2008).
- 71 Chen, D. & Shao, Z. Surface exchange and bulk diffusion properties of Ba_{0.5}Sr_{0.5}Co_{0.8}Fe_{0.2}O_{3-δ} mixed conductor. *International Journal of Hydrogen Energy* **36**, 6948-6956, doi:10.1016/j.ijhydene.2011.02.087 (2011).

- 72 Katsuki, M., Wang, S., Dokiya, M. & Hashimoto, T. High temperature properties of $\text{La}_{0.6}\text{Sr}_{0.4}\text{Co}_{0.8}\text{Fe}_{0.2}\text{O}_{3-\delta}$ oxygen nonstoichiometry and chemical diffusion constant. *Solid State Ionics* **156**, 453-461 (2003).
- 73 Bouwmeester, H. J. M., Den Otter, M. W. & Boukamp, B. A. Oxygen transport in $\text{La}_{0.6}\text{Sr}_{0.4}\text{Co}_{1-y}\text{Fe}_y\text{O}_{3-\delta}$. *J Solid State Electr* **8**, 599-605, doi:10.1007/s10008-003-0488-3 (2004).
- 74 tenElshof, J. E., Lankhorst, M. H. R. & Bouwmeester, H. J. M. Chemical diffusion and oxygen exchange of $\text{La}_{0.6}\text{Sr}_{0.4}\text{Co}_{0.6}\text{Fe}_{0.4}\text{O}_{3-\delta}$. *Solid State Ionics* **99**, 15-22, doi:10.1016/s0167-2738(97)00263-4 (1997).
- 75 Lane, J. A. & Kilner, J. A. Measuring oxygen diffusion and oxygen surface exchange by conductivity relaxation. *Solid State Ionics* **136**, 997-1001, doi:10.1016/s0167-2738(00)00554-3 (2000).
- 76 Li, Y., Gerdes, K., Horita, T. & Liu, X. Surface Exchange and Bulk Diffusivity of LSCF as SOFC Cathode: Electrical Conductivity Relaxation and Isotope Exchange Characterizations. *J. Electrochem. Soc.* **160**, F343-F350, doi:10.1149/2.044304jes (2013).
- 77 ISHIGAKI, T., YAMAUCHI, S., KISHIO, K., MIZUSAKI, J. & FUEKI, K. Diffusion of Oxide Ion Vacancies in Perovskite-Type Oxides. *J Solid State Chem* **73**, 179-187 (1988).
- 78 De Souza, R. A. & Kilner, J. A. Oxygen transport in $\text{La}_{1-x}\text{Sr}_x\text{Mn}_{1-y}\text{Co}_y\text{O}_3$ perovskites Part I. Oxygen tracer diffusion. *Solid State Ionics* **106**, 175-187 (1998).
- 79 Carter, S. *et al.* Oxygen transport in selected nonstoichiometric perovskite-structure oxides. *Solid State Ionics* **53-56**, 597-605 (1992).
- 80 van der Haar, L. M., den Otter, M. W., Morskate, M., Bouwmeester, H. J. M. & Verweij, H. Chemical diffusion and oxygen surface transfer of $\text{La}_{1-x}\text{Sr}_x\text{CoO}_{3-\delta}$ studied with electrical conductivity relaxation. *J. Electrochem. Soc.* **149**, J41-J46, doi:10.1149/1.1446874 (2002).

- 81 Kubicek, M. *et al.* Oxygen Surface Exchange and Diffusion in $\text{La}_{1-x}\text{Sr}_x\text{CoO}_{3-\delta}$ Thin Films. *ACS Nano* **7**, 3276-3286 (2013).
- 82 Berenov, A. V., Atkinson, A., Kilner, J. A., Bucher, E. & Sitte, W. Oxygen tracer diffusion and surface exchange kinetics in $\text{La}_{0.6}\text{Sr}_{0.4}\text{CoO}_{3-\delta}$. *Solid State Ionics* **181**, 819-826, doi:10.1016/j.ssi.2010.04.031 (2010).
- 83 Egger, A., Bucher, E., Yang, M. & Sitte, W. Comparison of oxygen exchange kinetics of the IT-SOFC cathode materials $\text{La}_{0.5}\text{Sr}_{0.5}\text{CoO}_{3-\delta}$ and $\text{La}_{0.6}\text{Sr}_{0.4}\text{CoO}_{3-\delta}$. *Solid State Ionics* **225**, 55-60, doi:10.1016/j.ssi.2012.02.050 (2012).
- 84 Egger, a., Bucher, E. & Sitte, W. Oxygen Exchange Kinetics of the IT-SOFC Cathode Material $\text{Nd}_2\text{NiO}_{4+\delta}$ and Comparison with $\text{La}_{0.6}\text{Sr}_{0.4}\text{CoO}_{3-\delta}$. *J Electrochem Soc* **158**, B573-B579, doi:10.1149/1.3569697 (2011).
- 85 vanDoorn, R. H. E. *et al.* Surface oxygen exchange of $\text{La}_{0.3}\text{Sr}_{0.7}\text{CoO}_{3-d}$. *Solid State Ionics* **96**, 1-7 (1997).
- 86 Fullarton, I. C. *et al.* Study of Oxygen Ion Transport in Acceptor Doped Samarium Cobalt Oxide. *Ionics* **1**, 51-58, doi:10.1007/bf02426008 (1995).
- 87 Yeh, T. C., Routbort, J. L. & Mason, T. O. Oxygen transport and surface exchange properties of $\text{Sr}_{0.5}\text{Sm}_{0.5}\text{CoO}_{3-\delta}$. *Solid State Ionics* **232**, 138-143, doi:10.1016/j.ssi.2012.11.024 (2013).
- 88 Ritzmann, A. M., Munoz-Garcia, A. B., Pavone, M., Keith, J. A. & Carter, E. A. Ab Initio DFT plus U Analysis of Oxygen Vacancy Formation and Migration in $\text{La}_{1-x}\text{Sr}_x\text{FeO}_{3-\delta}$ ($x=0, 0.25, 0.50$). *Chem. Mat.* **25**, 3011-3019, doi:10.1021/cm401052w (2013).
- 89 Lumeij, M. *et al.* Influence of the $\text{Ba}^{2+}/\text{Sr}^{2+}$ content and oxygen vacancies on the stability of cubic $\text{Ba}_x\text{Sr}_{1-x}\text{Co}_{0.75}\text{Fe}_{0.25}\text{O}_{3-\delta}$. *Phys. Chem. Chem. Phys.* **16**, 1333-1338, doi:10.1039/c3cp53958j (2014).

- 90 Efimov, K., Xu, Q. A. & Feldhoff, A. Transmission Electron Microscopy Study of Ba_{0.5}Sr_{0.5}Co_{0.8}Fe_{0.2}O_{3- δ} Perovskite Decomposition at Intermediate Temperatures. *Chem Mater* **22**, 5866-5875, doi:10.1021/cm101745v (2010).
- 91 Setevich, C., Mogni, L., Caneiro, A. & Prado, F. Characterization of the La_{1-x}Ba_xCoO_{3- δ} (0 \leq x \leq 1) System as Cathode Material for IT-SOFC. *J Electrochem Soc* **159**, B73-B80, doi:10.1149/2.043201jes (2012).
- 92 Kim, G. *et al.* Rapid oxygen ion diffusion and surface exchange kinetics in PrBaCo₂O_{5+x} with a perovskite related structure and ordered A cations. *J. Mater. Chem.* **17**, 2500-2505, doi:10.1039/b618345j (2007).
- 93 Grimaud, A. *et al.* Oxygen reduction reaction of PrBaCo_{2-x}Fe_xO_{5+ δ} compounds as H⁺-SOFC cathodes: correlation with physical properties. *J. Mater. Chem. A* **2**, 3594-3604, doi:10.1039/c3ta13956e (2014).
- 94 Burriel, M. *et al.* Anisotropic Oxygen Ion Diffusion in Layered PrBaCo₂O_{5+ δ} . *Chem. Mat.* **24**, 613-621, doi:10.1021/cm203502s (2012).
- 95 Tarancon, A., Skinner, S. J., Chater, R. J., Hernandez-Ramirez, F. & Kilner, J. A. Layered perovskites as promising cathodes for intermediate temperature solid oxide fuel cells. *J. Mater. Chem.* **17**, 3175-3181, doi:10.1039/b704320a (2007).
- 96 Taskin, A. A., Lavrov, A. N. & Ando, Y. Achieving fast oxygen diffusion in perovskites by cation ordering. *Appl. Phys. Lett.* **86**, doi:10.1063/1.1864244 (2005).
- 97 Boehm, E. *et al.* Oxygen diffusion and transport properties in non-stoichiometric Ln(2-x)NiO(4+ δ) oxides. *Solid State Ionics* **176**, 2717-2725, doi:10.1016/j.ssi.2005.06.033 (2005).
- 98 Yashima, M. *et al.* Structural disorder and diffusional pathway of oxide ions in a doped Pr(2)NiO(4)-based mixed conductor. *J. Am. Chem. Soc.* **130**, 2762-2763, doi:10.1021/Ja711478h (2008).

- 99 Zheng, K., Gorzkowska-Sobas, A. & Swierczek, K. Evaluation of Ln(2)CuO(4) (Ln:La, Pr, Nd) oxides as cathode materials for IT-SOFCs. *Mater. Res. Bull.* **47**, 4089-4095, doi:DOI 10.1016/j.materresbull.2012.08.072 (2012).
- 100 Skinner, S. J. & Kilner, J. A. A Comparison of The Transport Properties of La(2-x)Sr(x)Ni(1-y)Fe(y)O(4+delta) where $0 < x < 0.2$ and $0 < y < 0.2$. *Ionics* **5**, 171-174, doi:10.1007/bf02375836 (1999).
- 101 Skinner, S. J. & Kilner, J. A. Oxygen diffusion and surface exchange in La_{2-x}Sr_xNiO_{4+delta}. *Solid State Ionics* **135**, 709-712, doi:10.1016/s0167-2738(00)00388-x (2000).
- 102 Odier, P., Allancon, C. & Bassat, J. M. Oxygen exchange in Pr₂NiO_{4+delta}, at high temperature and direct formation of Pr₄Ni₃O_{10-x}. *J. Solid State Chem.* **153**, 381-385, doi:DOI 10.1006/jssc.2000.8786 (2000).
- 103 Railsback, J. G., Gao, Z. & Barnett, S. A. Oxygen electrode characteristics of Pr₂NiO_{4+delta}-infiltrated porous (La_{0.9}Sr_{0.1})(Ga_{0.8}Mg_{0.2})O_{3-delta}. *Solid State Ionics* **274**, 134-139, doi:10.1016/j.ssi.2015.03.030 (2015).
- 104 Zhou, X. D. *et al.* Electrochemical performance and stability of the cathode for solid oxide fuel cells: V. high performance and stable Pr₂NiO₄ as the cathode for solid oxide fuel cells. *Electrochim. Acta* **71**, 44-49, doi:10.1016/j.electacta.2012.03.067 (2012).
- 105 Nomura, T., Nishimoto, S., Kameshima, Y. & Miyake, M. Electrode properties of doped Pr₂NiO₄-based oxide cathode for intermediate-temperature SOFCs. *J. Ceram. Soc. Jpn.* **120**, 534-538, doi:DOI 10.2109/jcersj2.120.534 (2012).
- 106 Yashima, M., Yamada, H., Nuansaeng, S. & Ishihara, T. Role of Ga³⁺ and Cu²⁺ in the High Interstitial Oxide-Ion Diffusivity of Pr₂NiO₄-Based Oxides: Design Concept of Interstitial Ion Conductors through the Higher-Valence d(10) Dopant and Jahn-Teller Effect. *Chem. Mat.* **24**, 4100-4113, doi:10.1021/cm3021287 (2012).

- 107 Wang, Y. F., Cheng, J. G., Jiang, Q. M., Yang, J. F. & Gao, J. F. Preparation and electrochemical performance of $\text{Pr}_2\text{Ni}_{0.6}\text{Cu}_{0.4}\text{O}_4$ cathode materials for intermediate-temperature solid oxide fuel cells. *J. Power Sources* **196**, 3104-3108, doi:DOI 10.1016/j.jpowsour.2010.11.106 (2011).
- 108 Woolley, R. J. & Skinner, S. J. Functionally graded composite $\text{La}_2\text{NiO}_{4+\delta}$ and $\text{La}_4\text{Ni}_3\text{O}_{10-\delta}$ solid oxide fuel cell cathodes. *Solid State Ionics* **255**, 1-5, doi:DOI 10.1016/j.ssi.2013.11.041 (2014).
- 109 Choi, S., Yoo, S., Shin, J. Y. & Kim, G. High Performance SOFC Cathode Prepared by Infiltration of $\text{La}_n(\text{+})\text{Ni}_n\text{O}_{3n(\text{+})}$ ($n=1, 2, \text{ and } 3$) in Porous YSZ. *J. Electrochem. Soc.* **158**, B995-B999, doi:Doi 10.1149/1.3598170 (2011).
- 110 Lou, Z. L. *et al.* Preparation and electrochemical characterization of Ruddlesden-Popper oxide $\text{La}_4\text{Ni}_3\text{O}_{10}$ cathode for IT-SOFCs by sol-gel method. *J. Solid State Electrochem.* **17**, 2703-2709, doi:10.1007/s10008-013-2150-z (2013).
- 111 Takahashi, S., Nishimoto, S., Matsuda, M. & Miyake, M. Electrode Properties of the Ruddlesden-Popper Series, $\text{La}_{n+1}\text{Ni}_n\text{O}_{3n+1}$ ($n=1, 2, \text{ and } 3$), as Intermediate-Temperature Solid Oxide Fuel Cells. *J. Am. Ceram. Soc.* **93**, 2329-2333, doi:DOI 10.1111/j.1551-2916.2010.03743.x (2010).
- 112 Amow, G., Davidson, I. J. & Skinner, S. J. A comparative study of the Ruddlesden-Popper series, $\text{La}_{(n+1)}\text{Ni}_{(n)}\text{O}_{(3n+1)}$ ($n=1, 2 \text{ and } 3$), for solid-oxide fuel-cell cathode applications. *Solid State Ionics* **177**, 1205-1210, doi:DOI 10.1016/j.ssi.2006.05.005 (2006).
- 113 Zinkevich, M. & Aldinger, F. Thermodynamic analysis of the ternary La-Ni-O system. *J. Alloy. Compd.* **375**, 147-161, doi:DOI 10.1016/j.jallcom.2003.11.138 (2004).
- 114 Boehm, E. *et al.* Oxygen transport properties of $\text{La}_2\text{Ni}_{1-x}\text{Cu}_x\text{O}_{4+\delta}$ mixed conducting oxides. *Solid State Sci.* **5**, 973-981, doi:10.1016/S1293-2558(03)00091-8 (2003).
- 115 Sayers, R., De Souza, R. A., Kilner, J. A. & Skinner, S. J. Low temperature diffusion and oxygen stoichiometry in lanthanum nickelate. *Solid State Ionics* **181**, 386-391, doi:10.1016/j.ssi.2010.01.016 (2010).

- 116 Kilner, J. A. & Shaw, C. K. M. Mass transport in $\text{La}_2\text{Ni}_{1-x}\text{Co}_x\text{O}_{4+d}$ oxides with the K_2NiF_4 structure. *Solid State Ionics* **154-155** 523-527 (2002).
- 117 Mauvy, F. *et al.* Oxygen electrode reaction on $\text{Nd}_2\text{NiO}_{4+y}$ cathode materials : impedance spectroscopy study. *Solid State Ionics* **158**, 17-28 (2003).
- 118 Yakal-Kremiski, K., Mogni, L. V., Montenegro-Hernandez, A., Caneiro, A. & Barnett, S. A. Determination of Electrode Oxygen Transport Kinetics Using Electrochemical Impedance Spectroscopy Combined with Three-Dimensional Microstructure Measurement: Application to $\text{Nd}_2\text{NiO}_{4+}$ *J. Electrochem. Soc.* **161**, F1366-F1374, doi:10.1149/2.0521414jes (2014).
- 119 Hayd, J., Dieterle, L., Guntow, U., Gerthsen, D. & Ivers-Tiffée, E. Nanoscaled $\text{La}_{0.6}\text{Sr}_{0.4}\text{CoO}_{3-\delta}$ as intermediate temperature solid oxide fuel cell cathode: Microstructure and electrochemical performance. *J. Power Sources* **196**, 7263-7270, doi:10.1016/j.jpowsour.2010.11.147 (2011).
- 120 Mortensen, J. E., Sogaard, M. & Jacobsen, T. Analytical, 1-Dimensional Impedance Model of a Composite Solid Oxide Fuel Cell Cathode. *J. Electrochem. Soc.* **161**, F161-F175, doi:10.1149/2.077401jes (2013).
- 121 Murray, E. P., Sever, M. J. & Barnett, S. A. Electrochemical performance of $(\text{La}, \text{Sr})(\text{Co}, \text{Fe})\text{O}_{3-\delta}/(\text{Ce}, \text{Gd})\text{O}_2$ composite cathodes. *Solid State Ionics* **148**, 27-34 (2002).
- 122 Ding, D., Li, X. X., Lai, S. Y., Gerdes, K. & Liu, M. L. Enhancing SOFC cathode performance by surface modification through infiltration. *Energ Environ Sci* **7**, 552-575, doi:10.1039/c3ee42926a (2014).
- 123 Nicholas, J. D., Wang, L., Call, A. V. & Barnett, S. A. Use of the Simple Infiltrated Microstructure Polarization Loss Estimation (SIMPLE) model to describe the performance of nano-composite solid oxide fuel cell cathodes. *Phys. Chem. Chem. Phys.* **14**, 15379-15392, doi:10.1039/c2cp43370b (2012).

- 124 Hong, T., Zhang, L., Chen, F. L. & Xia, C. R. Oxygen surface exchange properties of La_{0.6}Sr_{0.4}Co_{0.8}Fe_{0.2}O_{3-(delta)} coated with Sm_xCe_{1-x}O_{2-(delta)}. *J. Power Sources* **218**, 254-260, doi:10.1016/j.jpowsour.2012.07.004 (2012).
- 125 Mutoro, E., Crumlin, E. J., Biegalski, M. D., Christen, H. M. & Shao-Horn, Y. Enhanced oxygen reduction activity on surface-decorated perovskite thin films for solid oxide fuel cells. *Energy Environ. Sci.* **4**, 3689-3696, doi:Doi 10.1039/C1ee01245b (2011).
- 126 Nicholas, J. D. & Barnett, S. A. Validation of the Simple Infiltrated Microstructure Polarization Loss Estimation (SIMPLE) Model Using Single Layer, Nano-Composite Sm_{0.5}Sr_{0.5}CoO_{3-x}-Ce_{0.9}Gd_{0.1}O_{1.95} Solid Oxide Fuel Cell Cathodes. *Ionic and Mixed Conducting Ceramics 7* **28**, 39-58, doi:10.1149/1.3495831 (2010).
- 127 Nicholas, J. D., Wang, L., Call, A. V. & Barnett, S. A. Use of the Simple Infiltrated Microstructure Polarization Loss Estimation (SIMPLE) model to describe the performance of nano-composite solid oxide fuel cell cathodes. *Phys Chem Chem Phys* **14**, 15379-15392, doi:10.1039/c2cp43370b (2012).
- 128 Baumann, F. S. *et al.* Quantitative comparison of mixed conducting SOFC cathode materials by means of thin film model electrodes. *J. Electrochem. Soc.* **154**, B931-B941, doi:10.1149/1.2752974 (2007).
- 129 Energy, U. S. D. o. *Fuel Cell Program Overview*, <<https://www.netl.doe.gov/File%20Library/Events/2014/2014%20SECA%20workshop/Shailesh-Vora.pdf>> (
- 130 Malzbender, J., Batfalsky, P., Vaßen, R., Shemet, V. & Tietz, F. Component interactions after long-term operation of an SOFC stack with LSM cathode. *Journal of Power Sources* **201**, 196-203, doi:10.1016/j.jpowsour.2011.10.117 (2012).

- 131 Liu, Y. L., Thyden, K., Chen, M. & Hagen, A. Microstructure degradation of LSM-YSZ cathode in SOFCs operated at various conditions. *Solid State Ionics* **206**, 97-103, doi:10.1016/j.ssi.2011.10.020 (2012).
- 132 Yokokawa, H., Tu, H. Y., Iwanschitz, B. & Mai, A. Fundamental mechanisms limiting solid oxide fuel cell durability. *J. Power Sources* **182**, 400-412, doi:10.1016/j.jpowsour.2008.02.016 (2008).
- 133 Jørgensen, M. J., Holtappels, P. & Appel, C. C. Durability test of SOFC cathodes. *Journal of Applied Electrochemistry* **30**, 411-418, doi:10.1023/a:1003987318963 (2000).
- 134 Zhan, Z. *et al.* Syngas Production By Coelectrolysis of CO₂/H₂O: The Basis for a Renewable Energy Cycle. *Energy & Fuels* **23**, 3089-3096, doi:10.1021/ef900111f (2009).
- 135 Hauch, A., Jensen, S. H., Ramousse, S. & Mogensen, M. Performance and durability of solid oxide electrolysis cells. *J. Electrochem. Soc.* **153**, A1741-A1747, doi:10.1149/1.2216562 (2006).
- 136 Keane, M., Mahapatra, M. K., Verma, A. & Singh, P. LSM-YSZ interactions and anode delamination in solid oxide electrolysis cells. *International Journal of Hydrogen Energy* **37**, 16776-16785, doi:http://dx.doi.org/10.1016/j.ijhydene.2012.08.104 (2012).
- 137 Mawdsley, J. R., Carter, J. D., Kropf, A. J., Yildiz, B. & Maroni, V. A. Post-test evaluation of oxygen electrodes from solid oxide electrolysis stacks. *International Journal of Hydrogen Energy* **34**, 4198-4207, doi:10.1016/j.ijhydene.2008.07.061 (2009).
- 138 Graves, C., Ebbesen, S. D. & Mogensen, M. Co-electrolysis of CO₂ and H₂O in solid oxide cells: Performance and durability. *Solid State Ionics* **192**, 398-403, doi:10.1016/j.ssi.2010.06.014 (2011).
- 139 Chen, K. & Jiang, S. P. Failure mechanism of (La,Sr)MnO₃ oxygen electrodes of solid oxide electrolysis cells. *International Journal of Hydrogen Energy* **36**, 10541-10549, doi:10.1016/j.ijhydene.2011.05.103 (2011).

- 140 Virkar, A. V. Mechanism of oxygen electrode delamination in solid oxide electrolyzer cells. *International Journal of Hydrogen Energy* **35**, 9527-9543, doi:<http://dx.doi.org/10.1016/j.ijhydene.2010.06.058> (2010).
- 141 Malzbender, J., Batfalsky, P., Vassen, R., Shemet, V. & Tietz, F. Component interactions after long-term operation of an SOFC stack with LSM cathode. *J. Power Sources* **201**, 196-203, doi:[10.1016/j.jpowsour.2011.10.117](https://doi.org/10.1016/j.jpowsour.2011.10.117) (2012).
- 142 Jorgensen, M. J., Holtappels, P. & Appel, C. C. Durability test of SOFC cathodes. *J Appl Electrochem* **30**, 411-418, doi:[Doi 10.1023/A:1003987318963](https://doi.org/10.1023/A:1003987318963) (2000).
- 143 Keane, M., Mahapatra, M. K., Verma, A. & Singh, P. LSM-YSZ interactions and anode delamination in solid oxide electrolysis cells. *International Journal of Hydrogen Energy* **37**, 16776-16785, doi:[10.1016/j.ijhydene.2012.08.104](https://doi.org/10.1016/j.ijhydene.2012.08.104) (2012).
- 144 Knibbe, R., Traulsen, M. L., Hauch, A., Ebbesen, S. D. & Mogensen, M. Solid Oxide Electrolysis Cells: Degradation at High Current Densities. *J Electrochem Soc* **157**, B1209-B1217, doi:[10.1149/1.3447752](https://doi.org/10.1149/1.3447752) (2010).
- 145 Hughes, G. A., Yakal-Kremiski, K. & Barnett, S. A. Life testing of LSM-YSZ composite electrodes under reversing-current operation. *Phys Chem Chem Phys* **15**, 17257-17262, doi:[10.1039/c3cp52973h](https://doi.org/10.1039/c3cp52973h) (2013).
- 146 Simner, S. P., Anderson, M. D., Engelhard, M. H. & Stevenson, J. W. Degradation Mechanisms of La-Sr-Co-Fe-O₃ SOFC Cathodes. *Electrochem. Solid State Lett.* **9**, A478-A481, doi:[10.1149/1.2266160](https://doi.org/10.1149/1.2266160) (2006).
- 147 Harrison, W. A. Origin of Sr segregation at La_{1-x}Sr_xMnO₃ surfaces. *Phys. Rev. B* **83**, 155437, doi:[Artn 155437 Doi 10.1103/Physrevb.83.155437](https://doi.org/10.1103/Physrevb.83.155437) (2011).

- 148 Crumlin, E. J. *et al.* Surface strontium enrichment on highly active perovskites for oxygen electrocatalysis in solid oxide fuel cells. *Energy Environ. Sci.* **5**, 6081-6088, doi:Doi 10.1039/C2ee03397f (2012).
- 149 Kubicek, M., Limbeck, A., Fromling, T., Hutter, H. & Fleig, J. Relationship between Cation Segregation and the Electrochemical Oxygen Reduction Kinetics of La_{0.6}Sr_{0.4}CoO_{3-δ} Thin Film Electrodes. *J. Electrochem. Soc.* **158**, B727-B734, doi:Doi 10.1149/1.3581114 (2011).
- 150 Jung, W. & Tuller, H. L. Investigation of surface Sr segregation in model thin film solid oxide fuel cell perovskite electrodes. *Energy & Environmental Science* **5**, 5370–5378, doi:10.1039/c1ee02762j (2012).
- 151 Oh, D., Gostovic, D. & Wachsman, E. D. Mechanism of La_{0.6}Sr_{0.4}Co_{0.2}Fe_{0.8}O₃ cathode degradation. *J. Mater. Res.* **27**, 1992-1999, doi:Doi 10.1557/Jmr.2012.222 (2012).
- 152 Wang, H. Q. *et al.* Mechanisms of Performance Degradation of (La,Sr)(Co,Fe)O_{3-δ} Solid Oxide Fuel Cell Cathodes. *J Electrochem Soc* **163**, F581-F585, doi:10.1149/2.0031607jes (2016).
- 153 Druce, J. *et al.* Surface termination and subsurface restructuring of perovskite-based solid oxide electrode materials. *Energy Environ. Sci.* **7**, 3593-3599, doi:10.1039/c4ee01497a (2014).
- 154 Mutoro, E. *et al.* Reversible Compositional Control of Oxide Surfaces by Electrochemical Potentials. *J. Phys. Chem. Lett.* **3**, 40-44, doi:Doi 10.1021/Jz201523y (2012).
- 155 Finsterbusch, M., Lussier, A., Schaefer, J. A. & Idzerda, Y. U. Electrochemically driven cation segregation in the mixed conductor La_{0.6}Sr_{0.4}Co_{0.2}Fe_{0.8}O_{3-δ}. *Solid State Ionics* **212**, 77-80, doi:DOI 10.1016/j.ssi.2012.02.006 (2012).
- 156 Baumann, F. S. *et al.* Strong performance improvement of La_{0.6}Sr_{0.4}Co_{0.8}Fe_{0.2}O_{3-δ} SOFC cathodes by electrochemical activation. *J. Electrochem. Soc.* **152**, A2074-A2079, doi:Doi 10.1149/1.2034529 (2005).
- 157 Chakrave.Bk. Grain Size Distribution in Thin Films .1. Conservative Systems. *J Phys Chem Solids* **28**, 2401-&, doi:Doi 10.1016/0022-3697(67)90026-1 (1967).

- 158 Chakrave.Bk. Grain Size Distribution in Thin Films .2. Non-Conservative Systems. *J Phys Chem Solids* **28**, 2413-&, doi:Doi 10.1016/0022-3697(67)90027-3 (1967).
- 159 Shah, M., Voorhees, P. W. & Barnett, S. A. Time-dependent performance changes in LSCF-infiltrated SOFC cathodes: The role of nano-particle coarsening. *Solid State Ionics* **187**, 64-67, doi:10.1016/j.ssi.2011.02.003 (2011).
- 160 Shah, M., Hughes, G. A., Voorhees, P. W. & Barnett, S. A. Stability and Performance of LSCF-infiltrated SOFC Cathodes: Effect of Nano-Particle Coarsening. *Ecs Transactions* **35**, 2045-2053, doi:10.1149/1.3570195 (2011).
- 161 Hughes, G. A., Yakal-Kremski, K., Call, A. V. & Barnett, S. A. Durability Testing of Solid Oxide Cell Electrodes with Current Switching. *J. Electrochem. Soc.* **159**, F858-F863, doi:10.1149/2.008301jes (2012).
- 162 E. Ivers-Tiffée, A. W., H. Schichlein. *Electrochemical impedance spectroscopy*. (John Wiley & Sons, 2010).
- 163 Hughes, G., Railsback, J., Butts, D. & Barnett, S. A. Electrochemical Performance of Solid Oxide Cell Oxygen Electrodes Under Pressurization. *Ecs Transactions* **68**, 687-697 (2015).
- 164 Cronin, J. S., Wilson, J. R. & Barnett, S. A. Impact of pore microstructure evolution on polarization resistance of Ni-Yttria-stabilized zirconia fuel cell anodes. *J. Power Sources* **196**, 2640-2643, doi:10.1016/j.jpowsour.2010.10.084 (2011).
- 165 Philippeau, B., Mauvy, F., Mazataud, C., Fourcade, S. & Grenier, J. C. Comparative study of electrochemical properties of mixed conducting Ln(2)NiO(4) (+) (δ) (Ln = La, Pr and Nd) and La_{0.6}Sr_{0.4}Fe_{0.8}Co_{0.2}O₃ (-) (δ) as SOFC cathodes associated to Ce_{0.9}Gd_{0.1}O₂ (-) (δ), La_{0.8}Sr_{0.2}Ga_{0.8}Mg_{0.2}O₃ (-) (δ) and La₉Sr₁Si₆O_{26.5} electrolytes. *Solid State Ionics* **249**, 17-25, doi:10.1016/j.ssi.2013.06.009 (2013).

- 166 Takahashi, S., Nishimoto, S., Matsuda, M. & Miyake, M. Electrode Properties of the Ruddlesden-Popper Series, $\text{La}_{n+1}\text{Ni}_n\text{O}_{3n+1}$ ($n=1, 2, \text{ and } 3$), as Intermediate-Temperature Solid Oxide Fuel Cells. *J Am Ceram Soc* **93**, 2329-2333, doi:DOI 10.1111/j.1551-2916.2010.03743.x (2010).
- 167 Khandale, A. P., Punde, J. D. & Bhoga, S. S. Electrochemical performance of strontium-doped neodymium nickelate mixed ionic-electronic conductor for intermediate temperature solid oxide fuel cells. *J Solid State Electr* **17**, 617-626, doi:DOI 10.1007/s10008-012-1892-3 (2013).
- 168 Harris, W. M. *et al.* Three-dimensional microstructural mapping of poisoning phases in the Neodymium Nickelate solid oxide fuel cell cathode. *Solid State Ionics* **237**, 16-21, doi:DOI 10.1016/j.ssi.2013.01.020 (2013).
- 169 Montenegro-Hernandez, A., Mogni, L. & Caneiro, A. Microstructure and reactivity effects on the performance of $\text{Nd}_2\text{NiO}_{4+\delta}$ oxygen electrode on $\text{Ce}_{0.9}\text{Gd}_{0.1}\text{O}_{1.95}$ electrolyte. *Int J Hydrogen Energ* **37**, 18290-18301, doi:DOI 10.1016/j.ijhydene.2012.09.071 (2012).
- 170 Montenegro-Hernandez, A., Vega-Castillo, J., Mogni, L. & Caneiro, A. Thermal stability of $\text{Ln}_2\text{NiO}_{(4+\delta)}$ (Ln: La, Pr, Nd) and their chemical compatibility with YSZ and CGO solid electrolytes. *International Journal of Hydrogen Energy* **36**, 15704-15714, doi:10.1016/j.ijhydene.2011.08.105 (2011).
- 171 Wan, J., Goodenough, J. B. & Zhu, J. H. $\text{Nd}_{(2-x)}\text{La}_x\text{NiO}_{(4+\delta)}$, a mixed ionic/electronic conductor with interstitial oxygen, as a cathode material. *Solid State Ionics* **178**, 281-286, doi:DOI 10.1016/j.ssi.2007.01.013 (2007).
- 172 Zhou, X. D. *et al.* Electrochemical performance and stability of the cathode for solid oxide fuel cells: V. high performance and stable Pr_2NiO_4 as the cathode for solid oxide fuel cells. *Electrochim Acta* **71**, 44-49, doi:DOI 10.1016/j.electacta.2012.03.067 (2012).
- 173 Ferchaud, C. *et al.* High performance praseodymium nickelate oxide cathode for low temperature solid oxide fuel cell. *J Power Sources* **196**, 1872-1879, doi:DOI 10.1016/j.jpowsour.2010.09.036 (2011).

- 174 Odier, P., Allancon, C. & Bassat, J. M. Oxygen exchange in Pr₂NiO_{4+δ}, at high temperature and direct formation of Pr₄Ni₃O_{10-x}. *J Solid State Chem* **153**, 381-385, doi:DOI 10.1006/jssc.2000.8786 (2000).
- 175 Yang, J. F. *et al.* Preparation and electrochemical properties of strontium doped Pr₂NiO₄ cathode materials for intermediate-temperature solid oxide fuel cells. *Int J Hydrogen Energ* **37**, 1746-1751, doi:DOI 10.1016/j.ijhydene.2011.09.146 (2012).
- 176 Yashima, M., Yamada, H., Nuansaeng, S. & Ishihara, T. Role of Ga³⁺ and Cu²⁺ in the High Interstitial Oxide-Ion Diffusivity of Pr₂NiO₄-Based Oxides: Design Concept of Interstitial Ion Conductors through the Higher-Valence d(10) Dopant and Jahn-Teller Effect. *Chem Mater* **24**, 4100-4113, doi:Doi 10.1021/Cm3021287 (2012).
- 177 Wang, Y. F., Cheng, J. G., Jiang, Q. M., Yang, J. F. & Gao, J. F. Preparation and electrochemical performance of Pr₂Ni_{0.6}Cu_{0.4}O₄ cathode materials for intermediate-temperature solid oxide fuel cells. *J Power Sources* **196**, 3104-3108, doi:DOI 10.1016/j.jpowsour.2010.11.106 (2011).
- 178 Nicholas, J. D. & Barnett, S. A. Measurements and Modeling of Sm_{0.5}Sr_{0.5}CoO_{3-x}-Ce_{0.9}Gd_{0.1}O_{1.95} SOFC Cathodes Produced Using Infiltrate Solution Additives. *J Electrochem Soc* **157**, B536-B541, doi:10.1149/1.3284519 (2010).
- 179 Chen, T. *et al.* Impregnated Nd₂NiO_{4+δ}- scandia stabilized zirconia composite cathode for intermediate-temperature solid oxide fuel cells. *J Power Sources* **269**, 812-817, doi:DOI 10.1016/j.jpowsour.2014.07.073 (2014).
- 180 Kovalevsky, A. V. *et al.* Oxygen permeability, stability and electrochemical behavior of Pr₂NiO_{4+δ}-based materials. *J Electroceram* **18**, 205-218, doi:DOI 10.1007/s10832-007-9024-7 (2007).
- 181 Yashima, M. *et al.* Structural disorder and diffusional pathway of oxide ions in a doped Pr(2)NiO(4)-based mixed conductor. *J Am Chem Soc* **130**, 2762-+, doi:Doi 10.1021/Ja711478h (2008).

- 182 Vohs, J. M. & Gorte, R. J. High-Performance SOFC Cathodes Prepared by Infiltration. *Adv. Mater.* **21**, 943-956, doi:10.1002/adma.200802428 (2009).
- 183 Druce, J. *et al.* Surface termination and subsurface restructuring of perovskite-based solid oxide electrode materials. *Energ Environ Sci*, doi:10.1039/C4EE01497A (2014).
- 184 Jensen, S. H., Sun, X., Ebbesen, S. D. & Chen, M. Pressurized Operation of a Planar Solid Oxide Cell Stack. *Fuel Cells* **16**, 205-218, doi:10.1002/fuce.201500180 (2016).
- 185 Singhal, S. C. Advances in solid oxide fuel cell technology. *Solid State Ionics* **135**, 305-313, doi:Doi 10.1016/S0167-2738(00)00452-5 (2000).
- 186 Yang, W. J. *et al.* Design performance analysis of pressurized solid oxide fuel cell/gas turbine hybrid systems considering temperature constraints. *J. Power Sources* **160**, 462-473, doi:10.1016/j.jpowsour.2006.01.018 (2006).
- 187 Burbank, W., Witmer, D. D. & Holcomb, F. Model of a novel pressurized solid oxide fuel cell gas turbine hybrid engine. *J. Power Sources* **193**, 656-664, doi:10.1016/j.jpowsour.2009.04.004 (2009).
- 188 Braun, R. J. & Kazempoor, P. in *Solid Oxide Fuel Cells: From Materials to System Modeling RSC Energy and Environment Series* (eds M. Ni & T. S. Zhao) 327-382 (Royal Soc Chemistry, 2013).
- 189 Sun, X. *et al.* Thermodynamic analysis of synthetic hydrocarbon fuel production in pressurized solid oxide electrolysis cells. *International Journal of Hydrogen Energy* **37**, 17101-17110, doi:10.1016/j.ijhydene.2012.08.125 (2012).
- 190 Bierschenk, D. M., Wilson, J. R., Miller, E., Dutton, E. & Barnett, S. A. A Proposed Method for High Efficiency Electrical Energy Storage Using Solid Oxide Cells. *Ecs Transactions* **35**, 2969-2978, doi:10.1149/1.3570297 (2011).

- 191 Kazempoor, P. & Braun, R. J. Model validation and performance analysis of regenerative solid oxide cells for energy storage applications: Reversible operation. *International Journal of Hydrogen Energy* **39**, 5955-5971, doi:http://dx.doi.org/10.1016/j.ijhydene.2014.01.186 (2014).
- 192 Drevet, C., Henault, M. & Fouletier, J. Oxygen electrode reaction on stabilized zirconia under high oxygen pressure (up to 100 bar). *Solid State Ionics* **136**, 807-812, doi:Doi 10.1016/S0167-2738(00)00543-9 (2000).
- 193 Matsui, T., Futamura, M., Kikuchi, R. & Eguchi, K. in *Solid Oxide Fuel Cells 10 Vol. 7 ECS Transactions* (eds K. Eguchi, S. C. Singhai, H. Yokokawa, & H. Mizusaki) 851-858 (Electrochemical Society Inc, 2007).
- 194 Zhou, L. *et al.* Performance of an anode-supported tubular solid oxide fuel cell (SOFC) under pressurized conditions. *Electrochim. Acta* **53**, 5195-5198, doi:10.1016/j.electacta.2008.02.032 (2008).
- 195 Thomsen, E. C., Coffey, G. W., Pederson, L. R. & Marina, O. A. Performance of lanthanum strontium manganite electrodes at high pressure. *J. Power Sources* **191**, 217-224, doi:10.1016/j.jpowsour.2009.02.057 (2009).
- 196 Willich, C. W., C.; Seidler, S.; Leucht, F.; Henke, M.; Kallo, J.; Maier, U.; Friedrich, K. A. *Pressurized Solid Oxide Fuel Cells: Operational Behavior*. (German Aerospace Center, German Aerospace Center (DLR), Pfaffenwaldring 38-40, 70569 Stuttgart, Germany, 2011).
- 197 Lankhorst, M. H. R. & tenElshof, J. E. Thermodynamic quantities and defect structure of $\text{La}_{0.6}\text{Sr}_{0.4}\text{Co}_{1-y}\text{Fe}_y\text{O}_{3-\delta}$ ($y=0-0.6$) from high-temperature coulometric titration experiments. *J Solid State Chem* **130**, 302-310, doi:DOI 10.1006/jssc.1997.7378 (1997).
- 198 Nakamura, T., Yashiro, K., Sato, K. & Mizusaki, J. Oxygen nonstoichiometry and chemical stability of $\text{Nd}_{2-x}\text{Sr}_x\text{NiO}_{4+\delta}$. *J Solid State Chem* **182**, 1533-1537, doi:10.1016/j.jssc.2009.03.021 (2009).

- 199 Call, A. V., Railsback, J. G., Wang, H. Q. & Barnett, S. A. Degradation of nano-scale cathodes: a new paradigm for selecting low-temperature solid oxide cell materials. *Phys Chem Chem Phys* **18**, 13216-13222, doi:10.1039/c6cp02590k (2016).
- 200 Dellis, J.-L. *Zfit*, <http://www.mathworks.com/matlabcentral/fileexchange/19460-zfit> (2014).
- 201 J.-P. Diard, B. L. G., C. Montella. (Bio-Logic SAS Instruments, 2013).
- 202 Endler-Schuck, C., Joos, J., Niedrig, C., Weber, A. & Ivers-Tiffée, E. The chemical oxygen surface exchange and bulk diffusion coefficient determined by impedance spectroscopy of porous La_{0.58}Sr_{0.4}Co_{0.2}Fe_{0.8}O_{3-δ} (LSCF) cathodes. *Solid State Ionics* **269**, 67-79, doi:10.1016/j.ssi.2014.11.018 (2015).
- 203 Lu, Y. X., Kreller, C. & Adler, S. B. Measurement and Modeling of the Impedance Characteristics of Porous La_{1-x}Sr_xCoO_{3-δ} Electrodes. *J Electrochem Soc* **156**, B513-B525, doi:10.1149/1.3079337 (2009).
- 204 Ried, P., Bucher, E., Preis, W., Sitte, W. & Holtappels, P. Characterisation of La_{0.6}Sr_{0.4}Co_{0.2}Fe_{0.8}O_{3-δ} and Ba_{0.5}Sr_{0.5}Co_{0.8}Fe_{0.2}O_{3-δ} as Cathode Materials for the Application in Intermediate Temperature Fuel Cells. *Solid Oxide Fuel Cells 10 (Soft-X), Pts 1 and 2* **7**, 1217-1224, doi:10.1149/1.2729221 (2007).
- 205 Bouwmeester, H. J. M., Den Otter, M. W. & Boukamp, B. A. Oxygen transport in La_{0.6}Sr_{0.4}Co_{1-y}Fe_yO_{3-δ}. *J Solid State Electr* **8**, 599-605, doi:10.1007/s10008-003-0488-3 (2004).
- 206 Esquirol, A., Brandon, N. P., Kilner, J. A. & Mogensen, M. Electrochemical characterization of La_{0.6}Sr_{0.4}Co_{0.2}Fe_{0.8}O₃ cathodes for intermediate-temperature SOFCs. *J Electrochem Soc* **151**, A1847-A1855, doi:10.1149/1.1799391 (2004).
- 207 Murray, E. P., Sever, M. J. & Barnett, S. A. Electrochemical performance of (La,Sr)(Co,Fe)O₃-(Ce,Gd)O₃ composite cathodes. *Solid State Ionics* **148**, 27-34 (2002).

- 208 Mauvy, F. *et al.* Electrode properties of $\text{Ln}(2)\text{NiO}(4+\delta)$ ($\text{Ln} = \text{La}, \text{Nd}, \text{Pr}$) - AC impedance and DC polarization studies. *J Electrochem Soc* **153**, A1547-A1553, doi:10.1149/1.2207059 (2006).
- 209 Escudero, M. J., Aguadero, A., Alonso, J. A. & Daza, L. A kinetic study of oxygen reduction reaction on La_2NiO_4 cathodes by means of impedance spectroscopy. *J Electroanal Chem* **611**, 107-116, doi:10.1016/j.jelechem.2007.08.006 (2007).
- 210 Wilson, J. R., Cronin, J. S. & Barnett, S. A. Linking the microstructure, performance and durability of Ni-yttria-stabilized zirconia solid oxide fuel cell anodes using three-dimensional focused ion beam scanning electron microscopy imaging. *Scr. Mater.* **65**, 67-72, doi:10.1016/j.scriptamat.2010.09.025 (2011).
- 211 Hauch, A., Ebbesen, S. D., Jensen, S. H. & Mogensen, M. Solid oxide electrolysis cells: Microstructure and degradation of the Ni/yttria-stabilized zirconia electrode. *J. Electrochem. Soc.* **155**, B1184-B1193, doi:10.1149/1.2967331 (2008).
- 212 Graves, C. Reversing and Repairing Microstructure Degradation in Solid Oxide Cells During Operation. *Solid Oxide Fuel Cells 13 (Sofc-Xiii)* **57**, 3127-3136, doi:10.1149/05701.3127ecst (2013).
- 213 Hughes, G. A., Yakal-Kremiski, K. & Barnett, S. A. Life testing of LSM-YSZ composite electrodes under reversing-current operation. *Physical chemistry chemical physics : PCCP* **15**, 17257-17262, doi:10.1039/c3cp52973h (2013).
- 214 Kazempoor, P., Wendel, C. H. & Braun, R. J. Pressurized Regenerative Solid Oxide Cells for Electrical Energy Storage. *Ecs Transactions* **58**, 45-54, doi:Doi 10.1149/05837.0045ecst (2014).
- 215 Ebbesen, S. D., Jensen, S. H., Hauch, A. & Mogensen, M. B. High Temperature Electrolysis in Alkaline Cells, Solid Proton Conducting Cells, and Solid Oxide Cells. *Chem Rev* **114**, 10697-10734, doi:Doi 10.1021/Cr5000865 (2014).
- 216 Energy, U. S. D. o. Grid Energy Storage. (2013).

- 217 Simner, S. P., Anderson, M. D., Pederson, L. R. & Stevenson, J. W. Performance variability of La(Sr)FeO₃ SOFC cathode with Pt, Ag, and Au current collectors. *J. Electrochem. Soc.* **152**, A1851-A1859, doi:10.1149/1.1995687 (2005).
- 218 Oh, M., Unemoto, A., Amezawa, K. & Kawada, T. Material Stability and Cation Transport of La_{0.6}Sr_{0.4}Co_{0.2}Fe_{0.8}O_{3-δ} in SOFC Cathodic Conditions. *Solid Oxide Fuel Cells 12 (Soft Xii)* **35**, 2249-2253, doi:Doi 10.1149/1.3570220 (2011).
- 219 Comets, O. & Voorhees, P. W. The Stress Engendered by Oxygen Bubble Formation in the Electrolyte of Solid Oxide Electrolysis Cells. *Electrochemical Synthesis of Fuels 1* **41**, 123-128, doi:Doi 10.1149/1.3702419 (2012).
- 220 Hughes, G. A., Railsback, J. G., Yakal-Kremiski, K. J., Butts, D. M. & Barnett, S. A. Degradation of (La_{0.8}Sr_{0.2})(0.98)MnO_{3-δ}-Zr_{0.84}Y_{0.16}O_{2-γ} composite electrodes during reversing current operation. *Faraday Discuss* **182**, 365-377, doi:10.1039/c5fd00020c (2015).
- 221 Kim, S. J. & Choi, G. M. Stability of LSCF electrode with GDC interlayer in YSZ-based solid oxide electrolysis cell. *Solid State Ionics* **262**, 303-306, doi:10.1016/j.ssi.2014.01.001 (2014).
- 222 Tietz, F., Sebold, D., Brisse, A. & Schefold, J. Degradation phenomena in a solid oxide electrolysis cell after 9000 h of operation. *J. Power Sources* **223**, 129-135, doi:10.1016/j.jpowsour.2012.09.061 (2013).
- 223 The, D. *et al.* Microstructural comparison of solid oxide electrolyser cells operated for 6100 h and 9000 h. *J. Power Sources* **275**, 901-911, doi:10.1016/j.jpowsour.2014.10.188 (2015).
- 224 Zheng, Y. F. *et al.* Comparison of performance and degradation of large-scale solid oxide electrolysis cells in stack with different composite air electrodes. *International Journal of Hydrogen Energy* **40**, 2460-2472, doi:10.1016/j.ijhydene.2014.12.101 (2015).
- 225 Lay-Grindler, E. *et al.* Degradation Study of the La_{0.6}Sr_{0.4}Co_{0.2}Fe_{0.8}O₃ Solid Oxide Electrolysis Cell (SOEC) Anode after High Temperature Electrolysis Operation. *Solid Oxide Fuel Cells 13 (Soft-Xiii)* **57**, 3177-3187, doi:10.1149/05701.3177ecst (2013).

- 226 Choi, M. B., Singh, B., Wachsman, E. D. & Song, S. J. Performance of $\text{La}_{0.1}\text{Sr}_{0.9}\text{Co}_{0.8}\text{Fe}_{0.2}\text{O}_{3-\delta}$ and $\text{La}_{0.1}\text{Sr}_{0.9}\text{Co}_{0.8}\text{Fe}_{0.2}\text{O}_{3-\delta}\text{-Ce}_{0.9}\text{Gd}_{0.1}\text{O}_2$ oxygen electrodes with $\text{Ce}_{0.9}\text{Gd}_{0.1}\text{O}_2$ barrier layer in reversible solid oxide fuel cells. *J. Power Sources* **239**, 361-373, doi:10.1016/j.jpowsour.2013.03.154 (2013).
- 227 Virkar, A. V. in *Engineered Ceramics* 59-76 (John Wiley & Sons, Inc., 2016).
- 228 Zhang, T. S., Ma, J., Kong, L. B., Hing, P. & Kilner, J. A. Preparation and mechanical properties of dense $\text{Ce}_{0.8}\text{W}_{0.2}\text{O}_{2-\delta}$ ceramics. *Solid State Ionics* **167**, 191-196, doi:10.1016/j.ssi.2003.11.025 (2004).
- 229 Pathak, S., Steinmetz, D., Kuebler, J., Payzant, E. A. & Orlovskaya, N. Mechanical behavior of $\text{La}_{0.8}\text{Sr}_{0.2}\text{Ga}_{0.8}\text{Mg}_{0.2}\text{O}_3$ perovskites. *Ceram Int* **35**, 1235-1241, doi:10.1016/j.ceramint.2008.06.013 (2009).
- 230 Gao, Z., Mogni, L. V., Miller, E. C., Railsback, J. G. & Barnett, S. A Perspective On Low-Temperature Solid Oxide Fuel Cells. *Energy & Environmental Science*, doi:10.1039/C5EE03858H (2016).
- 231 Kilner, J. A. & Burriel, M. Materials for Intermediate-Temperature Solid-Oxide Fuel Cells. *Annu Rev Mater Res* **44**, 365-393, doi:10.1146/annurev-matsci-070813-113426 (2014).
- 232 Stambouli, A. B. & Traversa, E. Solid oxide fuel cells (SOFCs): a review of an environmentally clean and efficient source of energy. *Renew Sust Energ Rev* **6**, 433-455, doi:Pii S1364-0321(02)00014-X Doi 10.1016/S1364-0321(02)00014-X (2002).
- 233 Laguna-Bercero, M. A. Recent advances in high temperature electrolysis using solid oxide fuel cells: A review. *J Power Sources* **203**, 4-16, doi:10.1016/j.jpowsour.2011.12.019 (2012).
- 234 Sundmacher, K., Rihko-Struckmann, L. K. & Galvita, V. Solid electrolyte membrane reactors: Status and trends. *Catalysis Today* **104**, 185-199 (2005).

- 235 Bouwmeester, H. J. M. Dense ceramic membranes for methane conversion. *Catalysis Today* **82**, 141-150 (2003).
- 236 Dyer, P. N., Richards, R. E., Russek, S. L. & Taylor, D. M. Ion transport membrane technology for oxygen separation and syngas production. *Solid State Ionics* **134**, 21-33 (2000).
- 237 Wang, L., Merkle, R., Mastrikov, Y. A., Kotomin, E. A. & Maier, J. Oxygen exchange kinetics on solid oxide fuel cell cathode materials-general trends and their mechanistic interpretation. *J Mater Res* **27**, 2000-2008, doi:Doi 10.1557/Jmr.2012.186 (2012).
- 238 Tarancon, A., Skinner, S. J., Chater, R. J., Hernandez-Ramirez, F. & Kilner, J. A. Layered perovskites as promising cathodes for intermediate temperature solid oxide fuel cells. *J Mater Chem* **17**, 3175-3181, doi:10.1039/B704320a (2007).
- 239 Kilner, J. A., DeSouza, R. A. & Fullarton, I. C. Surface exchange of oxygen in mixed conducting perovskite oxides. *Solid State Ionics* **86-8**, 703-709, doi:Doi 10.1016/0167-2738(96)00153-1 (1996).
- 240 Ratke, L. & Voorhees, P. W. *Growth and coarsening : Ostwald ripening in material processing*. (Springer, 2002).
- 241 Hayd, J., Dieterle, L., Guntow, U., Gerthsen, D. & Ivers-Tiffée, E. Nanoscaled La_{0.6}Sr_{0.4}CoO_{3-δ} as intermediate temperature solid oxide fuel cell cathode: Microstructure and electrochemical performance. *Journal of Power Sources* **196**, 7263-7270, doi:10.1016/j.jpowsour.2010.11.147 (2011).
- 242 Shah, M., Voorhees, P. W. & Barnett, S. A. Time-dependent performance changes in LSCF-infiltrated SOFC cathodes: The role of nano-particle coarsening. *Solid State Ionics* **187**, 64-67, doi:10.1016/j.ssi.2011.02.003 (2011).
- 243 Nelson, W. *Accelerated Testing: Statistical Models, Test Plans, and Data Analysis*. (John Wiley and Sons, Inc., 1990).

- 244 Wynblatt, P. & Gjostein, N. A. Model Study of Catalyst Particle Coarsening. *Scripta Metall Mater* **7**, 969-975, doi:Doi 10.1016/0036-9748(73)90151-8 (1973).
- 245 Harris, P. J. F., Boyes, E. D. & Cairns, J. A. The Sintering of an Alumina-Supported Platinum Catalyst Studied by Transmission Electron-Microscopy. *J Catal* **82**, 127-146, doi:Doi 10.1016/0021-9517(83)90124-0 (1983).
- 246 McCarty, J. G., Malukhin, G., Poojary, D. M., Datye, A. K. & Xu, Q. Thermal coarsening of supported palladium combustion catalysts. *J Phys Chem B* **109**, 2387-2391, doi:10.1021/jp048822w (2005).
- 247 Fleig, J. r. SOLID OXIDE FUEL CELL CATHODES: Polarization Mechanisms and Modeling of the Electrochemical Performance. *Annu. Rev. Mater. Res.* **33**, 361–382, doi:10.1146/annurev.matsci.33.022802.093258 (2003).
- 248 Nielsen, J. & Hjelm, J. Impedance of SOFC electrodes: A review and a comprehensive case study on the impedance of LSM:YSZ cathodes. *Electrochimica Acta* **115**, 31-45, doi:10.1016/j.electacta.2013.10.053 (2014).
- 249 Nielsen, J., Jacobsen, T. & Wandel, M. Impedance of porous IT-SOFC LSCF:CGO composite cathodes. *Electrochimica Acta* **56**, 7963-7974, doi:10.1016/j.electacta.2011.05.042 (2011).
- 250 Nielsen, J., Klemensø, T. & Blennow, P. Detailed impedance characterization of a well performing and durable Ni:CGO infiltrated cermet anode for metal-supported solid oxide fuel cells. *Journal of Power Sources* **219**, 305-316, doi:10.1016/j.jpowsour.2012.07.031 (2012).
- 251 Utz, A., Joos, J., Weber, A. & Ivers-Tiffée, E. Electrochemical Oxidation at SOFC Anodes: Comparison of Patterned Nickel Anodes and Nickel/8YSZ Cermet Anodes. 1669-1682, doi:10.1149/1.3570154 (2011).
- 252 Viswanathan, K., Iyer, P. V. R. & Mani, B. P. Estimation of Specific Surface-Area and Shape Factors. *Ind Eng Chem Proc Dd* **21**, 345-348, doi:DOI 10.1021/i200017a021 (1982).

- 253 Oksuzomer, M. A. F., Donmez, G., Sariboga, V. & Altincekic, T. G. Microstructure and ionic conductivity properties of gadolinia doped ceria ($Gd_xCe_{1-x}O_{2-x/2}$) electrolytes for intermediate temperature SOFCs prepared by the polyol method. *Ceram Int* **39**, 7305-7315, doi:10.1016/j.ceramint.2013.02.069 (2013).
- 254 DOE, U. S. Fuel Cell Technologies Office Multi-Year Research, Development, and Demonstration Plan - 3.4 Fuel Cells. (2014).
- 255 Burye, T. E. & Nicholas, J. D. Improving $La_{0.6}Sr_{0.4}Co_{0.8}Fe_{0.2}O_{3-\delta}$ infiltrated solid oxide fuel cell cathode performance through precursor solution desiccation. *Journal of Power Sources* **276**, 54-61, doi:Doi 10.1016/J.jpowsour.2014.11.082 (2015).
- 256 Gong, Y. H. *et al.* Stabilizing Nanostructured Solid Oxide Fuel Cell Cathode with Atomic Layer Deposition. *Nano Letters* **13**, 4340-4345, doi:Doi 10.1021/Nl402138w (2013).
- 257 Jung, W. & Tuller, H. L. Investigation of surface Sr segregation in model thin film solid oxide fuel cell perovskite electrodes. *Energ Environ Sci* **5**, 5370-5378, doi:10.1039/c1ee02762j (2012).
- 258 Kubicek, M., Limbeck, A., Fromling, T., Hutter, H. & Fleig, J. Relationship between Cation Segregation and the Electrochemical Oxygen Reduction Kinetics of $La_{0.6}Sr_{0.4}CoO_{3-\delta}$ Thin Film Electrodes. *J Electrochem Soc* **158**, B727-B734, doi:10.1149/1.3581114 (2011).
- 259 Druce, J. *et al.* Surface termination and subsurface restructuring of perovskite-based solid oxide electrode materials. *Energ Environ Sci* **7**, 3593-3599, doi:10.1039/c4ee01497a (2014).